TURBINE VANE GAS FILM COOLING WITH INJECTION IN THE LEADING EDGE REGION FROM A SINGLE ROW OF SPANWISE ANGLED HOLES

by

Gary J. Hanus, Research Assistant
Mel R. L'Ecuyer, Principal Investigator

FINAL REPORT

NASA Grant No. NGR 15-005-147
February 1972 through July 1975

Thermal Sciences and Propulsion Center
School of Mechanical Engineering
Purdue University
West Lafayette, Indiana 47907

Report Number TSPC TR-76-1

April 1976

TURBINE VANE GAS FILM COOLING WITH INJECTION IN THE LEADING EDGE REGION FROM A SINGLE ROW OF SPANWISE ANGLED HOLES

by

Gary J. Hanus, Research Assistant
Mel R. L'Ecuyer, Principal Investigator

FINAL REPORT

NASA Grant No. NGR 15-005-147
February 1972 through July 1975

Thermal Sciences and Propulsion Center
School of Mechanical Engineering
Purdue University
West Lafayette, Indiana 47907

Report Number TSPC TR-76-1

April 1976

PREFACE

The work described in this Final Report was performed by the Thermal Sciences and Propulsion Center, Purdue University, West Lafayette, Indiana, 47907, under the sponsorship of the NASA Lewis Research Center, Turbine Branch, Grant No. NGR15-005-147. The NASA Technical Officer for this grant was Mr. Harry W. Davison.

The experiments described herein were conducted at the NASA Lewis Research Center. The authors are indebted to the NASA personnel for the time and effort devoted to assist in the completion of this research. Those deserving of special recognition are: J. S. Clark, H. W. Davison, and D. J. Poferl of the Turbine Cooling Branch, C. R. Morse and J. W. Norris of the Research Operations Branch, E. A. Holmok, E. J. Maurer, and F. A. Smith of the Research Instrumentation Branch, R. G. Sheehan, B. K. Cieslak, J. H. Chargo and F. M. Nowak of Technical Services, and E. L. Nachman of Data Processing.

The results of this investigation were published in an abbreviated form as AIAA Paper No. 76-43, AIAA 14th Aerospace Sciences Meeting, January 1976.

TABLE OF CONTENTS

TABLE OF CONTENTS (cont'd)

TABLE OF CONTENTS (cont'd)

ABSTRACT

An experimental study of gas film cooling was conducted on a 3X size model turbine vane. Injection in the leading edge region was from a single row of holes angled in a spanwise direction. The suction surface injection configurations investigated were: injection angle, β = 18°, 35°; location of holes from stagnation, x_i/L_S = 0.083, 0.150, 0.228. Experiments were conducted at reduced freestream pressure and temperature to simulate a leading edge Reynolds number, $Re_D = 1.6 \times 10^5$ and a coolant-to-mainstream density ratio of $\rho_c/\rho_\infty \approx 2.18$. Measurements of the local heat flux downstream from the row of coolant holes, both with and without film coolant flow, were used to determine the film cooling performance presented in terms of the Stanton number ratio, ST_{FC}/ST_0. Results for a range of coolant blowing ratio, M = 0 to ≈ 2.0, indicate a reduction in heat flux of up to 15 to 30 percent at a point 10 to 11 hole diameters downstream from injection. An optimum coolant blowing ratio corresponds to a coolant-to-freestream velocity ratio in the range of 0.5. The shallow injection angle resulted in superior cooling performance for injection closest to stagnation, while the effect of injection angle was insignificant for injection further from stagnation.

NOMENCLATURE

A	area; constant in cooling effectiveness correlation
B	film cooling correlating parameter
b	exponent for (x'/MS) in effectiveness correlation
C	exponent for coolant Reynolds number in effectiveness correlation
C_D	drag coefficient for cylinder-in-crossflow
C_F	skin friction coefficient
C_{MF}	geometric modeling factor
C_p	specific heat at constant pressure
C_v	specific heat at constant volume
C^*	correction factor to account for real flow effects in slug flow analysis
d_0	coolant hole diameter
d_w	turbulence screen wire diameter
E	Eckert number, $V_\infty^2/C_p(T_{T_\infty} - T_w)$
F	force
G	Grashof number, $\rho^2 g\beta_0(T_{T_\infty} - T)L^3/\mu^2$
g	local acceleration of gravity
g_c	constant relating units of force, mass and length, $g_c = 32.17\ lb_m\text{-ft}/lb_f\text{-sec}^2$
H	test section duct height
H'	boundary layer shape factor
h	local heat transfer coefficient, $q''/(T_{T_\infty} - T_w)$

NOMENCLATURE (cont'd)

h'	local heat transfer coefficient with film cooling and $T_C = T_{T_\infty}$, $q''_{FC}/(T_{ADW} - T_{W,FC})$
$\overline{h}'$	laterally averaged heat transfer coefficient with $T_C = T_{T_\infty}$
I	momentum flux ratio, $\rho_C V_C^2/\rho_\infty V_\infty^2$
i	angle between surface and gradient of gravitational potential field
K	acceleration parameter, $(\nu_\infty/V_\infty^2)dV_\infty/dx$
k^*	proportionality constant
L	characteristic length; length of coolant slot
L'	length of film cooling hole
ℓ_1	shear-layer length of separation bubble
ℓ_2	reattachment length of separation bubble
M	blowing ratio, $\rho_C V_C/\rho_\infty V_\infty$
Ma	Mach number
$\dot{M}_e$	mass flux of entrained fluid into coolant jet
M_S	turbulence screen mesh spacing
m	meter (length or dimension)
$\dot{m}$	mass flowrate
$(m\delta)$	film cooling variable, function of B
N	number of film cooling holes
$\hat{n}$	unit normal vector
P	pressure
p	pressure
p'	dimensionless pressure, $p/\rho_\infty V_\infty^2$
Pr	Prandtl number

NOMENCLATURE (cont'd)

q	weight flow of coolant per unit width of plate
q"	heat flux
R"	characteristic radius
R'	radius of curvature
Re	Reynolds number
R	gas constant
S	coolant slot height
S_1	spacing between coolant hole centerlines
ST	Stanton number
T	temperature
$\overline{T}$	average boundary layer temperature
t	wall thickness
U,u	time averaged streamwise velocity
u'	fluctuating velocity component in streamwise direction; dimensionless velocity in x-direction, u/V_∞
V	velocity
v	velocity component in vertical direction
v'	dimensionless velocity in y-direction, v/V_∞
W	test section duct width
w	coolant weight flow
X	film cooling parameter according to Spalding
x	distance in streamwise direction
x'	distance downstream of cooling holes, $x-x_i$; also x/L
x*	dimensionless streamwise distance from cooling holes, x/d_0
y	vertical distance from surface

NOMENCLATURE (cont'd)

y'	dimensionless vertical distance, y/d_0; also y/L
y^*	penetration distance of coolant jet into boundary layer
z	spanwise or lateral coordinate
z'	dimensionless spanwise distance, z/d_0; also z/L

GREEK

α	streamwise injection angle; thermal diffusivity
α^*	dimensionless coolant jet trajectory parameter
α_1	component of compound injection angle measured from surface
α_2	component of compound injection angle measured clockwise from positive x-axis in x-z plane
β	spanwise injection angle
β'	ratio of orifice or venturi diameter to pipe diameter
β_0	coefficient of thermal expansion
$\overline{\beta}$	distance from effective origin of boundary layer
$\overline{\beta}_1$	distance from boundary layer origin to point where cooling effectiveness is unity
γ	ratio of specific heats, C_p/C_v
δ	boundary layer thickness
δ_1, δ^*	displacement boundary layer thickness
ϵ	cooling effectiveness, identical to η
ϵ_p	point source thermal diffusivity
η	cooling effectiveness parameter
η^*	dimensionless coordinate normal to surface
θ	momentum boundary layer thickness
θ'	dimensionless temperature $(T_{T_\infty} - \overline{T})/(T_{T_\infty} - T_W)$

NOMENCLATURE (cont'd)

μ	dynamic viscosity
ν	kinematic viscosity
ξ	dimensionless streamwise coordinate; coordinate along coolant jet axis
ρ	density
ρ'	dimensionless density
Φ	viscous dissipation function
Φ'	heat flux ratio, q''_{FC}/q''_0
χ	angle between x-axis and tangent to coolant jet trajectory
ω	power of temperature ratio for gas viscosity variation with temperature
ω'	frequency

SUBSCRIPTS

ADW	adiabatic wall condition
B	bulk
C	coolant
CHAR	characteristic
FC	film cooling condition
i	injection
ISO	isothermal condition
IW	impervious wall condition
J	jet
L	lower
LE	leading edge
0	initial condition

NOMENCLATURE (cont'd)

OPT	optimum condition
OPT,NEAR	optimum condition for q" measurement location nearest the injection holes
P	pressure surface
RE	at reattachment
REF	reference
RMS	root-mean-square
S	suction surface
SEP	at separation
SP	span
T	total condition
U	upper
W	wall
X	in streamwise direction
0	without film cooling
∞	freestream
Δ	based on boundary layer energy thickness
θ	based on boundary layer momentum thickness

I. INTRODUCTION

I.1. General Discussion

In many engineering applications, the successful performance of an overall system depends upon maintaining tolerable temperature levels at various times and locations within the working cycles of the individual components. This is especially true in the gas turbine industry as turbine efficiency and work output increase as the maximum cycle operating temperature is elevated. Consequently, to survive the severe thermal environment created by high combustor exit temperatures, the initial stages of the turbine must be cooled. Convective cooling, internal to turbine vanes and blades, has been used extensively; however, increased operating pressures and temperatures require external cooling to augment internal cooling configurations (1)*. Gas film cooling is one such external cooling technique.

Film cooling is accomplished by injecting, at discrete locations, a relatively cool, secondary fluid into the boundary layer of a surface exposed to a hot, primary mainstream flow. The injected coolant film is analogous to an external heat sink, providing a blanket protection that progressively deteriorates as the coolant film moves farther from the site of injection.

*Numbers in parentheses refer to REFERENCES.

The present investigation is concerned with determining the cooling effectiveness of a specific gas film cooling injection geometry located in the leading edge region of an inlet turbine vane. The following two sections will discuss the general film cooling problem, its relevance to gas turbine design and the impetus behind the present choice of injection configurations and parameters.

I.2. Statement of the Problem

Since trends point toward future gas turbine operating pressures and temperatures up to $4.05\times10^{6}\,N/m^{2}$ (40 atm) and 2200°K (3500°F), there is a need to thoroughly understand and improve upon current film cooling techniques in order to adequately augment internal cooling schemes.

The basic problem associated with film cooling is the determination of the degree to which a particular injection configuration can effectively reduce the local heat flux conditions downstream of injection. Figure 1 illustrates the basic gas film cooling configuration with a relatively cool fluid injected into the hot gas boundary layer at $x = x_i$. With zero film coolant flow, the surface heat flux for prescribed hot gas and wall temperatures is q''_o. With film coolant injection, the coolant film acts as an effective heat sink, reducing the surface heat flux downstream from injection to q''_{FC}. Thus, external film cooling reduces the amount of internal heat removal necessary to maintain the prescribed wall temperature for $x > x_i$. As the cool fluid elements move farther from injection the coolant film loses its "identity" as a protective layer due to an increase in the fluid element temperature and mixing with hot gas stream. Consequently, the reduced heat flux, q''_{FC}, approaches a

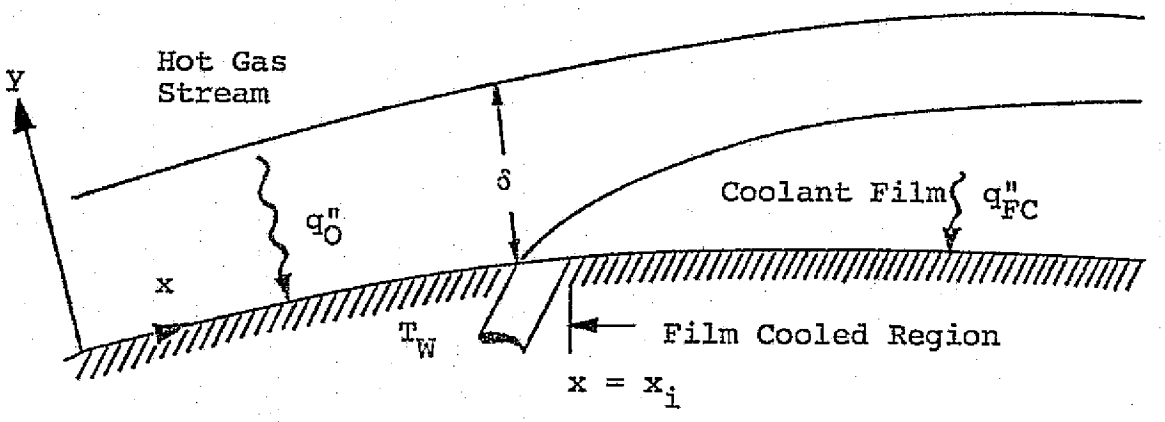

Figure 1. Illustration of Gas Film Cooling Process.

condition characteristic of the normal, uncooled boundary layer heat transfer for large distances downstream from injection. The primary objective of any film cooling study is to determine how effective a given coolant injection geometry is in reducing the local heat flux under a range of coolant and freestream flow conditions in order to identify configurations and flow conditions for optimum or most effective film cooling performance.

The subject investigation is concerned with a twofold problem in relation to gas film cooling for application to the design of high pressure and high temperature gas turbine engines:

(1) effective cooling of the high heat flux leading edge region of an inlet turbine vane subject to geometric injection constraints which may be imposed by significant leading edge surface curvature, and

(2) determining the heat flux reduction characteristic of the configuration implied in (1) at flow conditions that simulate the actual turbine environment.

The manner in which these two problems are confronted in the current study will now be discussed.

I.3. Research Objectives

The purpose of the subject investigation is to provide meaningful information on gas film cooling of turbine vanes in the form of correlations for the local surface heat flux reduction for use in the design of high temperature and high pressure gas turbine engines.

Film cooling configurations are considered that offer a practical solution to reducing the heat load in the leading edge region of an inlet turbine vane. Some of the most severe heat loads within the entire working cycle of the gas turbine engine are experienced at the leading edge of a first-stage, inlet turbine vane. Consequently, a film cooling configuration that can provide both uniform and effective film coverage would be required in this critical area. Conventional injection geometries, consisting of a row or multiple rows of holes angled to the surface in a streamwise direction, as depicted in Fig. 2(a), are frequently employed for turbine vane film cooling. However, the use of film cooling in the leading edge region is restricted by the surface which limits the minimum injection angle that can be used for coolant injection in the streamwise direction. As indicated in Fig. 2(a), for streamwise injection through a typical vane wall thickness of 1.27×10^{-3}m (0.050 inch) and leading edge radius of 5.08×10^{-3}m (0.20 inch), the shallowest possible injection angle would be near 41° with respect to the surface tangent. Steep injection angles enhance mixing between the coolant and mainstream and should be avoided.

An alternative film coolant injection configuration for the leading edge region is the use of coolant holes that are normal to the mainflow, yet angled to the surface in the lateral or spanwise direction as shown in Fig. 2(b). It has been shown (2) that a single hole with this orientation provides a wider field of film coverage than streamwise injection. Thus, in view of the surface curvature problem for leading edge cooling, the use of spanwise film coolant injection may provide the designer greater freedom to utilize shallow injection angles for improved film cooling performance.

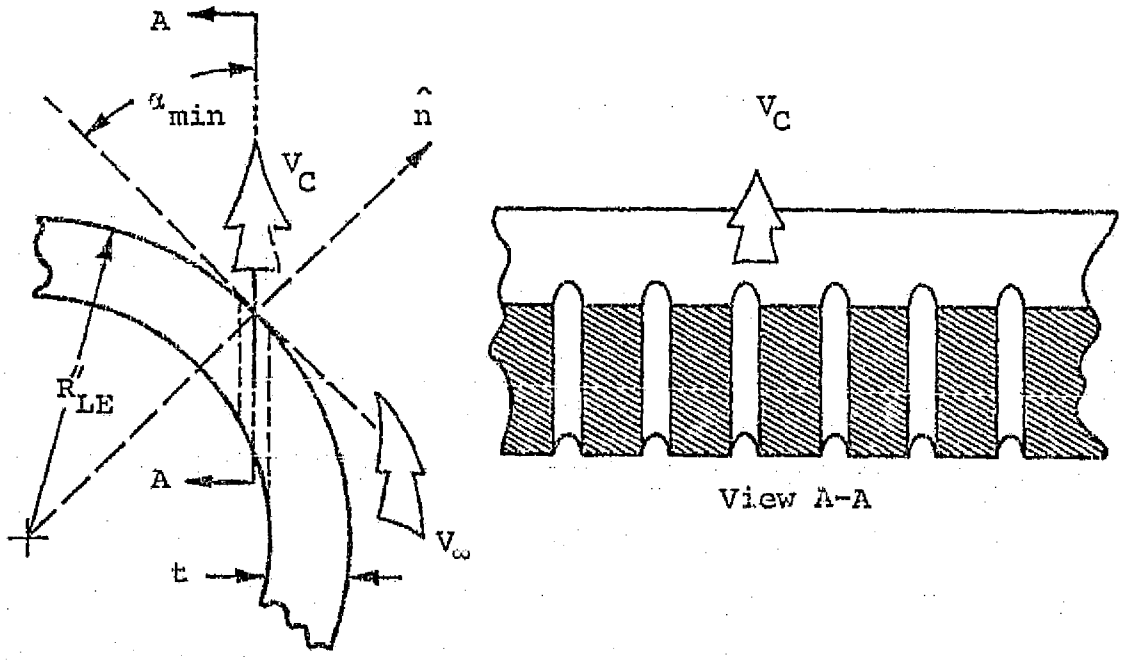

a. Streamwise Injection

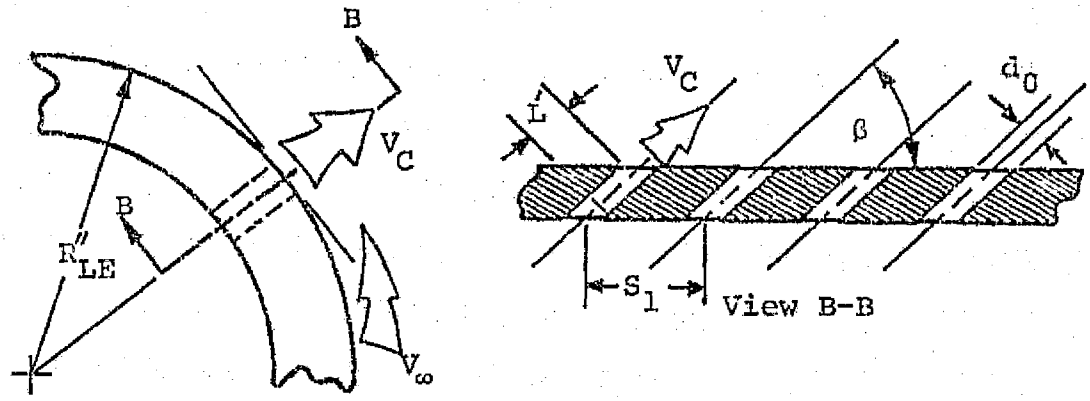

b. Spanwise Injection

Figure 2. Leading Edge Cooling Configurations.

In the present study, experiments were conducted to determine the film cooling performance for a single row of spanwise angled holes located in the leading edge region of a model turbine vane. The heat transfer and flow environment of the prototype high temperature, high pressure first stage turbine vane were simulated using a 3X size model vane positioned in a two-dimensional channel located downstream from a hot-gas generator. The inlet Reynolds Number $(Re)^*$, Mach number (Ma), and freestream turbulence intensity (Tu) were chosen to match the inlet conditions of the prototype vane. The model vane was oriented within the channel to reproduce the local Mach number distribution (Ma_X) and flow deflection of the prototype vane. The model vane test surfaces were water cooled (internally), independent of the gas film cooling system, in order to simulate a large freestream gas-to-wall temperature ratio (T_{T_∞}/T_W) representative of the boundary layer density variations for the high temperature prototype vane.

The film cooling experiments were conducted using a single row of spanwise angled holes (β = 18°, 35°), a hole spacing-to-diameter ratio (S_1/d_0) of 4.0, with the row of holes positioned at three different locations in the leading edge region. The injection of cool air ($T_C \approx T_W$) resulted in a hot gas-to-coolant temperature ratio of approximately 2.0. Miniature heat flux sensors were used to measure the local heat flux both with and without film coolant injection and the film cooling performance was presented in terms of the local Stanton number ratio, ST_{FC}/ST_0.

---

*Symbols introduced in parentheses are defined in the Nomenclature.

The objectives of the experimental film cooling study were to:

(1) measure the reduction in heat flux to the vane surface due to coolant injection from a single row of spanwise angled holes,

(2) determine the influence of the coolant injection angle, β,

(3) determine the influence of the location of the row of holes in the leading edge region, and

(4) determine, for the simulated turbine environment ($T_{T_\infty}/T_C \approx 2.0$), the film coolant flow conditions that result in the optimum film cooling performance.

The nature of the film coolant injection geometry studied, the range of cooling parameters investigated, and the presentation of heat transfer data obtained under simulated gas turbine conditions are the features of this investigation that will contribute to gas turbine design capabilities.

II. LITERATURE SURVEY

II.1. Background Information

Prior to a discussion of the literature concerning previous film cooling studies relevant to gas turbine cooling applications, a brief orientation will be presented. Familiarization with the various film cooling techniques in light of their utility for turbine applications, introduction to and definition of terms that characterize the "cooling effect" of injection, and a brief description of the physical significance of key cooling parameters are items that will be included to make the presentation of the literature review more meaningful.

A variety of methods can be used to effectively film cool a surface. The cool, secondary fluid may enter the external boundary layer through slots, holes, or a combination of the two. Figure 3 shows the basic geometric configurations used in gas turbine cooling. Tangential slots and slots with holes are well adapted to combustor liner cooling. Use of these techniques is not suitable for smaller components, such as turbine blades and vanes, for fabrication, structural, and aerodynamic reasons. Rows of angled holes, staggered rows of holes and interrupted, tangential slots in the vane and blade trailing edge are generally the accepted configurations for turbine applications. Although holes provide a practical answer for small component cooling, continuous, tangential slot

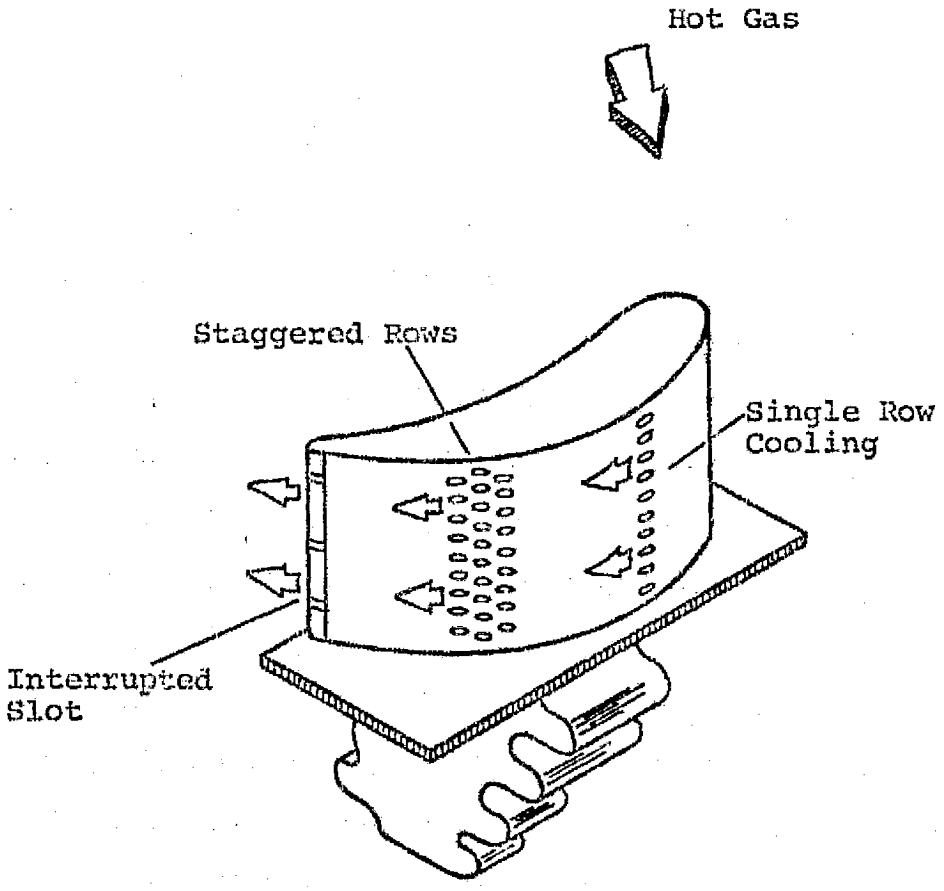

Figure 3. Typical Turbine Blade Film Cooling Configuration

injection has been demonstrated to show greater cooling potential in light of its minimal interaction with the hot primary mainstream.

In order to illustrate the comparative capability of cooling with a slot and a row of holes, Fig. 4(a) is presented. Sketches of the two cooling techniques are followed by representative cooling results. The basic features of the cooling techniques common to both configurations are the wall temperature downstream of injection (T_W), the coolant blowing ratio, $M = (\rho V)_c/(\rho V)_\infty$, the coolant injection angle (α), a characteristic injection dimension (slot width, S, or hole diameter, d_0), and the downstream distance (x) from the point of injection.

For an insulated wall, the downstream wall temperature (T_{ADW}, adiabatic wall temperature) represents the degree to which the hot gas (T_{T_∞}) has been reduced in temperature at x due to injection of cool air (T_C). This effective reduction in T_{T_∞} can be conveniently expressed as $(T_{T_\infty} - T_{ADW})/(T_{T_\infty} - T_C)$ and is commonly given the name, adiabatic wall cooling effectiveness (η_{ADW}).

The results presented in Fig. 4(a) show the variation in η_{ADW} with the dimensionless distance from injection $(x-x_i/d_0)$ for the two cooling techniques. A comparison is made between a single row of holes, angled in the freestream direction at 35° to the surface, and a two-dimensional slot at 30° to the wall. The holes are at 3 diameter spacings. The data shown represents both the effectiveness along the centerline of a hole and that characteristic of a lateral average across the span of the entire row. The slot effectiveness is represented with an equation by Hartnett, Birkebak and Eckert (3) that correlated their data for $(x'/MS) > 60$, where $x' = x - x_i$. Since the data for the row of holes

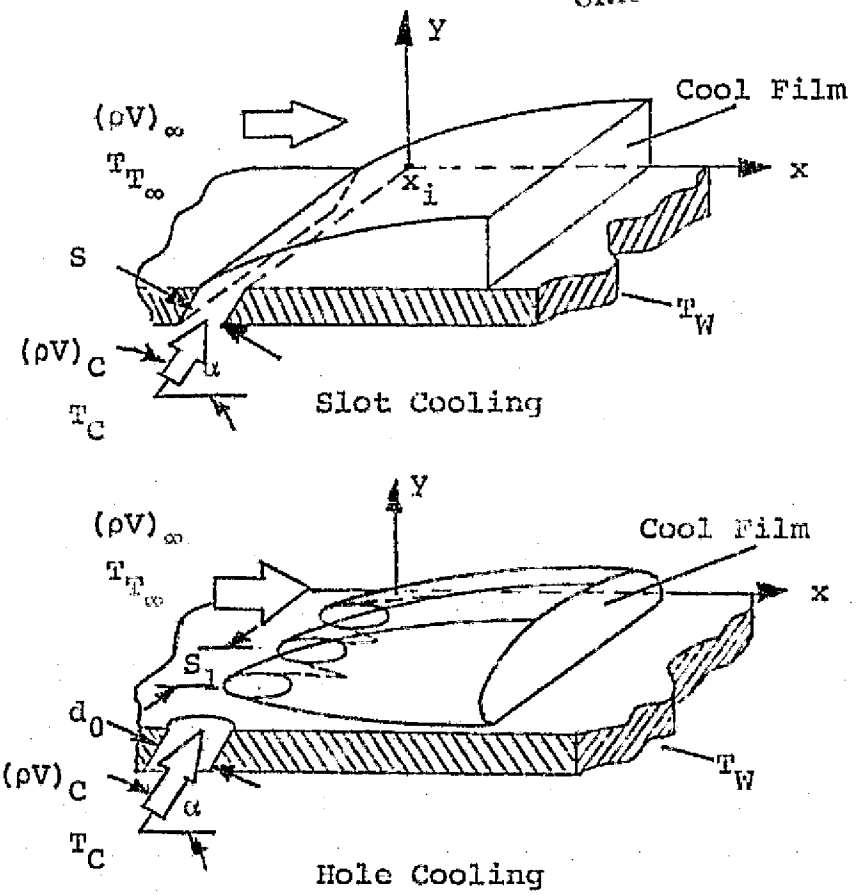

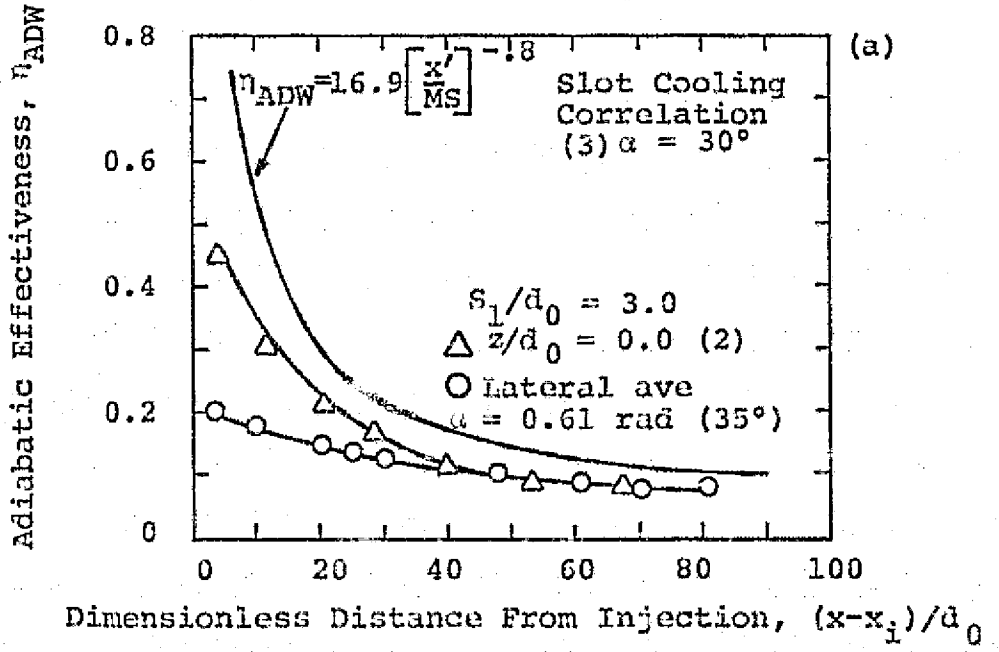

Figure 4(a). Comparison of Slot Cooling and a Single Row of Coolant Holes.

represents an optimum condition for that geometric configuration with M = 0.5, the slot effectiveness was calculated using an M of unity (an optimum coolant mass flux condition for slot cooling). The slot height S was then adjusted in order to inject the same amount of coolant mass as in the row of holes. For the given hole spacing ($S_1/d_0 = 3.0$), S was calculated to be $0.131d_0$.

The slot is shown to be 3 times more effective near injection ($x'/d_0 \approx 15$) and is still 40% better than the row of holes at 40 diameters downstream of injection. This comparison is based on the lateral average of the effectiveness. Though the slot configuration appears to be more effective than a row of holes, the decay rate of the cooling effectiveness for each technique is too severe for use in cooling extensive surface areas. A superposition of the effects of single row, hole cooling, by using multiple rows, would seem to be a logical extension in the development of practical cooling configurations.

As the number of rows of holes are increased over a specified surface area and the spacing between holes decreases, the closely-packed array approaches, in the limit, transpiration cooling (a cooling technique in which the coolant is injected uniformly over the entire surface through a porous media). Figure 4(b) shows a comparison both pictorially and graphically between transpiration and multiple row (also termed for many rows, "full-coverage") film cooling. The cooling parameters are essentially identical to those previously discussed with the added feature that the coolant flow is uniformly distributed over a transpired surface while, for multiple row cooling, injection occurs at discrete locations.

Figure 4(b) presents data from Choe, Kays and Moffat (4) for an 11 row array of holes at 5 diameter spacings and angled perpendicular to the

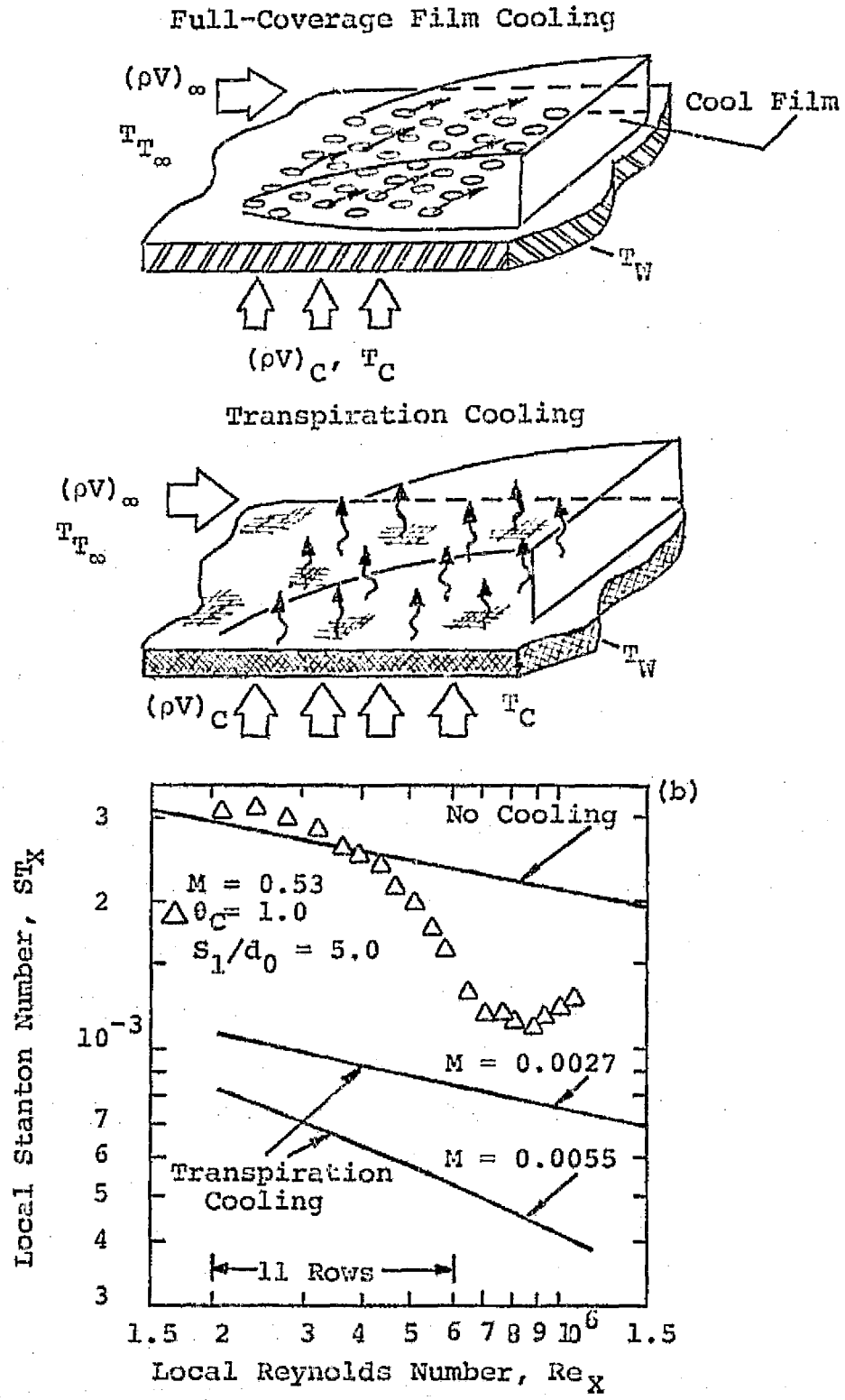

Figure 4(b). Comparison of Transpiration and Full Coverage Film Cooling.

main flow. An exit coolant temperature equal to the external wall temperature was prescribed ($\theta_C' = 1$). The local Stanton number (ST_x) is shown as a function of the local Reynolds number (Re_x) for a blowing ratio, M, of 0.53 (represented by symbols). The local Stanton number variation with Re_x is also shown as solid lines for an uncooled boundary layer and a transpired boundary layer at two different values of the blowing ratio, M (M = 0.0027 and 0.0055).

The results from the first 4 rows of holes (represented by the initial 4 symbols above the M = 0 line) show the initial penalty that must be paid in the form of increased heat transfer just due to the magnitude of the turbulent mixing generated by injection. Between rows 5 and 11 the heat transfer to the surface is reduced by nearly 40% over the uncooled wall (M = 0). Following the final injection row, the heat flux continues to decrease due to the termination of injection-related turbulence and the cool mass addition accumulated from the previous 11 rows. This so called "full-coverage" film cooling is compared to the heat transfer conditions that would exist over the same test area if the boundary layer was fully transpired. Blowing ratios (synonomous with mass flux ratio or M) of 0.0027 and 0.0055, representing one tenth and one fifth, respectively, of the total 11 row coolant flow rate are shown in relation to the full-coverage case. For transpiration mass flow rates approaching the total, hole coolant flow, there is at least an order of magnitude difference between the film cooled Stanton number, that can presently be achieved with full-coverage configurations, and the fully transpired boundary layer.

With film cooling from multiple hole configurations shown to be one practical means of achieving effective overall cooling, information

related to single row cooling under a variety of conditions is still necessary as a building block for predicting the performance of full-coverage configurations. Additional research to understand the physics of injection and to apply this knowledge to creative configuration concepts is necessary if the gap between practical cooling and transpiration cooling is to be closed.

Having placed the application of film cooling techniques in perspective, it is now appropriate to discuss in detail the manner in which the potential of various cooling configurations can be characterized. In addition, the relationship between the cooling potential and pertinent injection parameters will be noted.

II.1.1. Concept of Cooling Effectiveness

II.1.1.1. The Adiabatic Wall Temperature Effectiveness

The primary objective of film cooling research is to develop the capability of predicting wall temperature distributions on a film cooled surface. Eckert (5) postulated that the heat flux to a surface undergoing film cooling can be approximated by

$$q''_{FC} = h_0 \, (T_{ADW,FC} - T_{W,FC}) \tag{1}$$

where

q''_{FC} = wall heat flux with film cooling

h_0 = heat transfer coefficient without film cooling

$T_{ADW,FC}$ = adiabatic wall temperature with film cooling

T_W = actual wall temperature with film cooling

The film cooling adiabatic wall temperature, $T_{ADW,FC}$, reflects the degree to which the external hot gas has been reduced in temperature near the wall due to addition of a cooler fluid. This reduction in the local hot gas temperature is expressed as the following ratio

$$\eta_{ADW} = \frac{T_{T_\infty} - T_{ADW}}{T_{T_\infty} - T_C} \qquad (2)$$

and given the name adiabatic wall cooling effectiveness, η_{ADW}. Film cooling studies conducted over an adiabatic surface yield adiabatic wall temperature distributions that are functions of such parameters as the amount of mass injection, the angle of injection, freestream turbulence characteristics and the local nature of the boundary layer. The measured adiabatic wall temperature represents a characteristic temperature of the boundary layer at a particular location downstream from injection which the wall sees as the driving force for heat transfer.

Therefore, if one chooses a particular cooling scheme, the adiabatic effectiveness can be expressed as a known function of the distance from injection. Knowing the adiabatic wall temperature distribution from the effectiveness data then allows Eqn. (1) to be used to calculate the amount of heat removal needed in a design to maintain a specified wall temperature. A note of caution is in order, however, concerning the use of Eqn. (1). It was assumed that the local heat transfer coefficient was unaffected by the addition of mass into the boundary layer. Use of h_0 as the local heat transfer coefficient under film cooling conditions is only valid far from the injection site. As film coolant is introduced into the hot gas boundary layer, disturbances are created by the injection

process (i.e. highly energetic turbulent conditions are established) which enhance the transport of mass, momentum and energy. The region affected by these hydrodynamic "blowing effects" usually extends to fifty coolant hole diameters downstream of injection, but may reach as far as 80 to 100 diameters as shown in Fig. 5(a) and (b). Before Eqn. (1) can be applied near injection, the variation in the local heat transfer coefficient must be known.

For slot-type cooling, Fig. 5(a) shows the variation in the ratio of the local heat transfer coefficient with injection (h') to that without injection (h_0) for up to 90 slot widths downstream (6). The slot was angled at 30° to the surface and the blowing ratio, M, varied from 0.34 to 0.87. At M = 0.87, as much as a 40% increase in the local convective heat transfer coefficient was reported. This increase depends on M and can persist up to 40 slot widths downstream. The increase in (h'/h_0) is probably related to the turbulence generated by the interaction of the coolant stream and the main flow at injection.

Figure 5(b) shows a similar trend in the heat transfer coefficient for injection from a row of holes angled at 35° to the surface and at 3 hole diameter spacings (7). The ratio of the laterally averaged (across the span of the holes) heat transfer coefficient with injection, $\overline{h}'$, to that without injection, h_0, is shown as a function of M for downstream distances of 6.7 to 71.8 hole diameters. On the average, $\overline{h}'/h_0$ decreases from unity at M = 0 to a minimum of 0.92 at M = 0.5. For M > 0.5, the injection-related turbulence may be acting to increase $\overline{h}'/h_0$ in a monotonic fashion out to M = 2.0. At this condition $\overline{h}'/h_0$ increases to nearly 1.25 for regions near injection ($x'/d_0 < 10$). For the lower

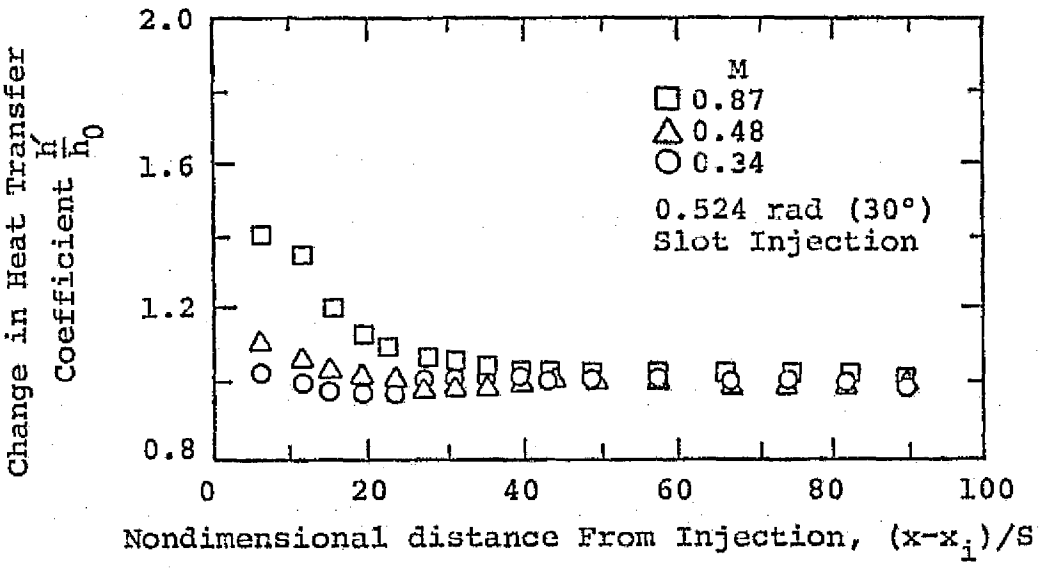

Figure 5(a). Increase in the Heat Transfer Coefficient With Blowing Ratio For a Slot (6).

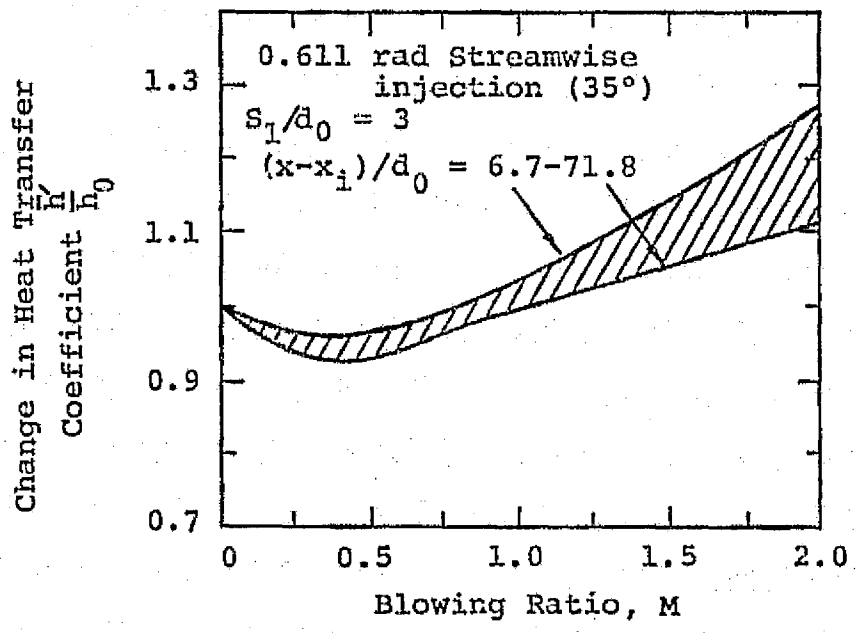

Figure 5(b). Increase in the Heat Transfer Coefficient With Blowing Ratio For a Row of Holes (7).

values of blowing ratio, $\overline{h}'/h_0$ changes only slightly downstream; however, for M > 1.0 the difference between the heat transfer coefficient near injection and far downstream begins to become more significant.

In summary, the adiabatic wall temperature approach to film cooling requires some basic qualifications. The use of Eq. (1) is valid only far from injection where hydrodynamic "blowing" effects have diminished. To use Eq. (1) near injection knowledge of the heat transfer coefficient, h', is essential. An alternate approach used to characterize film cooling effectiveness is outlined in the following section.

II.1.1.2. Cooling Effectiveness From Heat Transfer Data

The cooling effectiveness of an injection configuration can be defined from direct heat transfer measurements. Under this approach,

$$q''_{FC} = h_{FC} \left(T_{T_\infty} - T_{W,FC}\right) \tag{3}$$

where

h_{FC} = local heat transfer coefficient with film cooling

A cooling effectiveness can be defined from Eq. (3) to reflect the reduction in heat flux due to film cooling. Thus,

$$\frac{q''_0 - q''_{FC}}{q''_0} = 1 - \frac{h_{FC}}{h_0} \frac{\left[T_{T_\infty} - T_{W,FC}\right]}{\left[T_{T_\infty} - T_{W,0}\right]} \tag{4}$$

where

q''_0 = heat flux to wall without film cooling

$T_{W,0}$ = wall temperature without film cooling

When $T_{W,FC} \approx T_{W,O}$, Eq. (4) is given the name, isothermal cooling effectiveness, η_{ISO}, where

$$\eta_{ISO} = \frac{q''_O - q''_{FC}}{q''_O} = 1 - \frac{h_{FC}}{h_O} \tag{5}$$

This method of characterizing the cooling effectiveness incorporates into h_{FC} all of the phenomena of coolant injection; namely, (a) the heat-sinking effect responsible for lowering the hot gas temperature near the wall, and (b) the hydrodynamic effects of injection. More simply,

$$h_{FC} = h_{FC}\ (T_C,\ \text{hydrodynamic injection effects}) \tag{6}$$

In comparing the adiabatic wall effectiveness concept and the isothermal effectiveness concept one finds that both methods require an investigation of two unknowns; namely, (a) the determination of the coolant temperature effect on either T_{ADW} or (q''_{FC}/q''_O) and (b) the identification of the hydrodynamic "blowing effects" as manifest in either $\overline{h}'/h_O$ or (q''_{FC}/q''_O) at $T_C = T_{T_\infty}$. The isothermal effectiveness approach may prove more convenient in that heat transfer measurements are made to identify both items (a) and (b) above. The adiabatic wall effectiveness method first requires insulated wall temperature measurements and then a separate series of heat transfer measurements to identify $\overline{h}'/h_O$.

The film cooling effectiveness, whether adiabatic or isothermal, will be a function of numerous cooling parameters. The following discussion is intended to introduce these pertinent parameters in such a way as to build a foundation for a basic understanding of the phenomenon of gas film cooling.

II.1.2. Introduction to Parameters Affecting Cooling Effectiveness

The purpose of introducing the present section is to give the reader a general picture of the physical significance of some of the more important parameters that affect film cooling effectiveness. Documentation of statements made concerning the importance of each item will appear in the next section. The following discussion is intended only as a means to introduce the reader to the items which later will be presented in detail.

Application of film cooling techniques to protect critical components requires a detailed understanding of numerous hydrodynamic, geometric and thermodynamic variables that are characteristic of discrete, secondary, coolant injection. The dominant factors affecting the degree of interaction between a jet of cool injected fluid and an external, hot primary stream are: the coolant-freestream momentum flux ratio (or coolant-freestream mass flux ratio), the injection angle of the coolant jet relative to the surface and the coolant-freestream temperature ratio.

The trajectory of a jet injected into a hot gas mainstream depends to a great degree upon the momentum flux ratio, I, where

$$I = \frac{\rho_c V_c^2}{\rho_\infty V_\infty^2} = \left(\frac{V_c}{V_\infty}\right) M \qquad (7)$$

The greater the coolant jet momentum, the deeper the penetration of the jet into the mainstream. Furthermore, as noted in Eq. (7), increases in I will mean subsequent increases in the amount of coolant mass added to the boundary layer (i.e. mass flow of coolant is proportional to M). However a condition may be established at sufficiently large values of I in which the coolant mass that is added is no longer in the proximity of

the wall due to the extreme penetration. The resulting jet trajectory is conducive to enhanced mixing with the hot mainstream, realizing negligible cooling effects at the wall.

The trajectory of the coolant fluid is also related to both the degree of mainstream mass entrained into the injected jet and the drag forces acting on the exposed frontal area of the issuing jet. In the near regions of injection, the development of the coolant jet trajectory is dominated by any initial component of momentum parallel to the mainstream that may be imparted by angled injection. The combination of coolant momentum flux, mass entrainment and drag forces determines the extent to which the injected film covers the surface. In addition to keeping the injected jet as near the wall as practical, the coolant jet must function in a thermodynamic sense. The coolant temperature relative to the freestream level must provide the necessary heat sink capacity to aid in reducing the hot gas temperature near the wall. Variations in the coolant temperature must, however, be considered in light of its effect on the momentum flux ratio.

Covering the surface to be protected with a continuous, uniform, cool film is the ultimate objective with discrete (hole) injection. The two most significant parameters associated with uniform film coverage are the center-to-center, coolant-hole spacing and the number of rows of coolant holes employed. The larger the spacing ratio, the greater the opportunity for the mainstream, hot fluid to freely move between and under the discrete coolant jets. This promotes greater interaction between the hot primary and cold secondary fluids. Reducing the distance between adjacent coolant jets creates a greater barrier to the oncoming

mainstream, resulting in jet trajectories that are less penetrating and, at the same time, reducing the effective interaction zone between coolant jets. Adding additional rows of holes with staggered spacing configurations allows consecutive downstream cooling holes to carry on when upstream coolant injection has lost its cooling capacity. Multiple, staggered rows of holes approach the highly effective transpiration cooled configuration. Limitations on the amount of coolant fluid available would weigh heavily upon the decision to incorporate multiple-row or full-coverage film cooling.

The details of the coolant hole itself are coupled with the overall cooling performance of the injection jet. In order that the injected coolant mass leave the surface in some predetermined manner (i.e. injection angle relative to the surface) care must be exercised in choosing the hole size in relation to the surface material thickness. The hole length-to-diameter ratio (L'/d_0) must be of the order of 2 or greater to insure that the issuing jet does not leave the surface in a manner characteristic of thin-plate orifice flow. Small L'/d_0 ratios promote rapid mixing of the primary and secondary fluids, diffusing the coolant momentum equally in all directions and reducing the importance of angled injection to a second order effect.

When modeling a cooling configuration, the hole diameter in relation to the boundary layer characteristics is significant. As mentioned earlier, the coolant jet trajectory is influenced by drag forces created by the flow of the deflecting mainstream over and around the exposed frontal area of the cylinder-shaped core of the issuing jet. Equivalence of the momentum boundary layer thickness-to-coolant hole diameter ratio (θ_1/d_j)

in both a simulated and actual case insures that pressure forces or form drag terms will produce similar effects on the coolant jet trajectory.

The nature of the external flow field may have a significant effect on the manner in which a coolant film performs following injection. The existence of large scale mainstream turbulence of sufficient energy may effectively act as an additional mixing agent between the coolant and mainstream fluids. Freestream turbulence intensities near 20% (representative values at the exit of typical combustors) and the presence of turbulent "eddies" with scales of the order of the film-cooled boundary layer thickness can contribute significantly to the deterioration of any injected film. In addition to freestream turbulence effects, injecting into boundary layers of varying thicknesses will result in a greater deflection of the issuing jet toward the surface for a thinner boundary layer than for a thick one at the same freestream velocity. Finally, wall curvature may cause the film cooled boundary layer to be more stable or unstable, depending upon the nature of the curvature. Instability of the film coolant layer will lead to separation of the film from the surface, thereby promoting mixing with the primary mainstream.

The previous few pages have dealt with establishing a basis for understanding the physics of film injection. Those parameters considered important in determining the cooling potential of discrete secondary coolant injection have been presented and discussed in light of their physical significance. Documentation of the importance of such parameters can be found in a vast library of film cooling studies carried out over the past 30 years. A summary of the most significant investigations dealing with the effects of the major film injection parameters will now be presented.

II.2. Literature Review of Important Cooling Parameters

II.2.1. Effect of Coolant Injection Angle

For a given cooling scheme, it is the penetration of the coolant jet into the mainstream and consequent mixing that primarily causes the coolant to lose its "identity" as a protective, heat-sinking mechanism. This penetration depends on the momentum of the coolant relative to that of the mainflow as well as the manner in which this momentum is directed (as accomplished by the injection angle). The coolant is injected through the surface in a direction that can be described by two basic angles, α_1, and α_2 as shown by the sketch of the coolant coordinate system in Fig. 6(a). Film coolant may be injected through the surface along the streamwise direction with some streamwise angle α_1, maintaining $\alpha_2 = 0°$. This is represented by Fig. 6(b). For streamwise injection (α_1, $\alpha_2 = 0°$), α_2 is generally assumed to be zero and the streamwise configuration is described by the single angle, α (subscript dropped). Alternately, the film coolant may be injected in a spanwise or lateral direction (i.e. perpendicular to the mainstream flow) with α_1 at some value relative to the surface and $\alpha_2 = 90°$. This is represented by Fig. 6(c). For lateral injection (α_1, $\alpha_2 = 90°$), α_2 is assumed to be 90° and the lateral configuration is described by a single angle, β. In general there could be some compound angle of injection (α_1, α_2) with the film coolant having components in both the streamwise and spanwise directions.

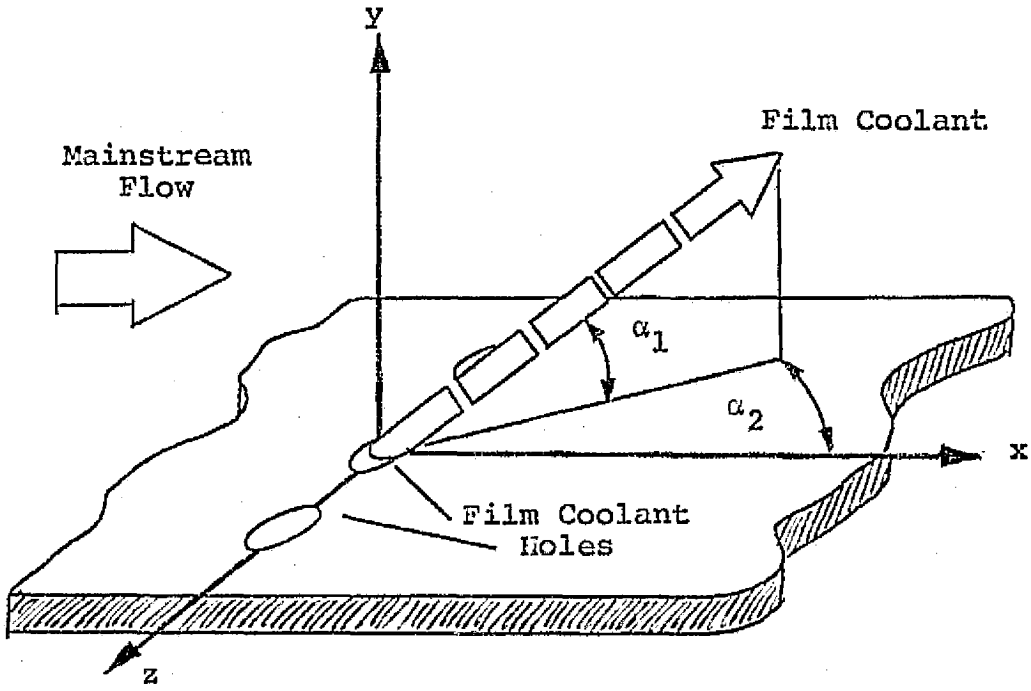

(a) General Coordinate System

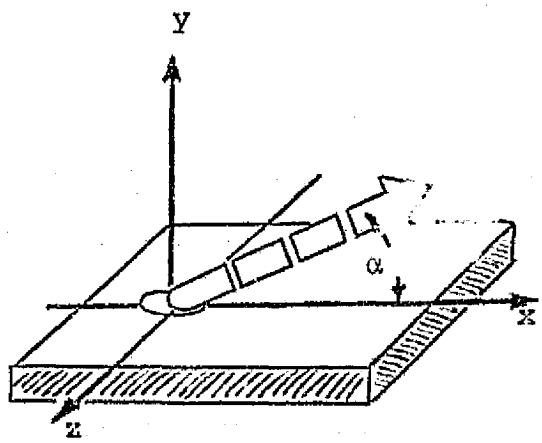

(b) Streamwise Injection

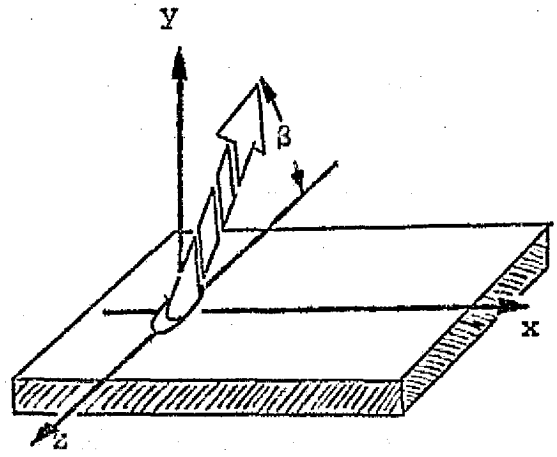

(c) Spanwise Injection

Figure 6. Definitions of Coolant Injection Angles.

The great majority of film cooling data in the literature deals only with streamwise (α) injection, since that configuration imparts a component of coolant momentum parallel to the mainstream, thus improving the cooling effect downstream from injection. Interest in spanwise injection (β) has stemmed from practical limitations of fabricating streamwise angled holes on curved surfaces, and from the possible enhancement of film coolant uniformity in the lateral (i.e. spanwise) direction. Relatively little film cooling data are available for spanwise injection, especially from a row of angled holes under conditions of high values of the local acceleration.

The effect of changing the injection angle has been well documented for 2-D slot injection and for streamwise injection from a single row of holes. The effects of changing the spanwise injection angle have been investigated for a single hole; however, no information is available for a row of spanwise angled holes. Papell (8) and Metzger et al. (9,10,11) have demonstrated the coolant may penetrate farther into the boundary layer as the angle of injection is increased from $\alpha = 0°$ (tangential slot) to $\alpha = 90°$. Figure 7(a) is from Papell and shows the variation in η_{ADW} with increasing injection angle for M of 0.5 to 4.5. The data is representative of one location downstream from injection corresponding to 26 slot heights ($x'/S = 26$). For tangential slot injection ($\alpha = 0°$) η_{ADW} is the highest for all M. As α increases η_{ADW} decreases. For M = 4.5, the decrease in effectiveness is more severe with increasing α, possibly due to excessive coolant penetration into the boundary layer at such large values of M.

Figure 7(b) describes the benefit of decreasing α from 90° to 35° for a single hole (2, 12). The cooling effectiveness is shown as a

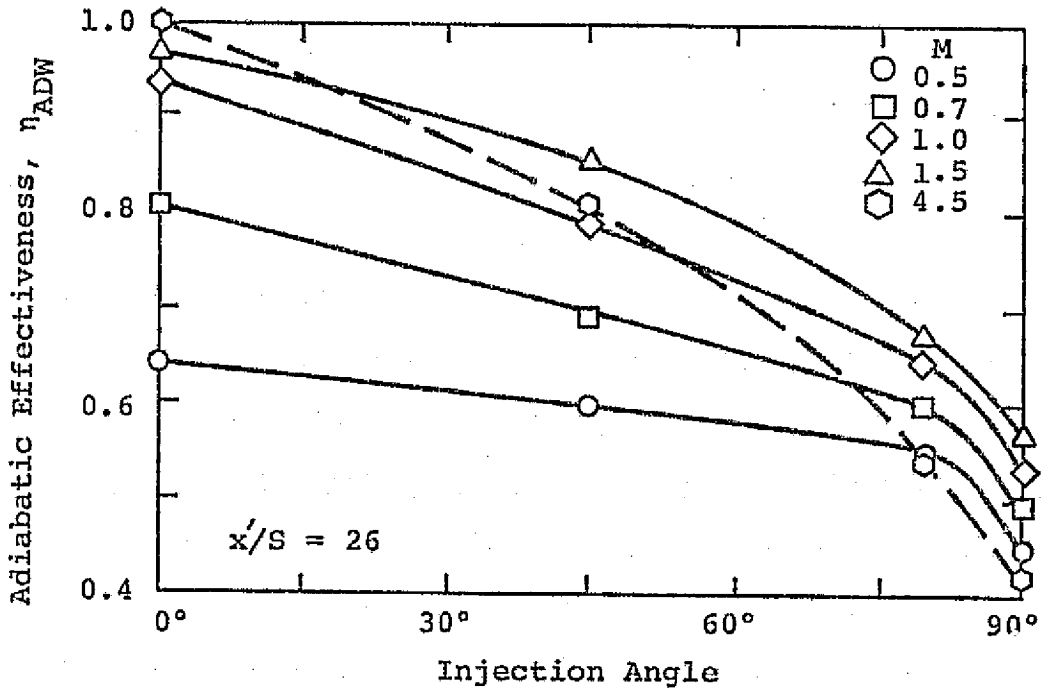

Figure 7(a). Effect of Coolant Injection Angle on Slot Cooling Effectiveness (8).

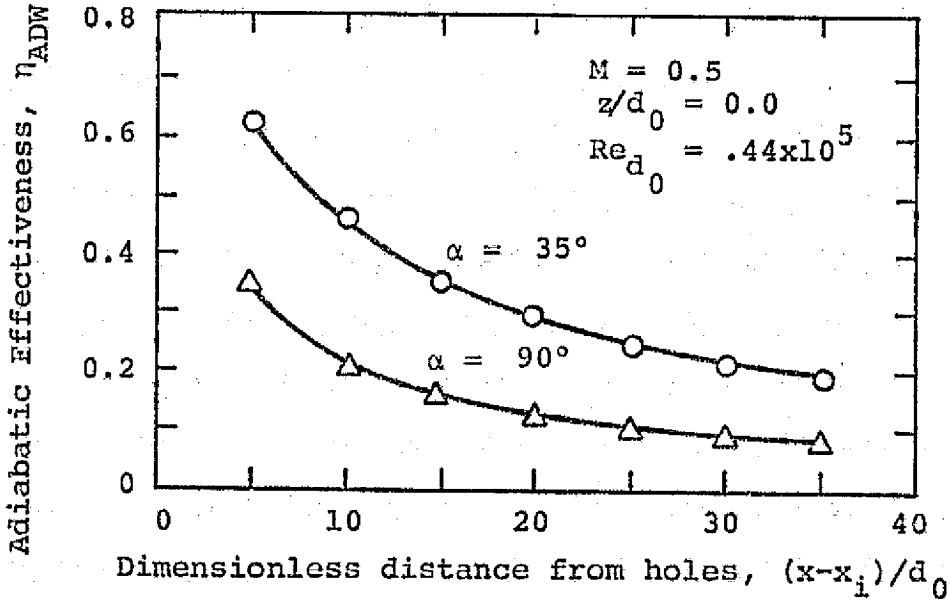

Figure 7(b). Effect of Coolant Injection Angle on Cooling Effectiveness From a Row of Holes (2, 12).

function of the distance from injection for M = 0.5. The data is representative of that along the coolant hole centerline extended in the streamwise direction. The freestream Reynolds number at injection based on the coolant hole diameter was 0.44×10^5. The shallower angle of 35° shows a cooling effectiveness nearly twice that of $\alpha = 90°$ for all the downstream distances investigated. It is expected that the same trend of improved cooling effectiveness with decreasing injection angles would apply in a comparison of a row of holes.

For spanwise injection, the effects of the coolant angle for a single hole are presented in Fig. 7(c) from Goldstein et al. (2). The figure shows contours of η_{ADW} as a function of lateral distance (z/d_0) and streamwise distance (x/d_0) from the hole. Three injection angles are compared at M = 0.5: $\alpha = 35°$, $\beta = 35°$ and $\beta = 15°$. Compared to $\alpha = 35°$ the results for $\beta = 35°$ show a somewhat wider field of film coverage; however, the maximum cooling effectiveness decreased from 0.4 to 0.3. Further changes in β from 35° to 15° show that the film coverage is extended even more. The highest η_{ADW} measured is still lower than for $\alpha = 35°$ at the same M of 0.5. This evidence of extended film coverage at shallow lateral angles would seem to imply that a <u>row</u> of spanwise-angled holes might be used to achieve more uniform film cooling downstream from injection than streamwise angled holes (at same spacing ratio). The cooling effectiveness for a row of spanwise-angled holes is expected to show even less spanwise variation than shown for the single spanwise-angled hole, with the cooling effects of neighboring coolant jets superimposing between holes.

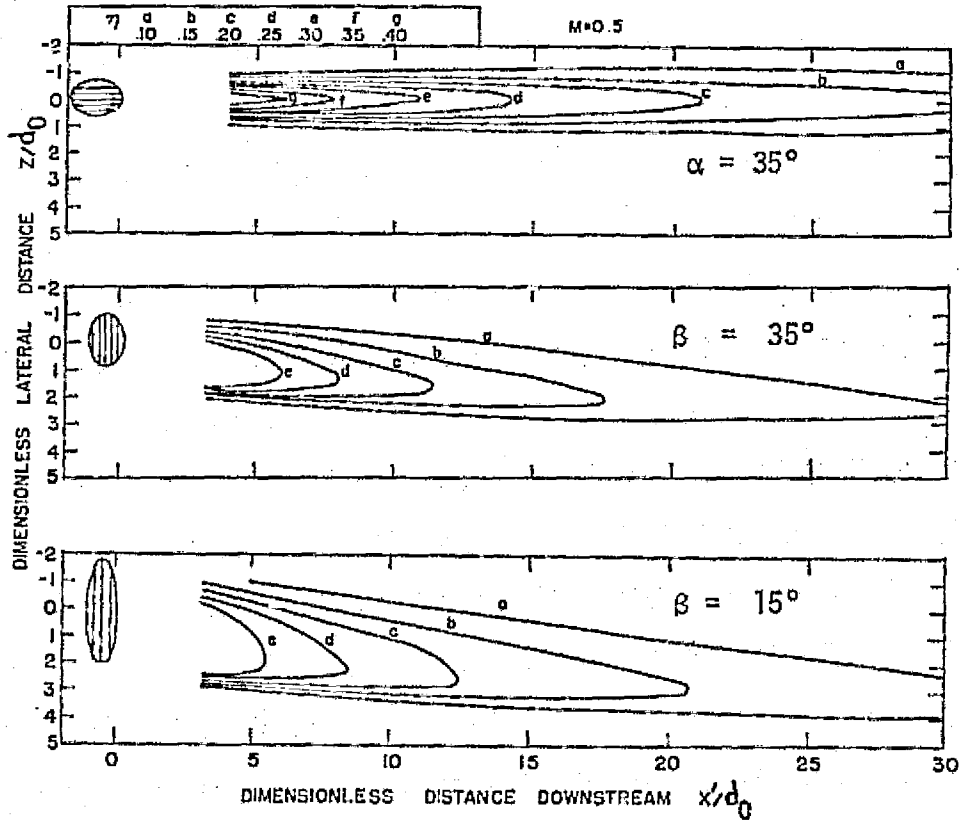

Figure 7(c). Lines of Constant Cooling Effectiveness For Streamwise and Lateral Injection Angles (2).

II.2.2. Effect of Blowing Ratio

In general, the coolant jet trajectory (i.e. penetration into the external boundary layer) is a function of the momentum flux ratio, I. However, for most cooling studies conducted with negligible density variations between the coolant and mainstream, the blowing ratio (mass flux ratio) M has served as the major correlating parameter. M is defined

$$M = \frac{\rho_c V_c}{\rho_\infty V_\infty} \tag{8}$$

It should be noted that for $\rho_c/\rho_\infty \approx 1$, $M = \sqrt{I}$ and, thus, not only serves as an indication of the relative mass addition but also reflects the relative momentum fluxes.

For 2-D, tangential slot cooling with the coolant gas temperature near the freestream level ($\rho_c \approx \rho_\infty$), values of M near 1.0 have been shown to yield the maximum cooling effectiveness (13, 14). Figure 8(a) shows the variation of the mass transfer equivalent of η_{ADW}, namely η_{IW}, with the blowing ratio for slot injection (η_{IW} is the impervious wall effectiveness with concentration levels analogous to the temperature levels of η_{ADW}). Results for two downstream locations of 50 and 100 slot heights are presented. Near M = 1.0 the effectiveness was a maximum for both locations. As M increases from unity the velocity ratio V_c/V_∞ must increase ($\rho_c \approx \rho_\infty$), yielding lower η_{IW} values. For M > 1.0 the relative differences in velocity between the coolant and freestream approach a condition in which mixing at the interface between the separate films increases.

It is possible, however, to increase M well past unity and have the effectiveness improve steadily. This is accomplished for a tangential

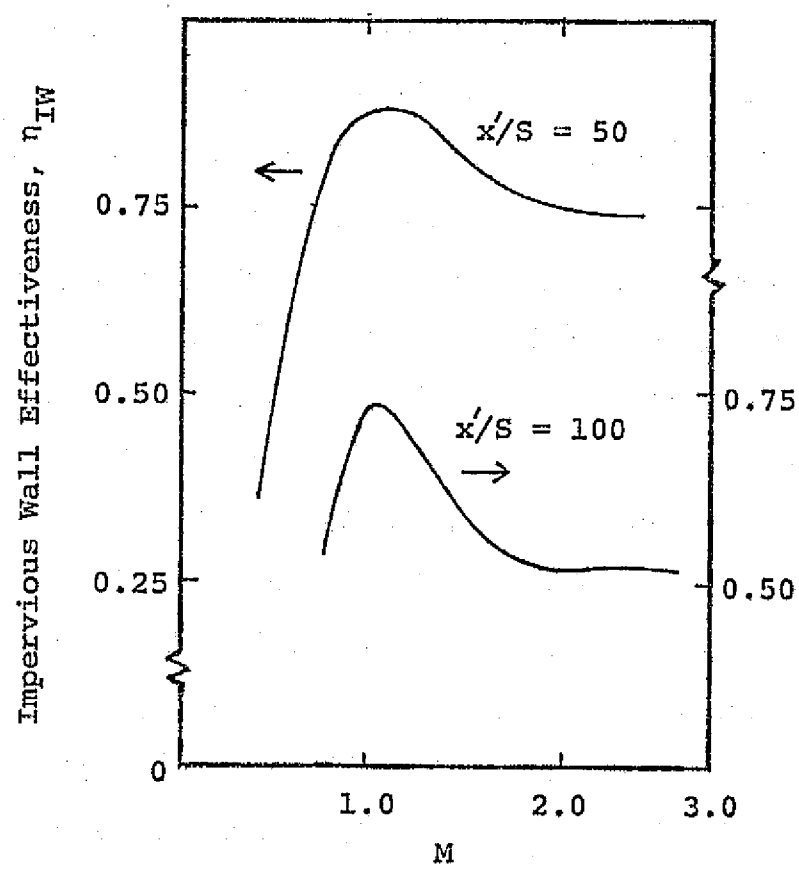

Figure 8(a). Effect of Blowing Ratio, M, on Cooling Effectiveness For Tangential Slot (13).

slot by holding the ratio of velocities near unity and allowing the coolant temperature (density) to change appropriately. This permits minimum interface mixing, due to the velocity ratio fixed at unity, yet allows the momentum of the coolant along the surface to increase. Burns and Stollery (15), using a mass transfer analogy for measuring a concentration cooling effectiveness, η_{IW}, as shown in Fig. 8(b), have demonstrated the gain in effectiveness by using a denser or cooler film with a velocity ratio, $V_C/V_\infty = 1.0$. The effectiveness, η_{IW}, increases at a fixed distance from injection (x'/S) for all increases in ρ_C/ρ_∞. It appears from the evidence of Fig. 8(a) and Fig. 8(b) that the velocity ratio, V_C/V_∞, may be a significant parameter in determining the overall cooling effect of increasing M (i.e. as M increases η_{ADW} may decrease if $V_C/V_\infty > 1$). For 2-D slot injection, V_C/V_∞ near unity results in the maximum effectiveness achievable for all ρ_C/ρ_∞.

Extension of the results pertaining to the blowing ratio effect on cooling from a 2-D slot to 3-D hole cooling is not possible. Coolant injected from a row of angled holes into a deflecting mainstream exhibits distinctively different behavior than that observed for the two-dimensional slot. Due to the ability of the mainstream gas to move between adjacent coolant jets and continually deform them downstream, an optimum blowing ratio for three-dimensional hole cooling can be expected to be quite different from the two-dimensional case. Liess and Carnel (16), Eckert et al. (17, 18), Goldstein et al. (2, 19), Eriksen (7, 20, 21), Amana et al. (22), and Louis et al. (23), have shown that an optimum cooling effectiveness from a row of holes is achieved at M = 0.5 for streamwise injection angles below 35°.

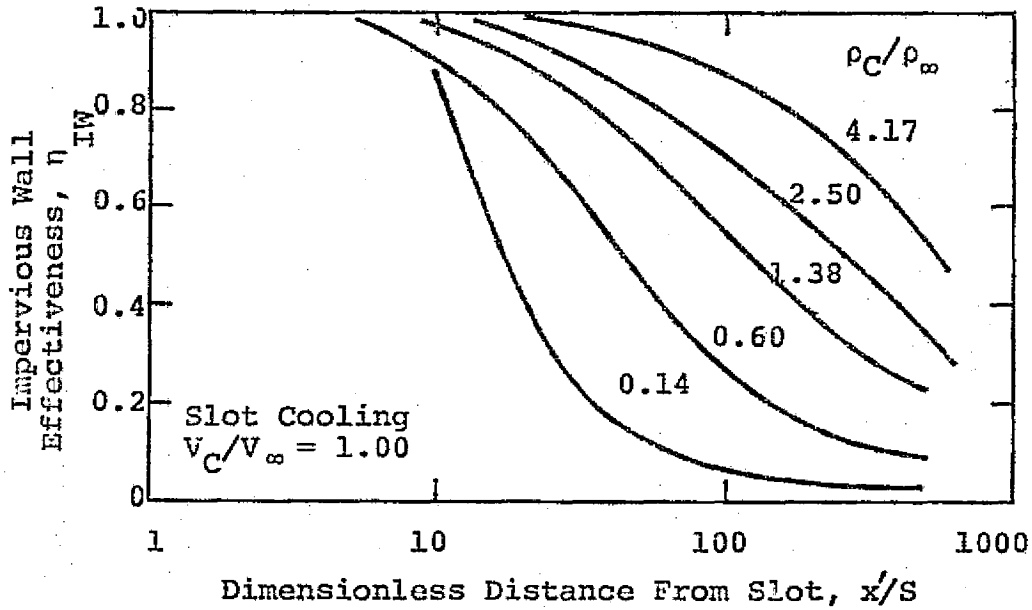

Figure 8(b). Effect of Density Ratio on Tangential Slot, Cooling Effectiveness (15).

Figure 8(c) shows the film cooling effectiveness as a function of M for a single hole and a row of holes both angled streamwise at 35° (2). The data is representative of 5 to 81 hole diameters downstream along a centerline through a coolant hole. Up to 11 hole diameters from injection the optimum M for highest η_{ADW} occurs at M = 0.5. For M > 0.5 in this region, η_{ADW} decreases due to greater jet penetration into the mainflow. However for distances from injection greater than 11 hole diameters, η_{ADW} reaches another maximum following M = 0.5. At M near 2.0, the adiabatic effectiveness at x'/d_0 = 80.67 is nearly the same as at M = 0.5 for x'/d_0 = 31.47. This improvement in η_{ADW} may be attributed to the spreading of the coolant jets, resulting in a cooling reinforcement as they begin to coalesce.

It is interesting to note that the optimum M of 0.5 actually represents a velocity ratio, V_C/V_∞ = 0.5 ($\rho_C/\rho_\infty \approx 1$ for the aforementioned study). The significance of this value was pointed out by Pederson (24). Figure 9 represents a portion of the results presented by Pederson in which the coolant density was changed from ρ_C/ρ_∞ of 0.75 to 4.17. Figure 9 shows a spanwise averaged η_{IW} (based on concentration measurements using a mass transfer analogy) as a function of M for a row of 35° streamwise angled holes at 3 diameter spacings. The data is for x'/d_0 = 10.29. Examination of Fig. 9 will reveal that the maximum effectiveness for each ρ_C/ρ_∞ occurs near a velocity ratio between 0.4 and 0.5. Apparently, an equilibrium condition is established at V_C/V_∞ = 0.5 between disturbances created by injection (i.e. local turbulence due to mixing brought on by increased coolant jet velocities) and additional heat sinking capacity due to increased cool mass addition.

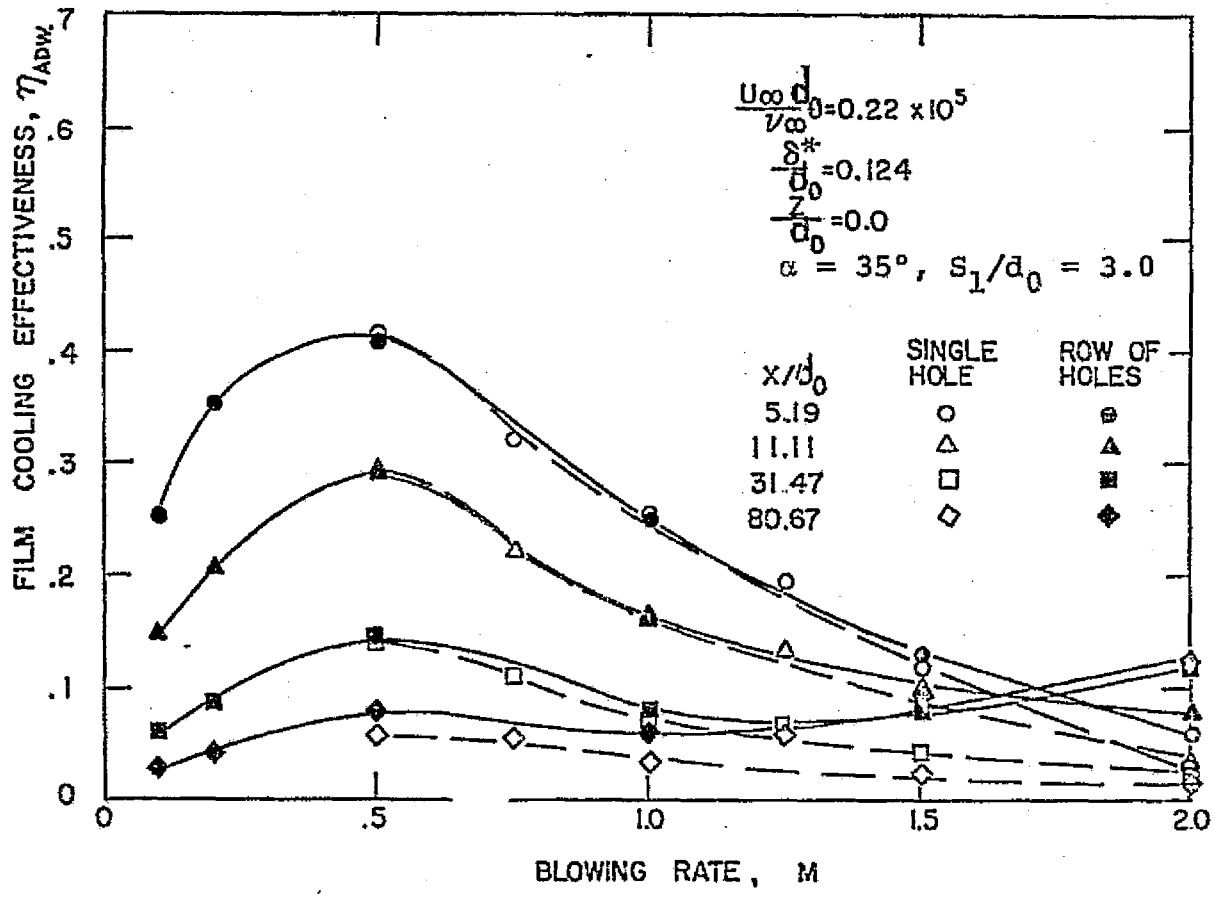

Figure 8(c). Effect of Blowing Ratio on Film Cooling Effectiveness For Single Hole and Multiple Hole Injection (2).

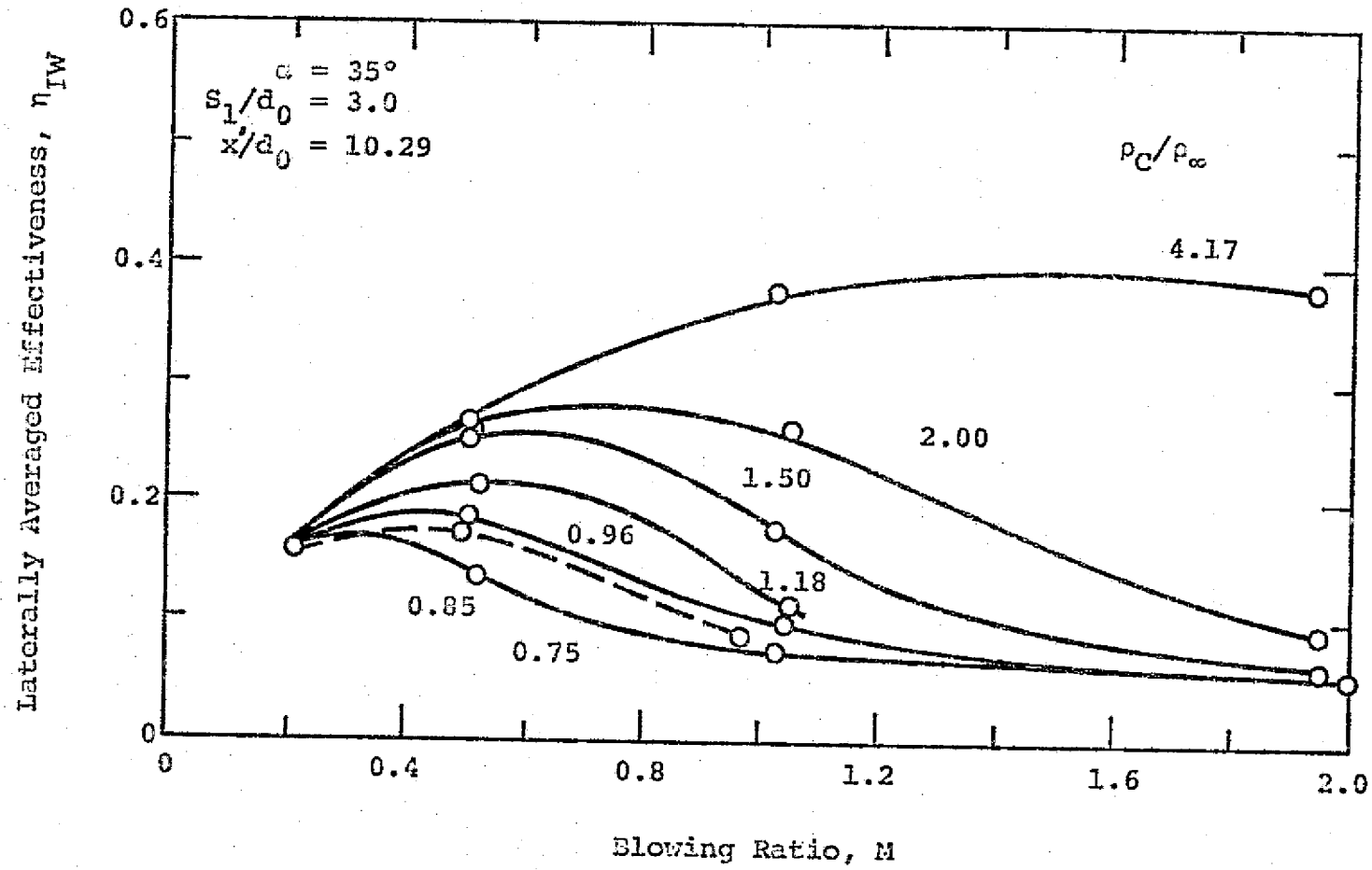

Figure 9. Effect of Large Density Ratios on Cooling Effectiveness (24).

The effect of M on η_{ADW} for spanwise injection is not well documented. Goldstein et al. (2) have found that for lateral coolant injection from a single hole, the field of film coverage is slightly reduced in going from M = 0.5 to 1.0. Figures 10(a) and (b) are effectiveness contours as a function of lateral distance (z/d_0) and streamwise distance (x'/d_0) for $\alpha = 35°$, $\beta = 35°$ and $\beta = 15°$. There does not appear to be a significant change in η_{ADW} levels in going from M = 0.5 to M = 1.0 for $\beta = 35°$ or $\beta = 15°$. At M = 1.0 the lateral coverage is reduced from M = 0.5. No definite conclusions can be drawn from this single hole data in order to predict the overall effect of M on the cooling effectiveness for a row of spanwise angled holes.

II.2.3. Effect of Injected Coolant Temperature

The coolant temperature is the driving mechanism responsible for lowering the effective boundary-layer gas temperature. Not only does lowering the coolant temperature provide an additional heat-sinking capacity to the injected film, but it also yields a lower trajectory of the injection jet for constant M (i.e. constant coolant mass addition).

Referring again to Fig. 9, dealing with the work of Pederson, the effect on η_{IW} of increasing the coolant density (i.e. decreasing the coolant temperature) from $\rho_c/\rho_\infty = 0.75$ to 4.17 is presented. At $x'/d_0 = 10.29$, η_{IW} increases at any M for increasing ρ_c/ρ_∞. It is not, however, the increase in ρ_c (i.e. decrease in T_c) which affects the improvement in the cooling effectiveness. Because ρ_c increases at a constant coolant mass addition (i.e. M a constant), the velocity ratio must decrease. This means at constant M, the highest coolant density dictates a velocity ratio which is characteristic of a minimum disturbance

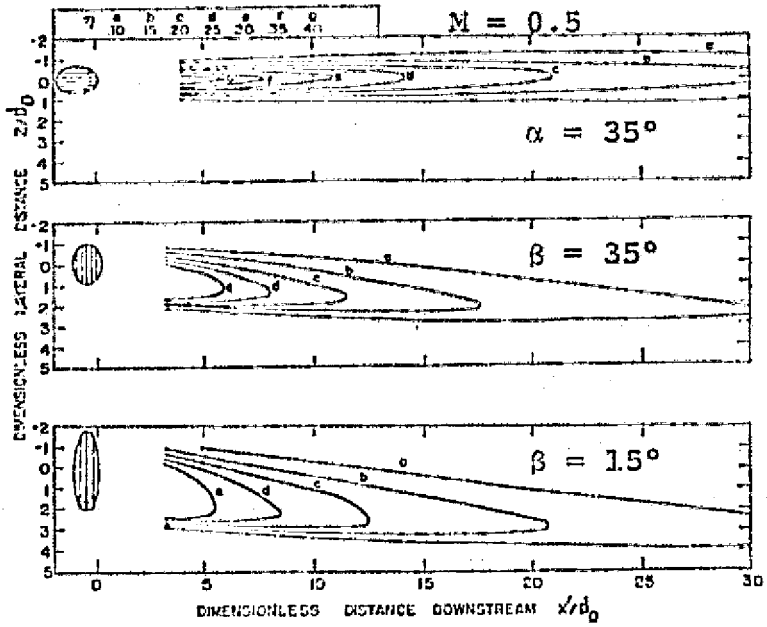

(a)

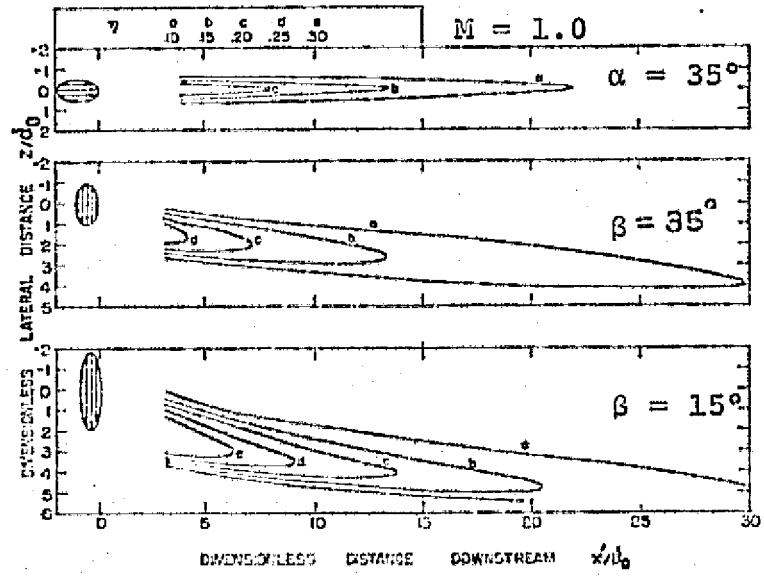

(b)

Figure 10. Lines of Constant Film Cooling Effectiveness For Single Hole Injection at M = 0.50 and M = 1.0 (2).

to the boundary layer. Consequently, the effective transport mechanism between the hot gas and injected, cool film is greatly reduced (i.e. the effectiveness is greater).

Additionally, lowering the coolant temperature (i.e. increasing ρ_c/ρ_∞) for constant M results in a more shallow coolant jet trajectory. Recall that

$$I = M \left(\frac{V_c}{V_\infty}\right) \tag{9}$$

and that for constant M and decreasing T_c, V_c/V_∞ must decrease. Consequently, I must decrease with a concomitant jet trajectory that keeps the coolant fluid nearer to the wall.

II.2.4. Injection Geometry Considerations

In addition to the coolant injection angle, there are a few other basic geometric factors that are intrinsic to a particular cooling scheme. Such items as the spacing between coolant holes, use of multiple rows of coolant holes in various configurations of staggered or in-line arrangements, hole length-to-diameter ratio and the thickness of the boundary layer at the point of injection are all necessary considerations when attempting to predict the overall cooling capability of coolant injection from a row of holes.

The effects of the coolant hole spacing on the cooling effectiveness are manifest in the degree to which the hot mainstream can freely move between and interact with the individual coolant jets. Liess and Carnel (16) investigated hole spacing-to-diameter ratios (S_1/d_0) of 2.22, 3.33 and 4.0. Their results appear in Fig. 11. The adiabatic cooling effectiveness is shown as a function of the dimensionless downstream

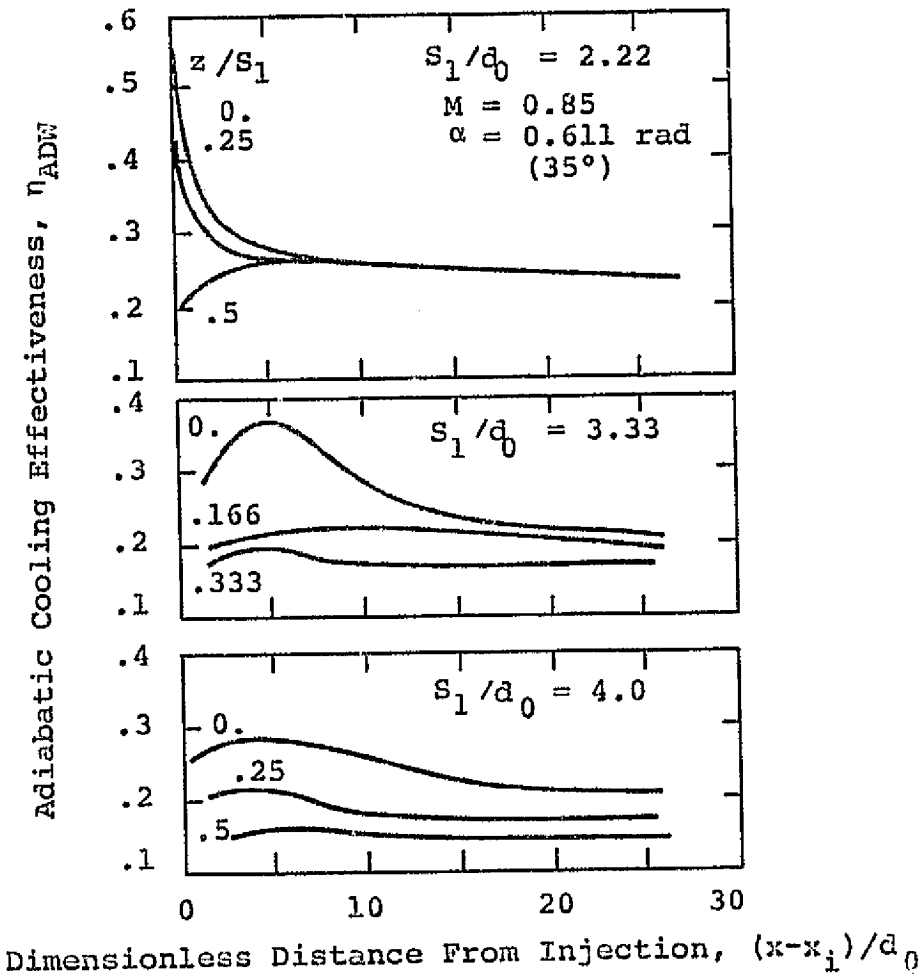

Figure 11. Effect of Coolant Hole Spacing on Coolant Effectiveness (16).

distance (x'/d_0) for a blowing ratio, M = 0.85. Spanwise variations of η_{ADW} are shown for each S_1/d_0 with values of z/S_1 (dimensionless spanwise distance between two holes) ranging from 0.5 (midway between adjacent holes) and 0 (in-line downstream with a hole).

Very near injection ($x'/d_0 \sim 1.0$), closer spacing of the holes ($S_1/d_0 = 2.22$) yields higher film effectiveness than for S_1/d_0 of 3.33 and 4.0. Further downstream, for x'/d_0 in the range of 2 to 10, η_{ADW} along the jet centerline temporarily increases as S_1/d_0 increases due to the three-dimensional effect of jet spreading and subsequent coalescence. However, for $x'/d_0 > 10$, lower values of the spacing ratio yield higher effectiveness for all remaining stations downstream as well as all lateral positions across the span of the test surface. A uniform, two-dimensional film is a desirable characteristic for any application of film cooling. As can be seen from Fig. 11 for M = 0.85, the data for the lowest value of the spacing ratio show essentially no lateral variation for distances beyond 13 hole diameters downstream. In contrast, the data for the larger values of the spacing ratio show significant lateral non-uniformity for distances up to 25 hole diameters. Liess and Carnel also noted that larger downstream distances are required for uniform spanwise film effectiveness if the blowing ratio is decreased from M = 0.85.

Practically speaking, the film effectiveness from a single row of holes falls to such a low value at such a rapid rate that multiple row cooling configurations may be necessary to cool any appreciable surface area. Arrangements of multiple row configurations also can compensate for the spanwise film non-uniformity from a single row, as staggered hole arrays fill in the gaps between holes downstream.

Louis et al. (23) demonstrated the effect of adding just an additional row of holes incorporating both 10° and 20° injection. The injection of additional mass and the modification of the effective decay characteristics of the film showed the double row of holes to be nearly as effective as a slot. Hiroki and Katsumata (25) measured approximately a 20% increase in the local film effectiveness by increasing a two row array to a four row configuration for cooling rates of 1% to 1.5% of the external gas flow.

Larger arrays of holes have been studied by Choe, Kays and Moffat (4). They used 11 rows of film cooling holes at hole array spacings of 5 and 10 hole diameters. The overall effect of the cooling scheme was defined as a reduction in the local measured Stanton number due to cooling over that for the uncooled condition. For the 10 diameter spacing configuration minimal decreases in the local Stanton number were recorded in comparison to the uncooled wall. However, reducing the spacing to 5 diameters caused the Stanton number to fall by 50% over the 10 diameter geometry.

Metzger, Takeuchi and Kuenstler (26) used 10 rows of 90° injection holes at a 4.8:1 pitch-to-diameter ratio to study the effects of staggered and in-line multiple row arrays. Rows of holes with all holes arranged in-line downstream proved inferior to staggered arrangements. In-line arrays prevented upstream cooling jets from filling in the spaces between the cooling holes on the next downstream row. Although multiple, staggered rows of holes (full coverage cooling) would seem necessary for cooling an extensive area, it should be noted that regions exist, such as in the turbine vane leading edge, in which high heat

fluxes are concentrated over short distances. Consequently, single row cooling configurations capable of effectively protecting such critical regions need to be investigated. Results from single row studies, as will be presented for this investigation, may also serve as "building blocks" to predict the overall cooling effect of a superposition of many similar rows of holes.

The injection scheme adopted in light of all its geometric, hydrodynamic and thermodynamic characteristics must also be viewed in relation to the nature of the local boundary layer at injection. Thicker momentum boundary layers allow the coolant injection jets to penetrate farther into the external mainstream for identical relative mass addition and momentum flux. Eriksen and Goldstein (7) and Goldstein, Eckert, Eriksen and Ramsey (2) have shown that increasing the boundary layer thickness at injection with constant mass addition leads to a reduction in the film effectiveness for a single hole. However, the effect of injecting at thicker boundary layer conditions is less severe for a row of holes, showing even a slight increase in the effectiveness for a 50% increase in displacement thickness-to-hole diameter ratio. Liess (27) reports varying the displacement boundary layer thickness from $\delta_1/d_0 = 0.1$ to 0.6 for a row of holes injected at 35° to the surface and in the streamwise direction. Figure 12 shows the variation in η_{ADW} with displacement boundary layer thickness-to-hole diameter ratio at M = 0.3 to 0.43. The effectiveness variation with δ_1/d_0 is shown for three downstream locations of $x'/d_0 = 10$, 30 and 50. For the given M, η_{ADW} was shown to decrease by as much as 50% from $\delta_1/d_0 = 0.1$ to 0.6. Figure 12 shows that the effectiveness decrease with increasing boundary layer thickness holds at least as far as 50 hole diameters downstream from injection.

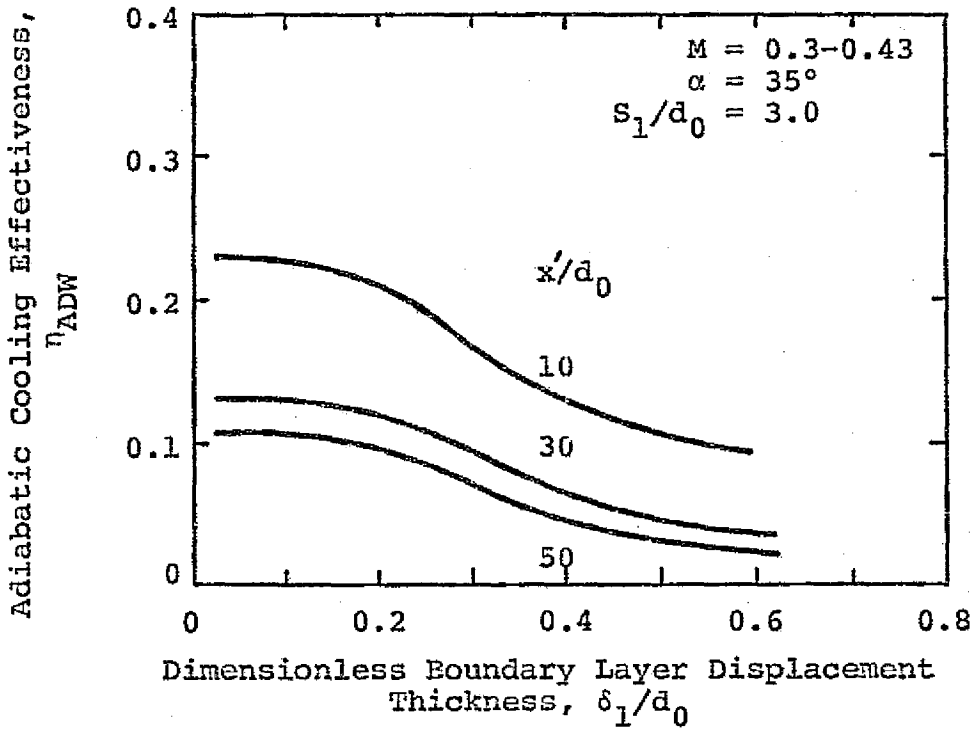

Figure 12. Variation in Cooling Effectiveness With Increasing Boundary Layer Displacement Thickness (27).

II.2.5. Effects of Freestream Conditions

Though the momentum flux ratio, angle and point of injection, and configuration geometry may be viewed as primary considerations in evaluating a film cooling scheme, a number of other parameters remain that may collectively result in a considerable perturbation to the expected film coolant performance.

For instance, the transport of heat and momentum are greatly enhanced in the presence of a mainstream containing large fluctuating velocity components. High levels of freestream turbulent kinetic energy (as manifest in the turbulence intensity, Tu_∞) will lead to enhanced mixing between the coolant jets and mainstream provided the external turbulence has energy of the same order as that created by coolant injection into the boundary layer. Such a condition may exist in the leading edge region of a turbine airfoil. Sutera, Meader and Kestin (28) and Sahed et al. (29,30) have shown that, if the oncoming turbulence scale of the freestream is larger than approximately three times the Hiemenz boundary layer thickness, considerable amplification of the turbulent fluctuations takes place in the stagnation region. Figure 13(a) demonstrates that at $\xi = 12.12$, where

$$\xi = \left(\frac{a}{\nu}\right)^{1/2} x \tag{10}$$

where $a = 4V_\infty/D$

V_∞ = freestream velocity

D = characteristic leading edge dimension

ν = kinematic viscosity

x = coordinate along surface

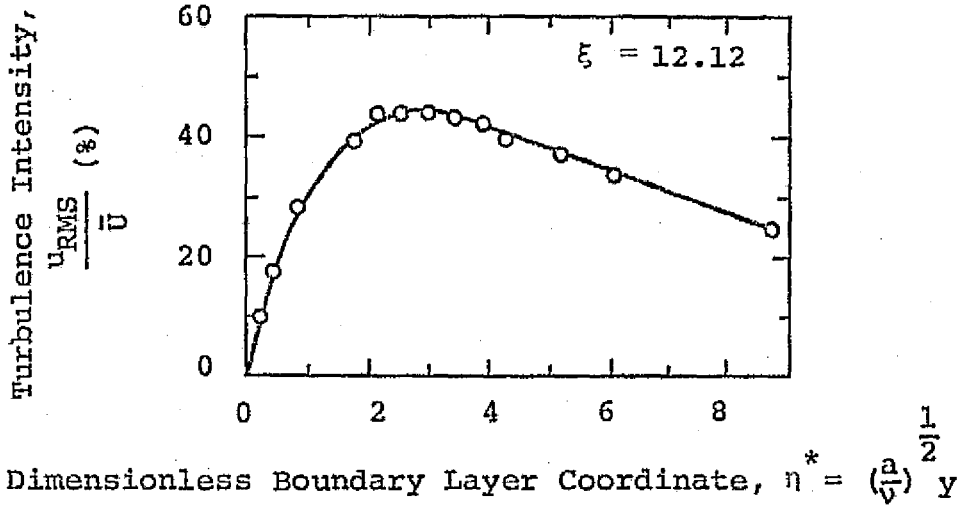

Figure 13(a). Turbulence Intensity in the Stagnation Region (30).

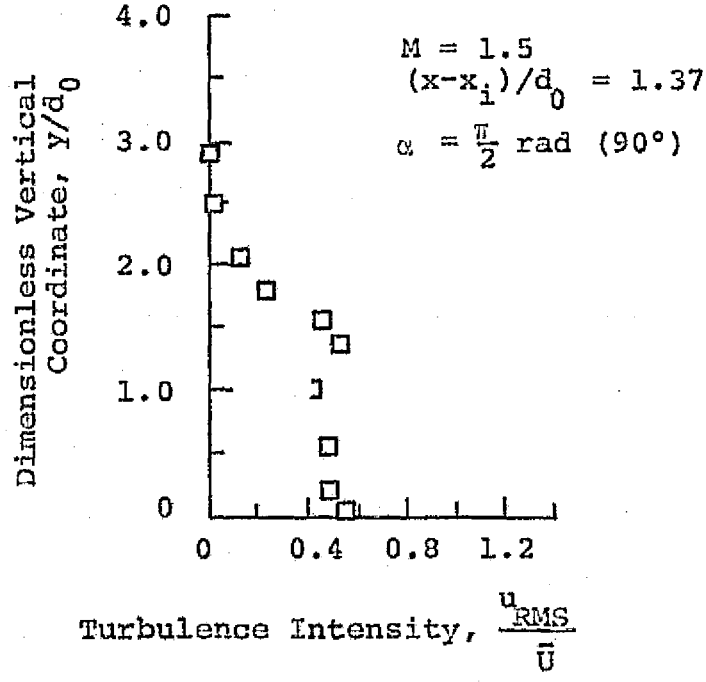

Figure 13(b). Turbulence Intensity Generated by Injection From a Single Normal Hole (32).

the intensity of the fluctuating velocity component in the direction of flow reaches up to 45% based on the freestream velocity at the outer edge of the boundary layer. Traci and Wilcox (31) present a stagnation region turbulence amplification model that also predicts dramatic effects. Depending on the freestream Reynolds number, the turbulent energy approaching the stagnation region can increase from 30% to 300%.

Ramsey and Goldstein (32) report turbulence intensities for 90° injection at blowing ratios of 1.5 and 2.0. Figure 13(b) shows that maximum values in the near injection region are of the same order as intensities generated in the stagnation region due to freestream vortex filament stretching. At lower blowing ratios associated with optimum effectiveness levels, the injection generated turbulence should diminish, increasing the dependency of the cooling effectiveness on the relatively high incident freestream turbulence levels.

Far removed from stagnation-region amplification effects, freestream turbulence levels should not significantly enhance the transport mechanisms already dominated by injection effects. Nominal turbulent boundary layer intensities are significantly lower than those turbulent conditions created by discrete coolant injection. Junkhan and Serovy (33) and Kearney et al. (34), under zero pressure gradient and strongly accelerated conditions respectively, show little or no effect on the local heat transfer through a turbulent boundary layer exposed to freestream intensities up to 10%. The three-dimensional vortex stretching phenomenon near a stagnation region appears to be the only freestream, turbulence-related condition that could possibly influence the mixing behavior characteristic of the highly energetic regions of the turbulent injection jets.

The effects of freestream acceleration due to large imposed pressure gradients on turbulent boundary layer heat transfer without film coolant injection have been well documented. Kays et al. (35, 36, 37, 38, 39) show a decrease in the local heat transfer for moderate values of the acceleration parameter, K, where

$$K = \frac{\nu}{V_\infty^2} \frac{dV_\infty}{dx} \tag{11}$$

where ν = kinematic viscosity

V_∞ = local velocity

x = coordinate along surface

Apparently, with increasing levels of K the boundary layer turbulence is suppressed, reaching a lower average turbulence intensity than exists without acceleration, yet still retaining a turbulent layer appearance. At $K > 3.3 \times 10^{-6}$ a steep drop in the Stanton number occurs, approaching a "laminarization" condition in which the heat transfer nearly approaches values characteristic of a laminar boundary layer.

As applied to film cooling applications, the effects of increased K on the overall heat transfer to a cooled surface were noted by Kays et al. (30). Depending upon the blowing ratio, increasing K can either increase or decrease the local heat transfer. However, for high transpiration blowing ratios ($M \sim 0.0062$), the Stanton number increased as much as 25% in varying K from 0 to 0.77×10^{-6}. For film injection from discrete locations (i.e. holes) much larger blowing ratios are generally maintained than those noted in the transpiration study. Consequently, the Stanton number should rise even higher than noted for the transpired condition of $M = 0.0062$. Heat transfer measurements of a film cooled, accelerated

boundary layer reflect both the boundary layer structure changes due to blowing as well as any acceleration induced mixing that may occur in the outer edges of the boundary layer due to large local velocity gradients.

Adiabatic wall temperature measurements for film coolant injection under varying degrees of freestream acceleration would not reflect acceleration-induced boundary layer perturbations (as do heat transfer measurements) but would give an indication of the degree of mixing which takes place between the coolant and mainstream due to imposed velocity gradients at injection. Changes in the adiabatic wall temperature (reflecting the degree to which the hot gas mainstream is reduced in temperature near the wall) due to acceleration were reported by Carlson and Talmor (40). They measured acceleration effects on η_{ADW} in the presence of freestream turbulence for 2-D slot film cooling. They found that favorable pressure gradients lowered the cooling effectiveness, except for the case in which high freestream turbulence intensity levels existed at injection. Initially the favorable pressure gradient tended to suppress the high turbulence level, and, hence, reduce the effective transport mechanism between the coolant and the mainstream. However, a condition was established once the turbulence was diminished in which the acceleration led to a deterioration of the film effectiveness.

Acceleration effects on η_{ADW} for three-dimensional hole injection were reported by Liess (27). At x'/d_0 of 10 and M = 0.5, η_{ADW} was reduced nearly 50% over the unaccelerated case for K near 0.4×10^{-6}. At M = 1.0, η_{ADW} was reduced 22% for a variation in K from approximately 0.14×10^{-6} to 0.4×10^{-6}.

In addition to pressure gradient effects, surface curvature introduces additional complications into determining film cooling behavior in accelerating flows. Nicholas and LeMeur (41) attempted to separate curvature effects from pressure gradient effects. They found that for film cooling on a convex surface the effectiveness was greater than on a flat plate of zero pressure gradient, but slightly lower than on a flat surface with a pressure gradient similar to the convex case. However, their results indicating an increase in the effectiveness for injection under a favorable pressure gradient over a flat plate condition are in disagreement with the majority of cooling studies conducted in the presence of freestream acceleration. For a concave wall, the effectiveness was generally lower than the zero pressure gradient results, except at very high blowing ratios (M = 2.0). The concave wall had a pressure distribution essentially equivalent to a flat plate. The effectiveness reduction due to concave curvature was as much as 30% far downstream from injection and negligible near injection for a blowing ratio of 1.0.

II.2.6. Models for Film Cooling Effectiveness

Numerous models and correlations for both slot and hole cooling have been developed without achieving applicability under all injection conditions and configurations. Instead of basing predictions on overall injection similarity parameters, the present trend of film cooling research is to understand the micro-nature of injection. Only in establishing the dependency of the mass, momentum and energy transport processes on injection conditions can a truly universal model be developed. Direct solution of the boundary layer equations, using various boundary conditions and transport models that are characteristic of individual

injection schemes, is necessary to achieve the degree of universality that is required in modern applications.

Until knowledge of the injected boundary layer microstructure is complete, familiarity with existing correlations is essential from a design viewpoint. These correlations are almost entirely two-dimensional but can provide a basis for understanding the trends and importance of injection parameters common to both two and three-dimensional cooling. Appendix A summarizes the majority of film cooling models and correlations for slot and hole cooling with their representative assumptions and applicability. The purpose of Appendix A is twofold: (1) to provide a foundation for the design of a film cooling configuration for a specific application under given constraints, and (2) to emphasize the need for a more fundamental approach to modeling film injection.

III. MODELING CRITERIA FOR GAS TURBINE FILM COOLING SIMULATION

As emphasized in Chapter I, the subject investigation addresses itself to the problem of cooling critical components of a gas turbine engine. Specifically, attention is focused on the high heat-flux, leading edge region of an inlet turbine vane. An injection geometry is proposed which is compatible with leading edge curvature constraints but must be qualified as to its film cooling effectiveness. Chapter II introduced the many pertinent parameters previously found to directly influence the cooling effectiveness, but offered no basic analytical justification of their relevance. The mathematical development of relationships which express the importance of characteristic similarity variables for coolant injection is a necessary exercise if the subject experimental study is to provide film cooling information directly transferable to high-temperature, high-pressure gas turbine applications.

The present Chapter will examine the features of gas film cooling using Fig. 14 as a basic model. A three region model is defined to characterize a film cooled surface: (1) the flow along the surface prior to injection, (2) the area of intensive coolant-jet and boundary layer interaction, and (3) the regime downstream from injection within which the disturbed, blown boundary layer seeks to re-establish normal similarity both hydrodynamically and thermodynamically. By examining the governing equations characteristic of the three regions, the governing parameters are identified such that an experimental study can be conducted at

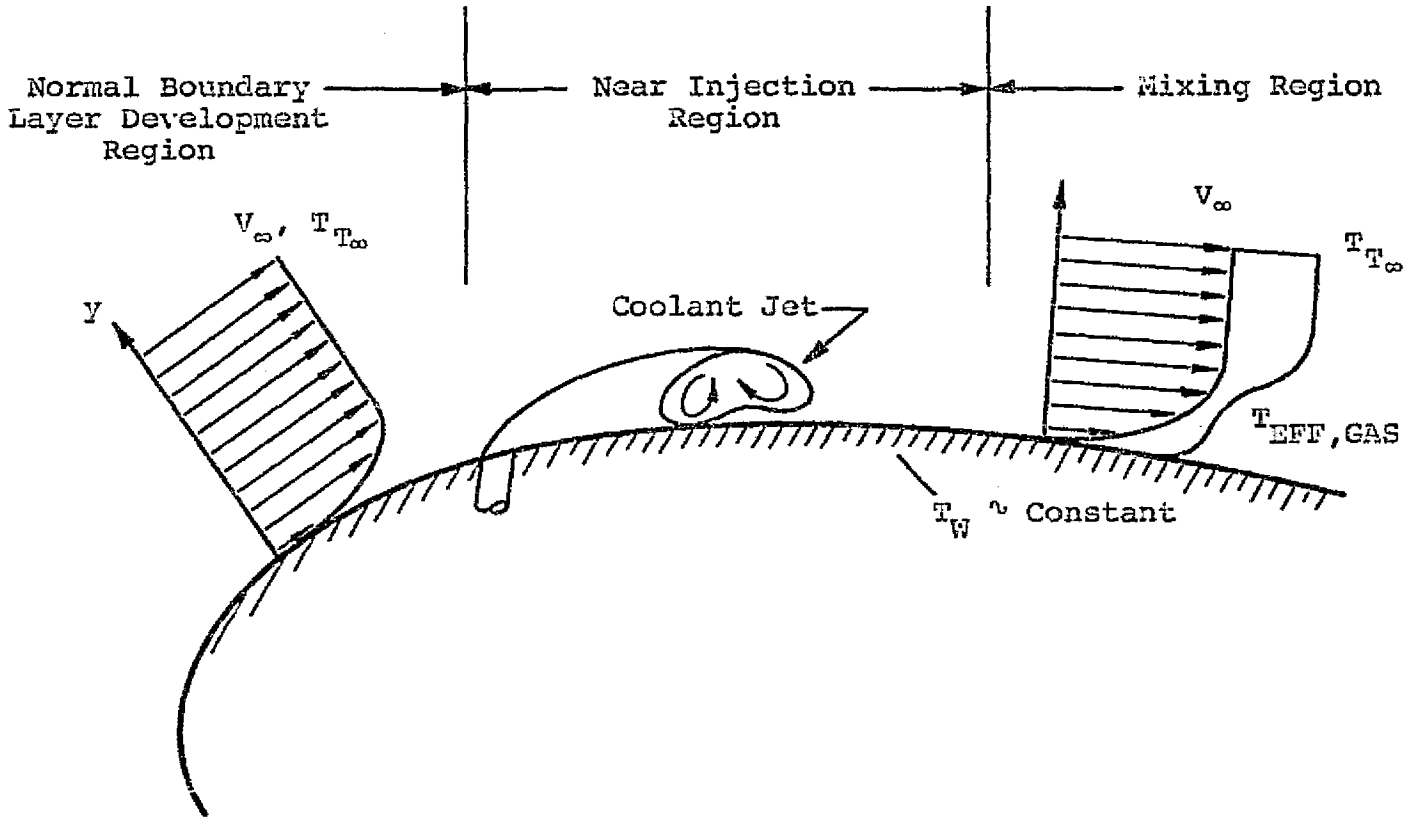

Figure 14. Three-Region Gas Film Cooling Model.

reduced flow conditions that closely approximates the heat transfer environment typical of high-pressure and high-temperature turbine operation.

III.1. Heat Transfer Modeling at Reduced Flow Conditions

Equations (12) and (13) are the non-dimensionalized boundary layer equations for x-momentum and energy (42) representing the initial region, prior to injection, of the three-region model.

$$\rho'\left(u' \frac{\partial u'}{\partial x'} + v' \frac{\partial u'}{\partial y'}\right) = \frac{-\partial p'}{\partial x'} + \frac{G}{Re^2} \rho' \theta' \cos i + \frac{1}{Re} \left(\frac{\partial^2 u'}{\partial y'^2}\right) \qquad (12)$$

$$\rho'\left(u' \frac{\partial \theta'}{\partial x'} + v' \frac{\partial \theta'}{\partial y'}\right) = \frac{1}{RePr} \left(\frac{\partial^2 \theta'}{\partial y'^2}\right) + E\left(u' \frac{\partial p'}{\partial x'}\right) + \frac{E}{Re} \Phi \qquad (13)$$

where

$$\theta' = \left(\frac{T_{T_\infty} - T}{T_{T_\infty} - T_W}\right)$$

G = Grashof number, $\rho^2 g \beta_o (T_{T_\infty} - T) L^3/\mu^2$

Re = Reynolds number, $\rho V_\infty x/\mu$

E = Eckert number, $V_\infty^2/C_p (T_{T_\infty} - T_W)$

i = angle between surface and direction of gradient of gravitational potential field

Φ = viscous dissipation function

It will be shown that by reproducing the same local Mach number and Reynolds number distribution along a geometrically similar surface, the dimensionless heat transfer will be similar. A relation exists between the total pressure and total temperature levels of an actual turbine environment and those at reduced conditions that will insure similarity in the local heat transfer.

For the special case of flow over a turbine airfoil, the ratio of inertial forces to bouyant forces is large (Re >> G), and Eqs. (12) and (13) reduce to

$$\rho'\left(u' \frac{\partial u'}{\partial x'} + v' \frac{\partial u'}{\partial y'}\right) = \frac{-\partial p'}{\partial x'} + \frac{1}{Re} \left(\frac{\partial^2 u'}{\partial y'^2}\right) \tag{14}$$

$$\rho'\left(u' \frac{\partial \theta'}{\partial x'} + v' \frac{\partial \theta'}{\partial y'}\right) = \frac{1}{RePr} \left(\frac{\partial^2 \theta'}{\partial y'^2}\right) + E\left(u' \frac{\partial p'}{\partial x'}\right) + \frac{E}{Re} \Phi \tag{15}$$

Solution of Eqs. (14) and (15) implies the functional dependence of the velocity and temperature fields,

$$\frac{u}{U_\infty} = \frac{u}{U_\infty} (x', y', z', Re, Pr, E) \tag{16}$$

$$\theta' = \frac{T_{T_\infty} - T}{T_{T_\infty} - T_W} = \frac{(T_{T_\infty} - T)}{\Delta T} (x', y', z', Re, Pr, E) \tag{17}$$

For conditions in which the Prandtl number does not vary significantly, and the kinetic energy available in the freestream for dissipation is small compared to the thermal energy, the heat transfer phenomena at reduced flow conditions will simulate those at elevated temperatures and pressures if equivalence in the Reynolds number is maintained. For the remainder of this chapter attention will be focused on maintaining similarity between actual turbine engine conditions (E) and those at reduced temperature and pressure characteristic of turbine modeling (M). Consequently, for similarity in heat transfer

$$Re_x^M = Re_x^E \tag{18}$$

where M ≡ model

E ≡ engine

provided similar geometries are considered.

By definition,

$$Re_x = \frac{\rho V x}{\mu} \tag{19}$$

and

$$V = MaV^* = Ma(\gamma g_c RT)^{1/2} \tag{20}$$

Using the compressible flow relations to define the freestream stagnation conditions external to the boundary layer,

$$T = \frac{T_{T_\infty}}{(1 + \frac{\gamma-1}{2} Ma^2)} \tag{21}$$

and

$$\rho = \frac{p}{RT} = \frac{P_{T_\infty}(1 + \frac{\gamma-1}{2} Ma^2)}{RT_{T_\infty}(1 + \frac{\gamma-1}{2} Ma^2)} \gamma/(\gamma-1) \tag{22}$$

The local Reynolds number can now be written as

$$Re_x = \frac{Ma_x(\gamma g_c)^{1/2} x}{\mu(RT_{T_\infty})^{1/2}} P_{T_\infty}(1 + \frac{\gamma-1}{2} Ma_x^2)^{-\frac{(\gamma+1)}{2(\gamma-1)}} \tag{23}$$

Requiring equivalence in the local Reynolds numbers between the model and the engine results in

$$\frac{Re_x^M}{Re_x^E} = 1 = \left(\frac{Ma_x^M}{Ma_x^E}\right)\left(\frac{\gamma^M}{\gamma^E}\right)^{1/2}\left(\frac{P_{T_\infty}^M}{P_{T_\infty}^E}\right)\left(\frac{R^E T_{T_\infty}^E}{R^M T_{T_\infty}^M}\right)^{1/2} \times$$

$$\frac{[1 + \frac{\gamma^E-1}{2} Ma_x^{E^2}]^{\frac{\gamma^E+1}{2(\gamma^E-1)}}}{[1 + \frac{\gamma^M-1}{2} Ma_x^{M^2}]^{\frac{\gamma^M+1}{2(\gamma^M-1)}}} \left(\frac{\mu^E}{\mu^M}\right)\left(\frac{x^M}{x^E}\right) \tag{24}$$

Provided the local Mach number can be simulated at geometrically similar locations such that

$$Ma_x^M = Ma_x^E \tag{25}$$

and

$$(x/L_{char})^M = (x/L_{char})^E \tag{26}$$

then Eq. (24) can be rewritten using Eq. (25) and (26) as

$$\frac{Re_x^M}{Re_x^E} = 1 = \left(\frac{\gamma^M}{\gamma^E}\right)^{1/2}\left(\frac{P_{T_\infty}^M}{P_{T_\infty}^E}\right)\left(\frac{R^E T_{T_\infty}^E}{R^M T_{T_\infty}^M}\right)^{1/2} f_1(Ma_x^M, Ma_x^E, \gamma^M, \gamma^E)\, C_{MF}\left(\frac{\mu^E}{\mu^M}\right) \tag{27}$$

where

$$f_1 = \frac{\left[1 + \frac{\gamma^E - 1}{2}(Ma_x^E)^2\right]^{(\gamma^E+1)/2(\gamma^E-1)}}{\left[1 + \frac{\gamma^M - 1}{2}(Ma_x^M)^2\right]^{(\gamma^M+1)/2(\gamma^M-1)}} \tag{28}$$

and

$$C_{MF} \equiv \text{geometric modeling factor} = \frac{L^M_{char}}{L^E_{char}}$$

$L^E_{char} \equiv$ characteristic dimension of engine component

$L^M_{char} \equiv$ characteristic dimension of similar model component

For large differences between engine and model conditions with $Ma_x^M = Ma_x^E$, f_1 does not significantly deviate from unity. For example, for T_{T_∞} = 1922°K (3460°R) and an ASTM-A-1 fuel-to-air ratio of 0.03, γ^E = 1.263. Using $T_{T_\infty}^M$ = 700°K (1260°R) and a natural gas fuel-to-air ratio of 0.01 (typical for reduced conditions simulating the engine

environment), $\gamma^M = 1.358$. Under these specifications f_1 ranges from 0.9895 at $Ma_x = 1.0$ to 0.9998 for $Ma_x = 0.10$. Therefore Eq. (27) can be approximated as

$$\frac{Re_x^M}{Re_x^E} = \left(\frac{\gamma^M}{\gamma^E}\right)^{1/2}\left(\frac{P_{T_\infty}^M}{P_{T_\infty}^E}\right)\left(\frac{R^E T_{T_\infty}^E}{R^M T_{T_\infty}^M}\right)^{1/2} C_{MF}\left(\frac{\mu^E}{\mu^M}\right) = 1 \qquad (29)$$

Equation (29) states that for modeling a given engine condition at a particular geometric scale factor, the reduced operating pressure is fixed once a total gas temperature is selected. It is recognized at this point that the development of the similarity criteria has neglected chemical modeling. For operation at high turbine inlet temperatures, the effects of the combustion processes may indeed be important. However, at reduced temperatures and pressures, simulation of chemical phenomena will not be attempted herein.

III.2. Identification of Pertinent Film Cooling Parameters

Simulation of the near injection region requires a consideration of the coolant-jet and hot gas boundary layer interaction. The degree of cooling achievable in this region is primarily dominated by the jet-trajectory. Immediately following injection, the coolant jets are acted upon inertially rather than in a viscous manner characteristic of turbulent mixing. The initial dynamic interaction of the boundary layer with the cylindrical profile of the coolant jet establishes the form drag forces that determine the jet trajectory. Keeping the jet axis near the wall, wholly within the boundary layer, is necessary to realize significant cooling effects.

In the following discussion, a simplified analysis of a jet in a crossflow is presented. This mathematical description of the trajectory of the jet, representative of injection from a film cooling hole, shows that the injection angle, coolant momentum, and boundary layer thickness at injection are the major parameters governing the jet trajectory.

Figure 15 shows a control volume for the analysis of an issuing coolant jet. It is assumed that the jet momentum along the y axis is constant and equal to the initial value,

$$\frac{d}{dy}\left[\sin \chi \int_{JET} \rho V_J^2 dA\right] = 0 \tag{30}$$

which can be integrated to give

$$\sin \chi \int_{JET} \rho V_J^2 dA = \rho_C V_C^2 A_o \sin \chi_o \tag{31}$$

where $\rho_C V_C^2$ = initial coolant momentum flux

A_o = area of coolant hole

χ_o = initial injection angle

The x-momentum equation for the jet can be written as

$$\frac{d}{dx}\left[\cos \chi \int_{JET} \rho V_J^2 dA\right] - \frac{V_\infty \ddot{M}_e \pi d_o}{\cos \chi} = F_{x,drag} \tag{32}$$

where $\ddot{M}_e$ is the mass flux entrained from the freestream and F_x is a drag force.

Assuming the entrainment is initially small, Eq. (32) can be approximated as

$$\frac{d}{dx}\left[\cos \chi \int_{JET} \rho V_J^2 dA\right] = F_{x,drag} \tag{33}$$

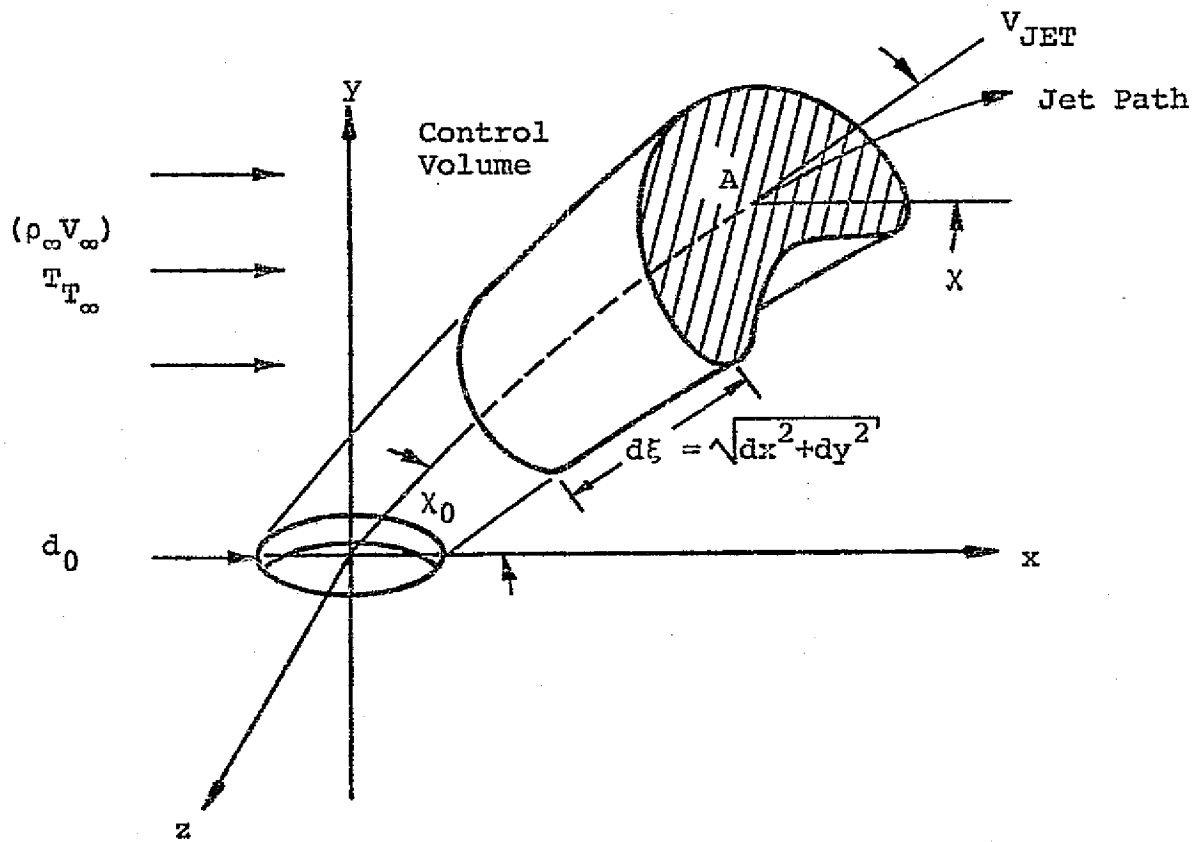

Figure 15. Illustration of Control Volume For Analysis of Film Coolant, Jet Trajectory.

The cylinder-in-crossflow drag force can be estimated as follows

$$F_X = \frac{1}{2} \rho_\infty V_\infty^2 d_0 \tan X \, C_D \tag{34}$$

where $\rho_\infty V_\infty^2$ = freestream momentum flux

d_0 = coolant hole diameter

C_D = cylinder-in-crossflow drag coefficient

Equation (34) represents the drag force per unit length on the jet core assuming no spreading and slug type flow. To account for the jet spread, Abramovich (43) suggests a linear relation

$$d = d_0\left(1 + a \frac{X}{d_0}\right) \tag{35}$$

where a = empirical spreading constant

Also a correction factor, C*, for non-slug type flow of an actual boundary layer can be used to adjust the drag force term. Equation (34) can now be expressed as

$$F_X = \frac{1}{2} \rho_\infty V_\infty^2 C_D C^* d_0 \left(1 + a \frac{X}{d_0}\right) \tan X \tag{36}$$

Thus Eq. (33) reduces to the form

$$\frac{d}{dx}\left[\cos X \int_{JET} \rho V_J^2 dA\right] = \frac{1}{2} \rho_\infty V_\infty^2 C_D C^* d_0 \left(1 + a \frac{x}{d_0}\right) \tan X \tag{37}$$

To simplify Eq. (37) further, the integral term may be expressed as

$$\cos X \int_{JET} \rho V_J^2 dA = \left(\frac{\cos X}{\sin X}\right) \sin X \int_{JET} \rho V_J^2 dA \tag{38}$$

and by using Eq. (31) in the following form

$$\cos \chi \int_{JET} \rho V_J^2 dA = \rho_C V_C^2 A_o \sin \chi_o \cot \chi \tag{39}$$

Eqn. (37) can be rewritten as

$$\rho_C V_C^2 A_o \sin \chi_o \frac{d}{dx} (\cot \chi) = \frac{1}{2} \rho_\infty V_\infty^2 C_D C^* d_o \left(1 + a \frac{x}{d_o}\right) \tan \chi \tag{40}$$

where

$$\cot \chi = \frac{dx}{dy} \tag{41}$$

Upon substitution of Eq. (41), Eq. (40) becomes a second-order, ordinary differential equation that can be integrated twice to yield,

$$y' = \frac{1}{\sqrt{\alpha^*}} \ell n \left[\frac{\alpha^* x'^2 + \frac{\alpha^* a}{2} x' + \sqrt{\alpha^* x'} + \frac{1}{\tan^2 \chi_o} + \frac{\sqrt{\alpha^* a}}{4}}{\frac{1}{\tan^2 \chi_o} + \frac{\sqrt{\alpha^* a}}{4}} \right] \tag{42}$$

where $\alpha^* = \dfrac{4 C_D C^*}{\pi I \sin \chi_o}$

$I = \rho_C V_C^2 / \rho_\infty V_\infty^2$

$y' = y/d_o$; $x' = x/d_o$

The ratio of the coolant momentum flux to the freestream momentum flux (I), together with the initial injection angle (χ_o) and character of the boundary layer at injection (C*) are shown in Eq. (42) to be important parameters in modeling the near injection regime.

Some caution must be exercised in using this jet trajectory model to fully explain film cooling effectiveness trends with variations in certain injection parameters. Freestream mass entrainment was neglected

in the development of Eq. (42). Although Eq. (42) may provide a reasonable estimate of the general jet location with respect to the wall, the film cooling effectiveness is expected to be strongly influenced by a mixing term (as represented by the jet entrainment). Thus, while Eq. (42) provides a reasonable representation of some of the more important film injection hydrodynamic parameters, an evaluation of the cooling effectiveness would require a more accurate treatment of the important mixing phenomena.

The final region of the film cooling model characterizes the mixing process between adjacent jets and the boundary layer. Up to this point, each jet development was analyzed individually and assumed to be independent of the proximity of neighboring jets (i.e. a row of holes). The third region of the film cooling model is now discussed in which it is assumed that all adjacent jets have coalesced and mixed to a uniform degree. Figure 16 is a sketch showing a control volume for analysis of the mixing between the coolant and the mainstream. The important coolant and freestream parameters that can be expected to govern the film cooling performance are deduced from a basic heat sink analysis following that presented by Goldstein (44). A characteristic temperature, representative of the average, mixed temperature of the film cooled boundary layer can be defined by an application of the conservation of mass and energy for a station, x, downstream from the near injection region. The mass flow in the boundary layer can be expressed as

$$\dot{m}_{out} = \dot{m}_C + \dot{m}_\infty \qquad (43)$$

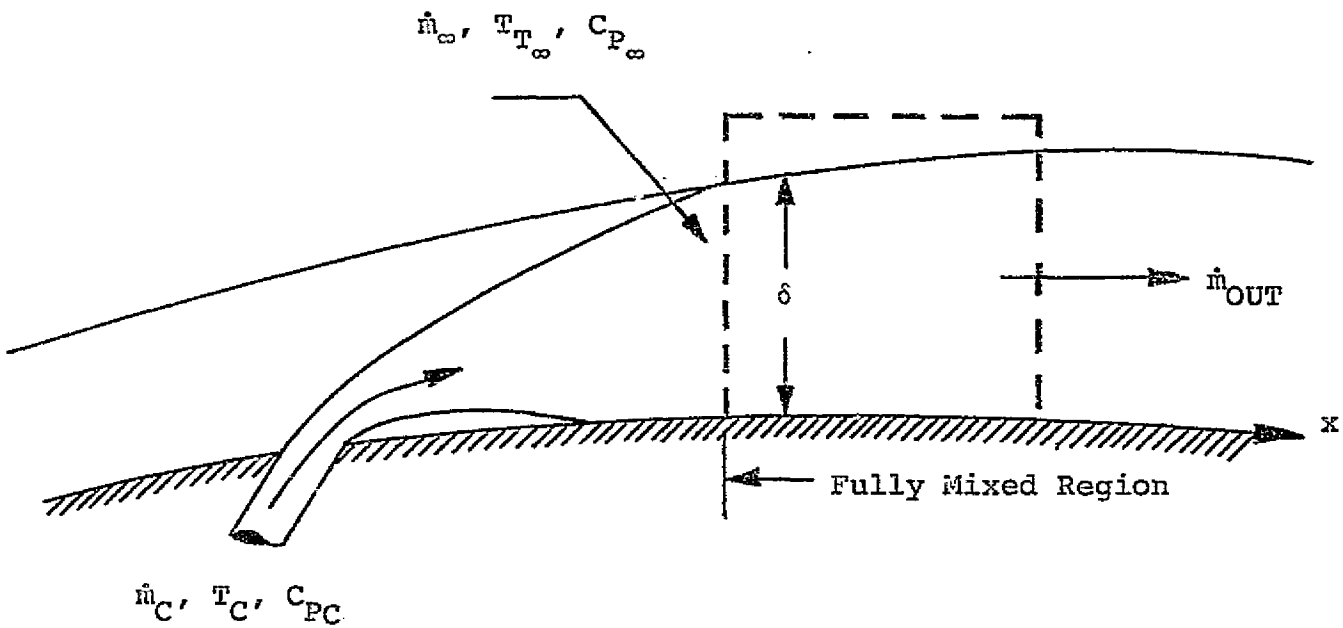

Figure 16. Illustration of Control Volume Used in Analysis of Fully Mixed Region.

where $\dot{m}_c$ = film coolant mass flow injected

$\dot{m}_\infty$ = boundary layer mass flow entrained from the freestream

If the wall over which the fluid flows is adiabatic, the energy equation yields

$$\dot{m}_c C_{pc} T_c + \dot{m}_\infty C_{p_\infty} T_\infty = \dot{m}_{out} \overline{C_p}\ \overline{T}_x \tag{44}$$

And combining Eqs. (43) and (44), assuming a constant specific heat (i.e. $C_{pc} \approx C_{p_\infty} \approx \overline{C_p}$), the average temperature characteristic of the completely mixed, film cooled boundary layer is obtained.

$$\overline{T}_x = \frac{\dot{m}_c T_c + \dot{m}_\infty T_\infty}{(\dot{m}_c + \dot{m}_\infty)} \tag{45}$$

$\overline{T}_x$ approximates the film cooled adiabatic wall temperature which governs the heat flux to the wall for the case of a cooled (non-adiabatic) surface (44).

The mass flow of the mainstream into the boundary layer control volume, $\dot{m}_\infty$, can be approximated by assuming a 1/7 power velocity profile and $\rho \approx \rho_\infty$.

$$\dot{m}_\infty = \int_0^\delta \rho u L_{sp} dy = \rho_\infty V_\infty L_{sp} \delta \int_0^1 \left(\frac{y}{\delta}\right)^{1/7} d\left(\frac{y}{\delta}\right) \tag{46}$$

where

L_{sp} = span of cooled surface

Equation (46) then reduces to

$$\dot{m}_\infty = 7/8\ \rho_\infty V_\infty \delta_x L_{sp} \tag{47}$$

where δ_x = boundary layer thickness at x

The coolant flow rate can be written as

$$\dot{m}_c = (\rho_c V_c)\, NA_{hole} = (\rho_c V_c)\, N\, \frac{\pi d_0^2}{2} \tag{48}$$

where N = number of film coolant holes

The average boundary layer temperature may then be written,

$$\overline{T}_x = \left[\frac{\dfrac{2\rho_c V_c\, N\pi\, d_0^2\, T_c}{7\rho_\infty V_\infty\, \delta_x L_{sp}} + T_\infty}{\dfrac{2\rho_c V_c\, N\pi\, d_0^2}{7\rho_\infty V_\infty\, \delta_x L_{sp}} + 1}\right] \tag{49}$$

For $L_{sp} \approx S_1 N$, Eq. (49) can be expressed as

$$\overline{T}_x = \left[\frac{\dfrac{2M\pi T_c}{7(\delta_x/d_0)(S_1/d_0)T_\infty} + 1}{\dfrac{2M\pi}{7(\delta_x/d_0)(S_1/d_0)} + 1}\right] T_\infty \tag{50}$$

Equation (50) has been developed simply to bring out the important features of coolant injection that are responsible for lowering the temperature of the mainstream boundary layer downstream of the coolant holes. Equation (50) indicates that as $M \to 0$ (i.e. no coolant injection into the hot gas boundary layer) $\overline{T}_x = T_\infty$. Also, as the coolant film moves farther from the injection site, for any M, (δ_x/d_0) will increase resulting in diminished effects of injection and $\overline{T}_x$ approaching T_∞.

Drawing on the information derived from the three-region film injection model, the following guidelines for proper experimental modeling were observed:

(1) to maintain similar velocity and temperature fields at reduced flow conditions, a unique relation between the total gas temperature and pressure is required,

(2) the momentum flux ratio, $\rho_c V_c^2/\rho_\infty V_\infty^2$, freestream mass entrainment ($\overline{M}_e$), the injection angle (X_0) and the state of the momentum boundary layer thickness at injection (C*) are significant parameters for the near-injection region, and

(3) the film coolant blowing ratio (M), the hole spacing (S_1/d_0), the boundary layer thickness ratio (δ_x/d_0), as well as the coolant-to-gas temperature ratio (T_c/T_∞) determine the downstream film cooling performance.

To achieve the objective of determining the cooling effectiveness of a proposed turbine vane leading-edge injection configuration, it is important to properly model each of the items described in the aforementioned film cooling model such that results obtained at reduced flow conditions (model) are applicable to film cooling under realistic engine conditions.

To maintain similarity between an engine cooling condition and a model simulation, for a typical hole spacing configuration and injection angle, equivalence of the mass and momentum flux ratios must be maintained.

$$M^M = \frac{(\rho_c V_c)^M}{(\rho_\infty V_\infty)^M} = \frac{(\rho_c V_c)^E}{(\rho_\infty V_\infty)^E} = M^E \tag{51}$$

and

$$I^M = \frac{(\rho_c V_c^2)^M}{(\rho_\infty V_\infty^2)^M} = \frac{(\rho_c V_c)^E}{(\rho_\infty V_\infty^2)^E} = I^E \tag{52}$$

Equations (51) and (52) can only be satisfied simultaneously when

$$\left(\frac{V_c}{V_\infty}\right)^M = \left(\frac{V_c}{V_\infty}\right)^E \tag{53}$$

Furthermore, Eqs. (51) and (53) require that

$$\left(\frac{\rho_c}{\rho_\infty}\right)^M = \left(\frac{\rho_c}{\rho_\infty}\right)^E \tag{54}$$

Equation (54) can also be expressed as

$$\frac{\left(\frac{P_c}{R_c T_c}\right)^M}{\left(\frac{P_\infty}{R_\infty T_\infty}\right)^M} = \frac{\left(\frac{P_c}{R_c T_c}\right)^E}{\left(\frac{P_\infty}{R_\infty T_\infty}\right)^E} \tag{55}$$

Rearranging Eq. (55), one finds that

$$(R_\infty T_\infty)^M = \left(\frac{R_\infty T_\infty}{R_c T_c}\right)^E \left(\frac{P_c}{P_\infty}\right)^E \left(\frac{P_\infty}{P_c}\right)^M (R_c T_c)^M \tag{56}$$

With the mass flux ratio and momentum flux ratios referenced to the exit conditions of the coolant holes,

$$\left(\frac{P_c}{P_\infty}\right)^E = \left(\frac{P_c}{P_\infty}\right)^M = 1 \tag{57}$$

Eq. (56) reduces to

$$(R_\infty T_\infty)^M = \left(\frac{R_\infty T_\infty}{R_c T_c}\right)^E (R_c T_c)^M \tag{58}$$

To simulate turbine cooling conditions (T_∞^E, T_c^E), a hot gas static temperature at injection, T_∞^M, can be determined from Eq. (58) by specifying a reduced coolant temperature, T_c^M. Knowing the Mach number

at injection (assumed to match the prototype) a total gas temperature, $T_{T_\infty}{}^M$, can be determined. Using Eq. (29), a reduced total pressure, $P_{T_\infty}{}^M$, is uniquely specified. With $P_{T_\infty}{}^M$, $T_{T_\infty}{}^M$ and the local Mach number distribution specified, similarity in heat transfer between the model and engine conditions is established.

By requiring an equivalence of I^E and I^M, sizing of the injection hole diameter relative to actual hardware can be accomplished. To maintain proper dynamic interaction between the coolant jets and the boundary layer, the ratio of the drag forces exerted on the issuing jets to the change in the coolant momentum flux from the plenum to the exit of the coolant hole must be maintained. Assuming that the coolant jet trajectory is influenced by drag forces indicative of the local momentum-thickness boundary layer, the following can be written

$$\frac{\left[\dfrac{(\rho_\infty V_\infty^2)(\theta_i d_0)}{(\rho_c V_c^2)(d_0^2)}\right]^E}{\left[\dfrac{(\rho_\infty V_\infty^2)(\theta_i d_0)}{(\rho_c V_c^2)(d_0^2)}\right]^M} = 1 \tag{59}$$

where θ_i = momentum boundary layer thickness at injection

However, since $I^E = I^M$, Eq. (59) can be expressed

$$(\theta_i/d_0)^E = (\theta_i/d_0)^M \tag{60}$$

At similar locations along the film cooled surface,

$$\theta_i{}^M = C_{MF}\,\theta_i{}^E \tag{61}$$

Substituting Eq. (61) into (60), determines the model coolant hole diameter as

$$d_0^M = C_{MF}\, d_0^E \tag{62}$$

Under the condition stated in Eq. (62) and assuming that the viscosity of the air varies as

$$\left(\frac{\mu}{\mu_{ref}}\right) = \left(\frac{T}{T_{ref}}\right)^{\omega} \tag{63}$$

over the range $T_C^M < T < T_\infty^E$, the coolant Reynolds numbers based on the coolant hole diameters are equivalent.

$$Re_{C,d_0}^M = Re_{C,d_0}^E \tag{64}$$

For a simulation in which L'/d_0 remains close to the actual wall thickness-to-hole diameter ratio for a turbine vane, Eq. (64) establishes the necessary condition for correctly modeling the dimensionless pressure drop and heat transfer through the coolant holes.

A mathematical justification has been presented for those film cooling similarity parameters previously noted to be important in modeling gas film cooling configurations (Chapter II. Literature Survey). The attention of the reader is now shifted to a description of the subject experimental investigation in which the concepts of Chapter III. (modeling) are applied to assess the cooling effectiveness of a proposed turbine-vane, leading-edge, cooling configuration.

IV. THE EXPERIMENTAL INVESTIGATION

IV.1. Experimental Apparatus

One of the major objectives of the present investigation was the simulation of the high pressure and high temperature turbine environment (as specified by Chapter III) suitable for modeling the heat transfer to a film cooled turbine vane. A geometric modeling factor was chosen such that the test vane was a 3X size representation of a prototype vane design for a high temperature and high pressure gas turbine engine. Figure 17 shows the prototype vane contour described by the tabulated nondimensional coordinates. The model leading edge radius was 0.0152m (0.6 in) with a vane span of 0.114m (4.5 in). A two-dimensional test section was constructed housing the suction and pressure surfaces of the vane model. The test section was located downstream from a hot-gas generator, capable of matching the test section inlet Mach number, Reynolds number and turbulence intensity with those characteristic of the prototype turbine inlet conditions. The details of the vane model were such that film coolant could be injected through a single row of holes with three different locations of the row relative to the stagnation point (3 locations on the suction surface and 3 on the pressure surface).

The following sections present a complete description of the capabilities of the experimental system, a description of the overall flow system, the turbulence generating inlet section, the two-dimensional

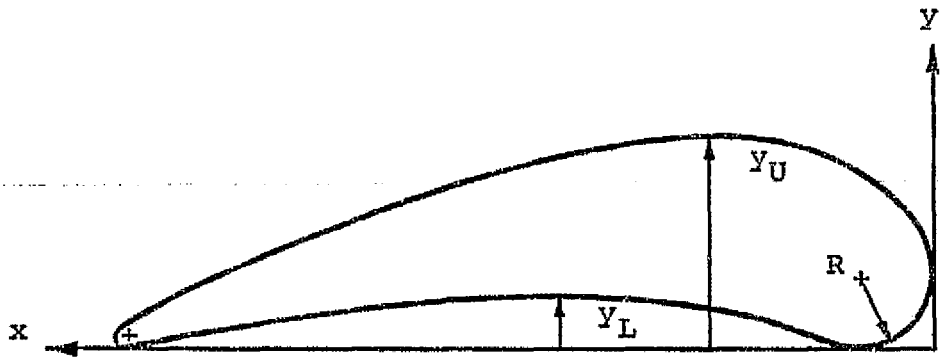

R = 0.0015m (0.6in)

x/R	$y_{L/R}$	$y_{U/R}$
0	0.333	0.333
0.082		0.550
.164		0.648
.246		0.723
.328		0.782
.410		0.830
.492	0.041	0.866
.574	0.075	0.897
.656	0.105	0.920
.738	0.130	0.935
.820	0.153	0.945
.902	0.172	0.950
.984	0.189	0.953
1.148	0.212	0.943
1.312	0.231	0.920
1.476	0.243	0.886
1.640	0.248	0.848
1.804	0.246	0.810
1.969	0.238	0.766
2.133	0.228	0.717
2.297	0.213	0.663
2.461	0.192	0.609
2.625	0.169	0.548
2.789	0.143	0.482
2.953	0.115	0.410
3.117	0.084	0.336
3.280	0.054	0.256
3.445	0.016	0.172
3.586	0.057	0.057

Figure 17. Dimensionless Coordinates of Vane Model.

vane channel, and a review of the various measurement techniques employed.

IV.1.1. General Flow System

Figure 18 is a simplified schematic of the overall flow system used in conducting this investigation. A high pressure air supply delivered air at pressures from 9.7 - 11.4 × 10^5 N/m^2 (139.7 - 164.7 psia) with mass flow rates up to 7.73kg/sec (17 lbm/sec). To provide control of the temperature to the test channel, the supply air was split into two paths: a by-pass line and a supply line for a natural gas combustor. Combustor exit air temperatures up to 1033°K (1860°R) were available with mixing of the combustor exit and by-pass air to provide a wide range of operating temperatures. The mixed heated air flowed through an S-shaped duct and a straight section 6.10m (20 ft) long × 0.254m (10 in) diameter, and then through a turbulence generation assembly before entering the vane channel test section. The flow into the vane test section was split into three legs: two .152m (6 in) by-pass lines and a .208m (8 in) mainflow line that were individually throttled before exhausting to a collection manifold. The manifold air was throttled prior to exhausting into an altitude chamber capable of back pressures from .254m (10 in) of mercury to atmospheric conditions. Figure 19 illustrates the flow system upstream from the test section. General features (indicated by the numbered arrows) include the natural gas combustor (1), the dilution-air supply line (2) and the S-duct leading to the test section (3). Figure 20 shows the turbulence generator section (1) and the vane channel (2) with the side cover-plate removed.

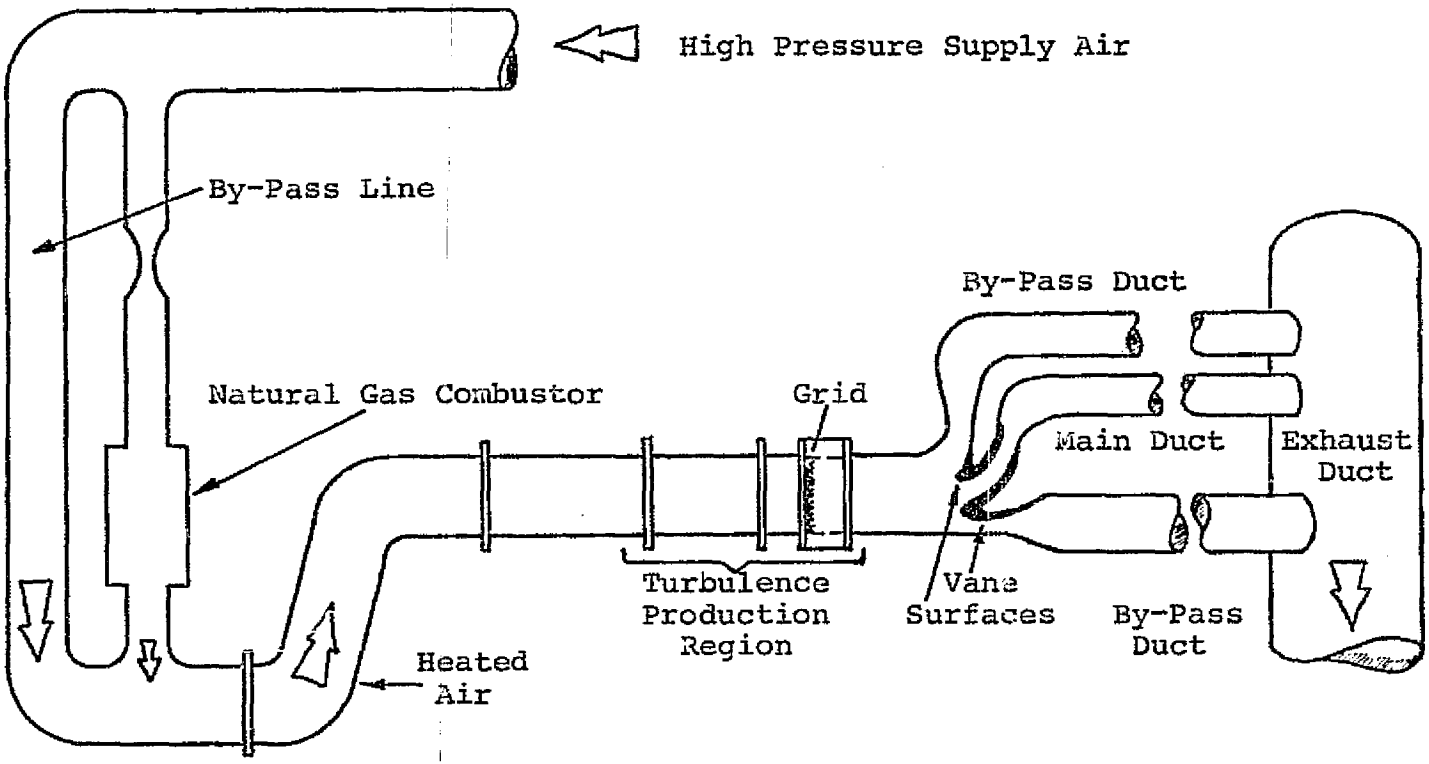

Figure 18. Test Facility Schematic.

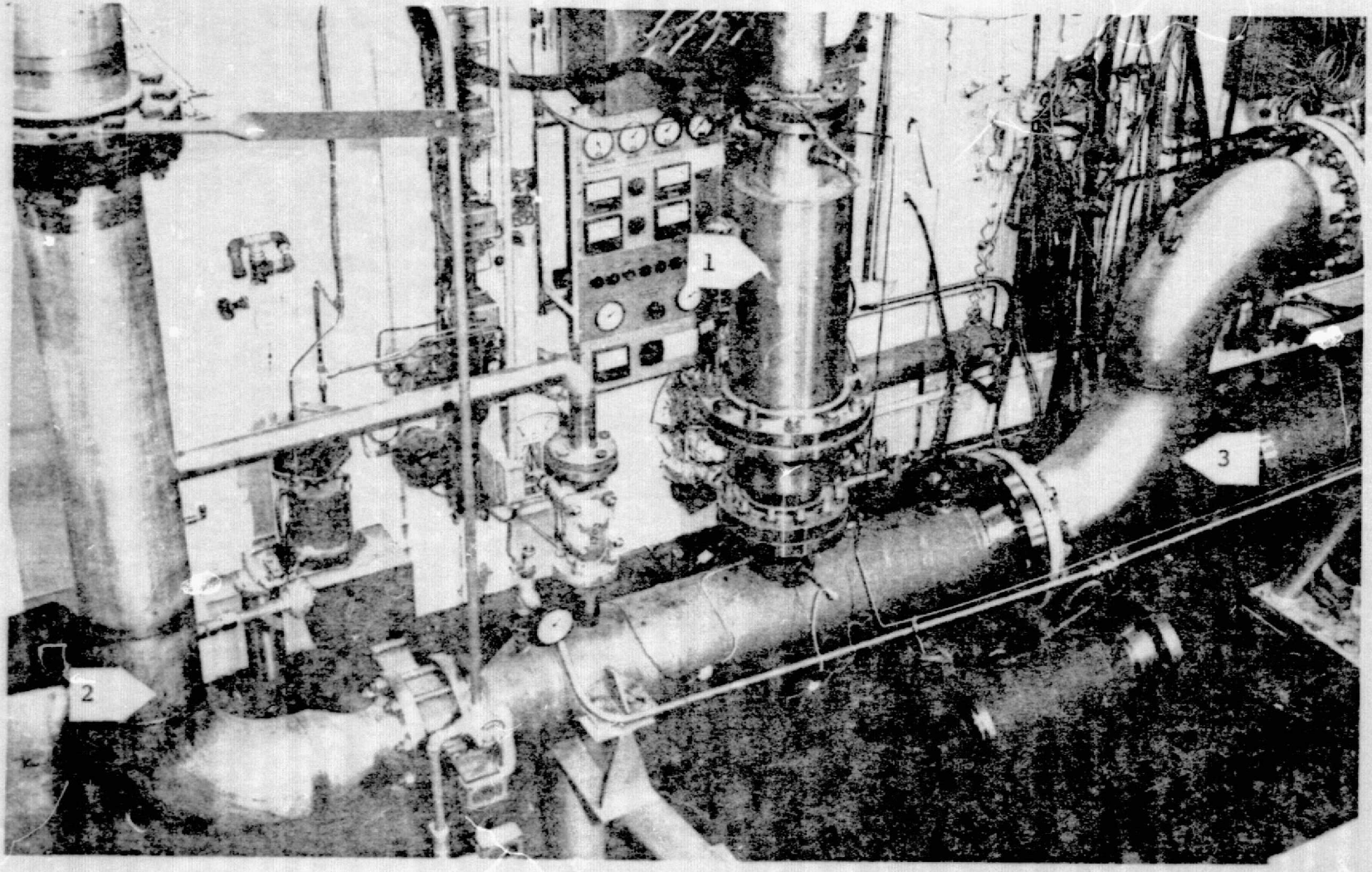

Figure 19. Photograph Showing Upstream Combustor (1), Dilution Air Supply (2) and S-duct (3).

Figure 20. Photograph Showing Turbulence Generating Inlet Section (1) and Test Vane Channel (2).

IV.1.2. Turbulence Generation Assembly

The turbulence generation assembly was designed to permit variation of the vane channel inlet freestream turbulence intensity from low to relatively high levels by utilizing screens of varying sizes located at selected positions upstream from the vane channel. Turbulence intensity measurements, using a hot film probe and anemometer, were made at the test section inlet as a function of screen size and eight upstream locations. Based on the screen wire diameter, d_W, the nondimensional distance from the screen to the hot film probe, x/d_W, could be varied from $x/d_W = 30$ to $x/d_W = 335$. Using the theory for decay of isotropic turbulence downstream from screens (45, 46), the turbulence intensity level (Tu_∞) created by the turbulence generation assembly was estimated to range from 1.4% to 12%.

Two types of screens were used in this investigation: (1) a screen with 1.59×10^{-3}m (0.0625 in) diameter wires (d_W) at 7.94×10^{-3}m (0.3125 in) center-to-center spacings (M_S), and (2) a 3.18×10^{-3}m (0.125 in) diameter wire mesh with 6.36×10^{-3}m (0.250 in) center-to-center spacing. The full details of the design of the turbulence section can be found in Appendix B.1.

IV.1.3. Test Section

The 3X size vane test section consisted of the two-dimensional channel formed by the suction and pressure surfaces of two adjacent turbine vanes. Figure 21 is a close-up illustration of the vane test section shown as item (2) in Figure 20. Figure 21 shows the test section (with cover plate removed) comprised of three flow channels: two by-pass legs (1, 2) and a main flow channel (3) formed by the suction surface of

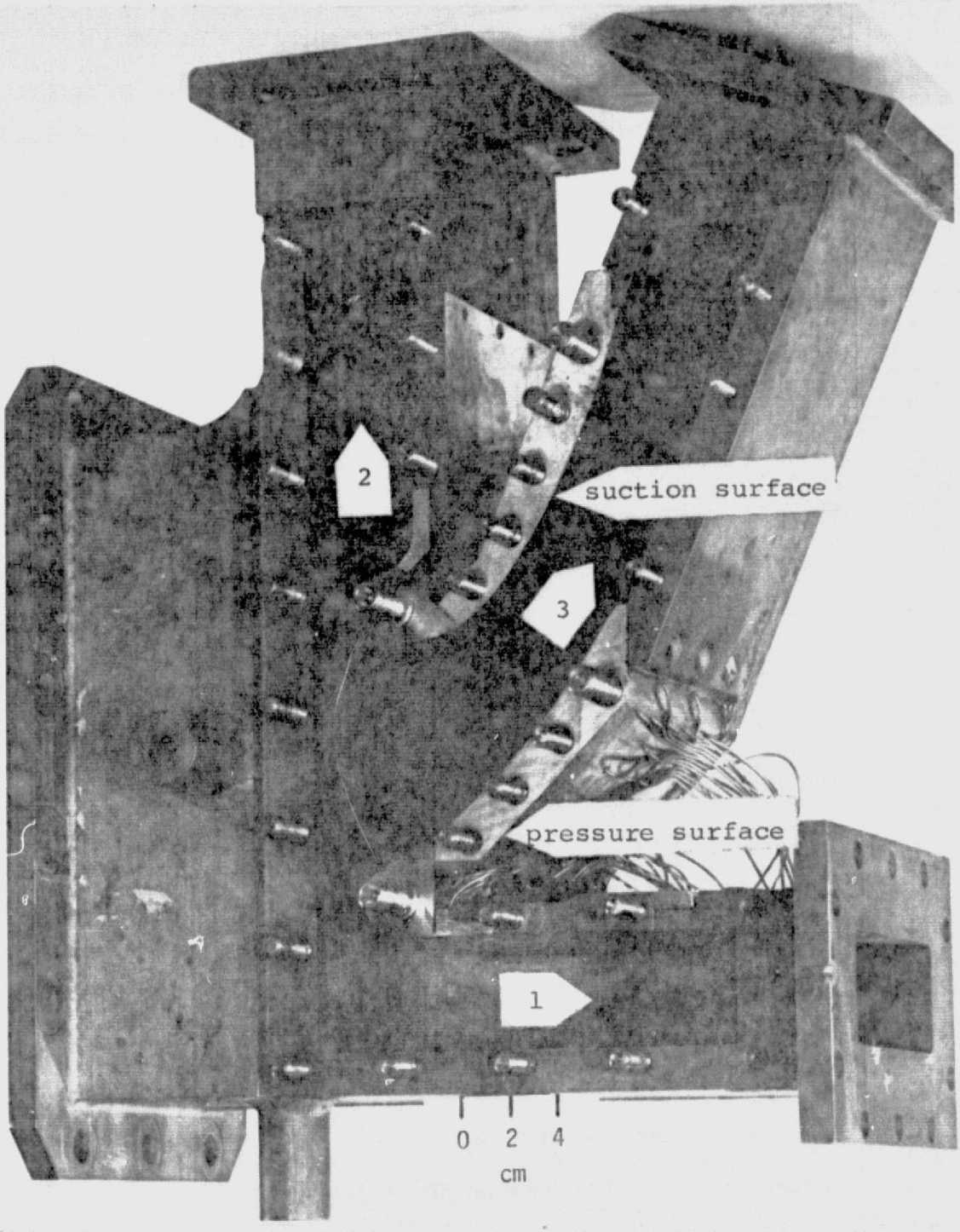

Figure 21. Photograph of Test Section Illustrating By-Pass Channels (1, 2) and Main Vane Channel (3).

one vane and the pressure surface of the adjacent vane. This channel design was chosen for its ease in instrumenting the vane test surface. As shown, the back sides of both vanes were open to the surroundings to facilitate access to all vane surface instrumentation. The two by-pass channels were throttled independently in order to split the test section inlet flow in the right proportions for proper control of the stagnation point at the vane leading edge.

Three main items constitute the test section when assembled: the main housing, the individual vane surfaces, and the side cover-plate. With the cover-plate removed (see Fig. 21), the vane surfaces were bolted to the opposite wall of the housing and to the exit ducts of the three flow passages. The two surfaces were positioned with their chord lines at 44.5° with respect to the mainstream flow direction, matching the orientation of the prototype vane. The cover plate was installed by bolting it to both the housing and the vane surfaces. Removal of the cover plate allowed immediate access to the vanes for both inspection and repair.

The stainless steel, main housing had a rectangular inlet area of 0.144m × 0.244m and, at the vane leading edge, was divided in the ratio of 1:1:2 for the two by-pass ducts and the vane channel, respectively. Three water-cooled access ports (0.0127m (0.5 in) diameter) for introducing traversing probes were located at the bottom and side walls of the housing, 0.0762m (3 in) upstream from the vane leading edge.

Figure 22 illustrates the construction details for the vane suction surface and Fig. 23 presents similar information for the vane pressure surface. The test vanes were constructed of contoured stainless steel

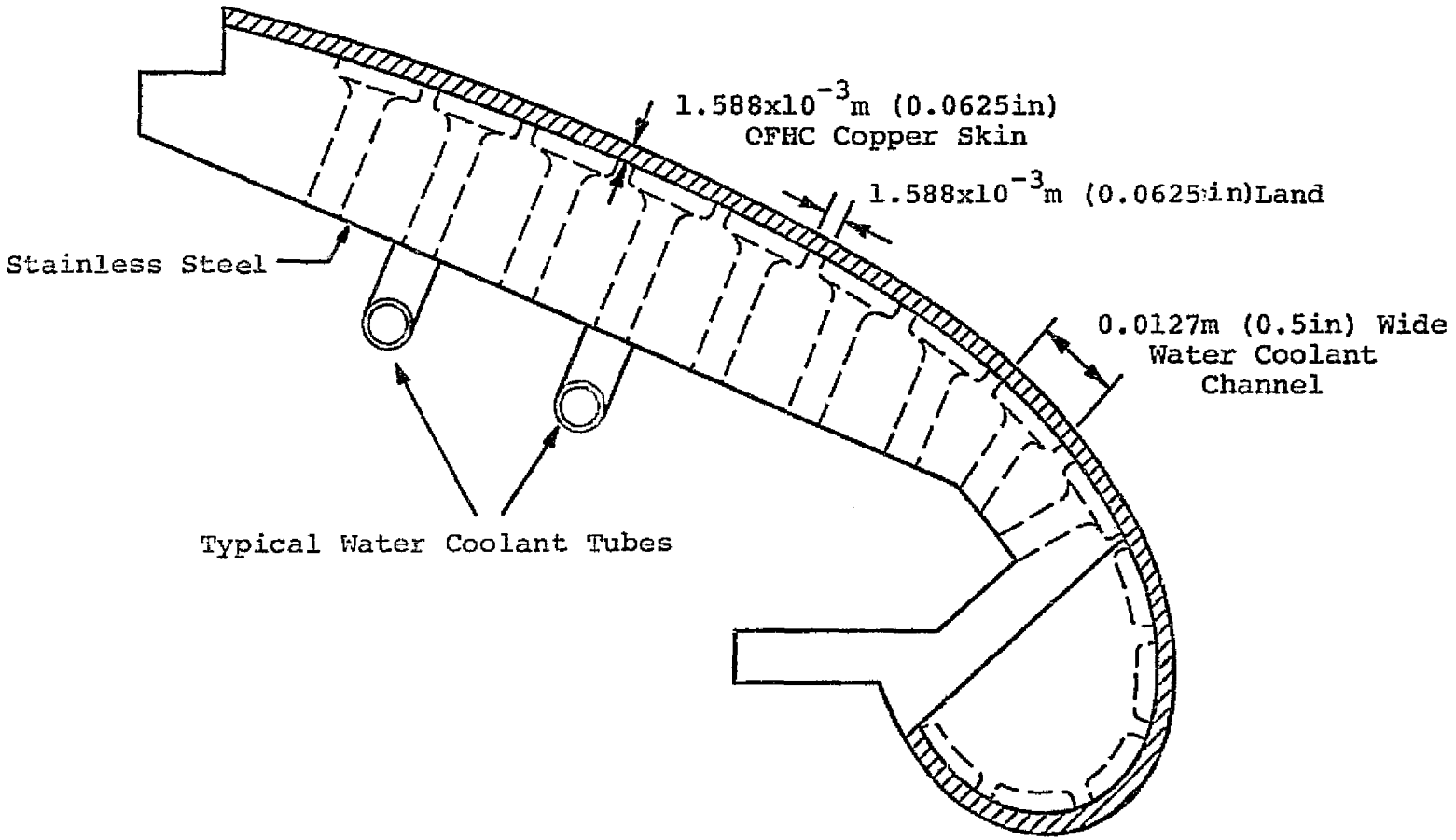

Figure 22. Construction Details For Suction Surface.

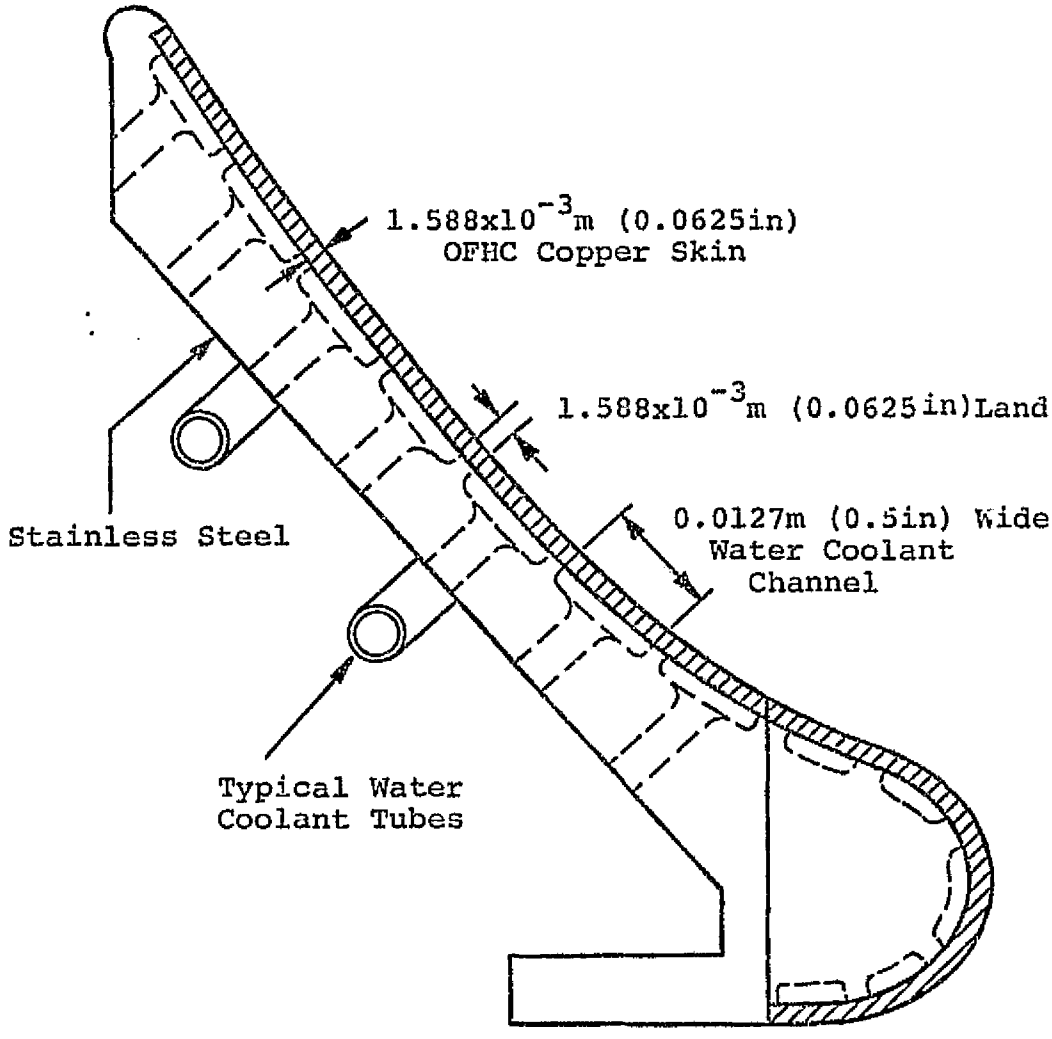

Figure 23. Construction Details For Pressure Surface.

inner structures over which copper skins (1.588×10^{-3}m (0.0625 in) thick, oxygen-free, high-conductivity copper) were attached. The copper skins were furnace brazed to the inner bodies along 1.588×10^{-3}m (0.0625 in) wide lands that separated water coolant channels running along the span of the vanes. The coolant channels were 1.588×10^{-3}m (0.0625 in) deep and 0.0127m (0.50 in) wide (along the surface contour) and carried a water flow of 0.063 to 0.126 liter/sec (1 to 2 gal/min) per channel. The coolant channels were closely spaced along the surface contours of both vanes and were individually throttled to provide variation of heat removal from the copper test surfaces. This design insured the capability of maintaining a uniform wall-temperature for the heat transfer experiments and, at the same time, permitted the vane surfaces to operate at a temperature level that simulated the freestream gas-to-wall temperature ratio of the prototype vane. Moderate wall temperatures were also necessary for proper operation of the heat flux sensors selected for use in this study.

Figure 24 illustrates another basic feature of the test vane design. Both the suction and pressure surfaces had removable leading edge sections. Three leading edge pieces were designed for each of the suction and pressure surfaces such that film coolant could be injected at three different locations relative to the stagnation point. Figure 24 shows typical cross-sectional views of the leading edge pieces, illustrating the film coolant supply line, the film coolant plenum chamber, the water coolant channels, and the stainless steel inner structure. The leading edge pieces for the pressure surface had film coolant plenum chambers located at 0.0054m (0.214 in), 0.020m (0.783 in)

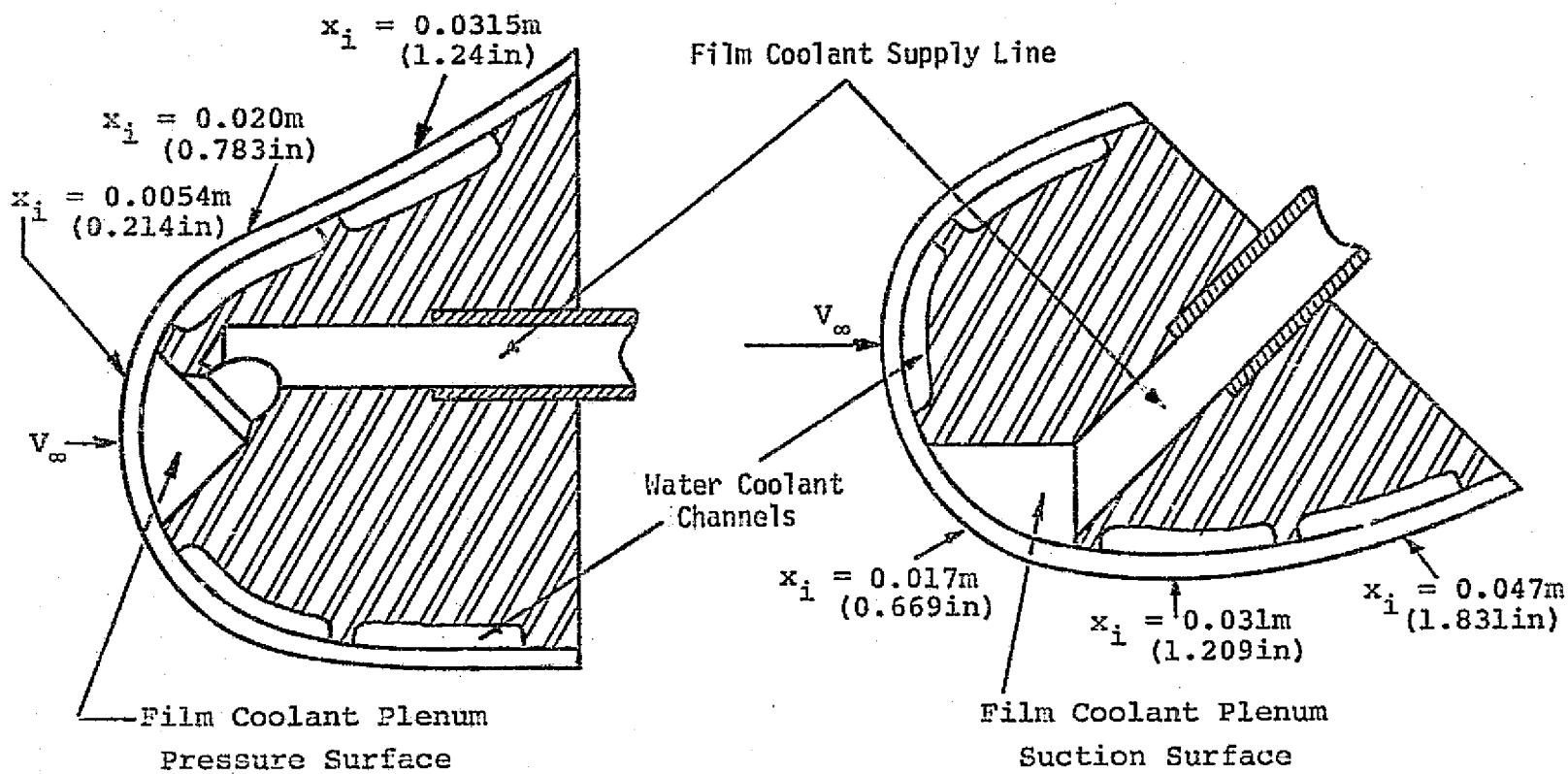

Figure 24. Details of Removable Leading Edge Pieces.

and 0.0315m (1.24 in) from the stagnation point. The configuration for film coolant injection at x_i = 0.0054m is shown in Fig. 24. The leading edge pieces for the suction surface had plenum chambers located at 0.017m (0.669 in), 0.0307m (1.209 in) and 0.047m (1.831 in) from the stagnation point.

IV.1.4. Instrumentation

IV.1.4.1. Mass Flow Measurements

Flowrates for the by-pass air, fuel, and combustion air and the hot gas flowrate through each leg of the vane channel were measured using thin plate orifices constructed to ASME standards. Film coolant flowrates were measured with small diameter venturi meters for low and intermediate coolant flowrates and turbine flowmeters for higher coolant flowrates.

IV.1.4.2. Inlet Flow Conditions

Inlet flow conditions to the vane channel were measured in a single plane perpendicular to the flow 0.0762m (3 in) upstream from the vane leading edges. Vertical and horizontal traverses in that plane were made with wedge-shaped, pitot-static and total temperature probes to map the total pressure, static pressure, and total temperature. The vane test section inlet total pressure (P_{T_∞}) and total temperature (T_{T_∞}) were defined as the mass average of the measured values averaged over the sector of the inlet plane which represented the flow viewed by the central vane test channel. This "averaging sector" extended from $0.3 \leq y/H \leq 0.7$ and $0.2 \leq z/W \leq 0.8$ in the measurement plane upstream from the test vanes (where H is the duct height and W is the spanwidth).

Measurements of the vane channel inlet turbulence intensity were made prior to the initiation of the vane film cooling test program. A hot film probe (Thermo-Systems, Incorporated (TSI) 1220-20) was used to measure inlet turbulence intensity levels, generated by upstream grids, over a range of inlet Reynolds number. Additional details of the measurement inlet flow conditions are presented in Appendix B.

IV.1.4.3. Test Surface Temperature Measurements

Wall temperature measurements were made using small diameter, swedge-type copper constantan thermocouples. The thermocouples were furnace brazed into designated hole locations on the vane test surface and were finished flush to the wall. Exposed-ball or bead-type thermocouples were used to measure coolant temperature in the film coolant plenum chamber. The exposed couples were positioned with the junctions at the center of the plenum chamber. Further details of the wall temperature instrumentation are included in Appendix B.

IV.1.4.4. Test Surface Wall Pressure Measurements

Vane surface static pressure measurements were made with flush mounted copper tubes brazed into the vane suction and pressure surfaces. Ports to monitor film coolant plenum pressure consisted of holes drilled through to the plenum and sealed on the back side with larger diameter stainless steel extension tubing. Details of the static pressure instrumentation are included in Appendix B.

IV.1.4.5. Test Surface Heat Flux Measurements

Direct measurements of the vane surface heat flux were made using miniature, Gardon-type, thin-foil heat flux gages (Model No. 2000, Thermogage, Inc.). The basic operating principle for the thin-foil Gardon transducer is illustrated in Fig. 25. A thin, circular constantan foil is fused to the end of a tubular, copper heat sink, forming a continuous copper-constantan thermocouple junction along the circumference of the foil. On the underside of the foil, a fine copper wire is joined to the center of the foil, forming a second thermocouple junction. Under operating conditions, the incident heat flux travels radially along the foil to the copper heat sink, establishing a parabolic radial temperature profile with a temperature difference from the center to the edge of the foil that is dependent on the magnitude of the incident heat flux (47). Due to the physical property variations of the constantan foil, and the change in the junction emf between the two copper-foil junctions, the differential emf between the two foil junctions becomes linearly dependent upon the magnitude of the incoming heat flux (48).

In order to minimize vane surface irregularities with gage installation and, at the same time, approach point-source measurements, a miniature gage design was chosen with a sensing surface dimension small in comparison to the characteristic dimensions of the vane test surface. Figure 26 is a detailed drawing of a heat flux sensor and the installation technique used in this investigation. The basic sensor was pressed into a 0.0037m (0.145 in) threaded (5-40 UNC) oxygen-free, high-conductivity copper plug. The sensor area itself was 5.08×10^{-4}m (0.02 in) in diameter with a foil 2.54×10^{-5}m (0.001 in) thick. A 5.08×10^{-5}m

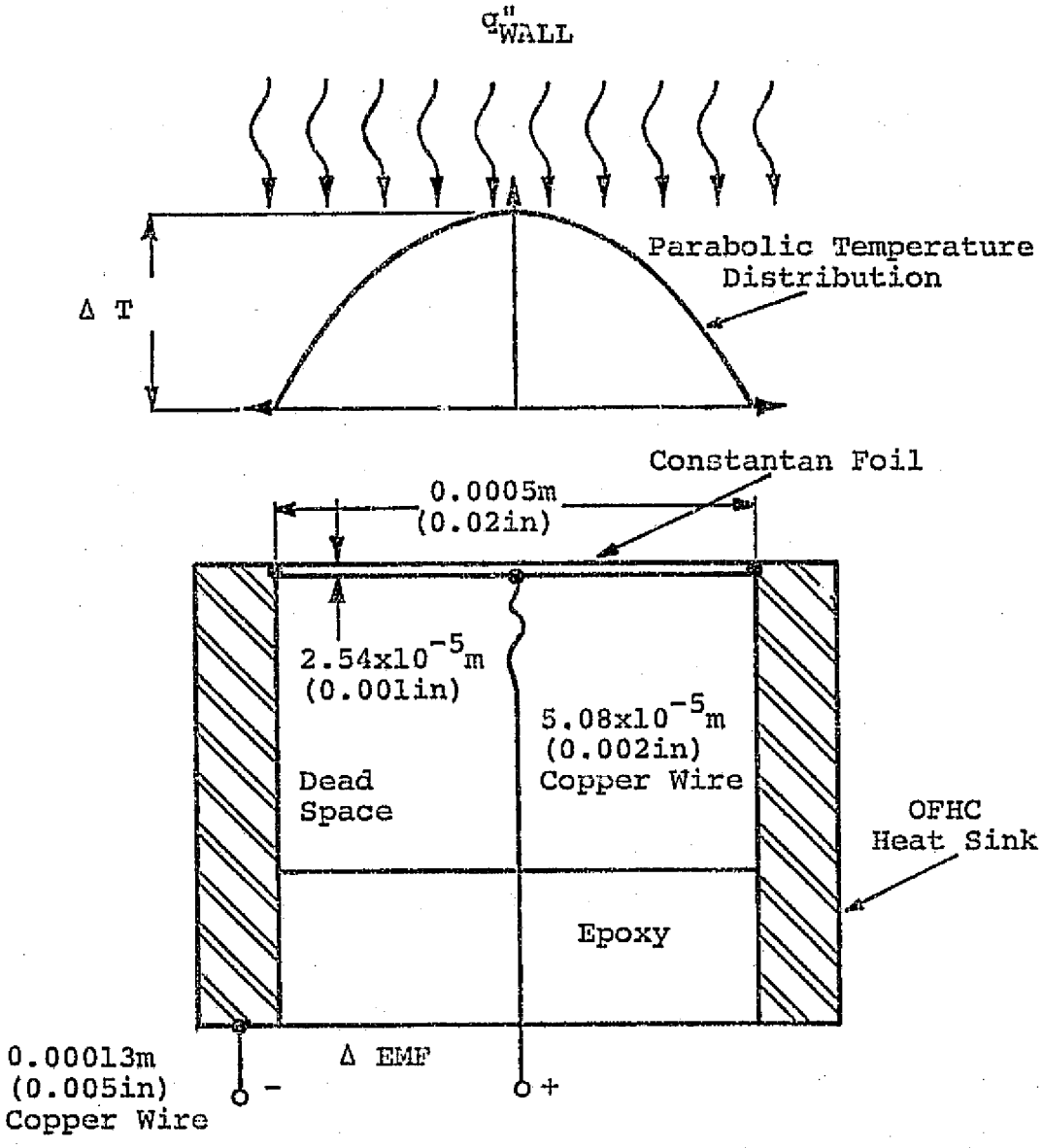

Figure 25. Details of Thin-Foil, Gardon Heat Flux Transducer.

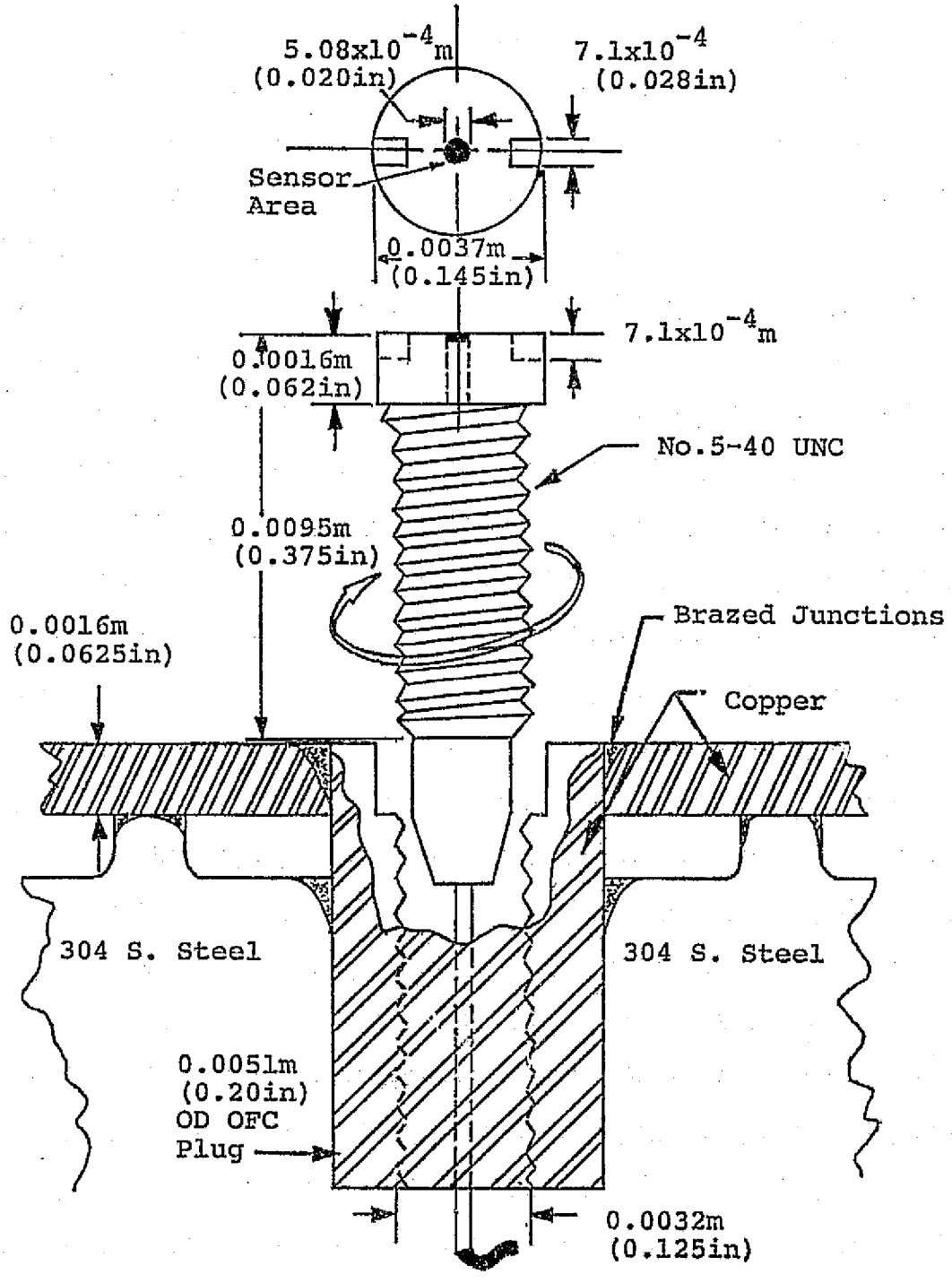

Figure 26. Technique For Installation of Heat Flux Transducers.

(0.002 in) diameter copper wire was laser-welded to the center of the foil from beneath. This wire and a 1.27×10^{-4}m (0.005 in) diameter copper, ground-wire (attached to the heat sink) were both coated with 5.08×10^{-5}m (0.002 in) of teflon, fully shielded, and brought out the bottom of the threaded plug. The heat flux gage was installed into the vane test surface by threading into an oxygen-free, high-conductivity copper plug mounted in the test surface wall. Each mounted gage was located within a water coolant channel, providing the maximum in heat sinking capability. The threaded portion of the gage was long enough to provide 10 to 11 threads of contact with the water-cooled plug.

With the sensor designed for a maximum temperature difference between the center and edge of the sensing foil of only 25°F, the maximum output level of the gage was in the microvolt range. Each gage, therefore, had an individually calibrated operational amplifier with a gain near 1000, to convert the transducer microvolt signal to a more convenient millivolt signal. The gages were calibrated with the amplifiers, and the gain adjusted to obtain a sensitivity of 8.64×10^{-3}mv/joule/sec - m^2 (10 mv/BTU/sec-ft^2).

Due to the extremely low level of the sensor output, caution was exercised in isolating the entire system from such environmental factors as random noise and changes in the ambient temperature. All solder connections were made with low-noise, cadmium-tin solder to eliminate any additional emf sources between the sensors and the amplifiers. The amplifiers have a characteristic drift of 3 millivolts per 10°F change in the ambient temperature (a zero shift and not a calibration change). Therefore, all amplifiers and associated electrical connections

were thermally isolated from ambient conditions using a sealed, styrofoam enclosure.

Calibration of the sensors followed the technique depicted in Fig. 27 and was performed by the sensor manufacturer, Thermogage, Inc. Each sensor was mounted on the center axis at the entrance to one of two, back-to-back (symmetrical) black-body cavities. The black body was a graphite assembly, tapered to achieve a uniform inside wall temperature with resistance heating. The heat flux source-temperature was monitored on the opposite side of the apparatus in a similar black body cavity using an optical pyrometer, with a calibration traced to the National Bureau of Standards. The length-to-diameter ratio of the cavity was large enough, coupled with the high emissivity of the walls, to simulate an emissivity of near unity in the vicinity of the sensor. A view factor between the black body opening and the sensor surface can be easily calculated and, knowing the radiative properties of the previously coated sensor, an accurate calibration was performed (49). Output from a typical calibration test is shown in Fig. 28. The calibration was accurate to within ± 3% of full scale with repeatability within 1/2% and a typical sensor response time of 2.4 milliseconds.

Interpretation of the sensor output requires some qualification. In order for the calibration to be valid, the sensor body temperature must be greater than 283°K (510°R) and less than 506°K (910°R). Outside this range, the change in emf of the thermocouple junctions is not compensated by the physical property changes of the foil to produce the typical linear calibration curve. Secondly, the gages must operate in a field of heat flux uniform over an area that is much greater than the

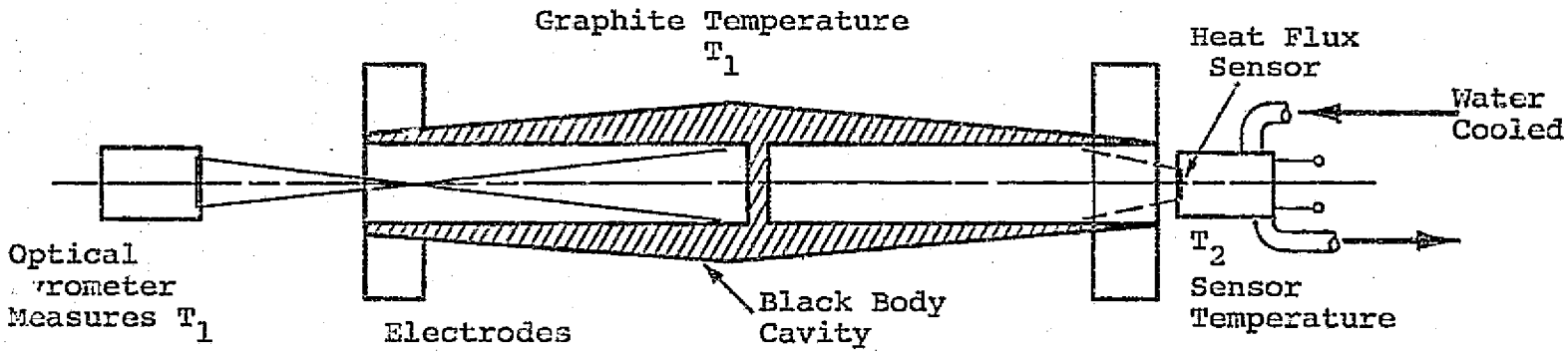

$$q'' = \sigma F_{12} \varepsilon (T_1^4 - T_2^4)$$

Figure 27. Heat Flux Sensor Calibration Technique.

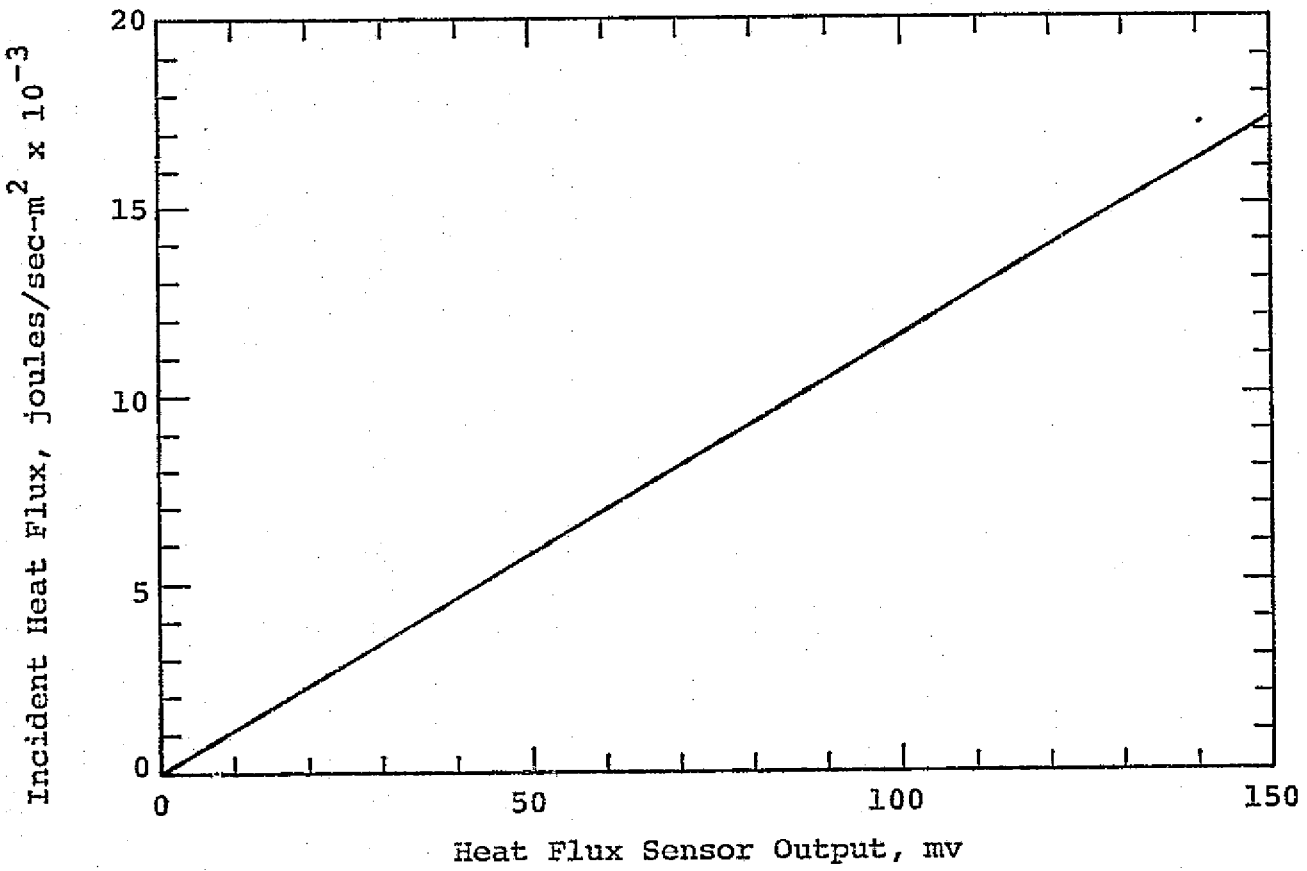

Figure 28. Typical Calibration Curve For a Heat Flux Transducer.

sensor area. These two restrictions posed no difficulty in conducting this investigation.

IV.1.4.6. Instrumentation Locations

Except for the heat flux sensors, all vane surface instrumentation was located at the lands separting the water coolant channels. At various stations along the vane surface contours, pressure taps and thermocouples were installed to determine the two-dimensionality of the flow and the uniformity of the wall temperature boundary condition. The heat flux sensors were positioned between lands at the center of the coolant channels. The requirement of maximum heat sinking for the sensors determined the spacing between gages in the chordwise direction. No more than one gage was installed per coolant channel to minimize pressure loss in the water coolant channel. Sensor mounting plugs were approximately one half the width of the coolant channel. The sensors were staggered with respect to the center span line to minimize the possible disturbance of local heat flux due to the influence of an upstream gage.

Tables 1, 2, and 3 list the locations of all suction and pressure surface instrumentation giving the coordinate x/L_S relative to the stagnation line for the three film coolant plenum configurations employed. Lateral (spanwise) spacing of the pressure taps, thermocouples and heat flux gages, z/L_S, are referenced with respect to the center span line. Film coolant plenum instrumentation is also referenced to the center of the plenum.

SUCTION SURFACE ($x_i/L_S = 0.083$, $L_S = 0.020$m)

	Pressure		Temperature		Heat Flux	
	x/L_S	z/L_S*	x/L_S	z/L_S	x/L_S	z/L_S
1	0.04	0.16	0.04	-0.16	0.14	0.004
2	0.04	-0.06	0.04	0.07	0.21	0.008
3	0.12	0.05	0.12	-0.05	0.32	0.00
4	0.12	-0.02	0.19	-0.04	0.39	0.02
5	0.19	0.15	0.19	-0.09	0.46	-0.02
6	0.19	0.03	0.36	0.13	0.53	0.05
7	0.19	-0.15	0.36	0.00	0.67	-0.05
8	0.28	0.02	0.36	-0.13	0.81	0.00
9	0.43	0.11	0.50	0.00		
10	0.43	0.00	0.64	0.00		
11	0.43	-0.11	0.77	0.00		
12	0.57	0.00	0.91	0.00		
13	0.70	0.00				
14	0.84	0.11				
15	0.84	0.00				
16	0.84	-0.11				

*z is referenced to centerspan

PRESSURE SURFACE ($x_i/L_p = 0.033$, $L_p = 0.016$m)

	Pressure		Temperature		Heat Flux	
	x/L_p	z/L_p	x/L_p	z/L_p	x/L_p	z/L_p
	-0.06	0.20	-0.06	0.09	0.11	0.04
	-0.06	-0.08	-0.06	-0.02	0.19	0.005
	0.06	0.26	0.06	-0.07	0.32	0.00
	0.06	0.06	0.15	-0.05	0.40	0.03
	0.15	0.19	0.15	-0.11	0.48	-0.03
	0.15	-0.04	0.36	0.16	0.57	0.06
	0.15	0.19	0.36	0.00	0.74	-0.06
	0.27	0.02	0.36	-0.16		
	0.44	0.14	0.53	0.00		
	0.44	0.00	0.69	0.00		
	0.44	-0.14	0.87	0.00		
	0.61	0.00				
	0.78	0.14				
	0.78	0.00				
	0.78	-0.14				

PLENUM INSTRUMENTATION

1	0.24	0.26	0.24	0.26
2	-0.01	-0.26	-0.01	-0.26
3	-0.24		-0.24	

Table 1. Pressure, Temperature and Heat Flux Measurement Locations For Suction and Pressure Surfaces For Configurations of $x_i/L_S = 0.083$ and $x_i/L_p = 0.033$.

SUCTION SURFACE ($x_i/L_S = 0.150$, $L_S = 0.020$m)

	Pressure		Temperature		Heat Flux	
	x/L_S	z/L_S*	x/L_S	z/L_S	x/L_S	z/L_S
1	0.04	0.16	0.04	-0.16	0.22	0.004
2	0.04	-0.06	0.04	-0.07	0.32	0.00
3	0.12	0.05	0.12	-0.05	0.39	0.02
4	0.12	-0.02	0.18	-0.04	0.46	-0.02
5	0.18	0.15	0.18	-0.09	0.53	0.05
6	0.18	0.03	0.36	0.13	0.67	-0.05
7	0.18	-0.15	0.36	0.00	0.81	0.00
8	0.28	0.02	0.36	-0.13		
9	0.43	0.11	0.50	0.00		
10	0.43	0.00	0.64	0.00		
11	0.43	-0.11	0.77	0.00		
12	0.57	0.00	0.91	0.00		
13	0.70	0.00				
14	0.84	0.11				
15	0.84	0.00				

*z is referenced to centerspan

PRESSURE SURFACE ($x_i/L_p = 0.121$, $L_p = 0.016$m)

	Pressure		Temperature		Heat Flux	
	x/L_p	z/L_p	x/L_p	z/L_p	x/L_p	z/L_p
1	-0.05	0.20	-0.05	0.09	0.20	0.005
2	-0.05	-0.08	-0.05	-0.21	0.32	0.00
3	0.07	0.26	0.07	-0.07	0.40	0.03
4	0.07	0.16	-0.05	-0.05	0.48	-0.03
5	0.16	0.19	0.16	-0.11	0.57	0.06
6	0.16	-0.04	0.36	0.16	0.74	-0.06
7	0.16	0.19	0.36	0.00		
8	0.27	0.02	0.36	-0.16		
9	0.44	0.14	0.53	0.00		
10	0.44	0.00	0.69	0.00		
11	0.44	-0.14	0.87	0.00		
12	0.61	0.00				
13	0.78	0.14				
14	0.78	0.00				
15	0.78	-0.14				

PLENUM INSTRUMENTATION

1	0.24	0.26	0.24	0.26
2	-0.03	0.05	-0.03	0.05
3	-0.24	-0.26	-0.24	-0.26

Table 2. Pressure, Temperature and Heat Flux Measurement Locations For Suction and Pressure Surfaces For Configurations of $x_i/L_S = 0.150$ and $x_i/L_p = 0.121$.

SUCTION SURFACE ($x_i/L_S = 0.228$, $L_S = 0.020$m)

	Pressure		Temperature		Heat Flux	
	x/L_S	z/L_S*	x/L_S	z/L_S	x/L_S	z/L_S
1	0.03	0.16	0.03	-0.16	0.32	0.00
2	0.03	-0.06	0.03	0.07	0.39	0.02
3	0.11	0.05	0.11	-0.05	0.46	-0.02
4	0.11	-0.02	0.18	-0.04	0.53	0.05
5	0.18	0.15	0.18	0.09	0.67	-0.05
6	0.18	0.03	0.36	0.13	0.81	0.00
7	0.18	-0.15	0.36	0.00		
8	0.28	0.02	0.36	-0.13		
9	0.43	0.11	0.50	0.00		
10	0.43	0.00	0.64	0.00		
11	0.43	-0.11	0.77	0.00		
12	0.57	0.00	0.91	0.00		
13	0.72	0.00				
14	0.84	0.11				
15	0.84	0.00				
16	0.84	-0.11				
17	-0.03	0.0				

*z is referenced to centerspan

PRESSURE SURFACE ($x_i/L_P = 0.193$, $L_P = 0.016$m)

	Pressure		Temperature		Heat Flux	
	x/L_P	z/L_P	x/L_P	z/L_P	x/L_P	z/L_P
	-0.05	0.20	-0.05	0.09	0.32	0.00
	-0.05	-0.08	-0.05	-0.21	0.40	0.03
	0.04	0.26	0.04	-0.07	0.48	-0.03
	0.04	0.06	0.14	-0.05	0.57	0.06
	0.14	0.19	0.14	-0.11	0.74	-0.06
	0.14	-0.04	0.36	0.16		
	0.14	-0.19	0.36	0.00		
	0.27	0.02	0.36	-0.16		
	0.44	0.14	0.53	0.00		
	0.44	0.00	0.69	0.00		
	0.44	-0.14	0.87	0.00		
	0.61	0.00				
	0.78	0.14				
	0.78	0.00				
	0.78	-0.14				

PLENUM INSTRUMENTATION

1	0.24	0.26
2	-0.03	0.05
3	-0.24	-0.26

Table 3. Pressure, Temperature and Heat Flux Measurement Locations For Suction and Pressure Surfaces For Configurations of $x_i/L_S = 0.228$ and $x_i/L_P = 0.193$.

IV.1.5. Measurement Systems

All pressure measurements were made using two methods: strain-gage type transducers or a digital automatic multiple pressure recording system. Each thermocouple was referenced to a 338°K (610°R) oven. The output from each heat flux sensor was amplified using operational amplifiers with a gain near 1000.

All data was digitally sampled and linked to an on-line computer as well as a central IBM 360 processing center. The on-line computer provided continuous information to a visual display unit for purposes of monitoring current flow conditions.

A detailed description of the measurement system including raw data conversion techniques, data monitoring, acquisition, storage and processing is presented in Appendix B.

IV.2. Description of Experiment

The reduction in the local heat flux due to film cooling from a single row of laterally angled holes in the leading edge region of the model turbine vane was measured under reduced flow conditions simulating a high temperature, high pressure turbine environment. The test surface was a 3X scale model of a prototype turbine inlet vane designed for operation at 1922°K (3000°F) inlet total temperature and $3.04 \times 10^6 N/m^2$ (441 psia) inlet total pressure. Simulation of these high temperature and pressure conditions was achieved in the subject investigation at a model inlet total pressure and total temperature of $3.1 \times 10^5 N/m^2$ (44.67 psia) and 698°K (1240°R), respectively, with a vane surface Mach number distribution that closely duplicated the prototype design. An

inlet Mach number of 0.22 and Reynolds number of 8×10^4 (based on the vane leading edge radius (0.0152m (0.6 in)) were employed throughout the film cooling experiments. The model inlet turbulence intensity (Tu_∞) was held constant at 6.6% by placement of a fine mesh screen ($M_S/d_W = 5.0$) at a location 0.533m (21 in) upstream from the model vane leading edge. The vane wall temperature was maintained at approximately isothermal conditions with $T_{T_\infty}/T_W = 2.15$, thus approximating a boundary layer with large density variations. Using ambient cooling air the dimensionless coolant temperature, θ_C', was near 1.03. With T_C at ambient conditions (294°K or 530°R), the inlet temperature (T_{T_∞}) of 698°K (1240°R) resulting from Eq. (58) satisfies the modeling requirement that M and I be maintained equivalent between the model and the prototype vane.

The film coolant injection geometry was chosen for possible application to future turbine designs. Coolant hole diameters were specified at 1.17×10^{-3}m (0.046 in) in an attempt to keep the local momentum boundary layer thickness-to-hole diameter ratio (θ_i/d_0) similar to expected engine conditions. Typically, at high temperatures and pressures, θ_i may vary from 5×10^{-6}m (1.97×10^{-4} in) near $x/L_S = 0$ (stagnation) to 2×10^{-5}m (7.87×10^{-4} in) at $x/L_S = 0.20$ (50). For a typical coolant hole diameter of 3.8×10^{-4} m (0.015 in), θ_i/d_0 may range from 0.013 to 0.0525 in the leading edge region. Length-to-diameter ratios (L'/d_0) of the coolant hole passages were specified at 3.0 for $\beta = 35°$ and 4.4 for $\beta = 18°$. A surface spacing-to-hole diameter ratio S_1/d_0 of 4.0 was selected to avoid highly non-uniform, spanwise film coverage.

The film cooling effectiveness of the subject cooling configuration was determined by comparing the measured heat flux with film cooling,

q''_{FC}, to that without cooling, q''_0, at dimensionless distances from injection, $(x-x_i)/d_0$, ranging from 10.45 to 126.11. The heat flux reduction was determined as a function of the blowing ratio, M, ranging from M = 0.1 to M = 2.2. To determine M ($M = \rho_C V_C/\rho_\infty V_\infty$) the coolant mass flux was assumed uniform across the span of the holes and equal to the total coolant mass flow divided by the total area of the coolant holes (19 coolant holes across a span of 0.114m (4.5 in)). The hot gas mass flux was determined from density and velocity values at injection, calculated from total gas temperature, total pressure and wall static pressure measurements.

Two injection angles were investigated: $\beta = 18°$ and $\beta = 35°$. Injection was from a single row of holes on both the suction and pressure surfaces with three different locations for the holes being investigated. On the suction surface, injection occurred at x/L_S values of 0.0833, 0.150 and 0.228 corresponding to θ_i/d_0 values of 0.013, 0.036 and 0.0514 with acceleration parameter, K_i, values of 7.9×10^{-6}, 0.723×10^{-6} and 0.656×10^{-6}, respectively. On the pressure surface, injection occurred at x/L_p values of 0.0333, 0.122 and 0.199 corresponding to θ_i/d_0 values of 0.0111, 0.0514 and 0.0827, and K_i values of 6.6×10^{-5}, -6.0×10^{-5} and 4.267×10^{-6}, respectively. These coolant hole locations were selected to represent possible regions of considerable curvature in which streamwise injection schemes may prove difficult.

Table 4 lists in detail a direct comparison between the freestream flow and film coolant parameters for a high temperature, high pressure engine environment and those conditions maintained in the subject model study.

PARAMETER	ENGINE	MODEL
T_{T_∞}, °K	1922	698
P_{T_∞}, N/m^2	3.04×10^6	3.1×10^5
T_C, °K	800	294
Ma_X	Design	Design
T_{T_∞}/T_W	2.0	2.15
Tu_∞, %	10-20%	6.6%
Ma_{INLET}	0.22	0.22-0.23
L.E. Radius, m	0.0051	0.0152
$Re_{LER,INLET}$	8×10^4	8×10^4

INJECTION PARAMETERS

$(\rho V)_C/(\rho V)$	0 → 2.5	0 → 2.5
Injection Angle	15° → 90° (α or β)	18°, 35° (β)
S_1/d_0	3.0 → 8.0	4.0
d_0, m	$2 \rightarrow 3.8 \times 10^{-4}$	1.17×10^{-3}
L'/d_0	3.0 → 5.0	3.0, 4.4
θ_i/d_0	0.013 → 0.0525	0.011 → 0.0827
$x_i/L_{S,P}$	0 → 0.25	0.083 → 0.228

Table 4. Comparison of Main Flow and Film Cooling Parameters For a Gas Turbine Engine With Those of the Subject Investigation.

The actual mechanics of recording the film cooling data are discussed in Appendix B.4. The essential features of the procedure include: (1) a horizontal and vertical traverse of the inlet plane to define the freestream total and static pressures and total temperature for each heat flux survey, and (2) a survey of the measured wall heat flux with the probes retracted to eliminate the effects of the probe wakes.

IV.3. Data Analysis

Heat flux measurements were made downstream of injection at locations ranging from $(x-x_i)/d_0$ of 10.45 to 126.11 for the suction surface and $(x-x_i)/d_0$ of 10.35 to 98.06 for the pressure surface. Heat flux levels with film cooling at these locations were compared to measurements at the same locations with no coolant flow. From this comparison a fractional reduction in the heat flux due to coolant flow was calculated and presented as a measure of the cooling effectiveness.

Under normal boundary layer conditions, the local heat flux to a surface can be written

$$q_0'' = h_0 \, (T_{T_\infty} - T_W) \tag{65}$$

where q_0'' = local heat flux without film cooling

h_0 = local convective heat transfer coefficient

T_{T_∞} = total gas temperature

T_W = local wall temperature

With the addition of film cooling, the local heat flux can be expressed in a similar manner.

$$q''_{FC} = h_{FC} (T_{T_\infty} - T_{W,FC}) \tag{66}$$

where

q''_{FC} = heat flux with film cooling

h_{FC} = local heat transfer coefficient with film cooling

$T_{W,FC}$ = local wall temperature with film cooling

Equation (66) combines all effects of the film injection phenomena into the single parameter, h_{FC}, which can be expected to depend on the following variables

$$h_{FC} = h_{FC}(M, V_C/V_\infty, \beta, \theta'_C, Tu_\infty, K_i, \text{etc.}) \tag{67}$$

This is in contrast to the use of an adiabatic wall temperature to characterize film cooling (5,44) in which the local film temperature is presented in terms of an adiabatic film cooling effectiveness while the heat transfer coefficient reflects only the hydrodynamic effects of coolant injection.

The film cooling results are presented as a fractional reduction in the local Stanton number where the local Stanton number is defined as

$$ST = \frac{q''}{(T_{T_\infty} - T_W)\rho_\infty V_\infty C_{p_\infty}} \tag{68}$$

Since the freestream parameters do not change with film cooling (i.e. ρ_∞, V_∞, C_{p_∞} remain constant with or without coolant injection), Eq. (68) can be used to express the local Stanton number reduction due to film cooling in the following manner

$$\frac{ST_{FC}}{ST_0} = \frac{q''_{FC}}{q''_0} \frac{(T_{T_\infty} - T_{W,0})}{(T_{T_\infty} - T_{W,FC})} \tag{69}$$

Under isothermal conditions, $T_{W,0} \approx T_{W,FC}$ (which holds for the highly cooled walls in this investigation), the heat flux data give the Stanton number ratio directly. Thus,

$$\frac{ST_{FC}}{ST_0} = \frac{q''_{FC}}{q''_0} \tag{70}$$

The isothermal film cooling effectiveness, η_{ISO}, is defined as

$$\eta_{ISO} = \frac{q''_0 - q''_{FC}}{q''_0} \tag{71}$$

which gives the Stanton number reduction as

$$\frac{ST_{FC}}{ST_0} = 1 - \eta_{ISO} \tag{72}$$

Having described the objectives, methodology and details of the subject investigation, Chapter V. will now present a summary of the experimental results. These results are divided into three categories: (1) documentation of the turbine environment, (2) non-film cooled (dry-wall) vane heat transfer, and (3) actual film cooling heat flux reductions. A detailed discussion is also included for each of the above items.

V. RESULTS AND DISCUSSION

V.1. Documentation of Modeling of Turbine Environment

The experimental model was employed to simulate both the inlet freestream conditions and the local vane surface conditions representative of a high temperature, high pressure gas turbine environment. At the inlet to the model vane channel the following conditions were maintained: (a) freestream Reynolds number (based on vane leading edge radius) of approximately 8×10^4, (b) freestream Mach number of 0.22, and (c) an inlet freestream turbulence intensity of 6.6%. Along the vane contour, the vane local conditions were as follows: (a) Mach number distribution approximating the prototype vane design calculations, (b) nearly uniform wall temperature with T_{T_∞}/T_W near 2.15 (representative of density variations through the boundary layer for a gas turbine vane), and (c) approximately constant dimensionless coolant temperature, θ'_C, of 1.03 (representative of coolant-to-gas density ratio typical of high temperature turbine operation).

Simulation of the inlet conditions for the vane prototype was achieved at a reduced inlet total pressure and total temperature of 3.1×10^5 N/m^2 (44.67 psia) and 689°K (1240°R), respectively. Under these conditions the following inlet velocity and temperature profiles were measured.

Figure 29 shows the nondimensional inlet velocity profile in the vertical direction. The inlet velocity, as compared to the sector-average velocity, is shown as a function of the duct height. The sector average velocity, representative of the flow through the vane channel, was defined

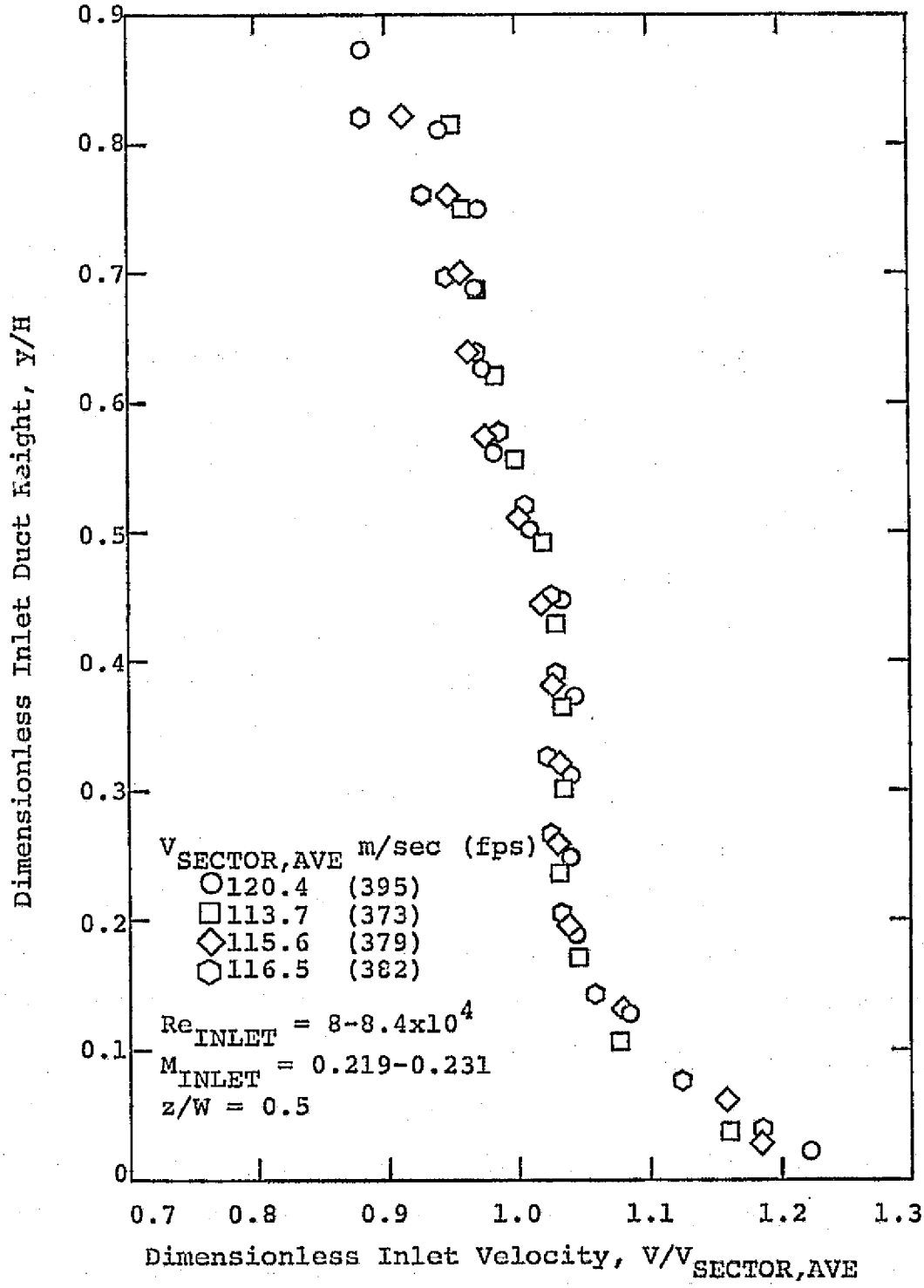

Figure 29. Variation of Inlet Velocity (Vertical Traverse).

as the mass average velocity for the sector, $0.3 \leq y/H \leq 0.7$ and $0.2 \leq z/W \leq 0.8$. Within the sector limits, the velocity did not vary more than 5% from the average. All vertical traverses were made at a fixed position spanwise in the channel at $z/W = 0.5$.

Figure 30 shows the variation of the nondimensional inlet velocity in the horizontal direction across the span of the duct. The profile is less flat in the spanwise direction than shown in Fig. 29 possibly due to a contraction in the lateral direction (2.22:1 area ratio) as the flow transitioned from a 0.254m (10 in) OD circular pipe to the 0.244m 0.114m (9.6 in × 4.5 in) test channel. Within the "sector-average" limits defined above, the velocity is shown to vary by as much as 10% from the sector average. This variation did not have a significant effect on the local vane surface measurements such as wall heat flux or calculated local velocity. The total and static pressure at the inlet plane was uniform within 1/2% of the calculated mean values.

Figure 31 presents the variation of the measured inlet total temperature, nondimensionalized with respect to the sector mass average total temperature, as a function of the inlet duct height. For the data shown, the inlet total temperature was uniform to within 1/2% of the sector average. Figure 32, presents similar data for the horizontal temperature variation, which shows some nonuniformity due to the lateral contraction from the initial circular duct. However, the deviation of the temperature in the spanwise direction (for the sector limits defined above) was never more than 1/2% of the sector average.

Based on the sector average values of the inlet velocity and total temperature shown previously, the experimental values of the inlet

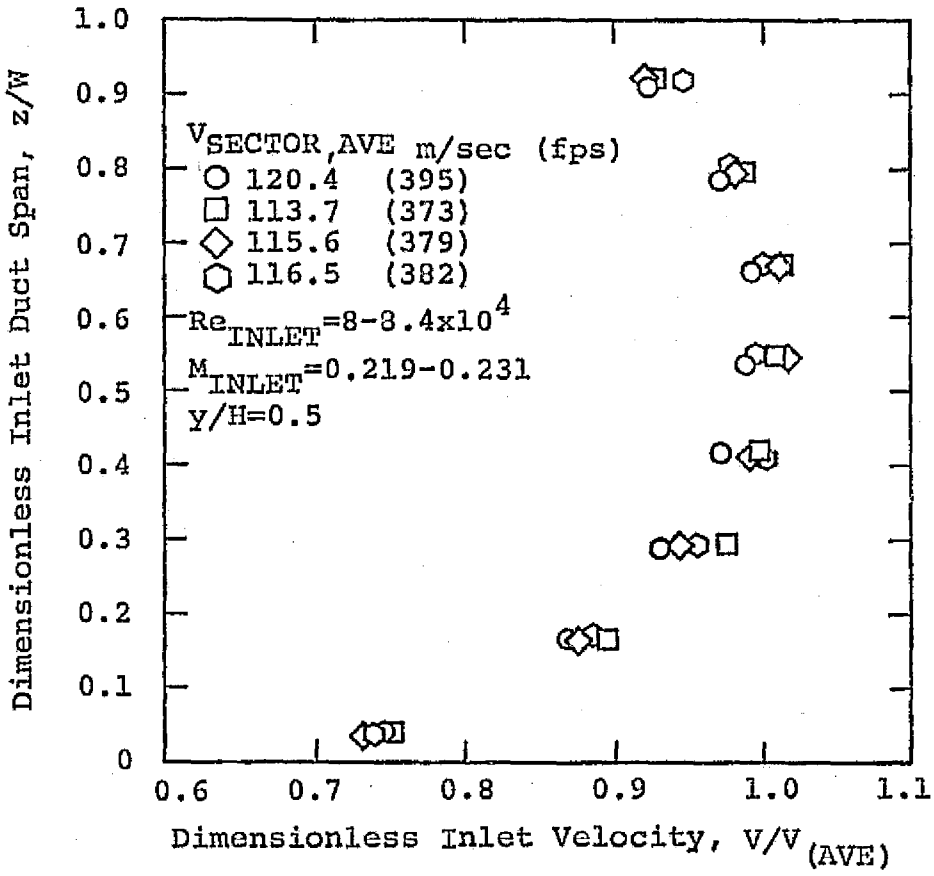

Figure 30. Variation of Inlet Velocity (Horizontal Traverse).

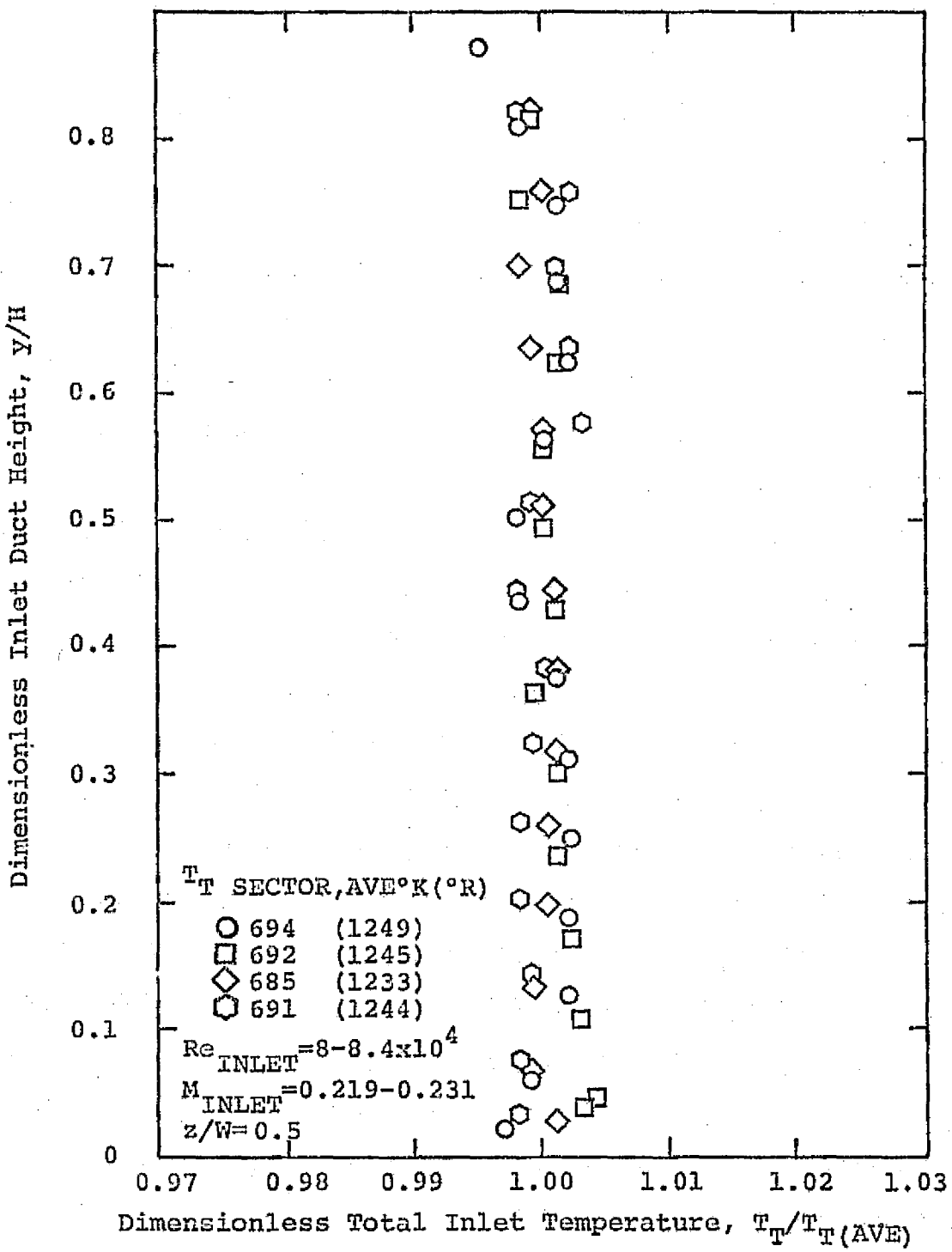

Figure 31. Variation of Inlet Total Temperature (Vertical Traverse).

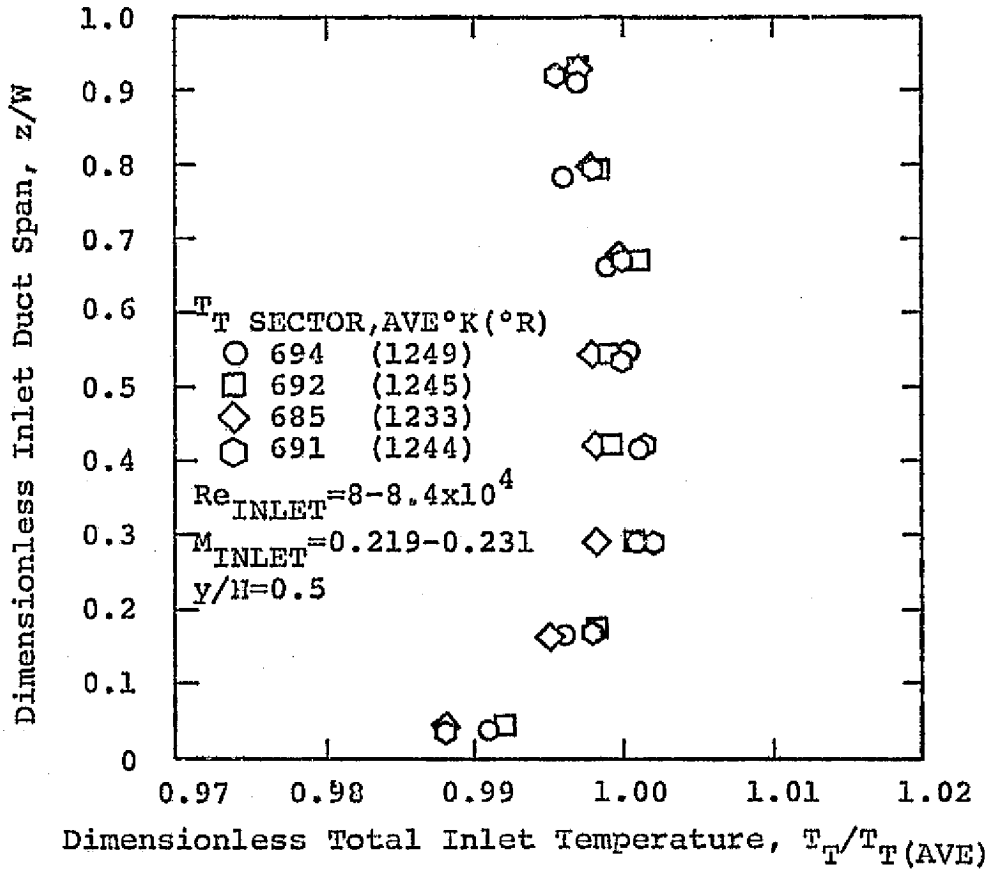

Figure 32. Variation of Inlet Total Temperature (Horizontal Traverse).

Reynolds number and the inlet Mach number ranged from 8.0 to 8.4 × 10^4, and 0.22 to 0.23, respectively. The prototype vane row is designed to operate at an inlet Mach number of 0.22 and an inlet Reynolds number of 8 × 10^4 (based on leading edge radius) with an inlet total temperature of 1922°K (3460°R), inlet total pressure of 3.06 × 10^6 N/m^2 (441 psia), and 55.67 kg/sec (122.5 lbm/sec) total air flow through the 36 vane ring.

To complete the documentation of the vane channel inlet conditions, the inlet turbulence intensity, Tu_∞, was measured 0.076m (3 inches) upstream of the vanes as a function of various screen types and positions. A hot film probe was oriented perpendicular to the flow at the midspan of the channel and a vertical traverse of the inlet turbulence intensity was made. A sector average intensity was calculated from those measurements for the sector between $0.3 \leq y/H \leq 0.7$.

The sector average turbulence intensity at the vane channel inlet are presented in Fig. 33 as a function of distance from the upstream screen. Intensity values of 6.6% to 10.5% were measured at inlet Reynolds numbers of 4.34, 6.51, 9.98, 11.29 × 10^4 (corresponding to inlet velocities of 30.5, 45.7, 70.1 and 79.2 m/sec). As suggested by Von Karman (51), the intensity data was found to correlate with the nondimensional distance from the grid based on the grid wire diameter rather than the grid mesh length. Three significant conclusions were drawn from the turbulence study: (1) the absolute level of the measured intensity is higher than values reported by Baines and Peterson (52) and Eckert, Sparrow and Newman (53) for turbulence decay downstream of a grid as shown in Fig. 33, (2) the variation of the gradient of the one-dimensional turbulent kinetic energy is representative of typical decay downstream

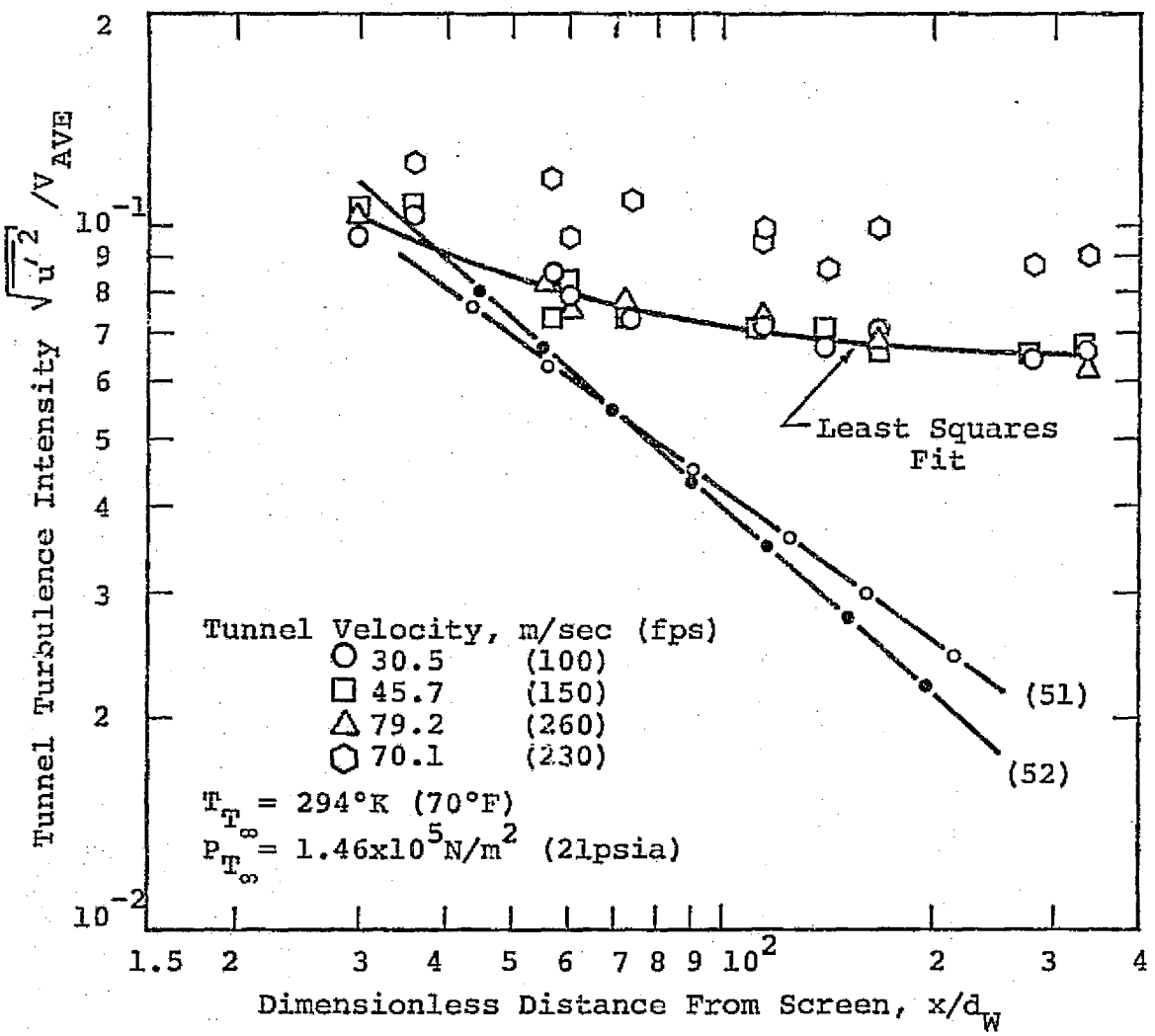

Figure 33. Grid-generated Inlet Turbulence Intensities.

from generating screens, and (3) the turbulence level is independent of the inlet Reynolds number over the range investigated.

A least-squares curve fit of the data (excluding the 70.1 m/sec results) in Fig. 33 is represented by the solid curve. The agreement with correlations reported for similar investigations (52,53) is poor, especially in the far downstream regions from the generating grid.

The only significant difference between the present data and the cited references is the character of the turbulent field prior to interaction with the generating grid. Clear tunnel intensities (no grid present) were generally reported from 1/2% to 1% (52,53). In the present study, clear tunnel intensities near 7% were measured. Since no provisions were made in this test facility to minimize clear tunnel conditions, it is reasonable to expect high overall values of turbulence. The close relationship between initial conditions and decay downstream from a grid was clearly demonstrated by Tsuji (54). Turbulence produced by a grid was shown to be superimposed on the high wave number range of that turbulence incident upon the grid. The decay of the spectral components after the initial stages most nearly resembles that of the initial intensity conditions. Such a progression of events seems to be substantiated in Fig. 33 as the intensity level for $x/d_w > 100$ appears to have approached that of the clear tunnel.

The abnormally high values of Tu at an inlet velocity of 70.1 m/sec (230 fps) were explained by a hot film probe resonance due to a vortex shedding phenomenon. At 70.1 m/sec, the Reynolds number based on the hot film probe wire diameter is 225 (a region in which vortex shedding is significant). At this Reynolds number, the Strouhal number

(Str = $\omega' d/V_\infty$, where ω' is frequency) is near 0.19, yielding a shedding frequency of about 40,000 Hz. During these measurements the turbulent signal was monitored with an oscilloscope. At 70.1 m/sec, the signal developed a large scale periodic pattern with a frequency of 20K Hz. At 79.2 m/sec, a similar regular signal appeared at 25K Hz, but of a much smaller amplitude.

The cantilevered probe in an oscillatory flow constitutes a non-linear vibratory system in which harmonics will naturally exist. The phenomenon of subharmonic response shows that the system may oscillate with a frequency of 1/2, 1/3, ..., 1/N of the applied forcing frequency. It appears that the forcing frequency due to vortex shedding at 40,000 Hz was able to induce and sustain subharmonic resonance of the probe at 1/2 of its forcing frequency. At vortex shedding frequencies greater than approximately 50K Hz, the forcing function is unable to sustain any induced vibration of significant amplitude that may affect the RMS signal. It was concluded that the data shown for a velocity of 70.1 m/sec is not representative of the grid generated turbulence.

Although the turbulence intensity levels are significantly higher than measured in other investigations, the gradient of the one-dimensional turbulent kinetic energy with respect to distance from the grid in the initial decay regime (just downstream of the grid) is well within the range of published values. Figure 34 shows the gradient of the turbulent kinetic energy in the main flow direction as a function of the dimensionless distance from the screen. The present data is represented by the solid line, as calculated from the least squares relation shown in Fig. 33. In addition to the data from references cited in Fig. 33, the data for

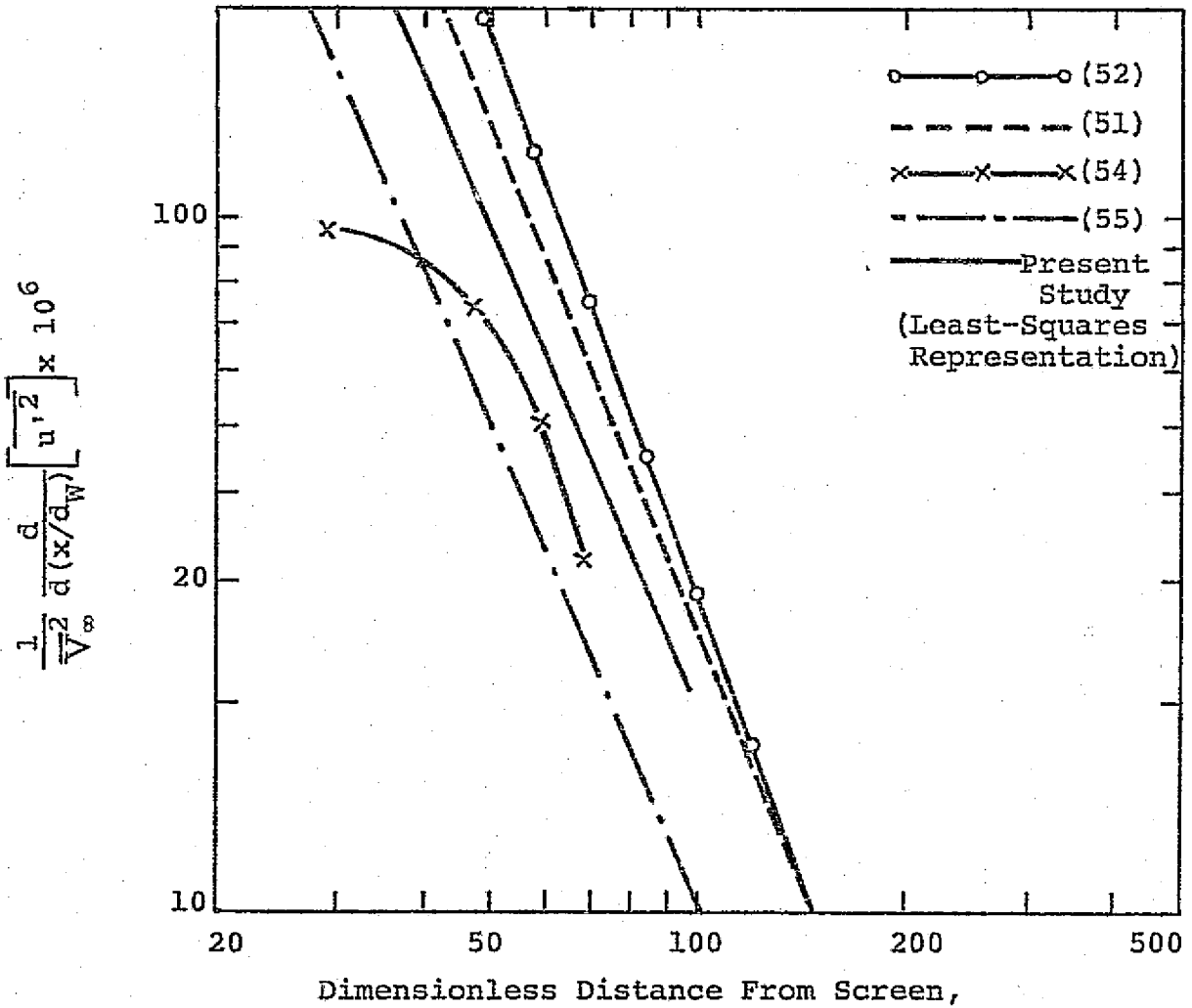

Figure 34. Gradient of One-Dimensional Turbulent Kinetic Energy With Distance From Screen (Comparison to Published Results).

Kestin and Wood (55) and Van Der Hegge Zijnen (56) are presented for comparison. Figure 34 shows that all the cited references, including the present investigation, report a change in the turbulent kinetic energy gradient that is related to approximately the negative third power of the dimensionless distance from the grid. The solid line for the subject investigation, was determined from the least squares quadratic representation of the data in Fig. 33. The minus three power is not representative of isotropic decay in the final period, but may describe the influence of any grid initial conditions.

All turbulence data were obtained at a total pressure of 1.46×10^5 N/m^2 (21 psia) and a total temperature of 294°K (70°F). Figure 33 represents data at these conditions for velocities of 30.5, 45.7, 79.2, and 70.1 m/sec. Within ± 10% of the least squares curve, there is no significant influence of the inlet Reynolds number on the magnitude of the generated turbulence intensity.

With the inlet total pressure and total temperature prescribed to properly model the engine conditions, similarity in the vane heat transfer, through matching of the local Reynolds number along the vane contour, can be achieved by reproducing the expected prototype Mach number distribution over the vane. Figure 35 presents the local Mach number variation with distance from the stagnation point for both the pressure and suction surfaces of the test vane. Data from a typical test point show that the scale model Mach number variation through the test channel matched the prototype design values reasonably well with a maximum deviation of 12% for the suction surface and 20% for the pressure surface. The large variation from design (20%) for the pressure surface occurred at

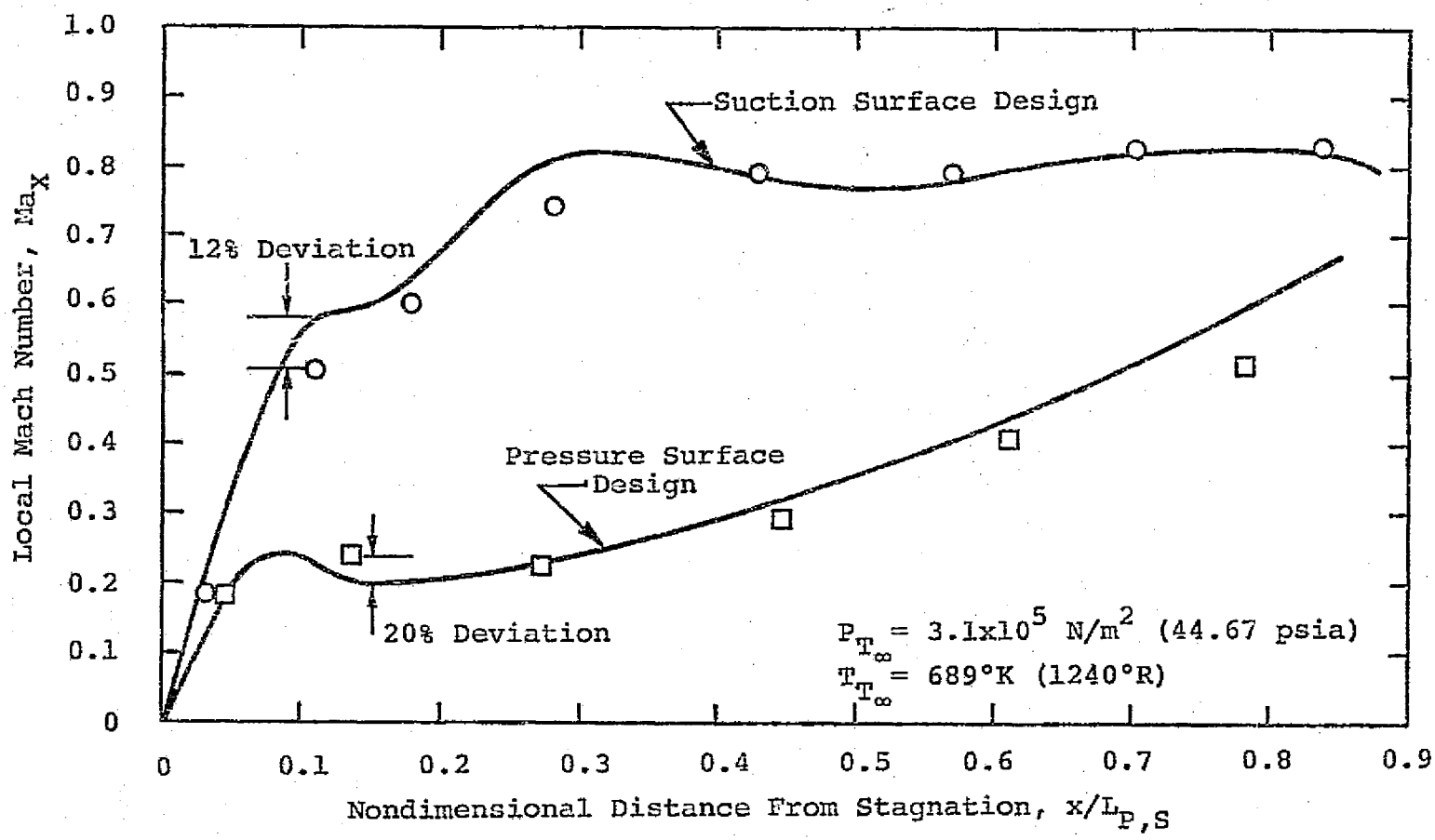

Figure 35. Local Mach Number Distribution Along Vane Contour.

x/L_p = 0.15, just downstream from an adverse pressure gradient region. In the discussion on dry wall (non-film cooled) heat transfer results, to be presented in a later section, evidence points toward possible flow separation in this adverse pressure gradient region.

The uniformity in the wall temperature boundary condition is shown in Fig. 36. The gas-to-wall temperature ratio is shown as a function of the nondimensional distance from stagnation for both the suction and pressure surfaces. The suction surface wall temperature varied no more than 5% from its mean value. The pressure surface wall temperature varied, at most 10% from its mean value. This 10% deviation occurred at the pressure surface trailing edge. At this location, the wall thermocouple was actually imbedded in the vane, stainless steel inner structure and indicated a higher temperature than those thermocouples within the water cooled copper skin.

Figure 37 illustrates the variation in the film coolant temperature both during a given test run (Run Number) and over a range of measurement periods. The coolant temperature measured in the film coolant plenum was corrected for heat pick-up through the vane wall. (See Appendix D for a discussion of the coolant plenum temperature calibration.) The variation in the dimensionless coolant temperature, θ'_C, for a particular day is shown as the solid vertical bands. The band length varies from day to day (Run Number to Run Number) due to the range of coolant flows investigated. For a wide range of M, the coolant temperature shows the greatest variation due to heat pick-up through the vane wall. During the entire film cooling study, the dimensionless coolant temperature did not deviate more than 7% from a mean value of 1.03.

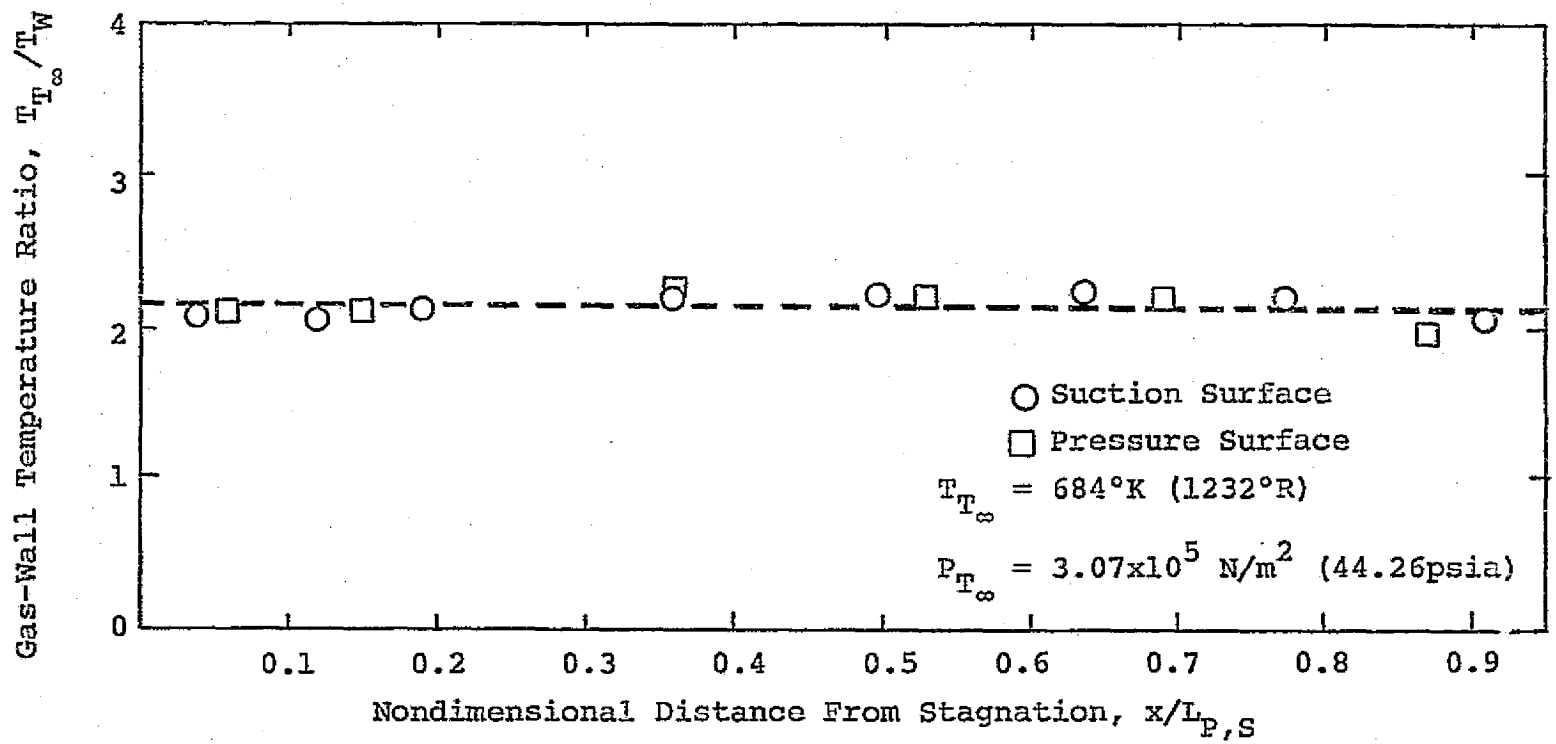

Figure 36. Typical Variation of Vane Gas-Wall Temperature Ratio.

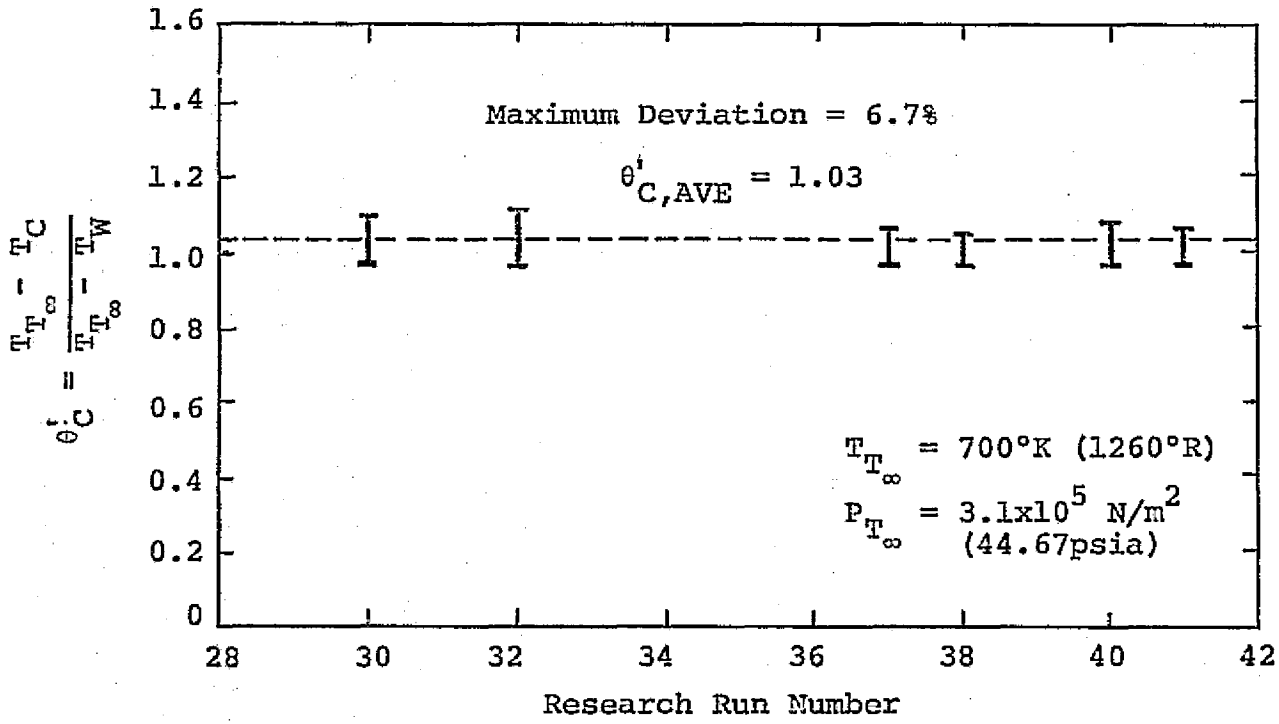

Figure 37. Variation in Dimensionless Coolant Temperature With Run Number.

For a mean gas-to-wall temperature ratio (T_{T_∞}/T_W) of 2.15, this corresponds to an average coolant-to-gas density ratio (ρ_C/ρ_∞) of approximately 2.18 characteristic of the film cooling experiments reported herein.

V.2. Non-Film Cooled (Dry-Wall) Vane Heat Transfer

Having matched the appropriate modeling parameters for both the vane channel inlet and vane local conditions, heat transfer data without film cooling were taken on both the suction and pressure surfaces of the vane to:

(1) compare the measured dimensionless dry-wall heat transfer Stanton number with the results from an existing analytical boundary layer prediction method,

(2) investigate the effect of the freestream turbulence intensity (Tu_∞) on the vane dry-wall heat transfer, and

(3) demonstrate that the heat flux measurement technique was reliable and durable under severe operating conditions.

V.2.1. Analytical Prediction Method

The boundary layer prediction method used for comparison with the subject experimental data was developed by W. M. Kays, et al., of Stanford University (57). A finite-difference technique is used to solve the conservation equations, including the turbulent kinetic energy equation (TKE). The basic numerical scheme in the solution of the conservation equations follows the Spalding and Patankar method (58). The prediction technique allows for the insertion of a variety of models for transport processes (with the freedom to modify these models using

empirical correlations) or to obtain results directly from the simultaneous solution of the turbulent kinetic energy equation and the other conservation equations.

The present version of the boundary layer program makes use of the concept of an eddy viscosity and thermal conductivity, which is helpful computationally. A mixing length hypothesis is used for the boundary layer turbulent transport in which the length scale varies linearly outside the viscous sublayer. Within the viscous region, the linear relation is modified using the Van Driest damping function with appropriately chosen empirical constants reflecting experimentally substantiated effects on the sublayer due to external effects such as acceleration, blowing, and suction.

Typical program inputs that are required include initial profiles for the velocity, enthalpy and turbulent kinetic energy. Appropriate wall boundary conditions are specified on mass addition and enthalpy. The mass addition capability can appropriately handle transpiration cooling; however, discrete film cooling (through holes) has not been modeled. An external pressure gradient can be specified by inputing an arbitrary velocity distribution external to the boundary layer. Laminar flow can be forced to transition to turbulent conditions by specifying a transition momentum-thickness Reynolds number, $Re_{\theta,TR}$. Finally, values of the freestream stagnation enthalpy, stagnation pressure and specific heat must also be supplied.

A typical program output can provide boundary layer profile predictions at each integration station. Hydrodynamic quantities are also computed such as the boundary layer thickness (δ), the displacement

thickness (δ_1), shape factor (H'), momentum thickness Reynolds number (Re_θ), skin friction coefficient (C_F) and acceleration parameter (K). Additionally, the values of the local Stanton number (ST_x), heat transfer coefficient (h_0) and energy thickness Reynolds number (Re_Δ) can be obtained.

The program can be operated in either of two modes. Mode (1) solves all the conservation equations with the exception of the turbulent kinetic energy equation. Laminar flow is assumed to develop until a specified value of the momentum thickness Reynolds number, $Re_{\theta,TR}$, is reached (an input variable for Mode (1) with suggested values from 200 to 300). At this point there is a smooth transition to turbulent flow. Mode (2) accomplishes the simultaneous solution of the conservation equations including the turbulent kinetic energy equation, (TKE).

V.2.2. Suction Surface Results

To determine the local Stanton number variation along the suction surface for comparison to predicted values, measurements of the local heat flux were made at 8 locations along the vane contour. By maintaining the local Mach number distribution similar to the vane prototype over a range of total pressures, heat flux measurements were recorded over a wide range of the local Reynolds number. Six total pressure levels were imposed, maintaining a constant T_{T_∞}/T_W. The inlet freestream turbulence intensity was varied from 6.6% to 10.5% over the range of total pressures investigated. Table 5 summarizes the inlet and local conditions for which dry wall heat transfer data were obtained.

Condition Held Constant

T_{T_∞} = 689°K (1240°R)

T_{T_∞}/T_W = 2.15

Design Ma_X Distribution

Conditions Varied

P_{T_∞} = $2.43 \times 10^5 \rightarrow 4.17 \times 10^5$ N/m^2
(35-60psia)

Tu_∞ = 6.6% (Fig.38)
8.0% (Fig.39)
10.5% (Fig.40)

Table 5. Summary of Conditions For Dry-Wall Heat Transfer Measurements.

Figure 38 shows the variation of the Stanton number along the suction surface with the local Reynolds number for an inlet freestream turbulence intensity of 6.6%. The data shown are represented by a least squares curve fit, designated by the solid line. The broken line is the prediction of the local Stanton number using the boundary layer program. Mode (2) (use of TKE equation) was employed in the prediction assuming negligible freestream turbulent kinetic energy.*

The data are shown to be distributed approximately ± 10% about the least squares curve. A comparison between the predicted and least squares representation of the measured Stanton numbers shows nearly an identical dependency on the Reynolds number, following approximately a -0.3 power of Re_x.

The predicted level of the Stanton number is approximately 10% higher than the least squares fit of the data. Two explanations are offered for this discrepancy: (1) the boundary layer program does not include the effect of surface curvature on the development of the hydrodynamic and thermal boundary layers except for axi-symmetric problems and (2) the vane surface may not have been smooth in the initial starting length region.

Curvature (with $dR'/dx > 0$, R' being the body radius) would affect the development of the hydrodynamic boundary layer in the same manner as a strong positive pressure gradient. Experimental evidence (38,39) has verified that sufficiently large values of K (local acceleration

*Predictions using Mode (2) with input freestream turbulence intensities from 0% to 10% showed no significant effect on the Stanton number which is in agreement with previous experiments (33)(34).

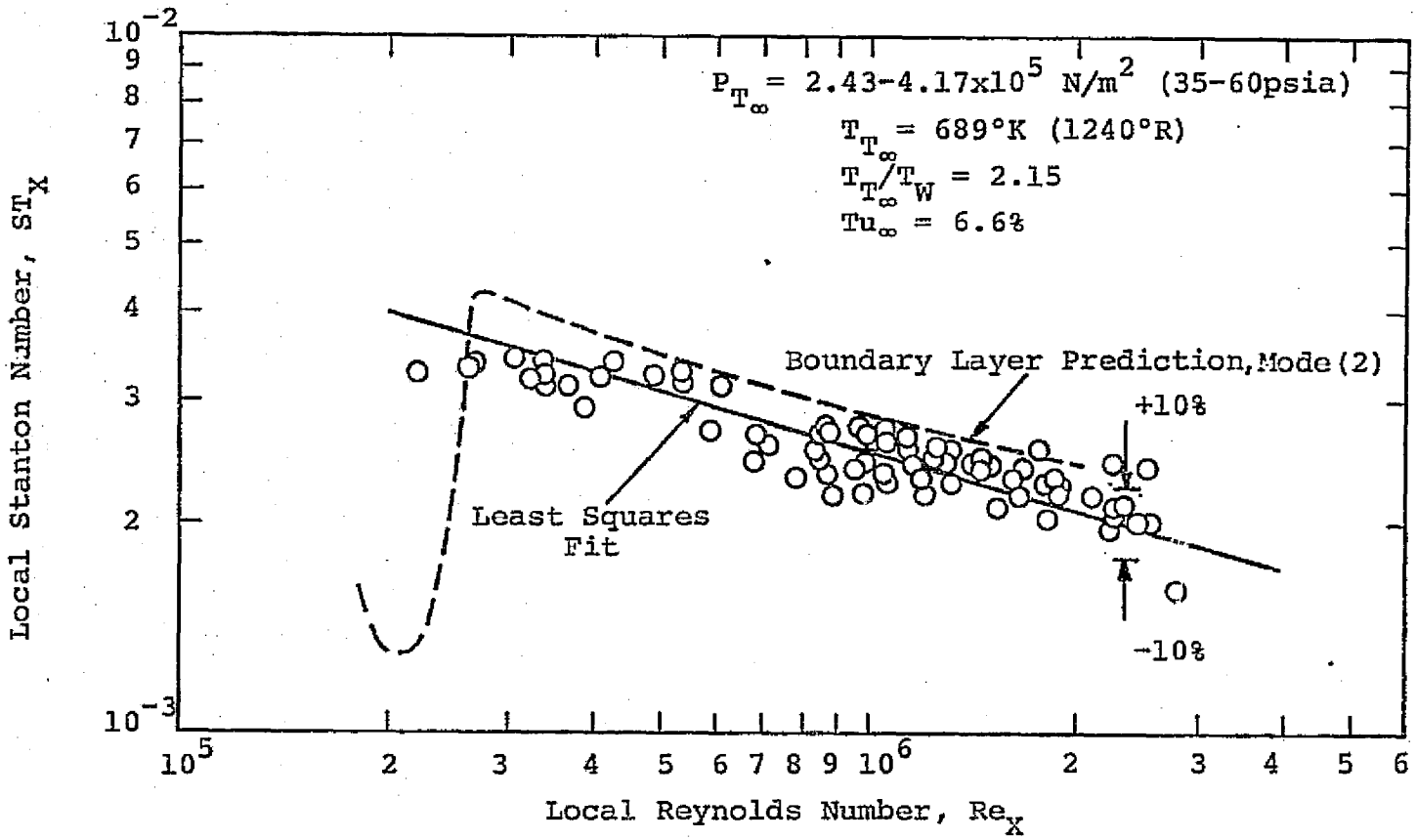

Figure 38. Suction Surface Stanton Number Variation With Reynolds Number at 6.6% Freestream Turbulence Intensity.

parameter) can depress the local Stanton number as the thermal boundary layer penetrates the hydrodynamic layer. Values of $\frac{1}{Re_\infty}\frac{dR'}{dx}$ of the order of 10^{-6} existed along the suction surface contour. Values of K near 10^{-6} have been shown experimentally to depress the local Stanton number approximately 3% to 4%. It appears that surface curvature may account for a portion of the difference between the measured and predicted Stanton numbers.

In addition to curvature effects, the measured ST_x could be indicative of a boundary layer that had transitioned to turbulent flow prior to the location which is characteristic of a smooth initial starting length. To predict such a behavior, the prediction curve would be shifted to the left on Fig. 38, resulting in a lower ST_x for a fixed Re_x. The combined effects of premature transition as well as surface curvature would appear to bring the data in closer agreement with the boundary layer prediction.

Figure 39 indicates the measured Stanton number variation (suction surface) with Re_x for an inlet turbulence intensity of 8.0%. The data is represented by a least squares curve within a ± 15% band. The measured ST_x correlates with the -0.15 power of Re_x and appears less sensitive to the Re_x than the prediction. Agreement of the data with the prediction improves at the higher Reynolds numbers, after being 20% lower near $Re_x = 3 \times 10^5$.

Figure 40 presents the ST_x variation with Re_x for an inlet Tu_∞ of 10.5%. The data is ± 20% about a least squares curve fit. The measured ST_x appears to depend on the -0.15 power of Re_x as in Fig. 39.

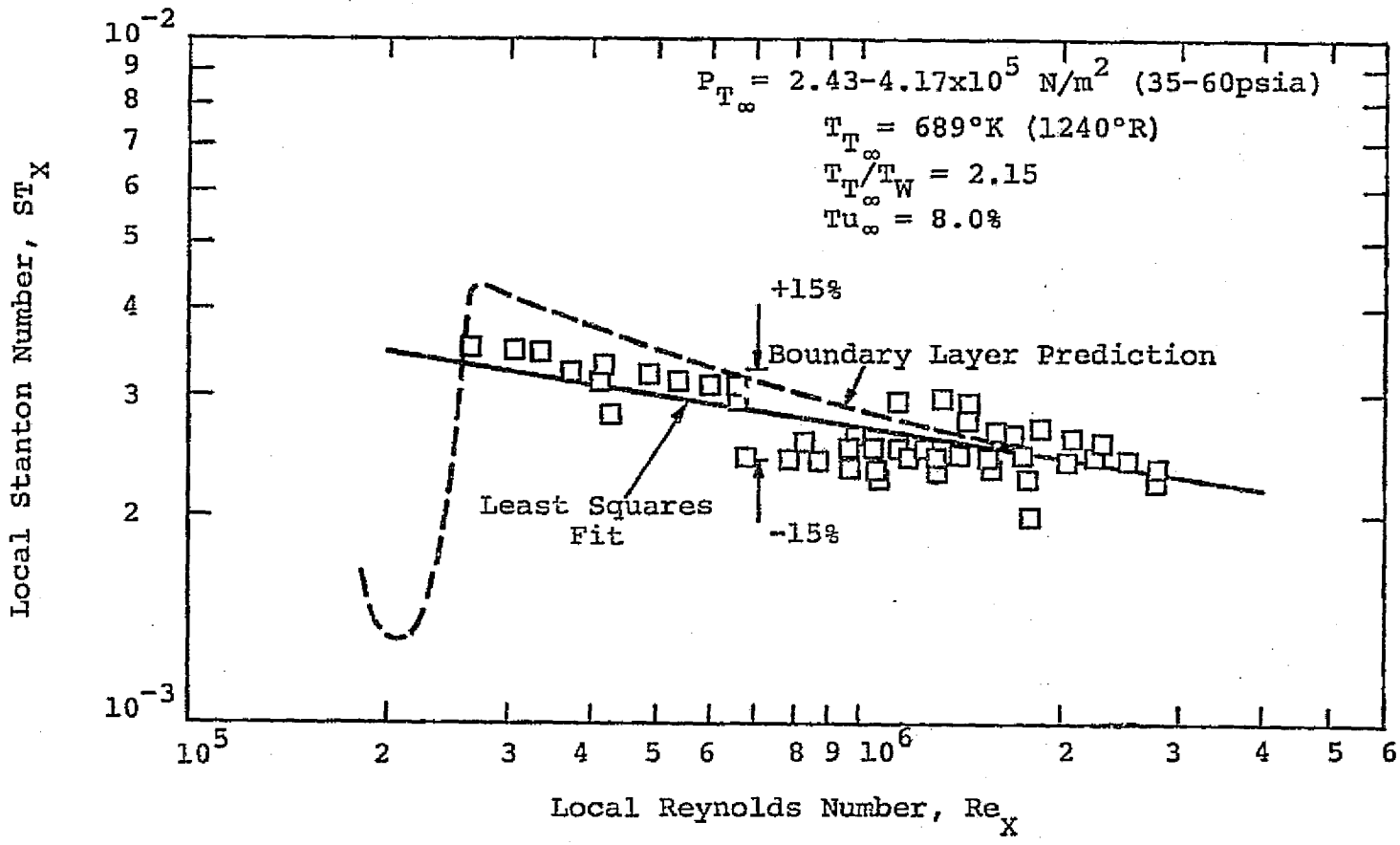

Figure 39. Suction Surface Stanton Number Variation With Reynolds Number at 8.0% Freestream Turbulence Intensity.

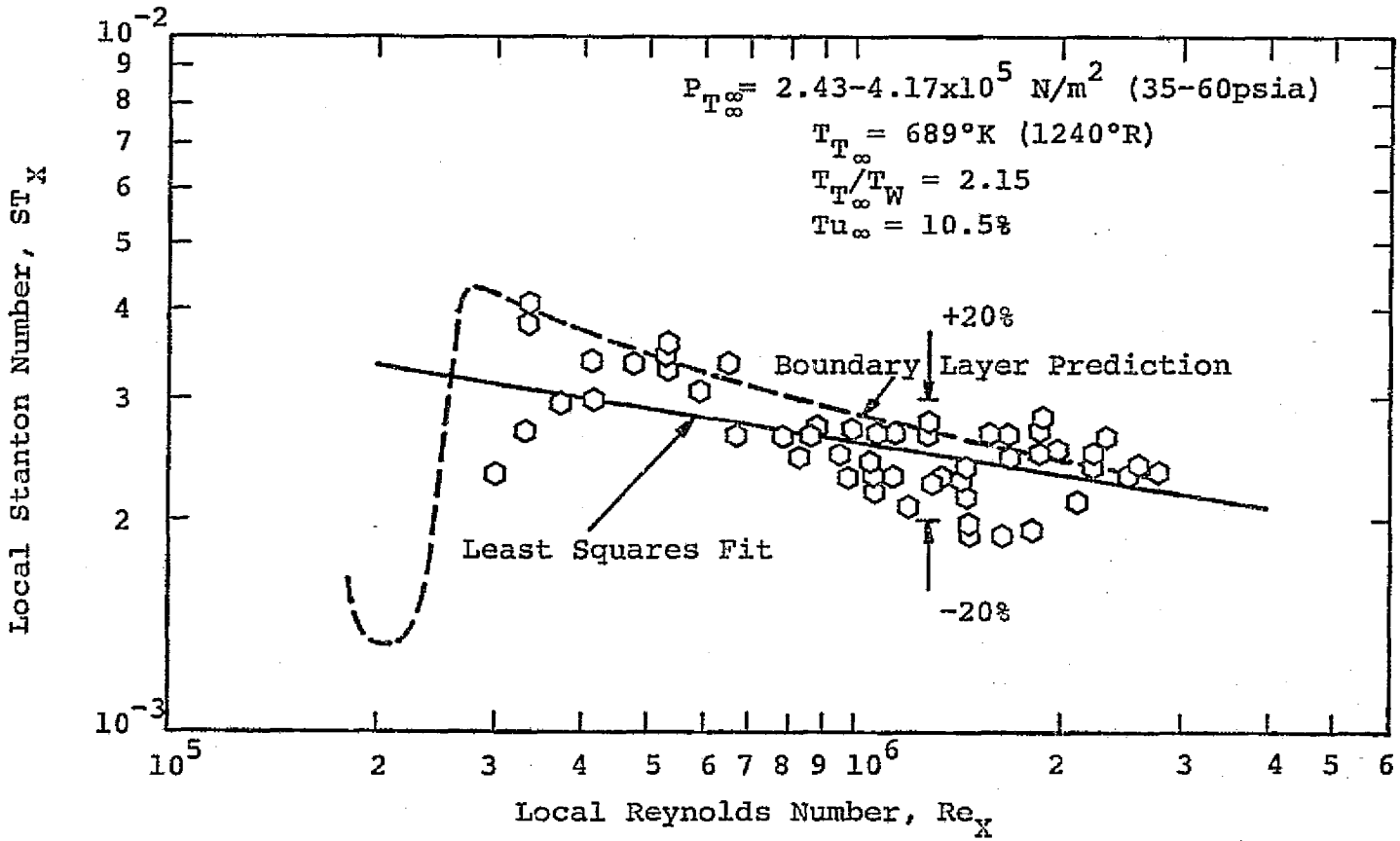

Figure 40. Suction Surface Stanton Number Variation With Reynolds Number at 10.5% Freestream Turbulence Intensity.

In comparison, Figs. 38, 39, and 40 show that a least squares curve fit of the Stanton number data follows approximately the same Re_x dependency as the prediction ($ST_x \propto Re_x^n$ where $n \simeq -0.15$ to -0.30). However, the overall level of the measured ST_x is 10% lower than predicted for a Tu_∞ of 6.6% and 20% lower, in the low Re_x range, for Tu_∞ of 8.0% and 10.5%. With increasing Tu_∞, scatter in the data appears to increase. Within the limits of the data scatter, there appears to be no definite change in the local Stanton number level for a variation in Tu_∞ from 6.6% to 10.5%. Since the Tu_∞ level effect was not marked and higher Tu_∞ levels indicated greater uncertainty in the heat flux measurement, the decision was made to conduct all subsequent film cooling experiments at the lowest value of Tu_∞ of 6.6%.

V.2.3. Pressure Surface Results

Figure 41 shows the data for the pressure surface, with the local Stanton number presented as a function of the local Reynolds number for the conditions listed in Table 5. The data encompasses all measurements of pressure surface dry-wall heat flux at all three Tu_∞ levels. The locations of the first three heat flux sensors are shown along the abscissa by their corresponding range of Re_x for the various total pressures imposed.

The subject data exhibits the general trend of a decreasing Stanton number with increasing Reynolds number. In the region $7\times10^4 \leq Re_x \leq 1.2 \times 10^5$, the Stanton number ranges from approximately 0.003 to 0.0023. A step increase in the Stanton number occurs near $Re_x = 1.25 \times 10^5$ with a subsequent general decrease with increasing Reynolds number. A slight

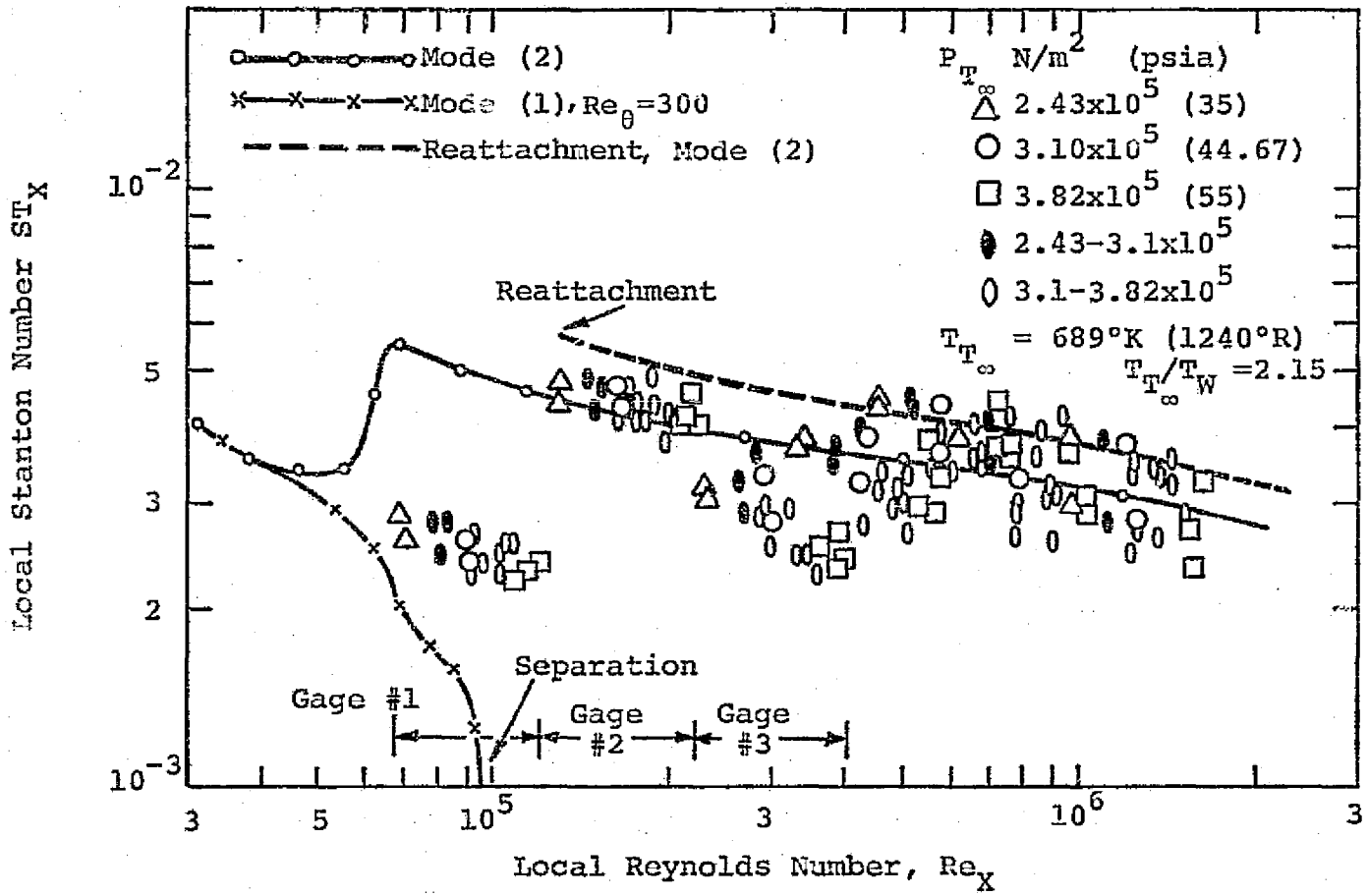

Figure 41. Pressure Surface Stanton Number Variation With Reynolds Number (Tu_∞ = 6.6 ÷ 10.5%).

depression in the Stanton number with an apparent recovery region is noted for the range $2.3 \times 10^5 \leq Re_x \leq 6.2 \times 10^5$.

An attempt to predict the local Stanton number for the pressure surface was made using Mode (2) of the boundary layer program, with a representative total pressure of 3.1×10^5 N/m^2 (50 psia) and negligible freestream turbulent kinetic energy. The resulting prediction is illustrated in Fig. 41 by the circled curve. The data follow the general trend of the prediction showing a decrease in ST_x for increasing values of Re_x with the exception of the Reynolds number range $7 \times 10^4 \leq Re_x \leq 1.2 \times 10^5$. In this lower Reynolds number range the measured Stanton number values were nearly 50% lower than the Mode (2) prediction. If one were to extend the Mode (2) prediction past the region of apparent transition ($\sim Re_x = 5.5 \times 10^4$), it would appear that the data encompassed in the area marked "gage #1" might be indicative of an extended laminar boundary layer. The sudden rise in the measured ST_x at $Re_x = 1.25 \times 10^5$ may appear to be a subsequent transition to turbulent conditions.

In an effort to account for the lower measured ST_x level in the "gage #1" region, Mode (1) of the prediction technique was used. Recall that Mode (1) corresponds to the solution of the conservation of mass, momentum and energy equations only. In this mode, the extent of the laminar boundary layer can be controlled by specifying a transition, momentum-thickness Reynolds number, $Re_{\theta,TR}$. To predict what may appear to be measured, laminar ST_x values out to $Re_x = 1.2 \times 10^5$, a transition Reynolds number, $Re_{\theta,TR}$, of 300 was specified. The results of this prediction appear as the crossed curve. A comparison of the data from "gage #1" with the Mode (1) prediction shows that, <u>at first</u>, the

predicted trend of the Stanton number indicates that agreement with the data may be good. Note that up to $Re_x = 5.5 \times 10^4$ the slope of the Mode (1) ST_x vs Re_x is nearly identical to the trend of the measured data. However, for $Re_x > 6 \times 10^4$ the difference between the predicted values and the data increases significantly. In fact, at $Re_x = 9.6 \times 10^4$ (which corresponds to $Re_\theta \simeq 200$ along the surface) separation is indicated by the Mode (1) prediction as the calculated wall shear stress becomes vanishingly small. The measured ST_x values in the region of "gage #1" do not appear representative of extended laminar flow. From this information the following conclusions were drawn from which a subsequent analysis could be initiated to explain the trends of the data:

(1) For Tu_∞ levels that were imposed during the measurement of the pressure surface ST_x, it seems unlikely that a laminar boundary layer would persist out to $Re_x = 1.2 \times 10^5$. This is substantiated by the predicted transition Re_x of 6.9×10^4 using Mode (2),

(2) By forcing laminar flow to a transition $Re_{\theta,TR}$ of 300, using Mode (1), there still appears to be a discrepancy between measurement and prediction,

(3) If the data between $7 \times 10^4 < Re_x < 1.2 \times 10^5$ is really characteristic of laminar flow then the data between $7 \times 10^4 < Re_x < 2.2 \times .0^5$ represent a laminar transition to turbulent flow conditions. However, the Re_x range through which the data would indicate a transition is too abrupt, and

(4) Laminar boundary layer separation is predicted at $Re_\theta = 200$ ($Re_x = 9.6 \times 10^4$). The data may actually be representative of separated flow.

From these observations, it appears most likely that separation occurred in a region near "gage #1". With this assumption, a separation bubble length model was used to predict reattachment as described in the following paragraphs.

Horton (59) suggests that a separation bubble consists of two regions: (1) a laminar shear layer of length ℓ_1, and (2) a reattachment zone of length ℓ_2. The separation bubble is then the sum of the lengths of these two regions. The laminar shear layer length is described in a modified fashion by Dunham (60) as

$$\frac{U_{SEP}\ell_1}{\nu} = 5000 + EXP\ (10.463 - 1.54\ Tu_\infty^{0.629}) \tag{73}$$

The reattachment length, ℓ_2 is defined according to Horton as

$$\ell_2 = \frac{(1 - \frac{U_{RE}}{U_{SEP}})\ \theta_{SEP}}{0.011233\ (\frac{U_{RE}}{U_{SEP}}) - 0.003033} \tag{74}$$

where U_{RE} = freestream velocity at reattachment

U_{SEP} = freestream velocity at separation

θ_{SEP} = momentum thickness at separation

For the conditions in Fig. 41, computations using Mode (1) yields, at separation

U_{SEP} = 103.6 m/sec (340 ft/sec)

$\nu = 1.9 \times 10^{-5}$ m^2/sec (2.1×10^{-4} ft^2/sec)

$\theta_{SEP} = 5.08 \times 10^{-5}$m (0.002 in)

Using a mean turbulence intensity of 8.0%, assumed representative of the data, ℓ_1 is calculated from Eq. (73) to be approximately 0.00612m (0.241 in).

Before ℓ_2 can be calculated, the local velocity at reattachment must be estimated. Figure 42 shows the local Mach number variation with non-dimensionalized distance along the pressure surface. The solid curve indicates the calculated design Mach number distribution. The locations of the heat flux gages are also indicated. The point of separation was predicted at $x/L_p = 0.125$ (obtained from Mode (1) with $P_{T_\infty} = 3.47 \times 10^5$ N/m^2 (50 psia)). For the range $0.125 \leq x/L_p \leq 0.275$, there appears to be little variation in the local velocity for the data shown. Thus, the value of U_{RE} is not sharply defined. A value for the reattachment velocity of $U_{RE} \approx 97.5$ m/sec (320 ft/sec), corresponding to a local Mach number near 0.20 was selected as representative of the data in Fig. 42. Therefore, using the predicted momentum thickness and separation velocity, ℓ_2 was calculated from Eq. (74) to be 4.06×10^{-4}m (0.016 in). A total separation bubble length, $(\ell_1 + \ell_2)$, was then computed to be 0.0066m (0.26 in), representing approximately 4% of the total pressure surface length. The selection of the reattachment velocity for use in the ℓ_2 calculation was somewhat arbitrary. However, since ℓ_2 contributed less than 10% to the total bubble length, U_{RE} had little influence on the total length, $\ell_1 + \ell_2$.

Erlich (61) presents another approximate method for the calculation of a separation bubble length based on flow visualization studies on an airfoil with a rapid change of curvature at the leading edge. Tests indicated that

$$\frac{(\ell_1 + \ell_2)}{\theta_{SEP}} = \text{constant} \tag{75}$$

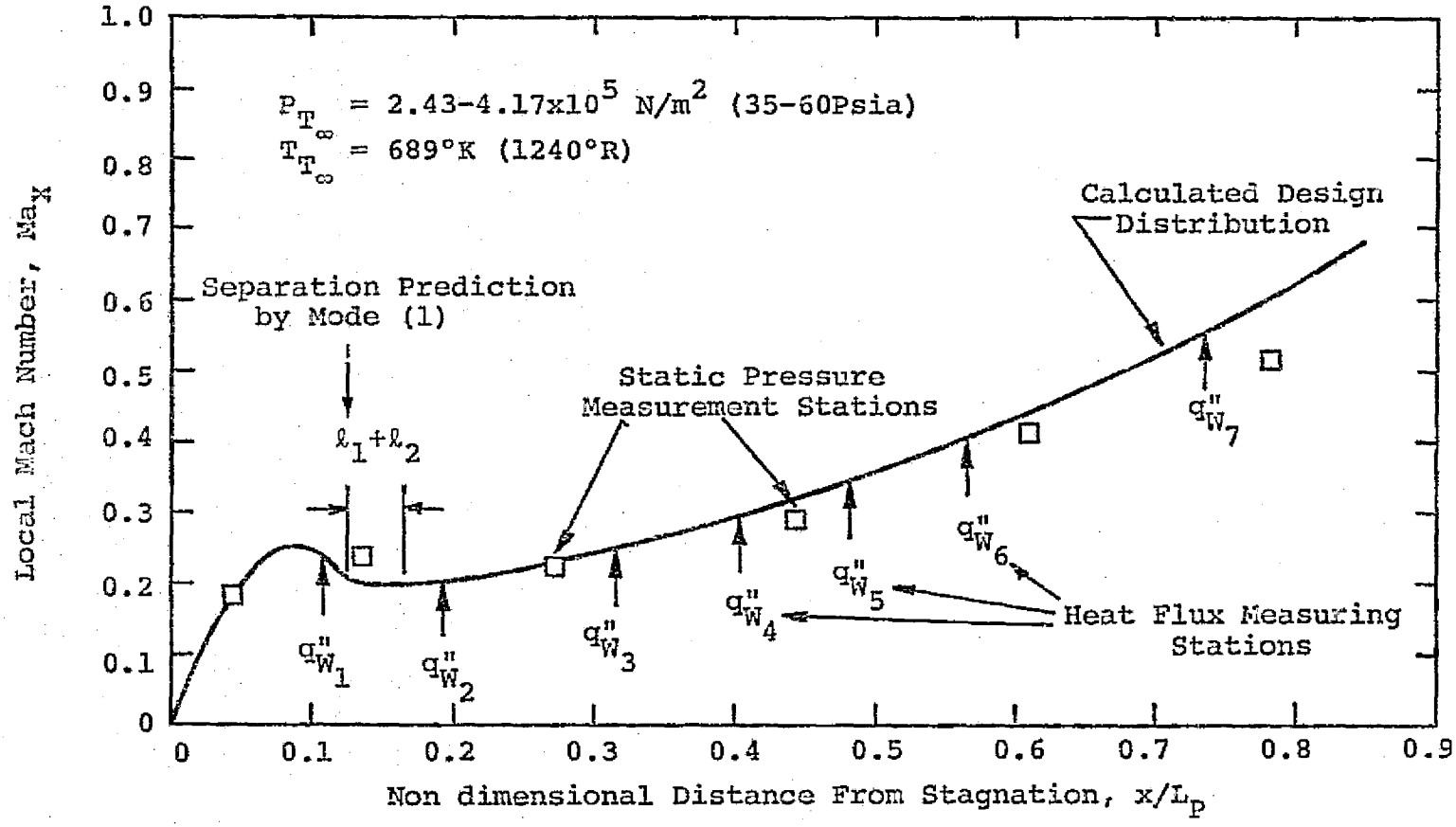

Figure 42. Variation in Local Mach Number At Various Pressure and Heat Flux Measurement Locations.

For conditions in which $200 \leq Re_{\theta,SEP} \leq 500$, this constant was found to be 120. Recalling that θ_{SEP} was 5.08×10^{-5}m the predicted bubble length from Eq. (75) is 6.1×10^{-3}m (0.24 in) or approximately 3.7% of the pressure surface length. This is in good agreement with the preceding results from Horton's analysis.

It will be recalled from the discussion of Fig. 41, that separation was predicted at $x/L_p = 0.125$ using Mode (1) with $Re_\theta = 300$. Adding the bubble length ($\ell_1 + \ell_2 \approx 0.04\ L_p$), reattachment was predicted to occur at $x/L_p = 0.165$, or at a value of $Re_{x,REATTACH} = 1.27 \times 10^5$, which is 32% greater than the Reynolds number at separation. Using Mode (2) of the prediction scheme, assuming the boundary layer reattaches at $Re_{x,REATTACH}$ with a subsequent turbulent behavior, the local Stanton number variation was predicted with the result shown as the broken line in Fig. 41. The data appear to agree with the trends predicted by the separation-reattachment model. The measured Stanton numbers are higher than predicted by laminar theory (Mode (1)) in the region of "gage #1", indicative of separated flow. Following reattachment, noted in the region marked "gage #2", the measured Stanton number level is representative of an established turbulent boundary layer. With the exception of the regime $2.2 \times 10^5 < Re_x < 7 \times 10^5$, the measured Stanton number values appear to be in reasonable agreement with the results predicted for a reattached turbulent boundary layer.

The trend of the experimental data for the region between $2.2 \times 10^5 < Re_x < 7 \times 10^5$, however, still needs to be qualified. It appears that, following reattachment, the measured Stanton number is initially depressed, but recovers to a level which is predicted for the reattached turbulent

boundary layer. The degree to which ST_x is depressed appears to be pressure dependent. At the lowest pressure level (2.43×10^5 N/m^2, 35 psia), indicated in Fig. 41 by triangles (Δ), the Stanton number is only slightly depressed, recovering to the predicted reattached turbulent boundary layer trend (broken line) near $Re_x = 4.5 \times 10^5$. At the highest pressure level (3.82×10^5 N/m^2, 55 psia), represented by squares ($\square$), the largest depression of the Stanton number was noted. At this high pressure level, ST_x did not begin to recover until $Re_x \approx 4 \times 10^5$. At $Re_x = 7 \times 10^5$ a full recovery was noted (i.e. a return to the trend of the broken line predicted by Mode (2) for reattachment). At an intermediate pressure (3.1×10^5 N/m^2, 44.67 psia), shown as circles (o), depression and recovery of ST_x occurred approximately midway between the values for the two extreme pressures. The solid vertical ellipses correspond to pressures between 2.43 and 3.1×10^5 N/m^2 (i.e. between the corresponding pressures of the triangles and circles) while the open ellipses represent pressures between 3.1 and 3.82×10^5 N/m^2 (i.e. between the corresponding pressures of the circles and the squares). At first glance these results seem somewhat inconsistent with the reattachment prediction; however, the separation-reattachment model is capable of explaining this "depression-recovery" region of the local Stanton number by a close examination of the boundary layer after reattachment which follows below.

Returning briefly to Fig. 42 the local Mach number is shown to remain relatively constant between $x/L_p = 0.20$ and 0.30. In fact, a slight deceleration may be indicated by the measured data even up to the location of the third heat flux sensor. A fairing through the wall pressure data indicates that the start of a favorable pressure gradient

may not occur until $x/L_p \approx 0.325$. The presence of freestream flow acceleration or deceleration will certainly affect the development of the reattached boundary layer and, therein, provides an explanation for the trends observed in Fig. 41.

With reattachment predicted near $Re_x = 1.27 \times 10^5$, the measured values of ST_x shown in Fig. 41 in the region marked "gage #2" are probably representative of the reattached flow striving to establish itself as a normal turbulent boundary layer. However, at reattachment the boundary layer may be relatively thick as a result of the previous separation phenomenon. In such a case it would not be unreasonable to assume that the hydrodynamic boundary layer (characterized for this discussion by the momentum thickness, θ) is much thicker than the thermal boundary layer (characterized by the boundary layer enthalpy thickness, Δ). Since no appreciable favorable pressure gradient is established until the near region of "gage #3", the reattached boundary layer cannot be thinned. In fact, it appears to thicken even more as evidence by the drop in ST_x between $2 \times 10^5 < Re_x < 4 \times 10^5$.

As indicated from Fig. 42, a noticeable freestream acceleration begins in the region of "gage #3" ($2 \times 10^5 < Re_x < 4 \times 10^5$). The onset of this acceleration directly affects the hydrodynamic boundary layer development. Due to the assumed condition of the boundary layer at reattachment (i.e. $\theta > \Delta$), this acceleration-dependent change of θ in relation to Δ can offer a reasonable explanation for the pressure dependent "recovery" region.

The effects of acceleration are characterized by the magnitude of the nondimensional acceleration parameter, K. As the acceleration

increases, K increases. Recall that K is defined as

$$K = \frac{\nu_\infty}{U_\infty^2} \frac{dU_\infty}{dx} \tag{76}$$

In the region marked "gage #3", Fig. 41, the pressure-dependent recovery of ST_x was noted, which corresponds to the initiation of local free-stream acceleration (Fig. 42). With increasing K, θ thins and rapidly approaches the local value of Δ. This amounts to concentrating the effective transport properties of the momentum boundary layer within the limits of the thermal boundary layer. Consequently, the Stanton number will increase as θ approaches Δ. The inverse situation, in which ST_x decreases for increasing K for Δ initially greater than θ, has been experimentally verified by Kays, Moffat and Thielbahr (39).

An explanation for the recovery of the Stanton number in the region following reattachment has been offered. However, the influence of the total pressure level on the initiation of recovery must be discussed. The data for the lowest pressure level (Δ symbols in Fig. 41) recovers sooner than the data for the higher pressure levels (o, $\square$ symbols). The delay of ST_x recovery with progressively higher pressure levels can be explained by referring to the definition of the acceleration parameter, K. As the pressure decreases, ν_∞ increases with a subsequent increase in K. Consequently, at the same sensor location (as shown in Fig. 41 within the limits specified by "gage #3) any increase in the local Stanton number (i.e. recovery) due to acceleration-related thinning of the boundary layer should be noticed first at the lower pressure levels (i.e. higher local value of K). This is substantiated by the data (Δ symbols) between $2 \times 10^5 < Re_x < 7 \times 10^5$ in which ST_x at the lowest pressure level

recovers quickly to near the predicted normal turbulent level. Data for the highest pressure level (□symbol) shows ST_x recovery delayed until a much higher Reynolds number. All the data between the two extreme pressure levels are consistent with this interpretation.

V.2.4. Summary

The previous sections have been concerned with emphasizing two main points: (1) an environment can be maintained at reduced flow conditions which simulates the high heat flux levels characteristic of high temperature and pressure gas turbine operation and (2) the thin-foil, Gardon-gage, heat flux measurement technique incorporated in this investigation can provide reliable heat transfer data under a large gas-to-wall temperature ratio ($T_{T_\infty}/T_W = 2.15$) representative of the significant density variations through the boundary layer of a high temperature inlet turbine vane. Having both established the proper modeling environment and qualified the basic measurement technique, the film cooling study was initiated, the results of which are presented in the following section.

V.3. Film Cooling Results

V.3.1. Presentation of the Data

The results of the subject film cooling study involving injection of cool air from a row of spanwise angled holes will now be presented. It is the sole purpose of this section to catalogue the recorded film cooling data in a convenient manner. Any comments concerning the data will be of a descriptive nature, restricted to pointing out general trends, noting various parameter levels of importance and making

appropriate comparisons. Discussion and analysis of the data will be thoroughly handled in the following section.

The data to be presented represent local heat flux measurements which were made at various locations on the vane surface downstream from the row of injection holes. Each figure which will follow represents the results from a particular heat flux sensor at a designated downstream position, $(x-x_i)/d_0$. The data are presented in terms of the local Stanton number reduction, ST_{FC}/ST_0, and are shown as a function of the coolant blowing ratio, M, for each $(x-x_i)/d_0$. Values of ST_{FC}/ST_0 were calculated from heat flux measurements giving the local Stanton number with no film cooling (ST_0) and the Stanton number for specified film cooling conditions (specified value of M).

Unless otherwise noted, all ST_{FC}/ST_0 values which appear as points on the following figures are mean values representing heat flux measurements that were approximately ± 2% to ± 6% from the mean. Larger deviations generally occurred near injection at high blowing ratios and these cases are documented with vertical bands designating the percent deviation from the mean. A few representative points in the lower blowing ratio regime are also banded showing the typical ± 2% to ± 6% variation. Figure 43 is a typical heat flux gage output visicorder trace for a sensor nearest the injection holes. A comparison is made showing the variation of the signal in relation to its mean for: (1) no blowing, (2) low blowing, M = 0.08, (3) moderate blowing, M = 0.84, and (4) strong blowing, M = 1.42. To eliminate extraneous data, the calculated mean Stanton number ratio (computed from mean heat flux levels) had to meet a specified qualification criterion; namely, the Stanton

number without film cooling (ST_0, reference condition) did not change significantly during a series of film cooling measurements. To determine if this constraint was met, the value of ST_0 was calculated from measurements before and after a range of coolant flow had been set and ST_{FC} measured. If ST_0 had changed no more than 2 to 3%, an average ST_0 was used to form the ratio, ST_{FC}/ST_0, for each coolant flow value. If ST_0 changed more than 3% during the experiments for a range of coolant flow, the data was discarded. The reader is referenced to Appendix C for a more complete discussion of the data qualification.

Table 6 outlines the manner in which the data for the suction surface is organized herein. Six cooling configurations were investigated: two injection angles β = 18° and β = 35° with three locations (for the single row of holes) relative to the stagnation point of x_i/L_S = 0.083, 0.150 and 0.228. Cases I through III correspond to the results for 18° injection for the three injection locations shown, with heat flux gages located at nondimensional distances from injection of $(x-x_i)/d_0$ as shown in Table 6. Cases IV through VI are for 35° injection at the same injection locations (x_i/L_S) as for 18° and for the same range of heat flux gage locations, $(x-x_i)/d_0$. Figures for each value of $(x-x_i)/d_0$ are presented as each case number is dealt with separately. Table 7 is a summary of the injection configurations for the pressure surface. Again, six cooling configurations were investigated: two spanwise injection angles of 18° and 35° at three injection locations relative to the stagnation point of x_i/L_P = 0.033, 0.121 and 0.193. Cases VII through IX represent results for 18° injection at the three injection locations for the range of heat flux gage locations $(x-x_i)/d_0$ shown. Cases X

Figure 43.

Typical Heat Flux Output From Visicorder.

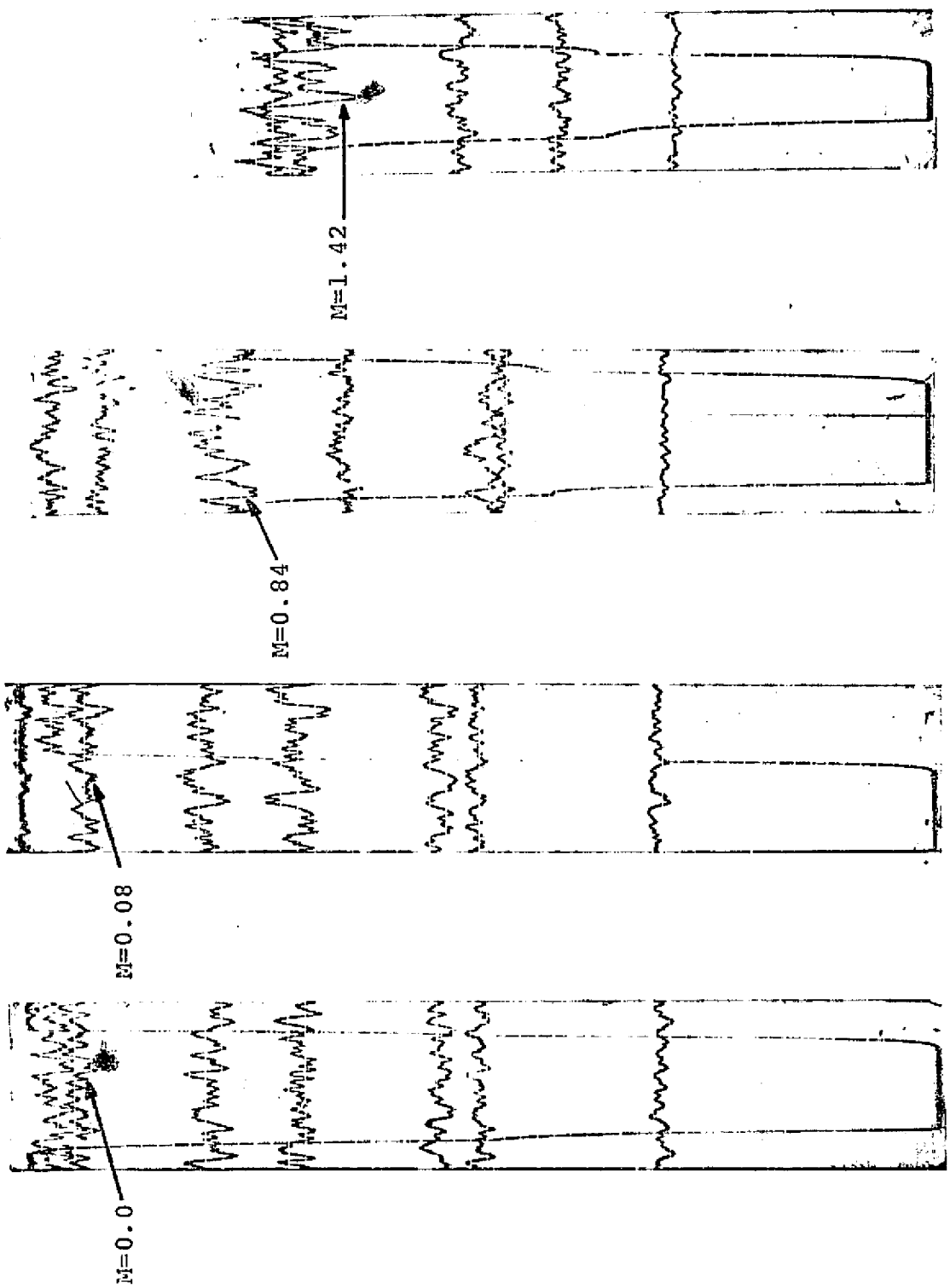

Figure 43.

Case No.	I	II	III	IV	V	VI
Injection Angle, β	18°	18°	18°	35°	35°	35°
Injection Distance From Stagnation x_i/L_S	0.083	0.150	0.228	0.083	0.150	0.228
	Dimensionless Distance From Injection $(x - x_i)/d_o$					
	10.45	11.54	16.29	10.45	11.54	16.29
	22.20	29.80	28.24	22.20	29.80	28.24
	42.55	41.76	41.07	42.55	41.76	41.07
	53.50	54.59	53.03	53.50	66.54	53.03
	66.33	66.54	100.85	66.33	90.46	100.85
	78.28	90.46		78.28	114.37	
	102.20	114.37		102.20		
	126.11			126.11		

Table 6. Summary of Cooling Configurations For Suction Surface Injection.

Case No.	VII	VIII	IX	X	XI	XII
Injection Angle, β	18°	18°	18°	35°	35°	35°
Injection Distance From Stagnation x_i/L_p	0.033	0.121	0.193	0.033	0.121	0.193
	Dimensionless Distance From Injection $(x - x_i)/d_0$					
	10.35	10.87	17.17	10.35	10.87	17.17
	22.09	27.17	29.35	22.09	27.17	29.35
	39.48	39.35	40.22	39.48	39.35	40.22
	51.65	50.22	51.96	51.65	50.22	51.96
	62.52	61.96	75.76	62.52	61.96	75.76
	74.26	85.76		74.26	85.76	
	98.06			98.06		

Table 7. Summary of Cooling Configurations For Pressure Surface Injection.

through XII are for $\beta = 35°$ at identical values of x_i/L_p and $(x-x_i)/d_0$ as in Cases VII to IX.

A least-squares curve fit is included with the data for each heat flux gage. In some cases (for those locations nearest injection), two least-squares curves were used to represent data within two distinct regimes. A smooth transition from one regime to the other was assumed consistent with the intersection of the two least-squares representations. A table will be presented summarizing all the least-squares equations representing the data.

Before the data are presented it would be helpful to briefly review those parameters which were held fixed during the course of the entire film cooling investigation. An inlet Reynolds number (based on the vane leading edge radius) of 8.0×10^4, an inlet Mach number of 0.22 and a freestream turbulence intensity of 6.6% were maintained throughout the experiments. A gas-to-wall temperature ratio (T_{T_∞}/T_W) of 2.15 was maintained as was the prototype vane local Mach number distribution. The film coolant was supplied at ambient conditions and the coolant temperature, corrected for heat pick-up through the vane surface, resulted in an average dimensionless coolant temperature, θ_C', of 1.03.

The data for Case I are presented in Figs. 44 to 51 corresponding to $(x-x_i)/d_0$ values ranging from 10.45 to 126.11 for constant values of $\beta = 18°$ and $x_i/L_S = 0.0833$. Figure 44, at $(x-x_i)/d_0 = 10.45$, shows that ST_{FC}/ST_0 decreases with increasing M up to M = 1.3. For M > 1.3, ST_{FC}/ST_0 begins to increase with further increases in the blowing ratio. Near M = 1.3 large amplitude oscillations in the measured heat flux were noted (as shown with a band about the mean). As M was increased beyond a value

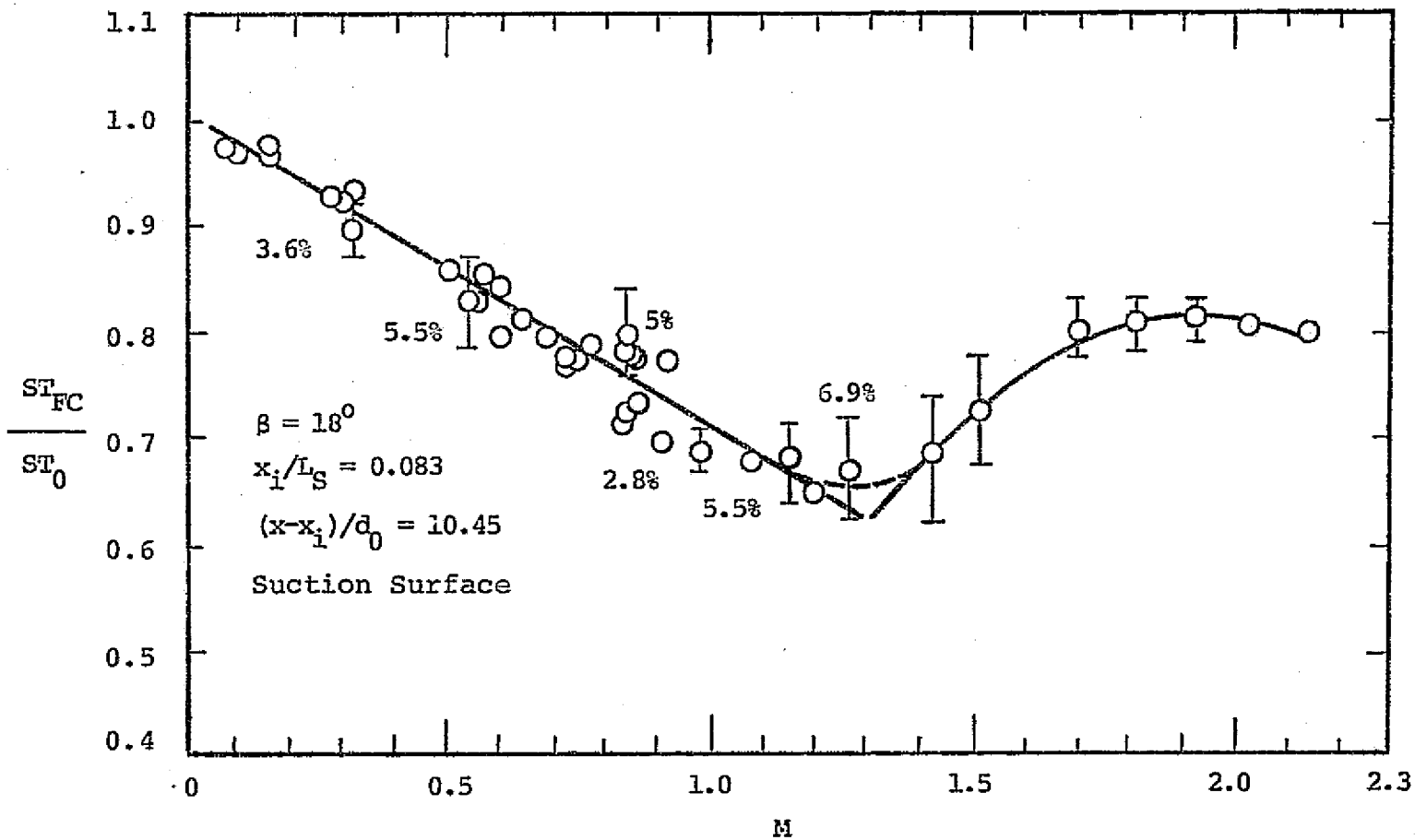

Figure 44. Film Cooling Stanton Number Ratio Variation With M, Case I, $(x-x_i)/d_0 = 10.45$.

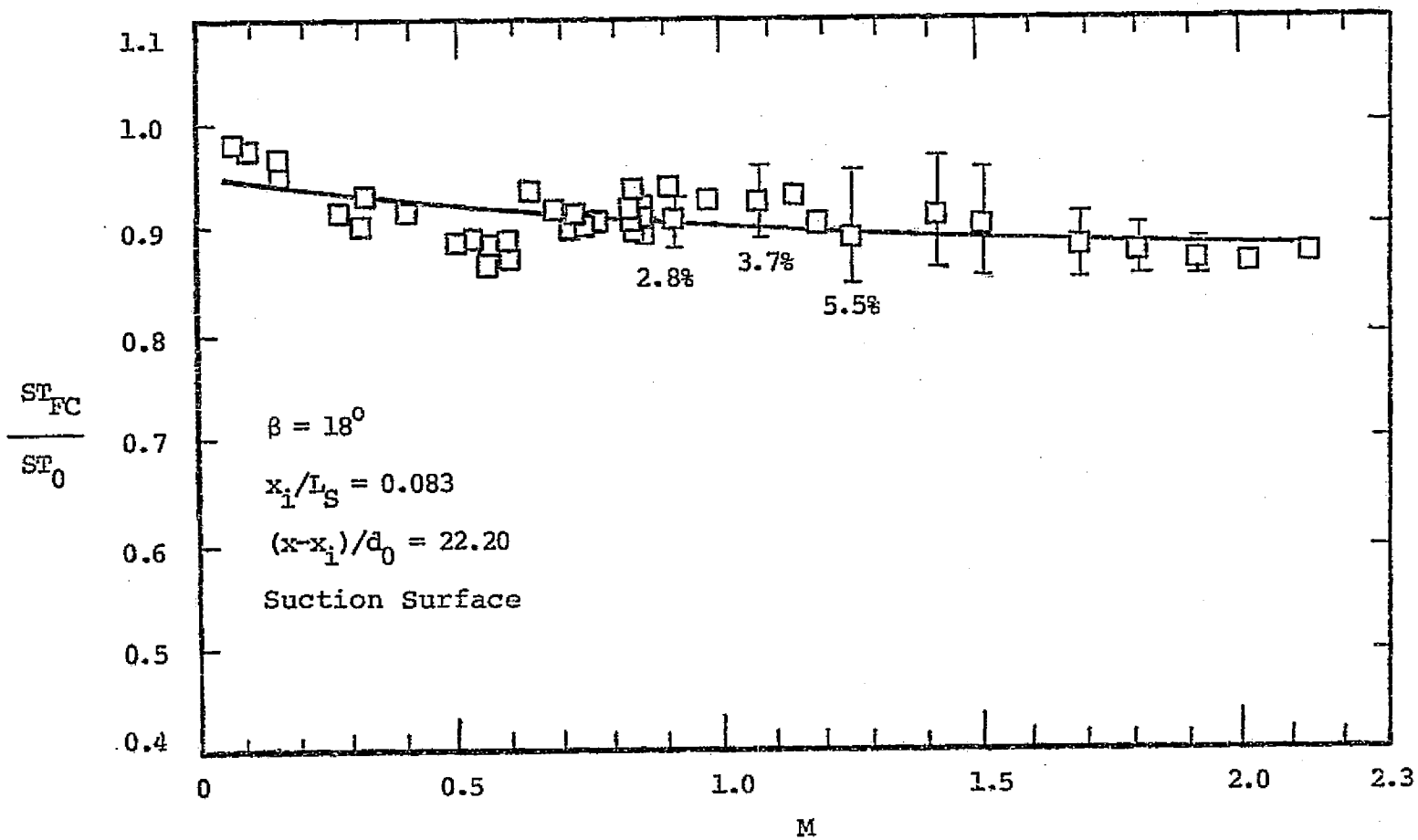

Figure 45. Film Cooling Stanton Number Ratio Variation With M, Case I, $(x-x_i)/d_0 = 22.20$.

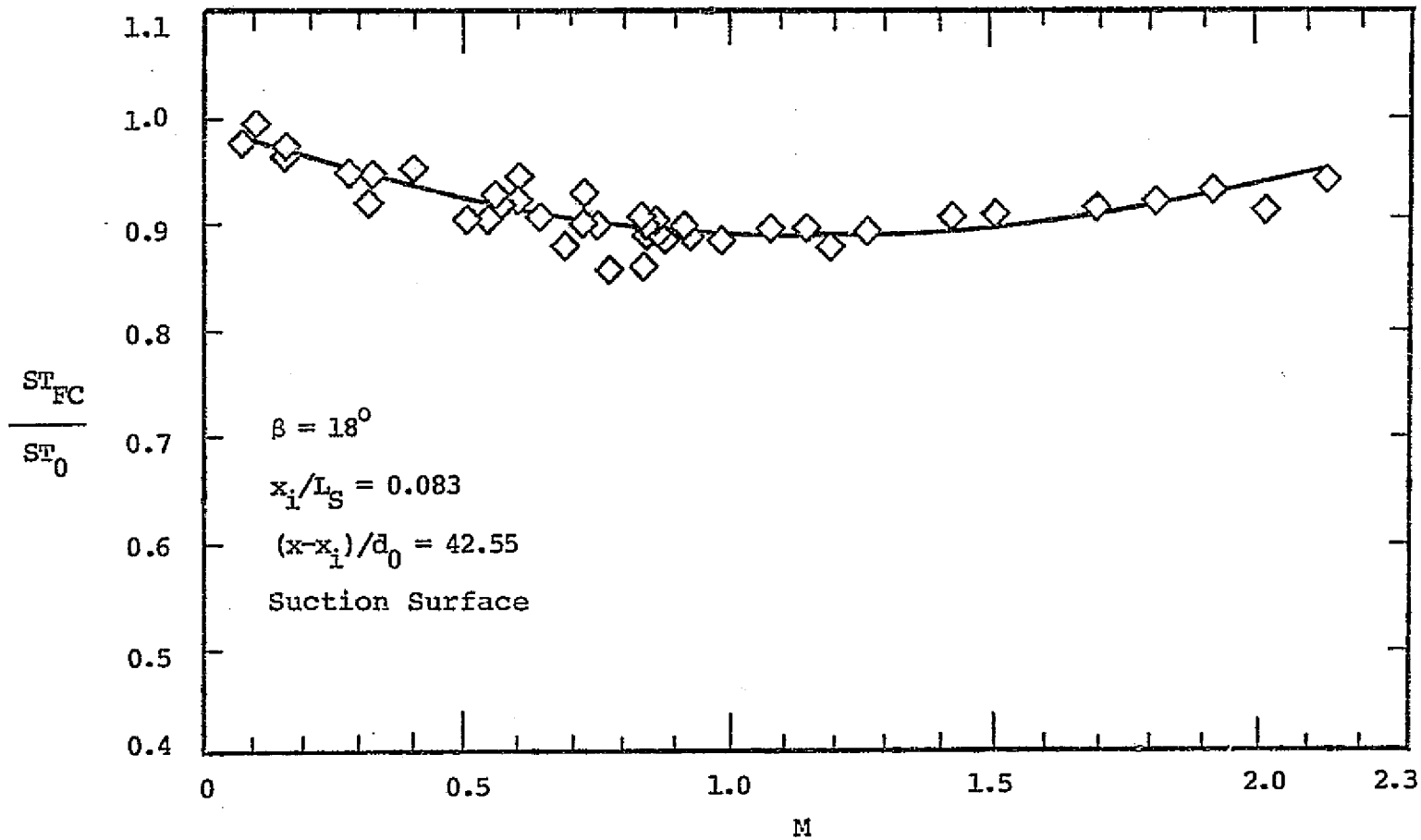

Figure 46. Film Cooling Stanton Number Ratio Variation With M, Case I, $(x-x_i)/d_0 = 42.55$.

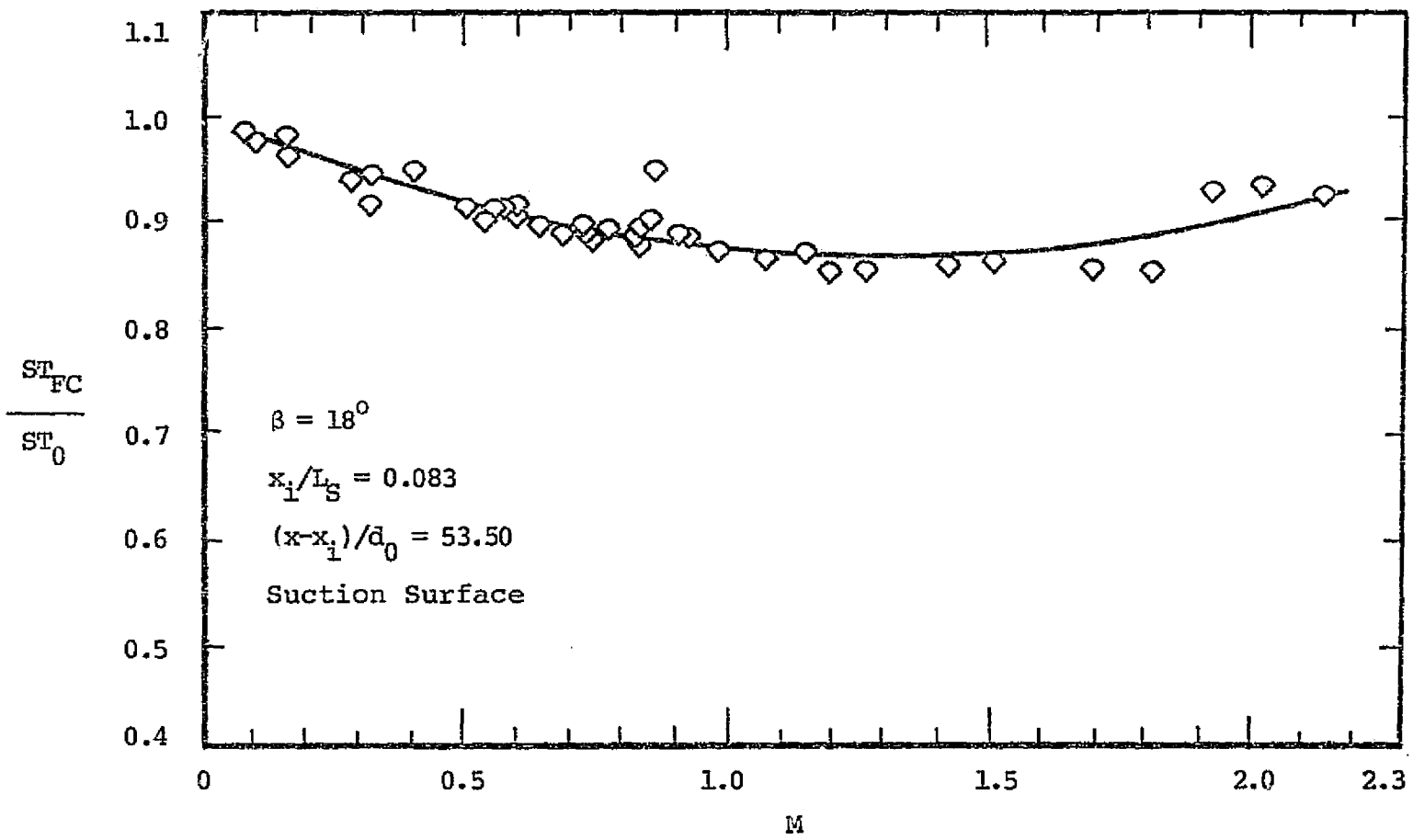

Figure 47. Film Cooling Stanton Number Ratio Variation With M, Case I, $(x-x_i)/d_0 = 53.50$.

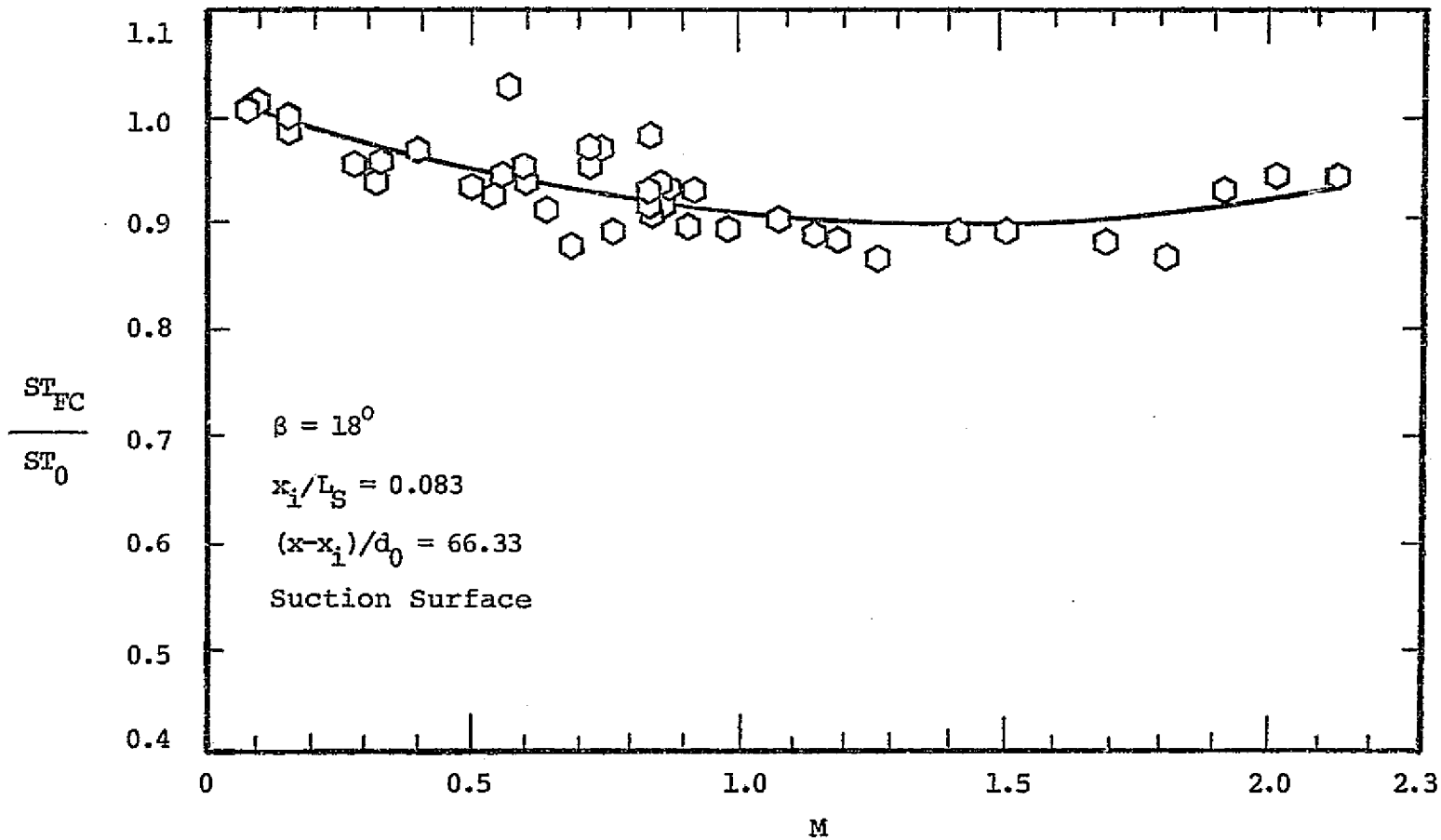

Figure 48. Film Cooling Stanton Number Ratio Variation With M, Case I, $(x-x_i)/d_0$ = 66.33

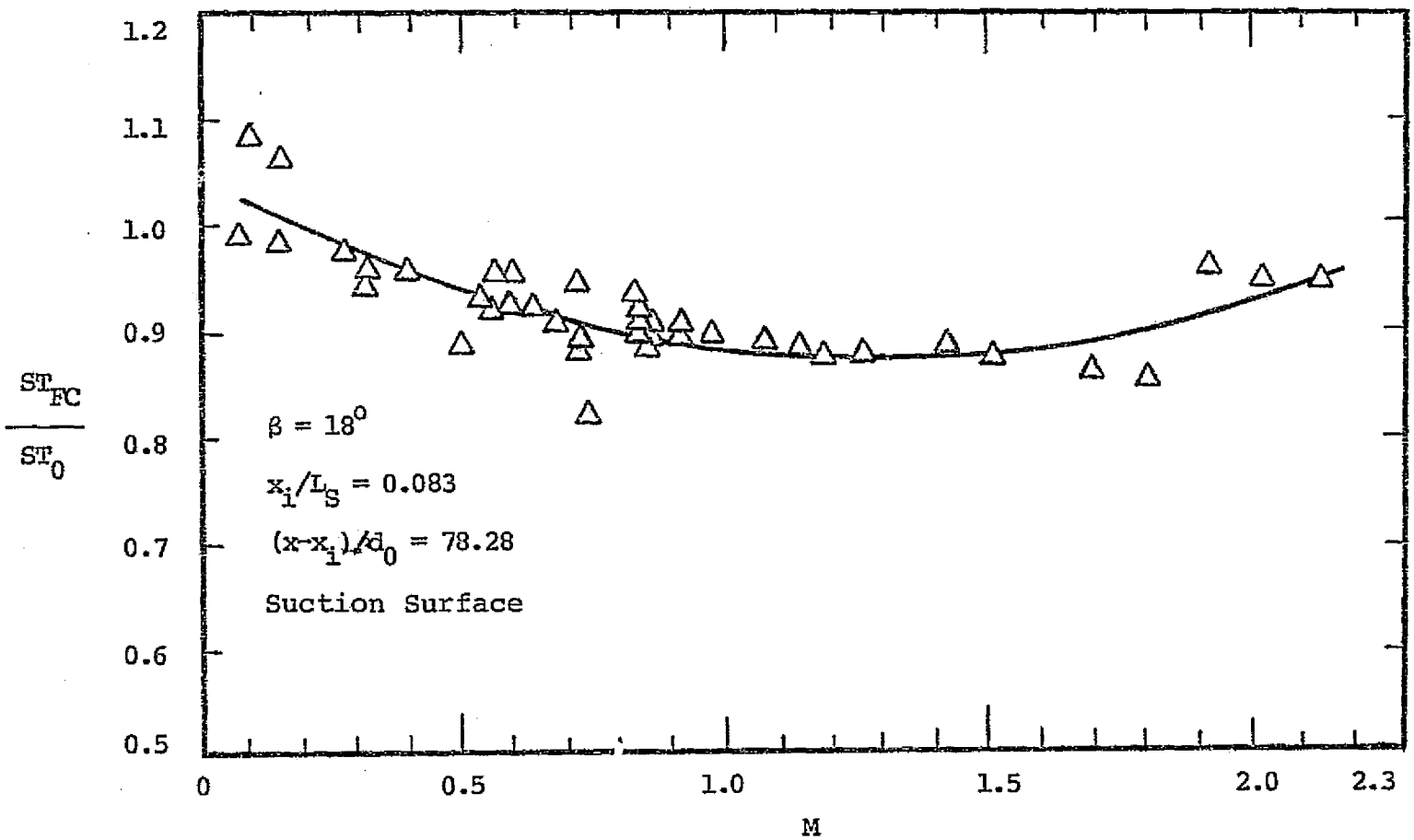

Figure 49. Film Cooling Stanton Number Ratio Variation With M, Case I, $(x-x_i)/d_0 = 78.28$.

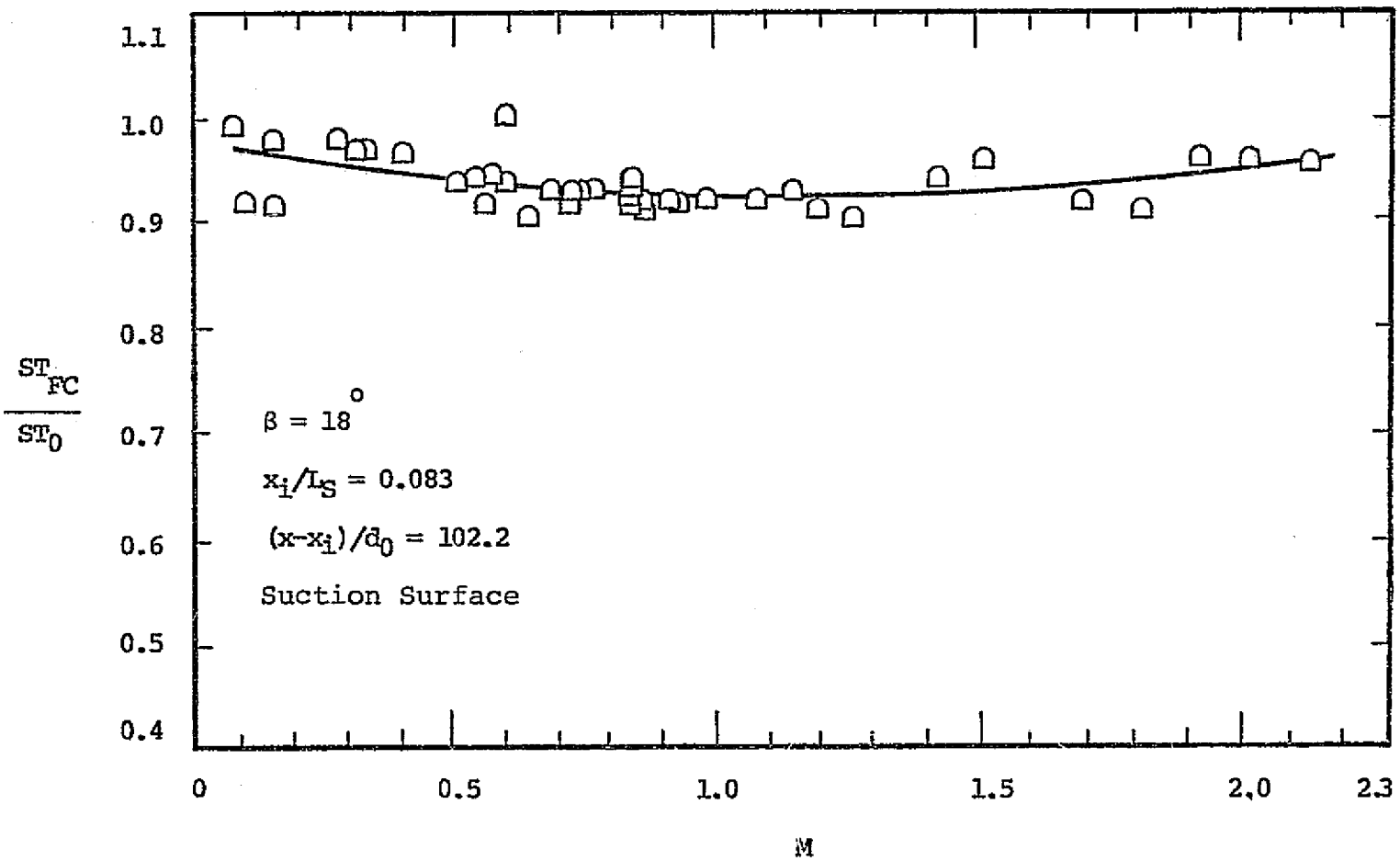

Figure 50. Film Cooling Stanton Number Ratio Variation With M, Case I, $(x-x_i)/d_0 = 102.2$.

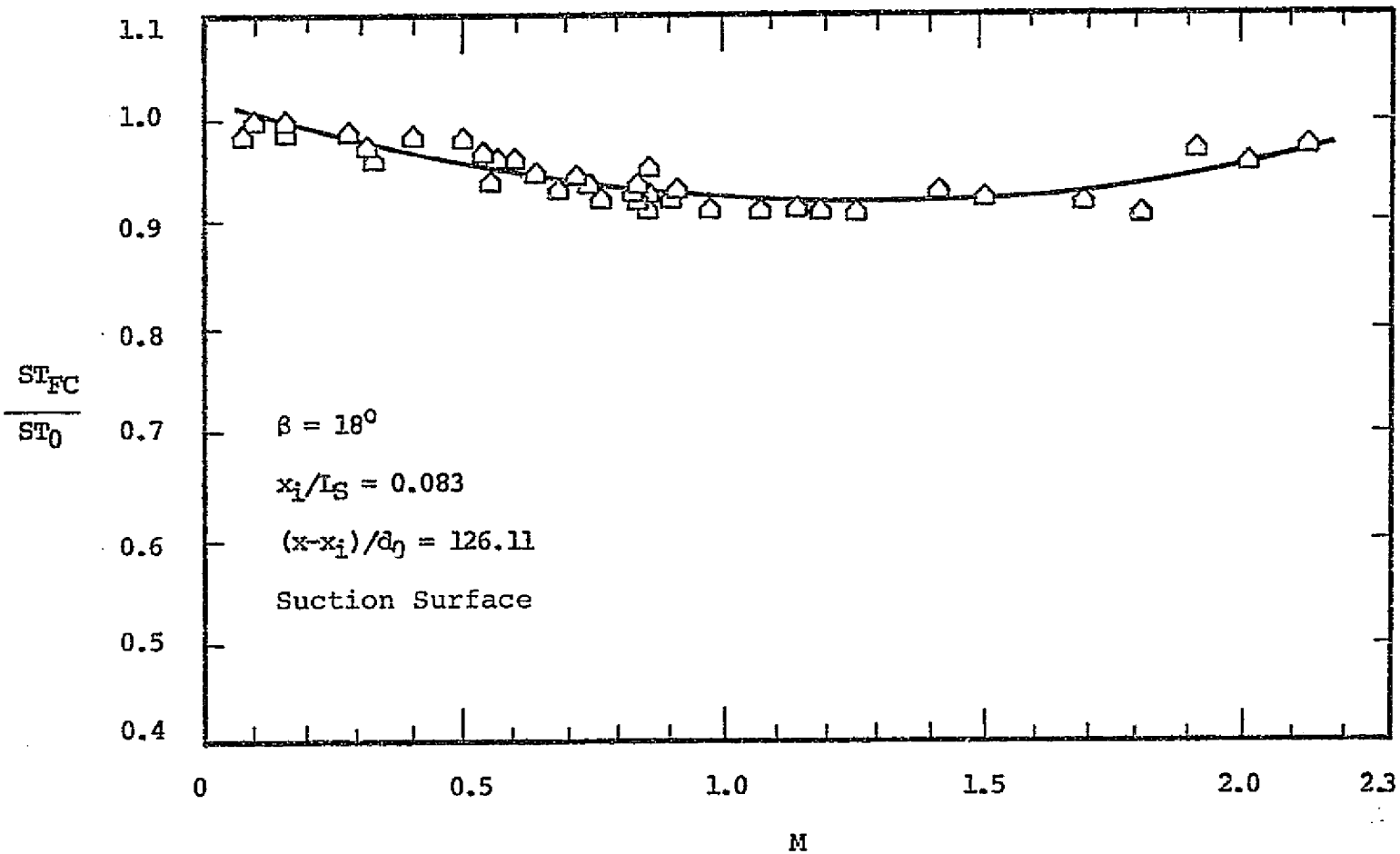

Figure 51. Film Cooling Stanton Number Ratio Variation With M, Case I, $(x-x_i)/d_0$ = 126.11.

CASE I

Figure	$(x-x_i)/d_0$	% Reduction in ST_0	M_{OPT}	% Deviation From Least-Squares
44	10.45	35	1.3	$\pm$5
45	22.20	(12 at M=2.15)	Not Defined	$\pm$5.5
46	42.55	12	1.2-1.4	$\pm$5
47	53.50	13.5	1.2-1.4	$\pm$5
48	66.33	10	1.3-1.5	$\pm$10
49	78.28	12.5	1.2-1.4	$\pm$10
50	102.20	7.5	1.1-1.3	$\pm$5
51	126.11	8.0	1.2-1.4	$\pm$5

Table 8. Summary of Details From Figures 44 to 51.

of 1.3, the oscillations diminished in magnitude until at M = 1.92 they represented only ± 2% of the mean ST_{FC}/ST_0. The minimum ST_{FC}/ST_0, occurring at M = 1.3, amounts to a 35% reduction in the local Stanton number from the non-film-cooled, dry-wall condition. However, for values up to M = 2.15, the value of ST_{FC}/ST_0 was always less than 1.0, showing approximately a 9% reduction in the heat flux for 1.8 < M < 2.15. The minimum Stanton number ratio which is observed for each $(x-x_i)/d_0$ occurs at a particular value of the blowing ratio, designated hereafter as the "optimum blowing ratio", M_{OPT}. The term $M_{OPT,NEAR}$ may be introduced in later discussions to describe the optimum blowing ratio found at the heat flux measurement location nearest to the coolant holes (i.e. smallest $(x-x_i)/d_0$).

Two least-squares representations of the data are shown in Fig. 44 as the solid line for the regions 0 < M < 1.3 and 1.3 < M < 2.14. Two curve fits were used to more accurately describe the data in each of these regions. Both curve fits represent the averaged data within ± 5%.

At $(x-x_i)/d_0$ = 22.20, Fig. 45 shows that ST_{FC}/ST_0 decreases in a monatonic fashion with increasing M. The lowest Stanton number ratio occurred at M = 2.15, the highest blowing ratio investigated for Case I. The ST_{FC}/ST_0 level out to M = 2.15 is higher than at $(x-x_i)/d_0$ = 10.45 for all M values being some 40% higher at M = 1.3 and 10% higher at M = 2.15. The least-squares curve fit represents the data within ± 5.5%.

Similar results for $(x-x_i)/d_0$ values from 42.55 to 126.11 are given in Figs. 46 to 51. In each of these figures, the value of ST_{FC}/ST_0 decreases with increasing M to an optimum value of $M(M_{OPT})$ corresponding to the lowest recorded film cooled Stanton number. All the locations

from $(x-x_i)/d_0$ = 42.55 to 126.11 exhibit a minimum ST_{FC}/ST_0 at a value of M similar to that at $(x-x_i)/d_0$ = 10.45. Following M_{OPT} a subsequent rise in ST_{FC}/ST_0 occurs with increasing M but never exceeds the value of 1.0 for values of M up to 2.15. Table 8 presents a summary of the significant details of Figs. 44 to 51 indicating the value of M at which film cooling was most effective (M_{OPT}) and the percent reduction from ST_0 at M_{OPT}. Between $(x-x_i)/d_0$ of 42.55 and 126.11 minimum values of ST_{FC}/ST_0 at M_{OPT} corresponded to a 7.5% to 13.5% reduction from ST_0. A general trend of lower percentage reductions from ST_0 with increased distance from injection was noted. Least-squares representations of the data were within ± 5% or ± 10%.

The results for Case II are shown in Figs. 52 to 58, representing heat flux measurements at $(x-x_i)/d_0$ from 11.54 to 114.37 for film coolant injection at x_i/L_S = 0.150 with β = 18° (see Table 6). Figure 52 shows ST_{FC}/ST_0 values as a function of M at $(x-x_i)/d_0$ = 11.54. The Stanton number ratio decreases with increasing M up to M ≈ 1.05, thus defining the value of M_{OPT} at which ST_{FC}/ST_0 was a minimum. This value of M_{OPT} was established by obtaining least-squares curve fits of the data using two separate linear functions. A smooth transition between the two functions was constructed consistent with the trend established by the data to give M_{OPT} ≈ 1.05. In the region M > 1.05, ST_{FC}/ST_0 increases, reaching a level of 0.97 at M = 2.37. Within this range of M, mean values of ST_{FC}/ST_0 represent actual levels that are ± 9% of the mean. The minimum value of ST_{FC}/ST_0, occurring at M_{OPT} = 1.05, amounts to a 38% reduction from ST_0 due to film cooling. The least-squares curves represent the average data within ± 10%.

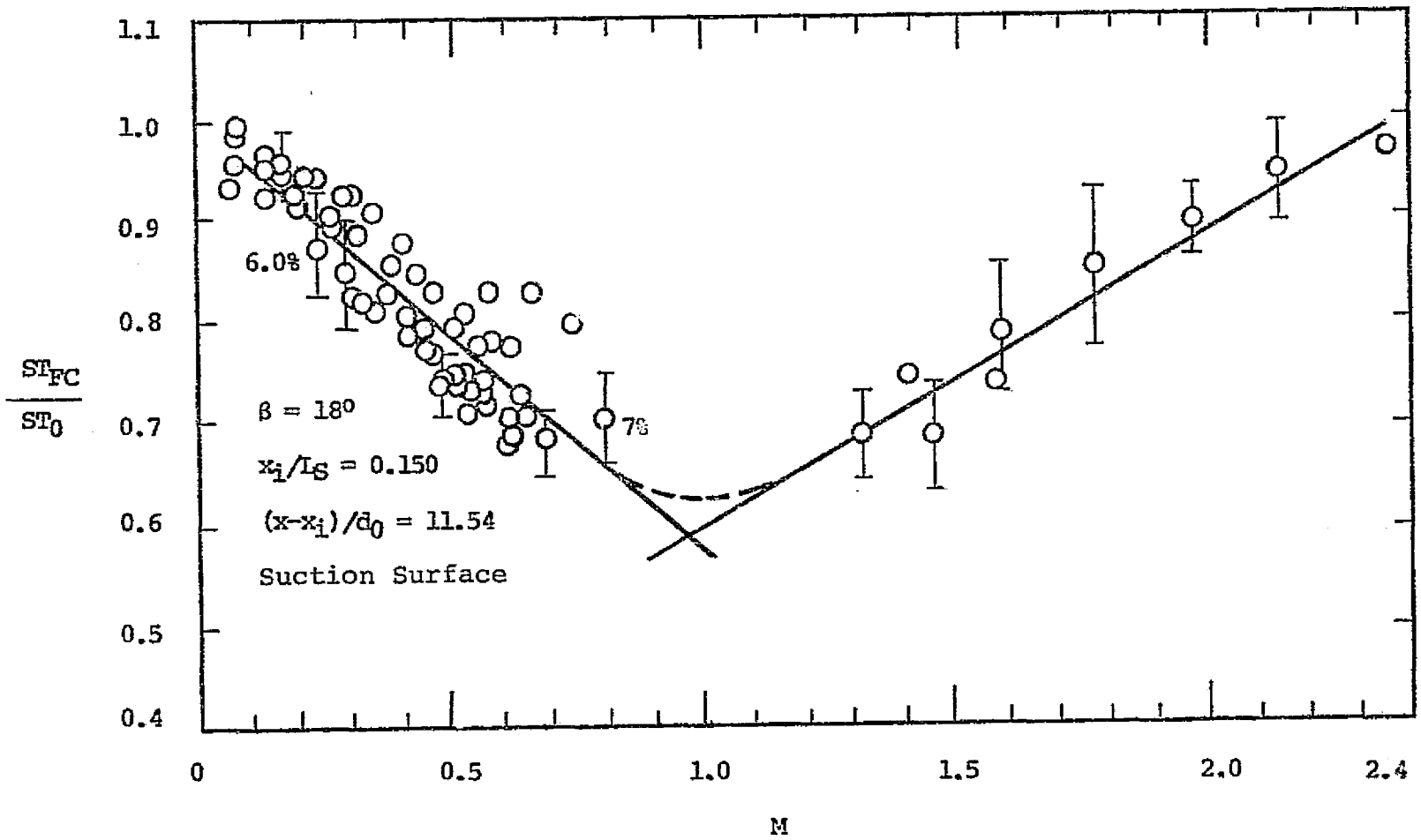

Figure 52. Film Cooling Stanton Number Ratio Variation With M, Case II, $(x-x_i)/d_0 = 11.54$.

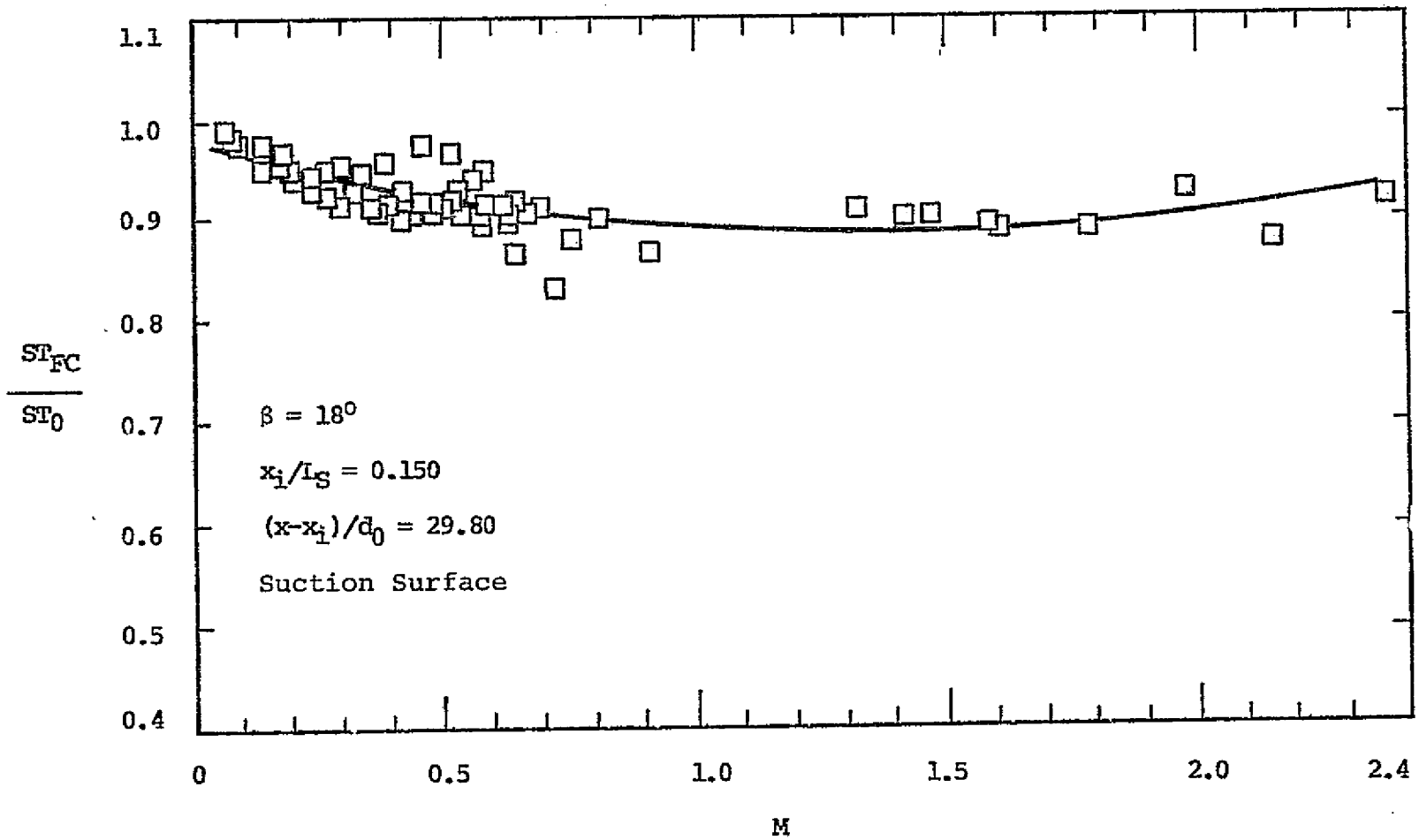

Figure 53. Film Cooling Stanton Number Ratio Variation With M, Case II, $(x-x_i)/d_0 = 29.80$.

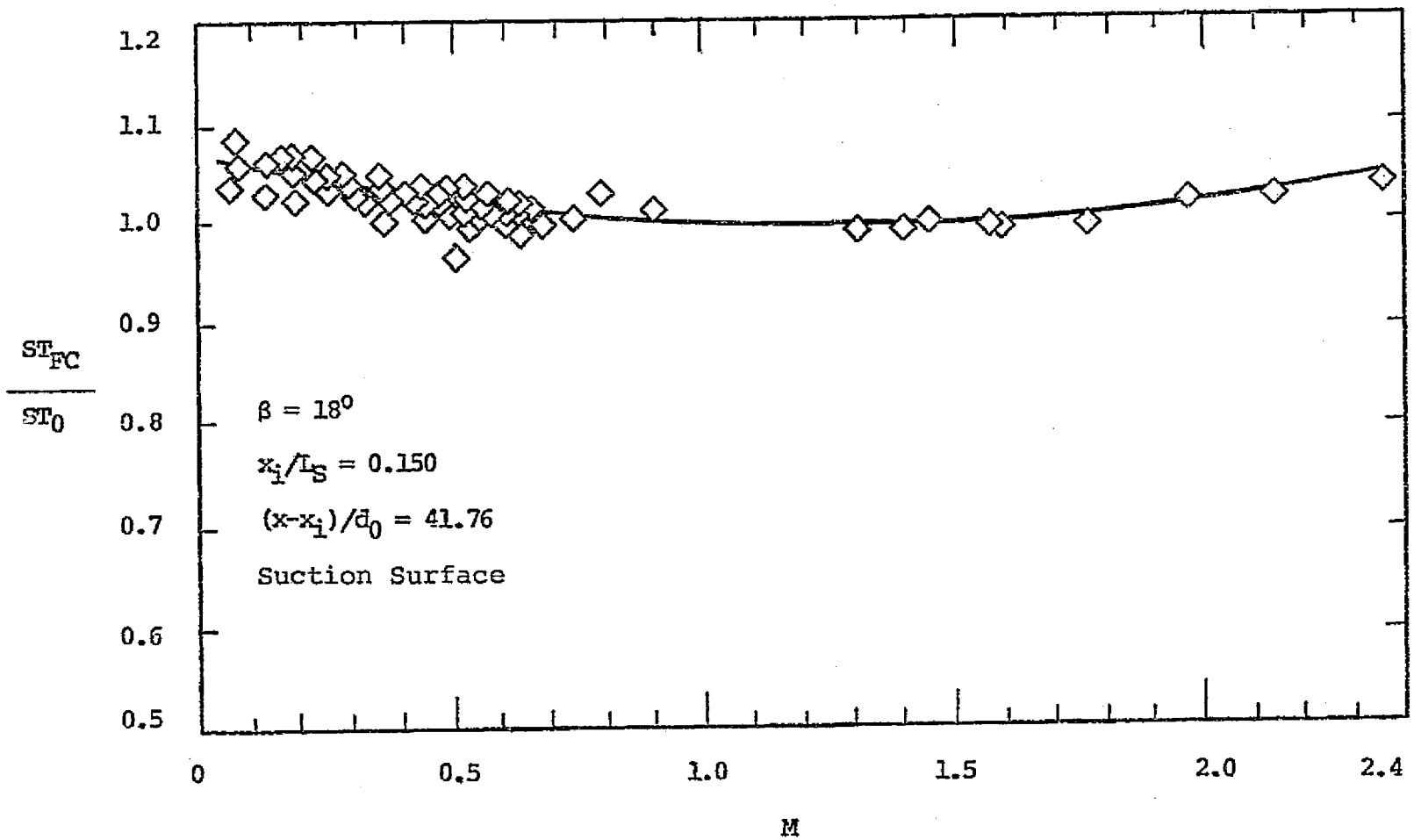

Figure 54. Film Cooling Stanton Number Ratio Variation With M, Case II, $(x-x_i)/d_0 = 41.76$.

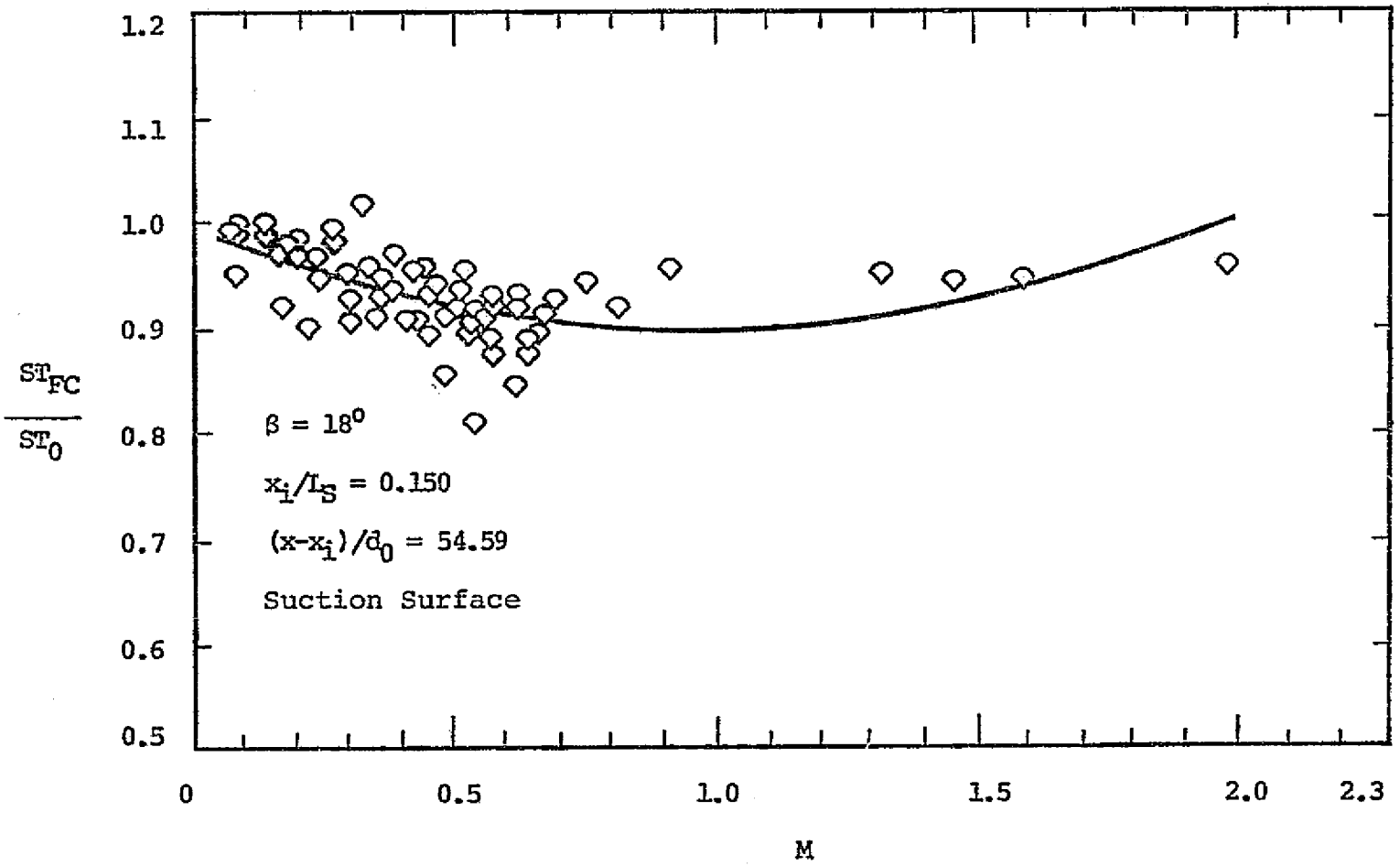

Figure 55. Film Cooling Stanton Number Ratio Variation With M, Case II, $(x-x_i)/d_o = 54.59$.

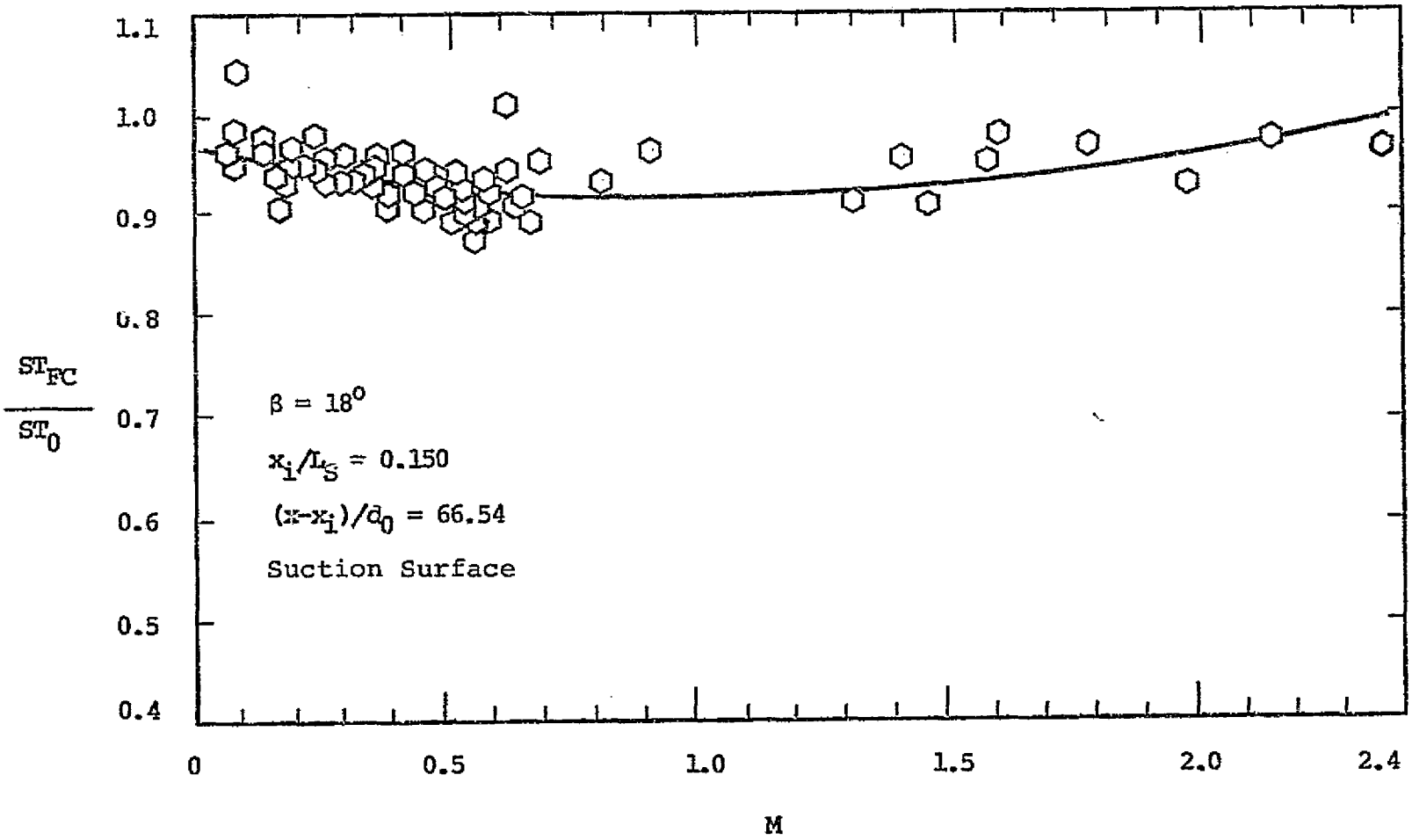

Figure 56. Film Cooling Stanton Number Ratio Variation With M, Case II, $(x-x_i)/d_0 = 66.54$.

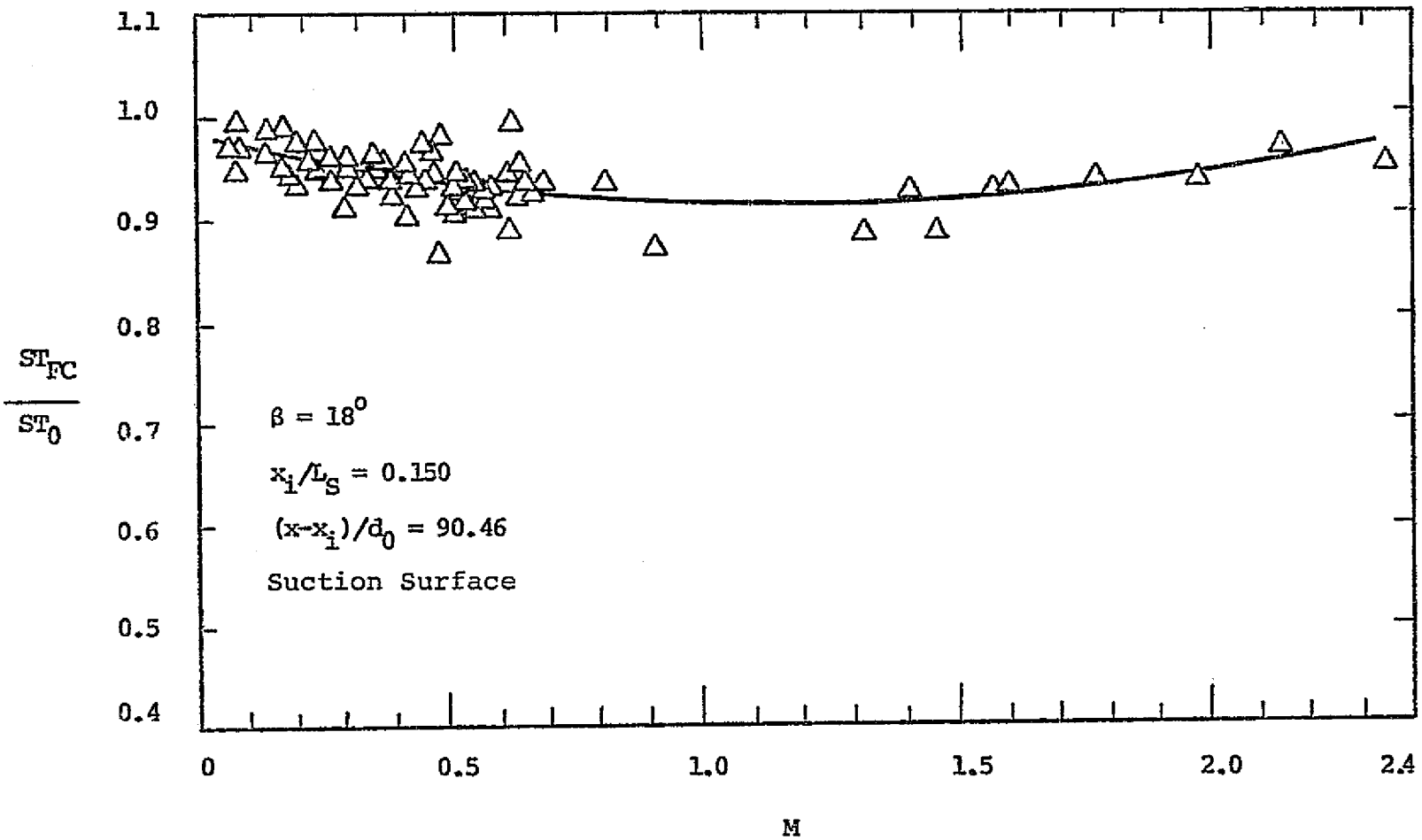

Figure 57. Film Cooling Stanton Number Ratio Variation With M, Case II, $(x-x_i)/d_0 = 90.46$.

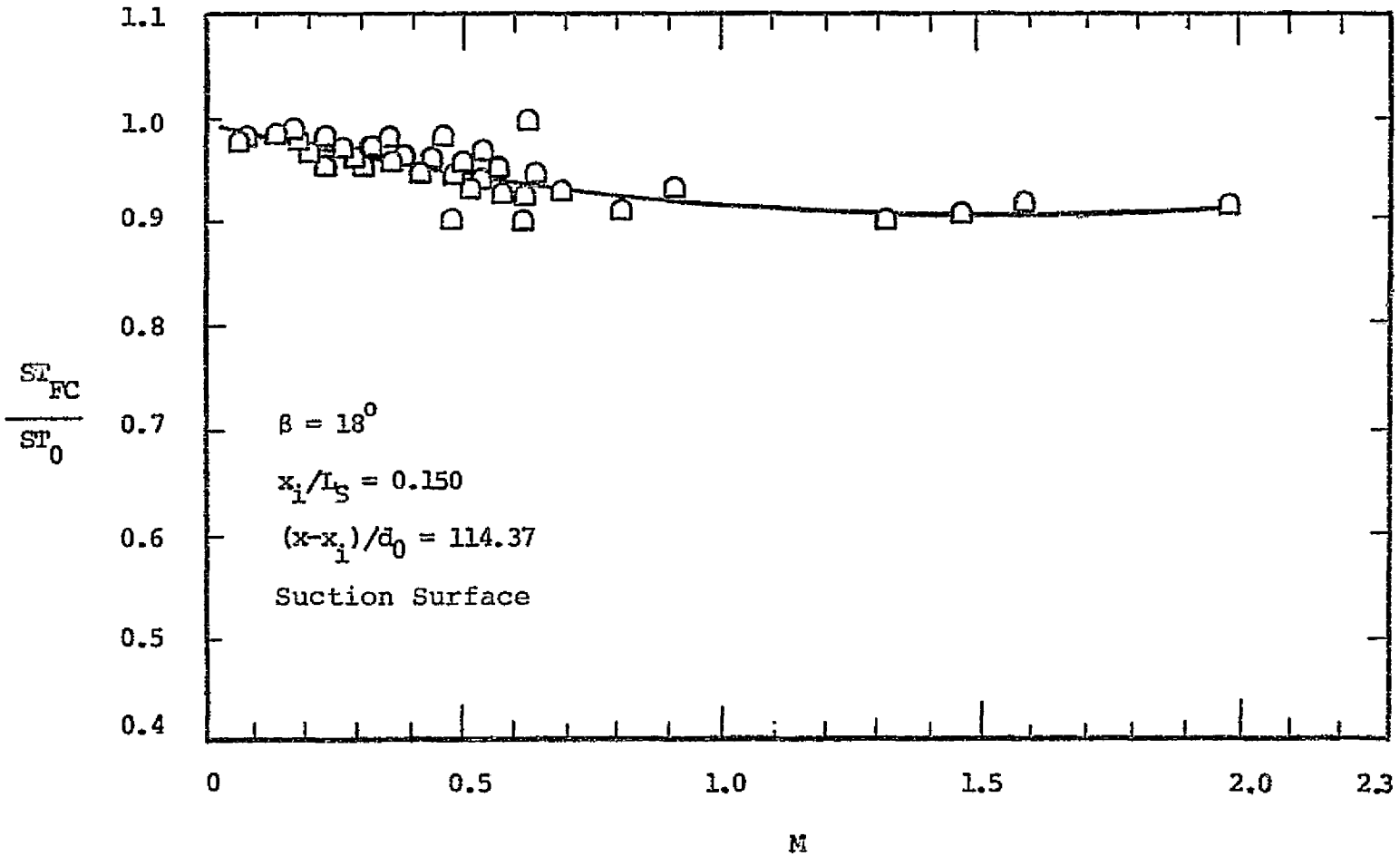

Figure 58. Film Cooling Stanton Number Ratio Variation With M, Case II, $(x-x_i)/d_0 = 114.37$.

CASE II

Figure	$(x-x_i)/d_0$	% Reduction in ST_0	M_{OPT}	% Deviation From Least-Squares
52	11.54	38	1.0	±10
53	29.80	11.5	1.2-1.5	±10
54	41.76	10.5	1.2-1.5	±5
55	54.59	10.0	1.0-1.2	±10
56	66.54	8.5	1.0-1.2	±10
57	90.46	9.0	1.1-1.3	±10
58	114.37	9.5	1.4-1.6	±5

Table 9. Summary of Details From Figures 52 to 58.

Table 9 lists the percentage reduction from ST_0 at each M_{OPT} for $(x-x_i)/d_0$ between 29.8 and 114.37 with the results for these remaining downstream locations of Case II presented in Figs. 53 to 58. For these figures ST_{FC}/ST_0 decreases to a minimum value for increasing M up to M_{OPT}. M_{OPT} for these locations has been defined within a range rather than a specific value due to the gradual trend of the data. For $(x-x_i)/d_0$ increasing from 11.54 the percentage reduction of ST_0 due to film cooling at $M = M_{OPT}$ decreases from 38% to approximately 9%. The range of values of M_{OPT} noted for $(x-x_i)/d_0 = 29$ to 114 bracket the value of M_{OPT} determined for the location nearest injection ($M_{OPT,NEAR}$). The range of M_{OPT} for each $(x-x_i)/d_0 > 11.54$ was determined from the least-squares curve fit which represented average ST_{FC}/ST_0 values within ± 5% and ± 10%.

The data for Case III with injection at $x_i/L_S = 0.228$ and $\beta = 18°$ are presented in Figs. 59 through 63 with a summary of the details listed in Table 10. Values of ST_{FC}/ST_0 are shown as a function of M for $(x-x_i)/d_0$ from 16.29 to 100.85. Figure 59 shows that at $(x-x_i)/d_0 = 16.29$ the Stanton number ratio decreases with increasing M up to $M_{OPT} = 0.50$. At this value of the blowing ratio the value of ST_{FC} was 16% lower than ST_0. For $M > M_{OPT}$, ST_{FC}/ST_0 increases with M and exceeds unity at an M value of approximately 1.55. Thus, for $M > 1.55$, the effects of film cooling were to increase the heat flux. As the blowing ratio exceeded $M_{OPT} = 0.5$, the measured heat flux began to oscillate with peak-to-peak levels which were larger than usual. The magnitude of these fluctuations is indicated in relation to the mean value of ST_{FC}/ST_0 by the vertical bands. The oscillations caused ST_{FC}/ST_0 to range from ± 7.5% to ± 12.5% of the mean.

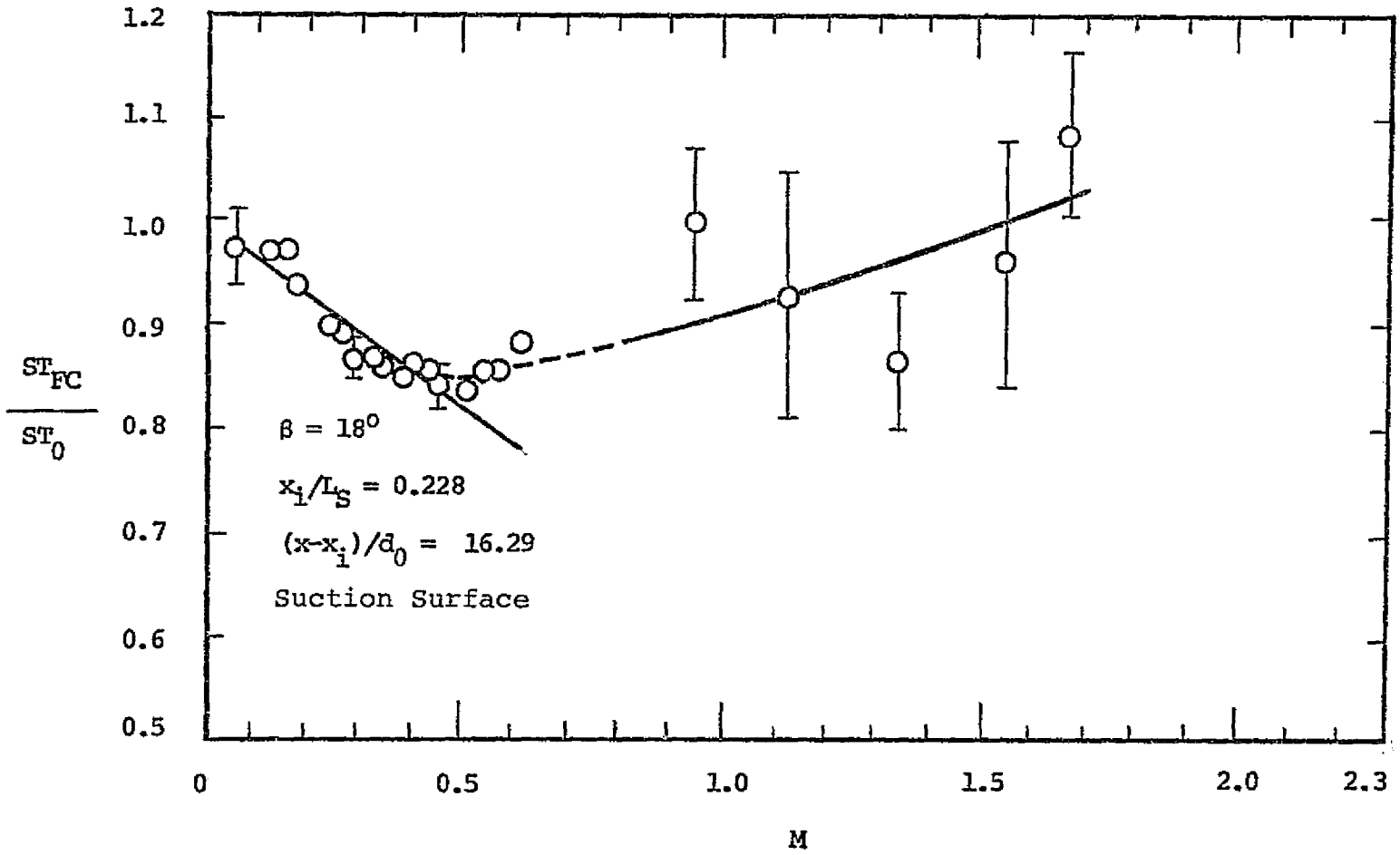

Figure 59. Film Cooling Stanton Number Ratio Variation With M, Case III, $(x-x_i)/d_0$ = 16.29.

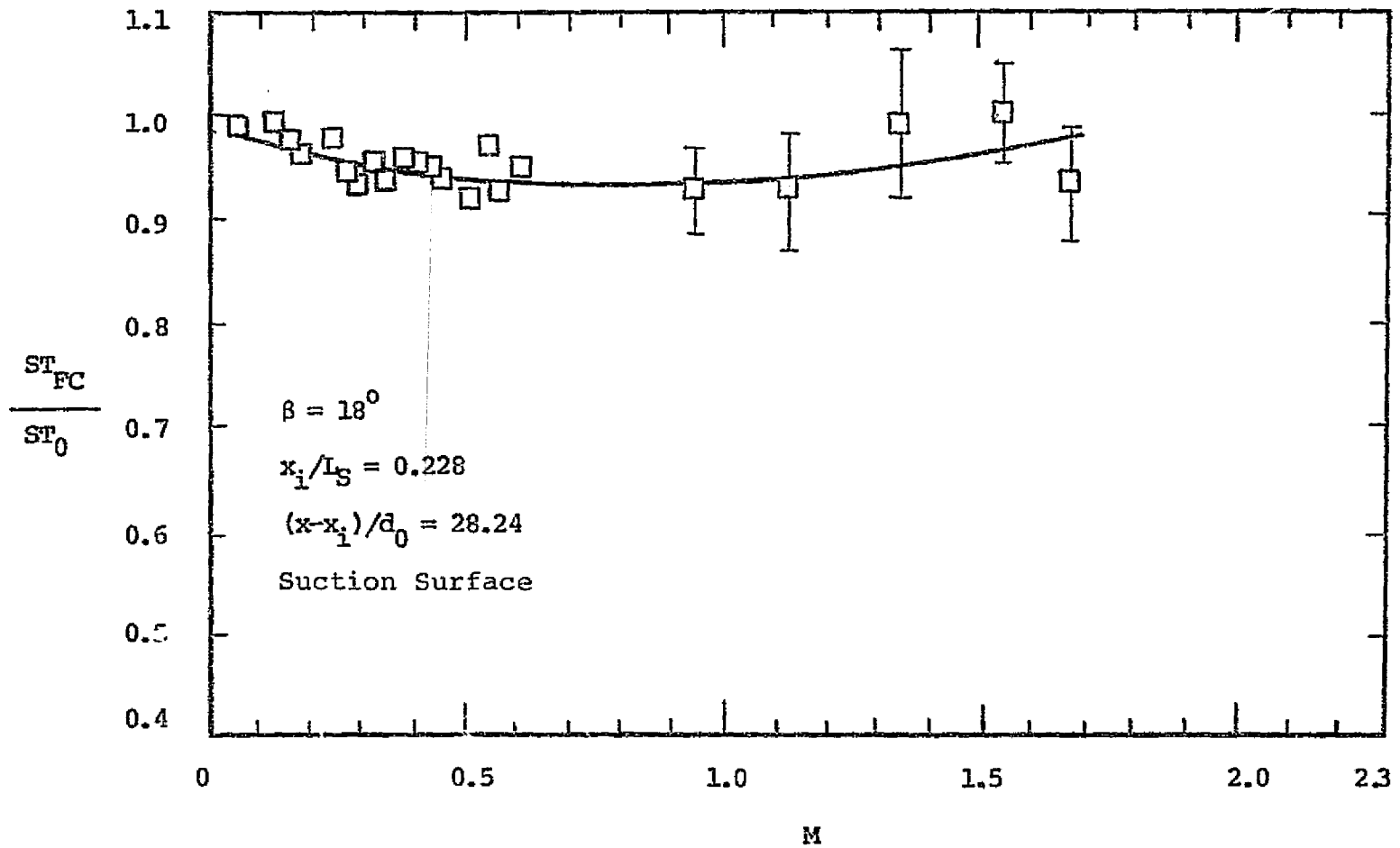

Figure 60. Film Cooling Stanton Number Ratio Variation With M, Case III, $(x-x_i)/d_0 = 28.24$.

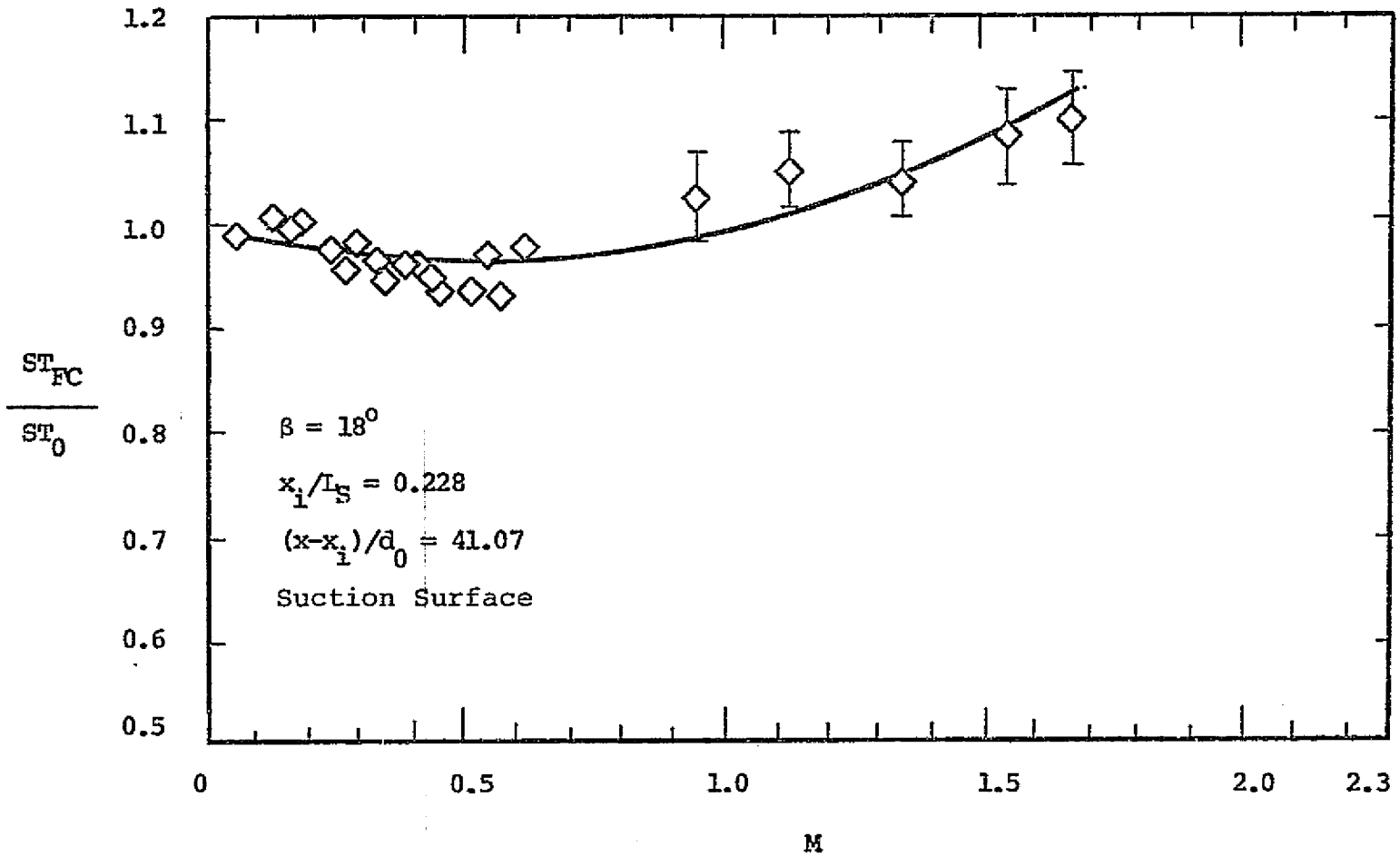

Figure 61. Film Cooling Stanton Number Ratio Variation With M, Case III, $(x-x_i)/d_0 = 41.07$.

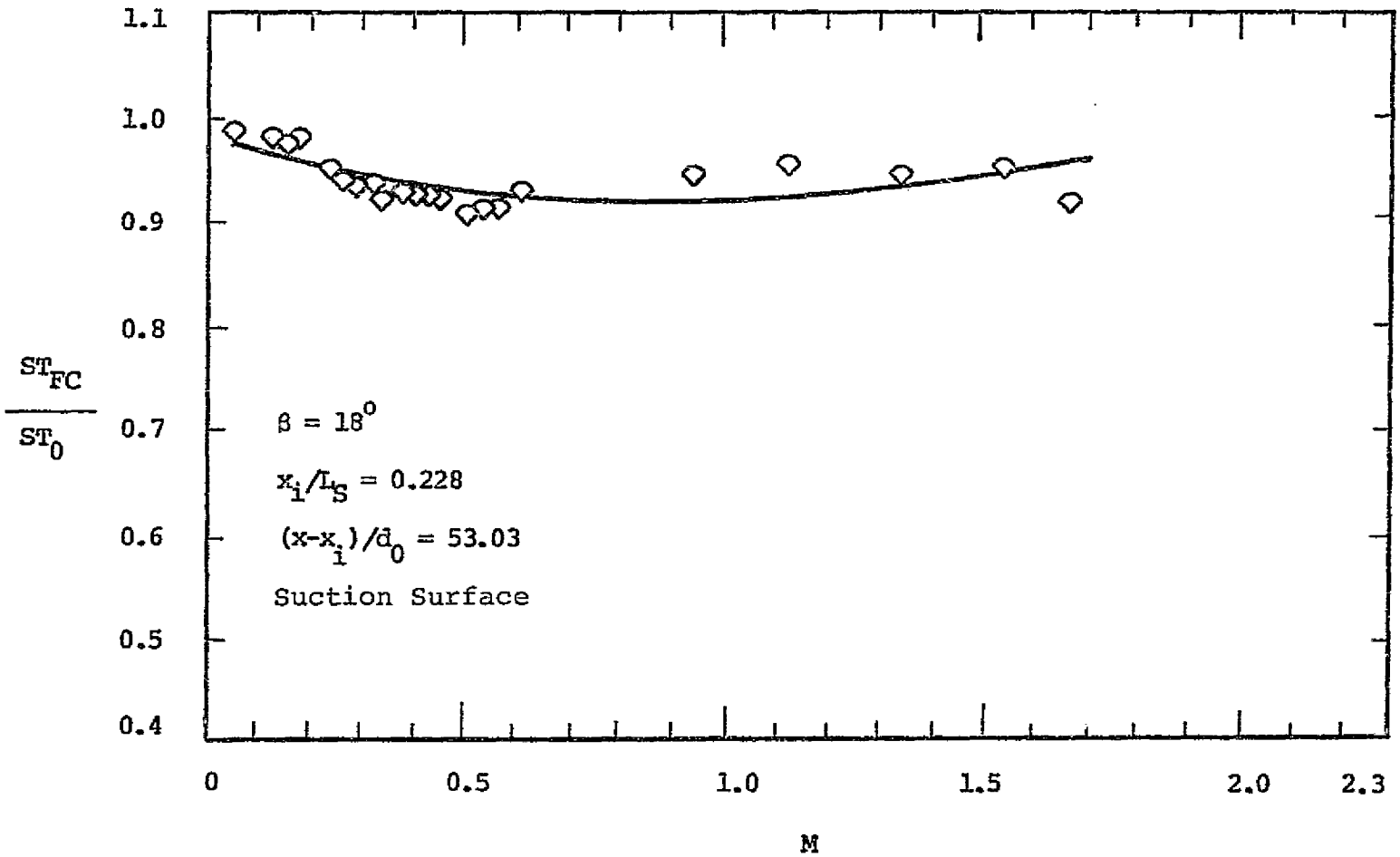

Figure 62. Film Cooling Stanton Number Ratio Variation With M, Case III, $(x-x_i)/d_0 = 53.03$.

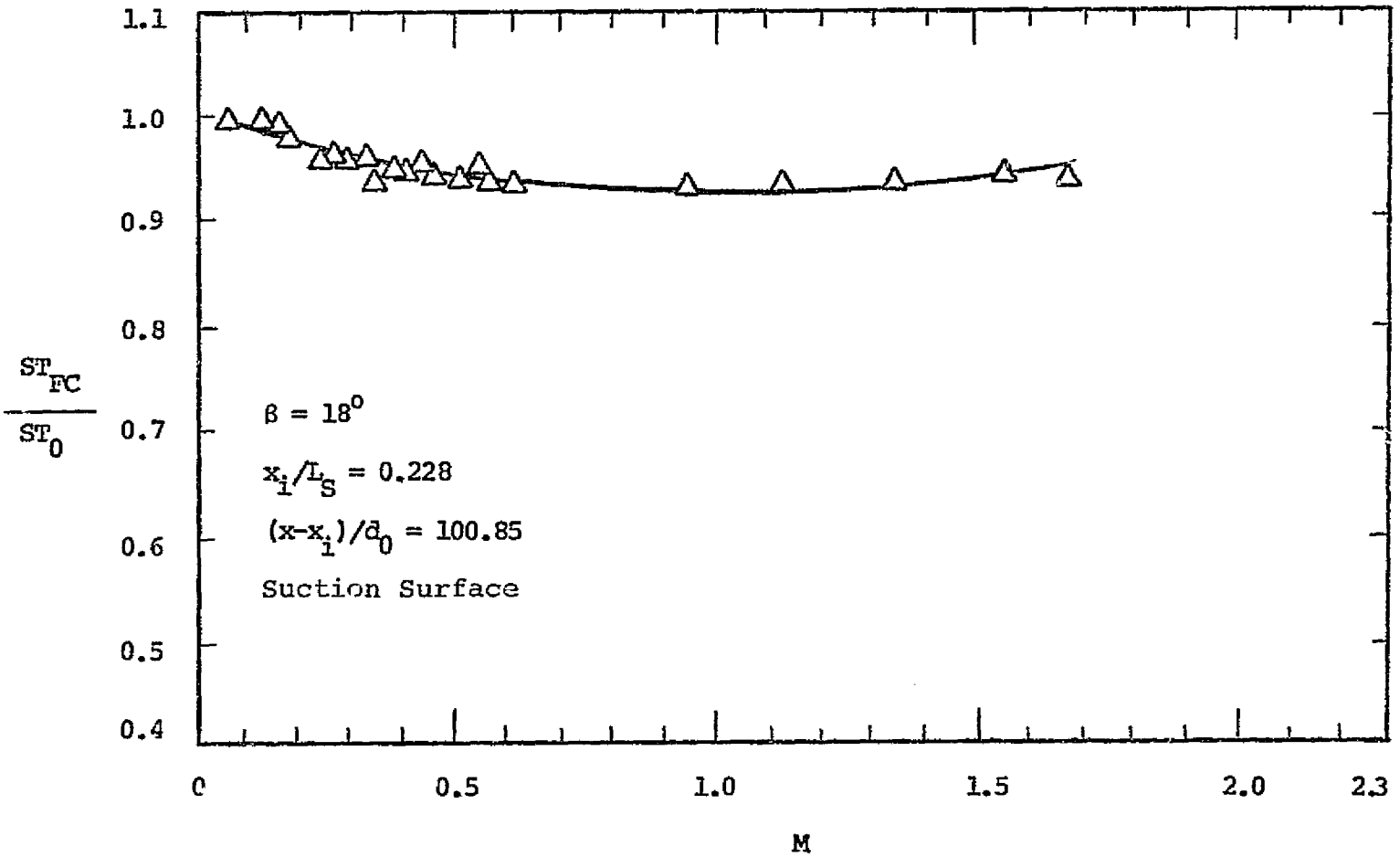

Figure 63. Film Cooling Stanton Number Ratio Variation With M, Case III, $(x-x_i)/d_0 = 100.85$.

CASE III

Figure	$(x-x_i)/d_0$	% Reduction in ST_0	M_{OPT}	% Deviation From Least-Squares
59	16.29	16	0.50	± 5 $M<M_{OPT}$ ± 25 $M>M_{OPT}$
60	28.24	7	0.8-1.0	± 11
61	41.07	4.5	0.50	± 6
62	53.03	8	0.8-1.0	± 5
63	100.85	7.5	0.8-1.0	± 2

Table 10. Summary of Details From Figures 59 to 63.

Figure 60, at $(x-x_i)/d_0 = 28.24$, shows ST_{FC}/ST_0 decreases up to M between 0.8 and 1.0. In this narrow M range, film cooling reduced the Stanton number 7%. For M > 1.0, ST_{FC} increases to within 2% of the value with no cooling at M = 1.67.

Farther downstream at $(x-x_i)/d_0 = 41.07$, Fig. 61 shows a greater dependency of ST_{FC}/ST_0 on M in the higher blowing ratio regions (M > 0.5) than at the previous location. A slight decrease in ST_{FC}/ST_0 was noted for M increasing to 0.5 at which point the ratio began to increase. At M = 0.5 a 4.5% reduction from ST_0 was measured. The rise in the Stanton number ratio for M increasing beyond 0.5 is rapid, yielding a value of 1.11 at M = 1.67.

The two measurement locations farthest from injection are presented in Figs. 62 and 63. At both locations a gradual ST_{FC}/ST_0 decrease with increasing M is shown out to a value near M = 1.0. At the highest M investigated (M = 1.67) a 5% reduction from ST_0 was measured at $(x-x_i)/d_0 = 53.03$. At the same value of M, a 7% reduction from ST_0 was noted for $(x-x_i)/d_0 = 100.85$.

Similar data with an injection angle of $\beta = 35°$ were obtained for $x_i/L_S = 0.0833$, 0.150 and 0.228. The data for Case IV with $\beta = 35°$ and $x_i/L_S = 0.0833$ are presented in Figs. 64 to 71 for $(x-x_i)/d_0$ from 10.45 to 126.11. It should be noted that the maximum value of M as shown in these figures varies from 0.88 to 2.30. The criterion for data qualification (see Appendix C) was not met in certain ranges of M for some heat flux gage locations and consequently the data for those ranges were discarded.

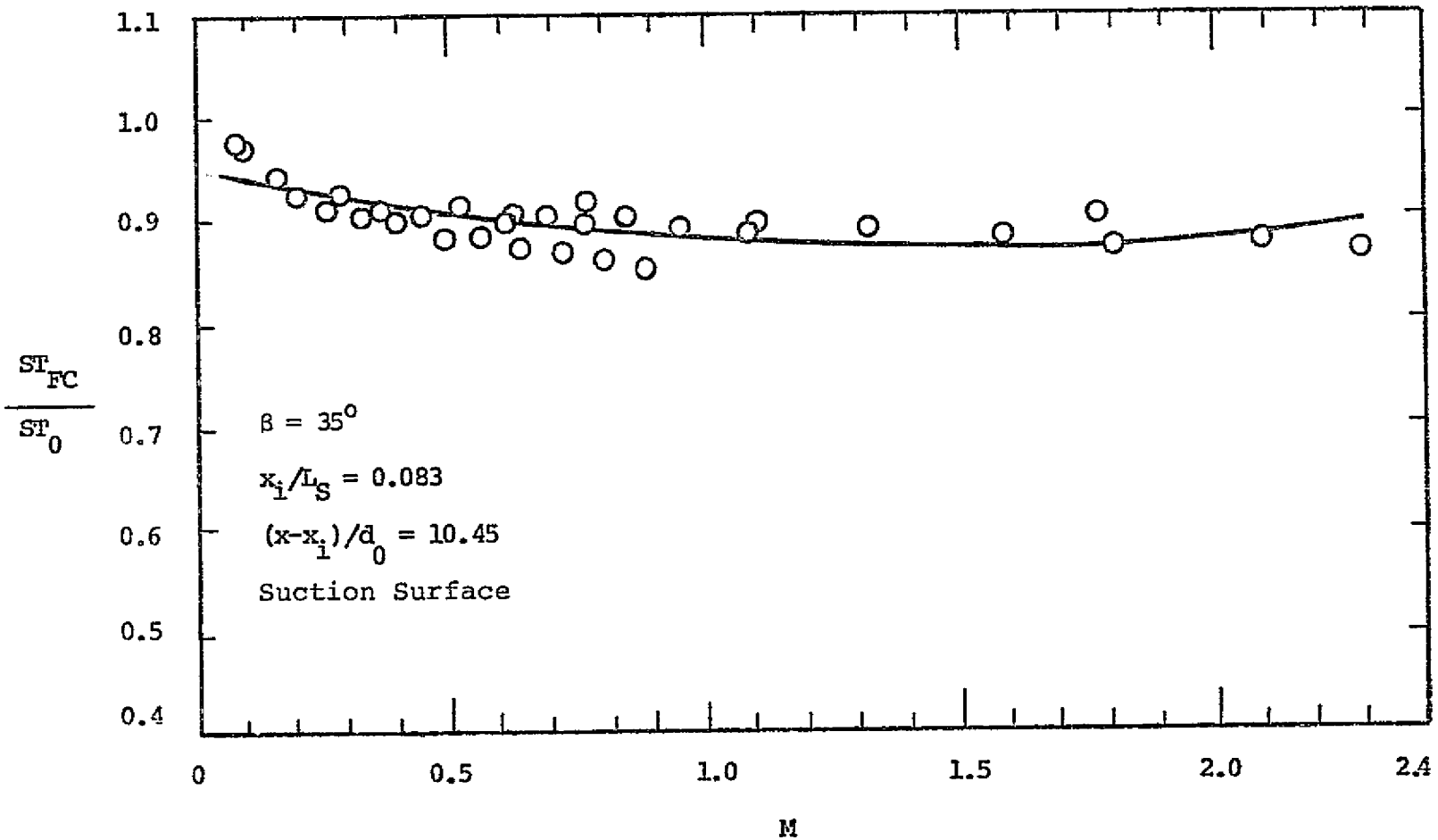

Figure 64. Film Cooling Stanton Number Ratio Variation With M, Case IV, $(x-x_i)/d_0 = 10.45$.

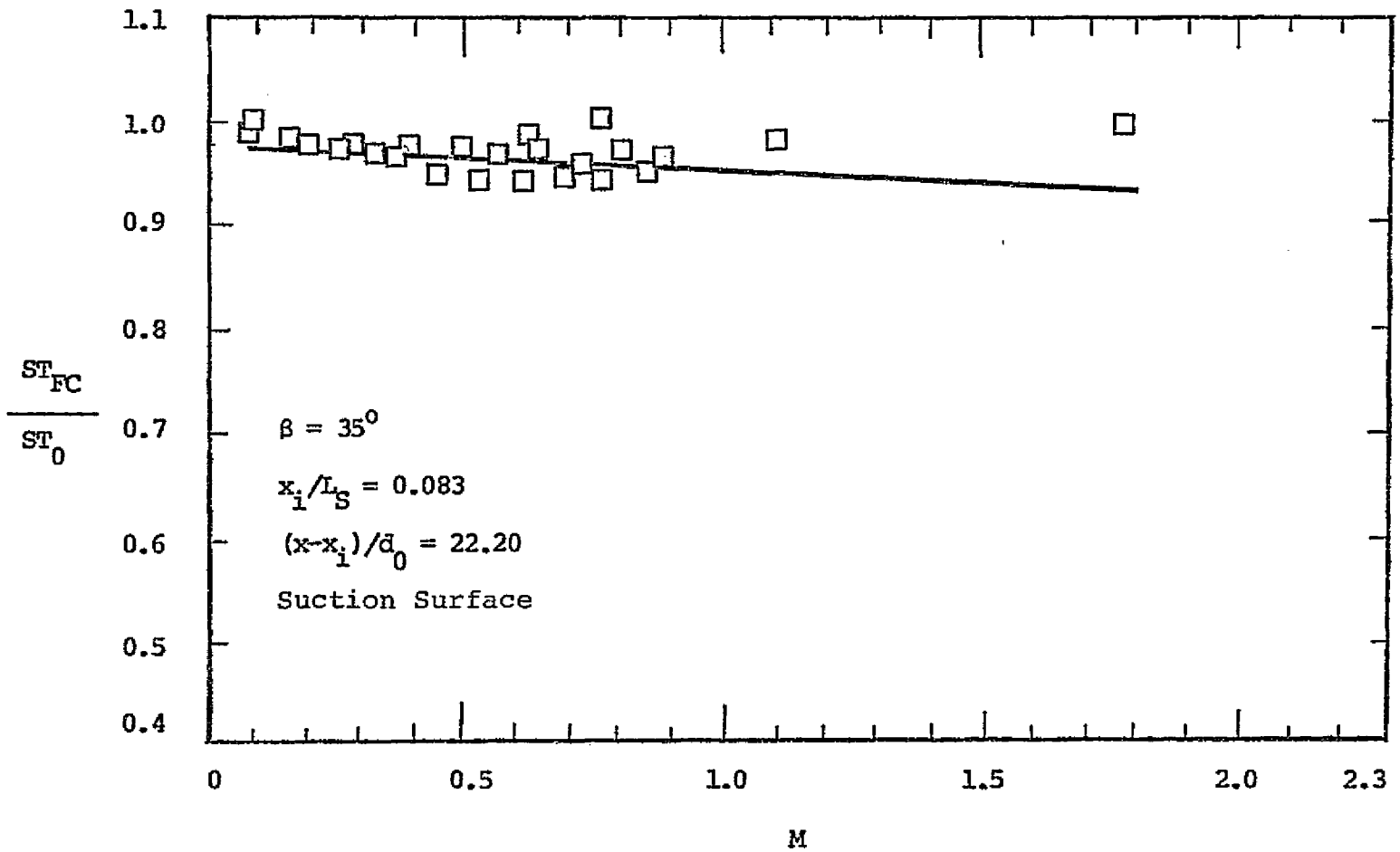

Figure 65. Film Cooling Stanton Number Ratio Variation With M, Case IV, $(x-x_i)/d_0$ = 22.20.

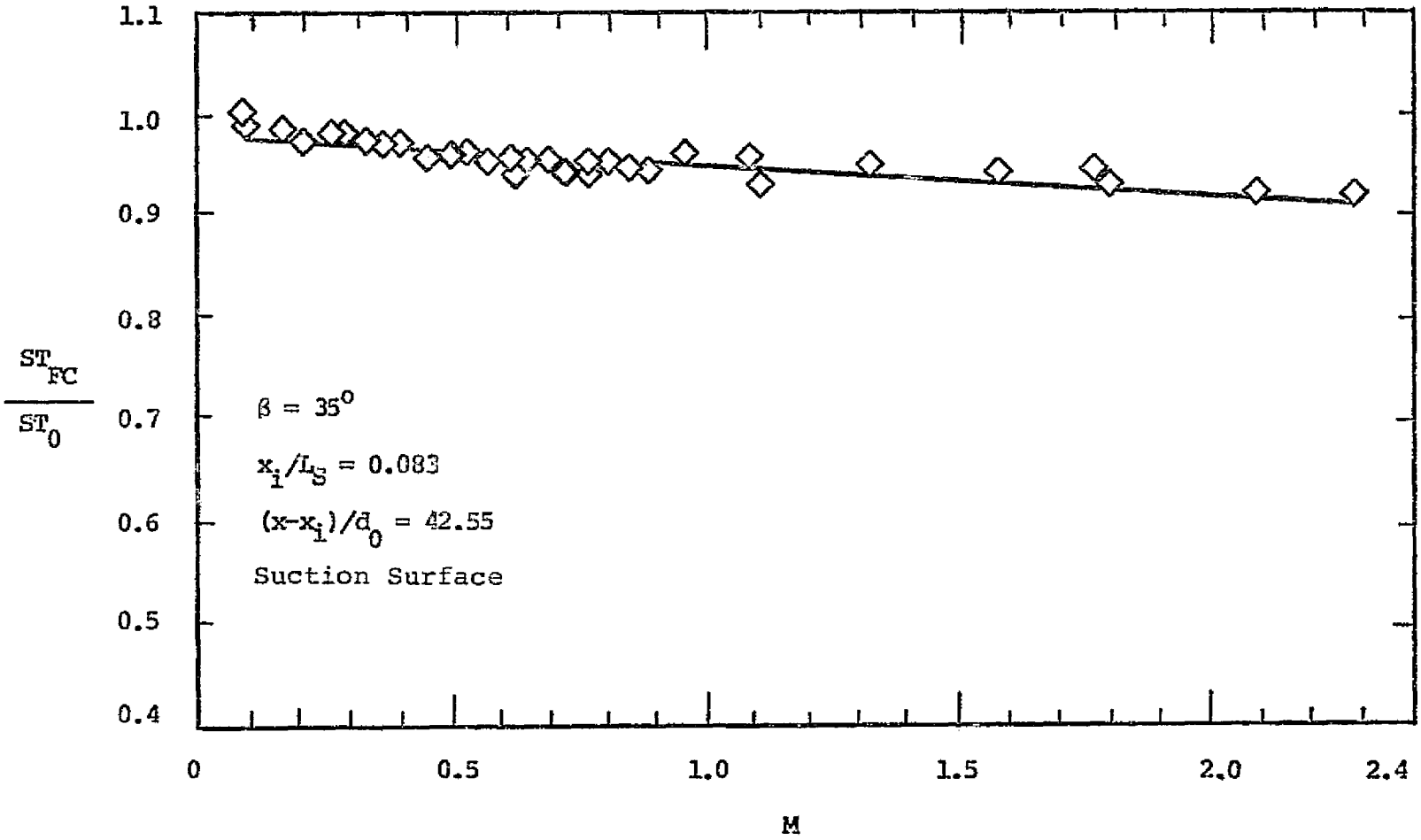

Figure 66. Film Cooling Stanton Number Ratio Variation With M, Case IV, $(x-x_i)/d_0 = 42.55$.

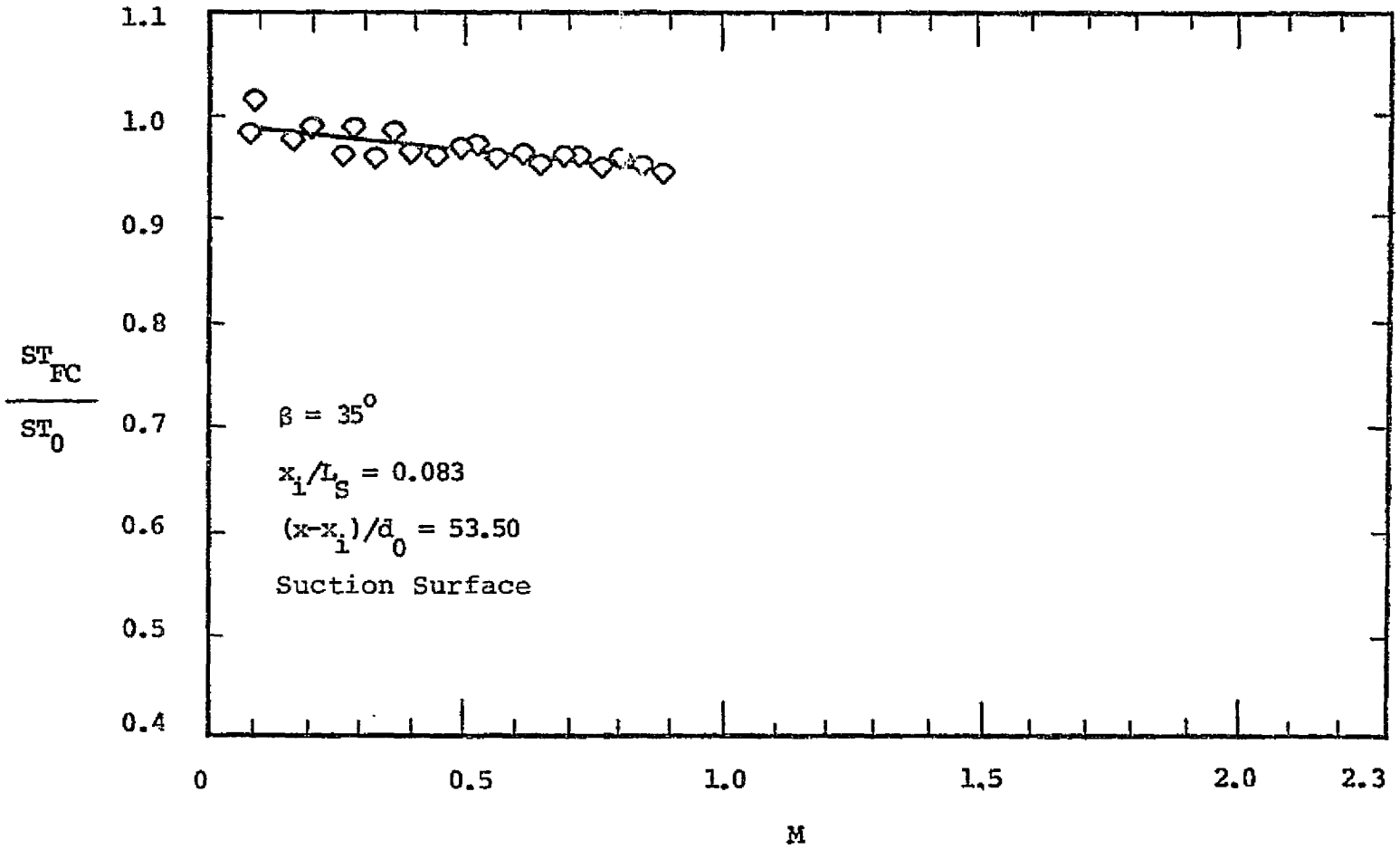

Figure 67. Film Cooling Stanton Number Ratio Variation With M, Case IV, $(x-x_i)/d_0 = 53.50$.

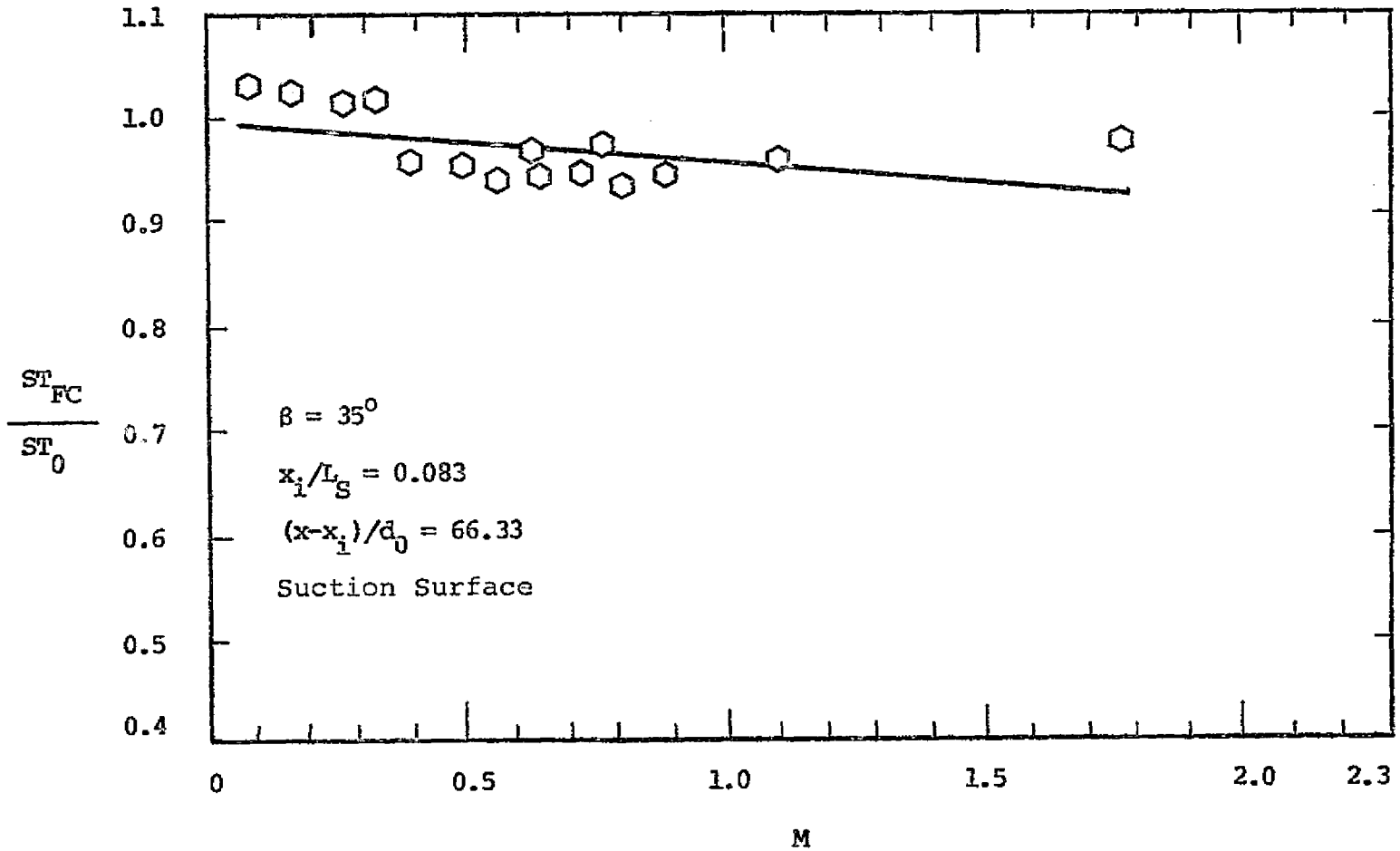

Figure 68. Film Cooling Stanton Number Ratio Variation With M, Case IV, $(x-x_i)/d_0 = 66.33$.

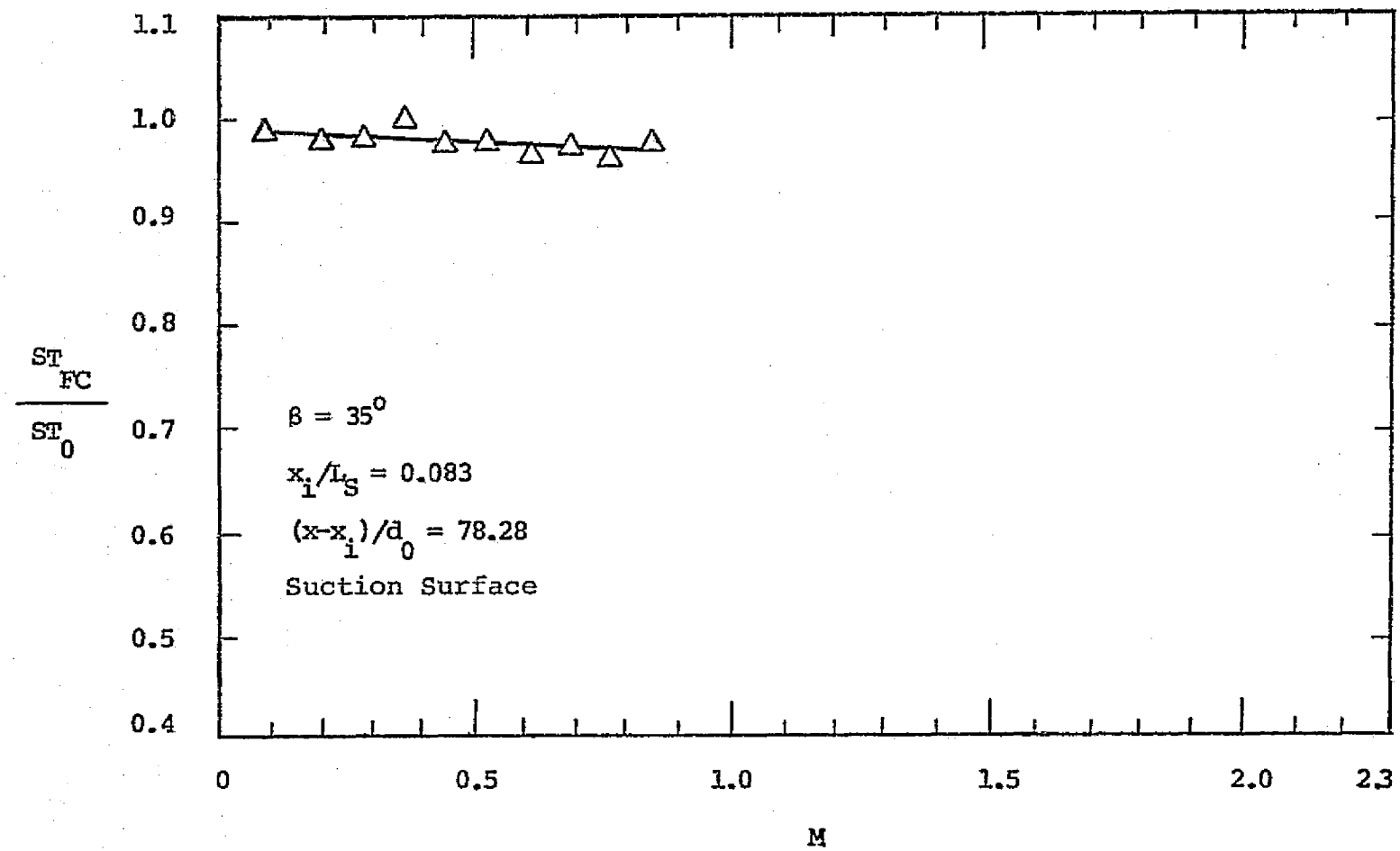

Figure 69. Film Cooling Stanton Number Ratio Variation With M, Case IV, $(x-x_i)/d_0 = 78.28$.

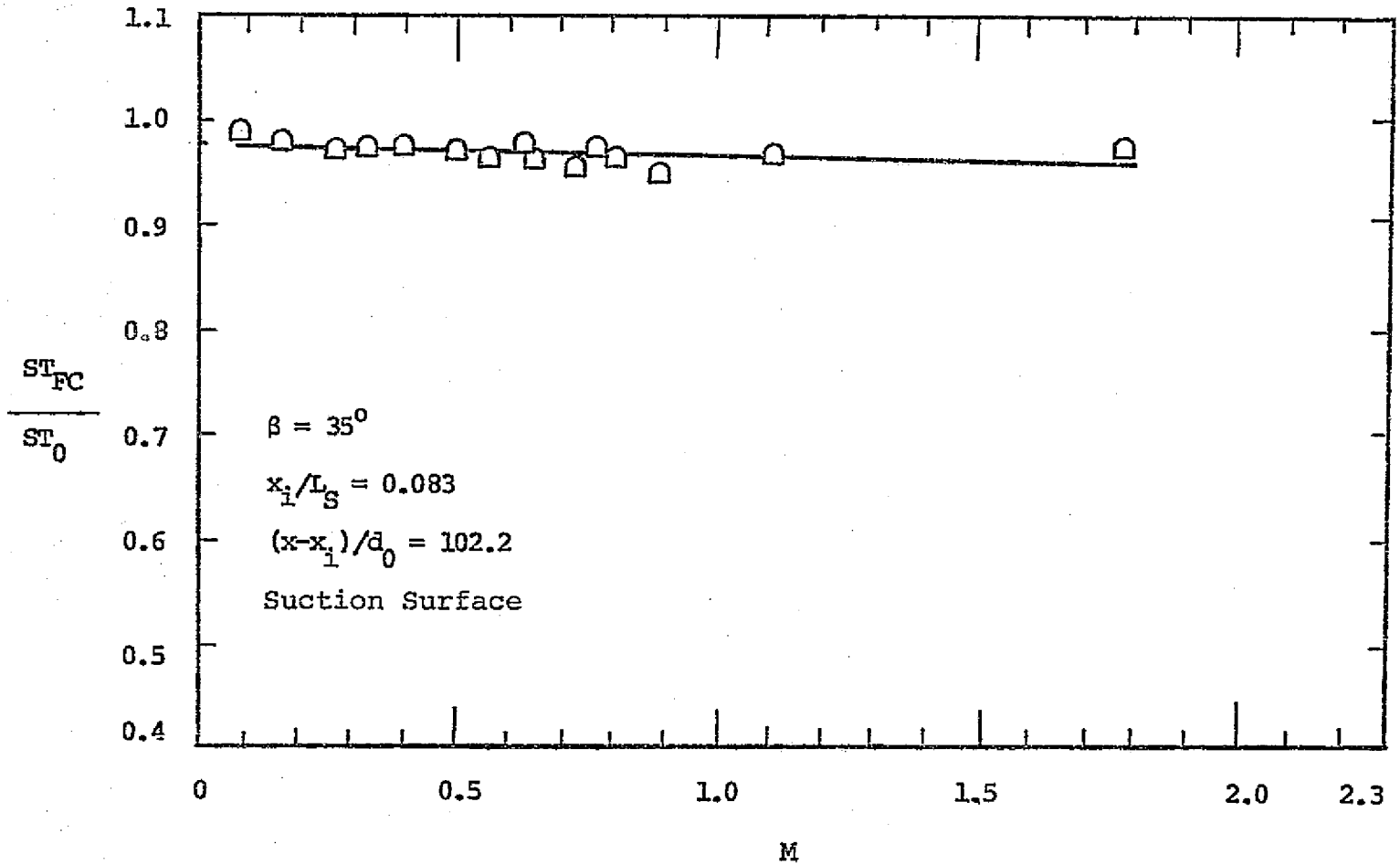

Figure 70. Film Cooling Stanton Number Ratio Variation With M, Case IV, $(x-x_i)/d_0 = 102.2$.

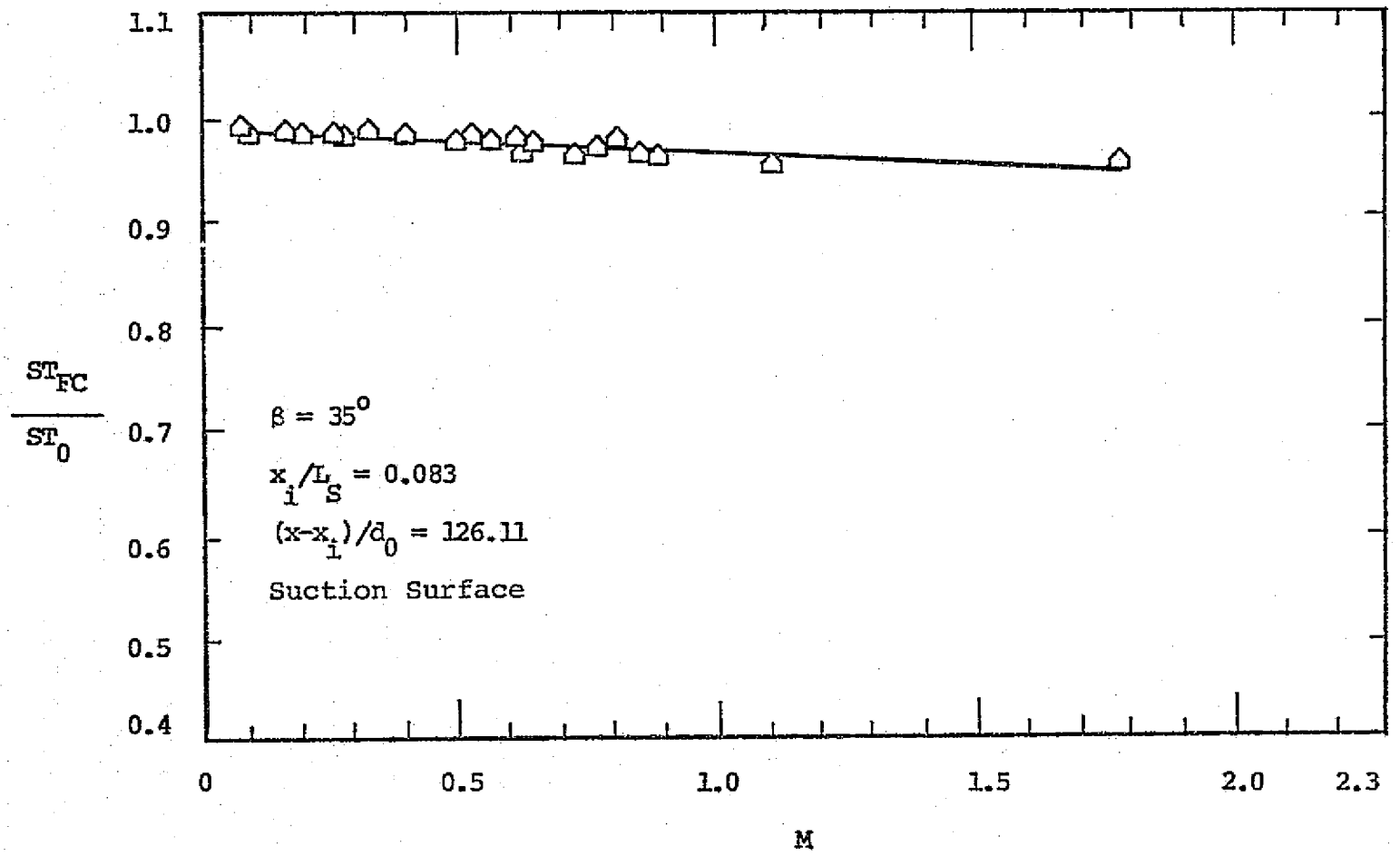

Figure 71. Film Cooling Stanton Number Ratio Variation With M, Case IV, $(x-x_i)/d_0 = 126.11$.

CASE IV

Figure	$(x-x)/d_0$	% Reduction in ST_0	M_{MAX}	% Deviation From Least-Squares
64	10.45	13	2.30	±5
65	22.20	7	1.78	±5
66	42.55	9	2.30	±5
67	53.50	5	0.88	±5
68	66.33	7	1.78	±5
69	78.28	3	0.85	±5
70	102.20	4	1.78	±3
71	126.11	5	1.78	±3

Table 11. Summary of Details From Figures 64 to 71.

Figure 64, at $(x-x_i)/d_0 = 10.45$, shows a gradual decrease in ST_{FC}/ST_0 for increasing M with no clear M_{OPT} apparent. Up to M = 2.3, the local Stanton number was reduced by 13% from ST_0. All the data is represented by a least-squares curve within ± 5%.

Similar results were found for Figs. 65 through 71 with Table 11 summarizing the important features for $(x-x_i)/d_0$ from 10.45 to 126.11. Up to the maximum M investigated, ST_{FC}/ST_0 showed a gradual decrease, with absolute levels dependent upon the value of $(x-x_i)/d_0$. Consequently, the maximum value of M is reported since no clear M_{OPT} was observed. For those locations in which ST_{FC}/ST_0 values were qualified up to M = 1.78, the Stanton number ratio varied from 0.93 at $(x-x_i)/d_0 = 22.2$ and 66.33 to values near 0.96 and 0.95 for $(x-x_i)/d_0 = 102.20$ and 126.11.

The results for Case V at $\beta = 35°$ and $x_i/L_S = 0.150$ are illustrated in Figs. 72 through 77. Figure 72 shows a reduction in the Stanton number ratio for increasing M at $(x-x_i)/d_0 = 11.54$. The minimum ST_{FC}/ST_0 value occurred at $M_{OPT} = 0.85$. At M_{OPT}, a 32% reduction from ST_0 was measured. For $M > M_{OPT}$, ST_{FC}/ST_0 rises to within 9% of ST_0 at M = 2.1. Two linear, least-squares representations of the data are illustrated with the data ± 5% about the line for $M < 0.8$ and ± 10% for $M > 0.8$.

Table 12 summarizes the results presented in Figs. 72 to 77. The figures show a general trend of a decreasing ST_{FC}/ST_0 with increasing M for all locations greater than $(x-x_i)/d_0 = 11.54$ with no obvious M_{OPT}. The lowest ST_{FC}/ST_0 occurs near the largest value of M investigated. At M = 2.1 the percent reduction from ST_0 due to film cooling ranged from 18% to 7.5%, decreasing as $(x-x_i)/d_0$ increases.

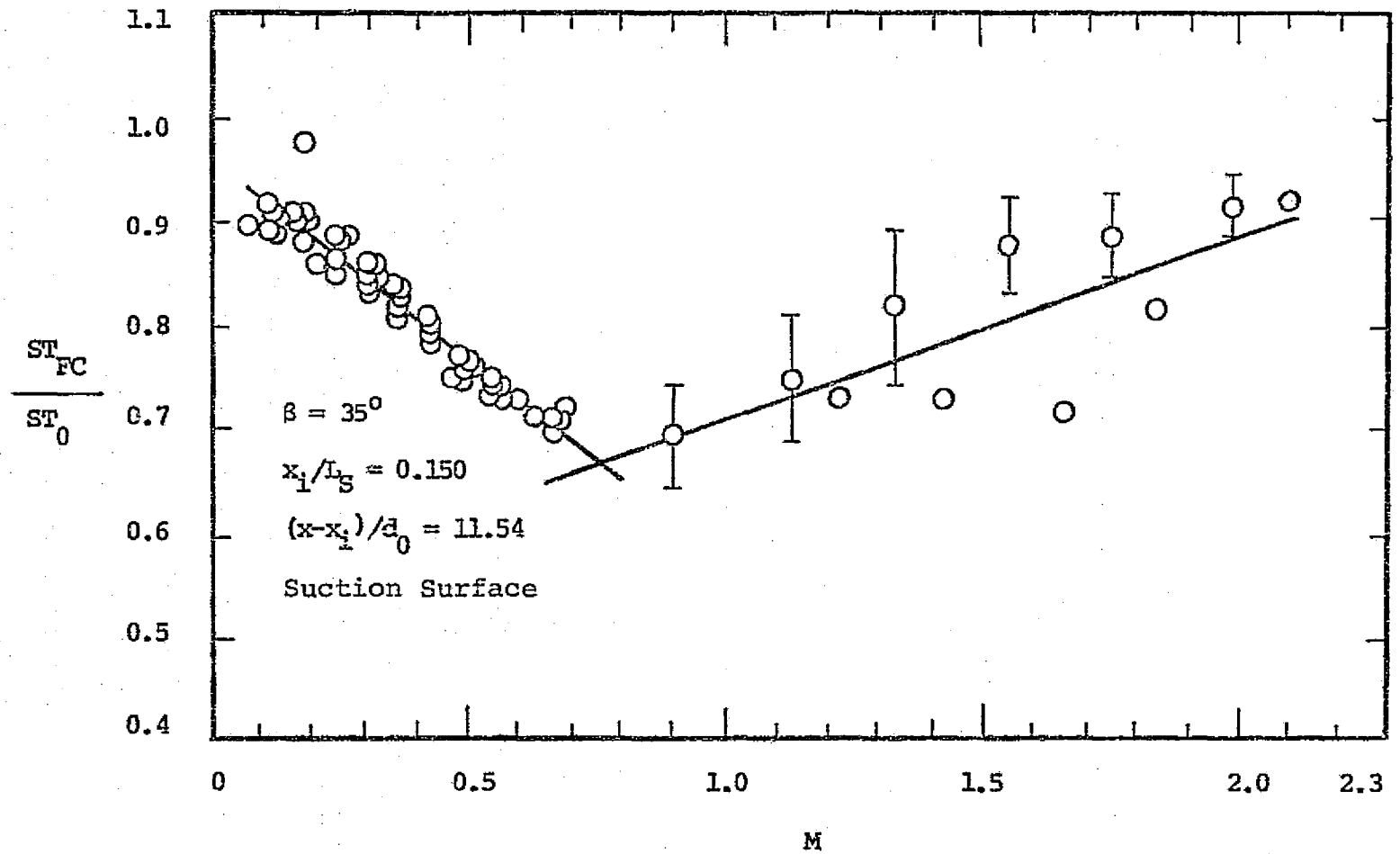

Figure 72. Film Cooling Stanton Number Ratio Variation With M, Case V, $(x-x_i)/d_0 = 11.54$.

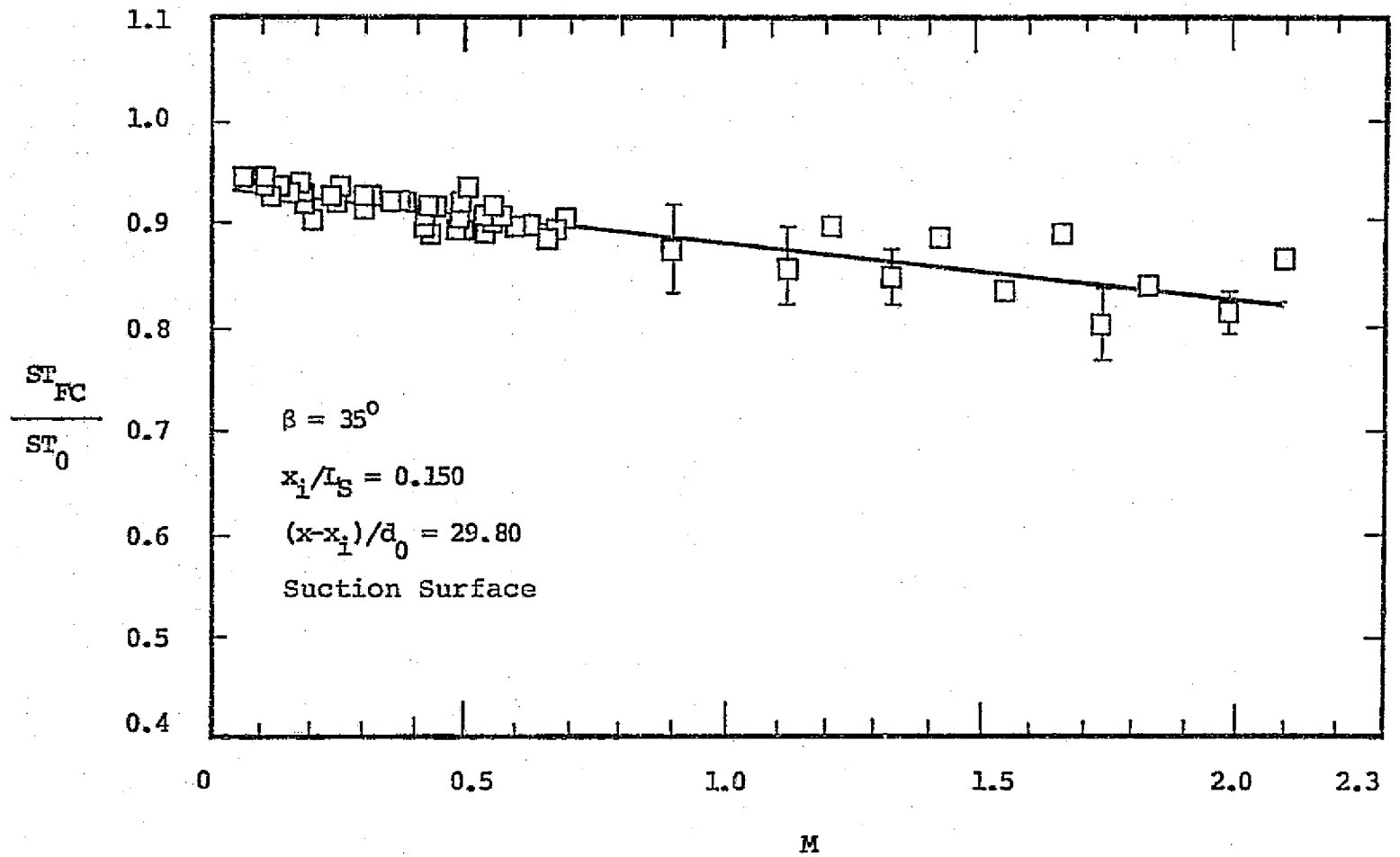

Figure 73. Film Cooling Stanton Number Ratio Variation With M, Case V, $(x-x_i)/d_0 = 29.80$.

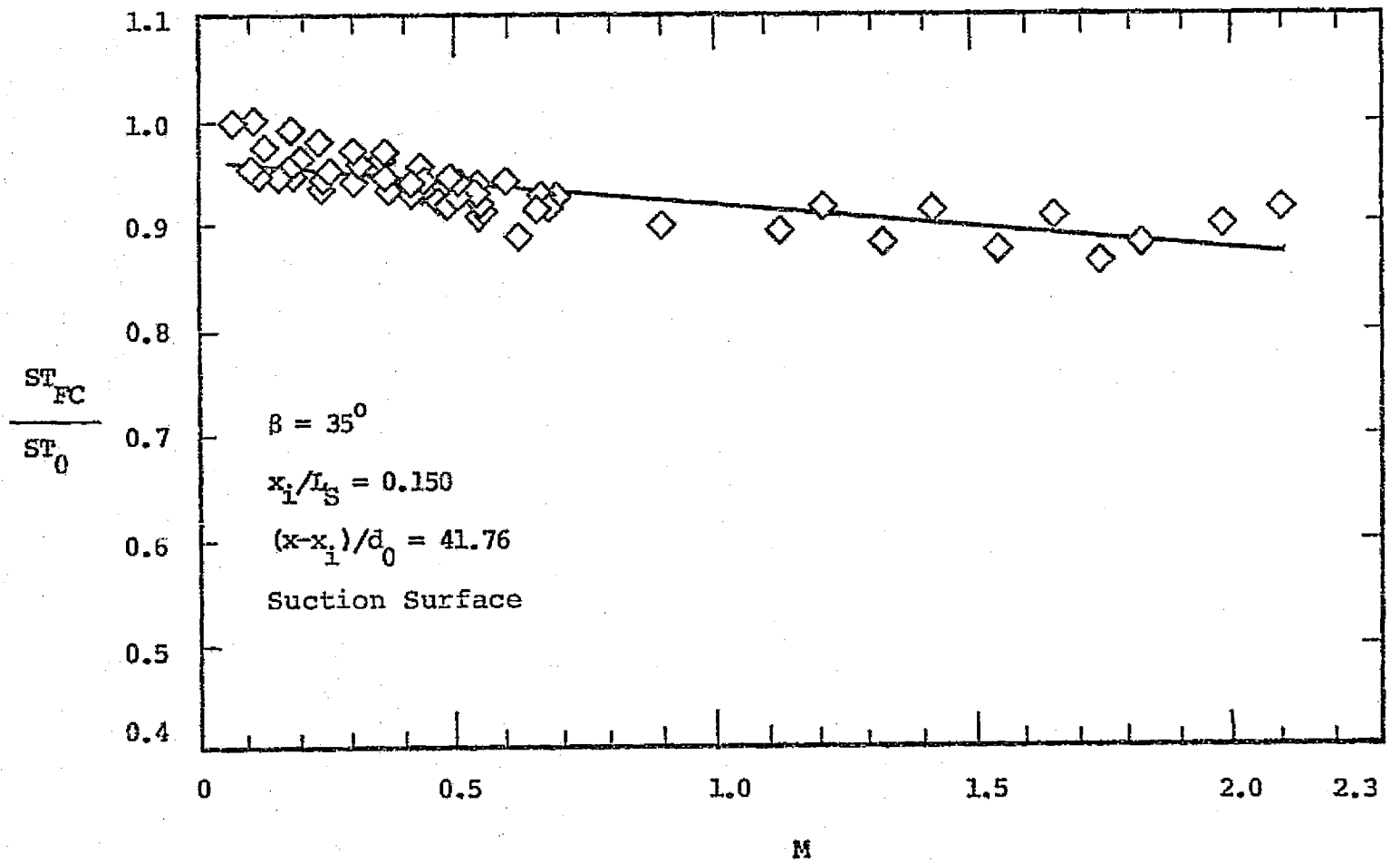

Figure 74. Film Cooling Stanton Number Ratio Variation With M, Case V, $(x-x_i)/d_0 = 41.76$.

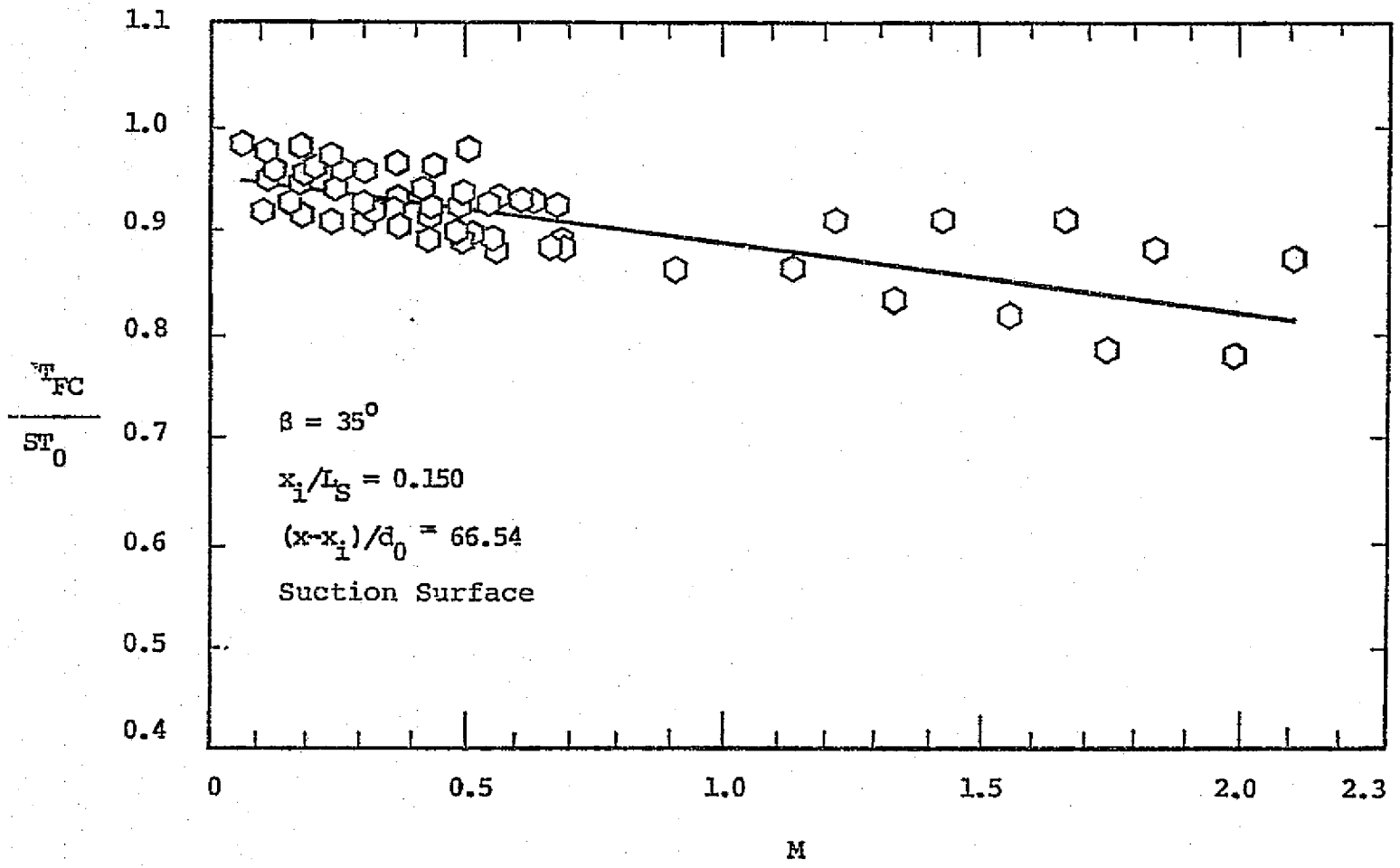

Figure 75. Film Cooling Stanton Number Ratio Variation With M, Case V, $(x-x_i)/d_0 = 66.54$.

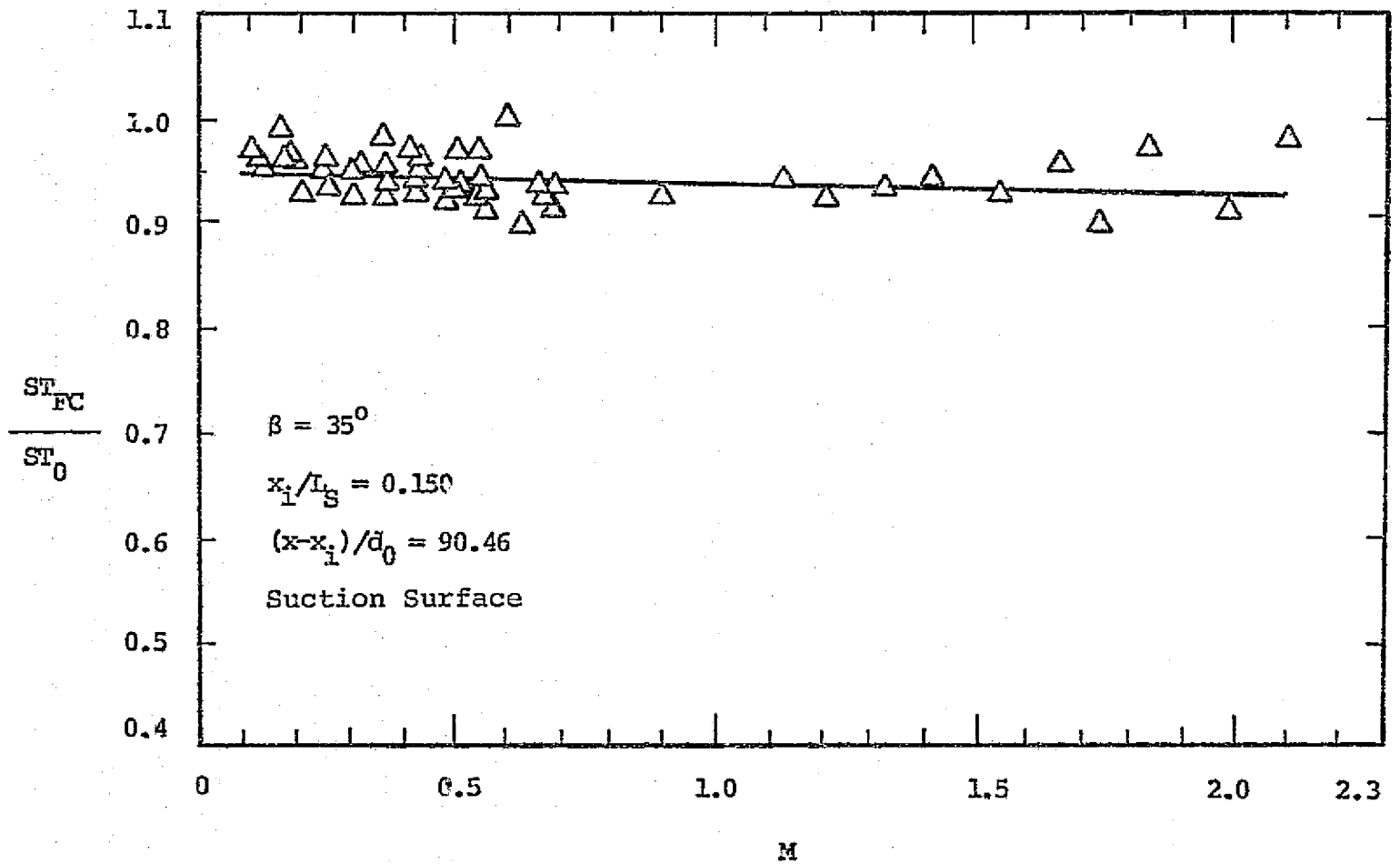

Figure 76. Film Cooling Stanton Number Ratio Variation With M, Case V, $(x-x_i)/d_0 = 90.46$.

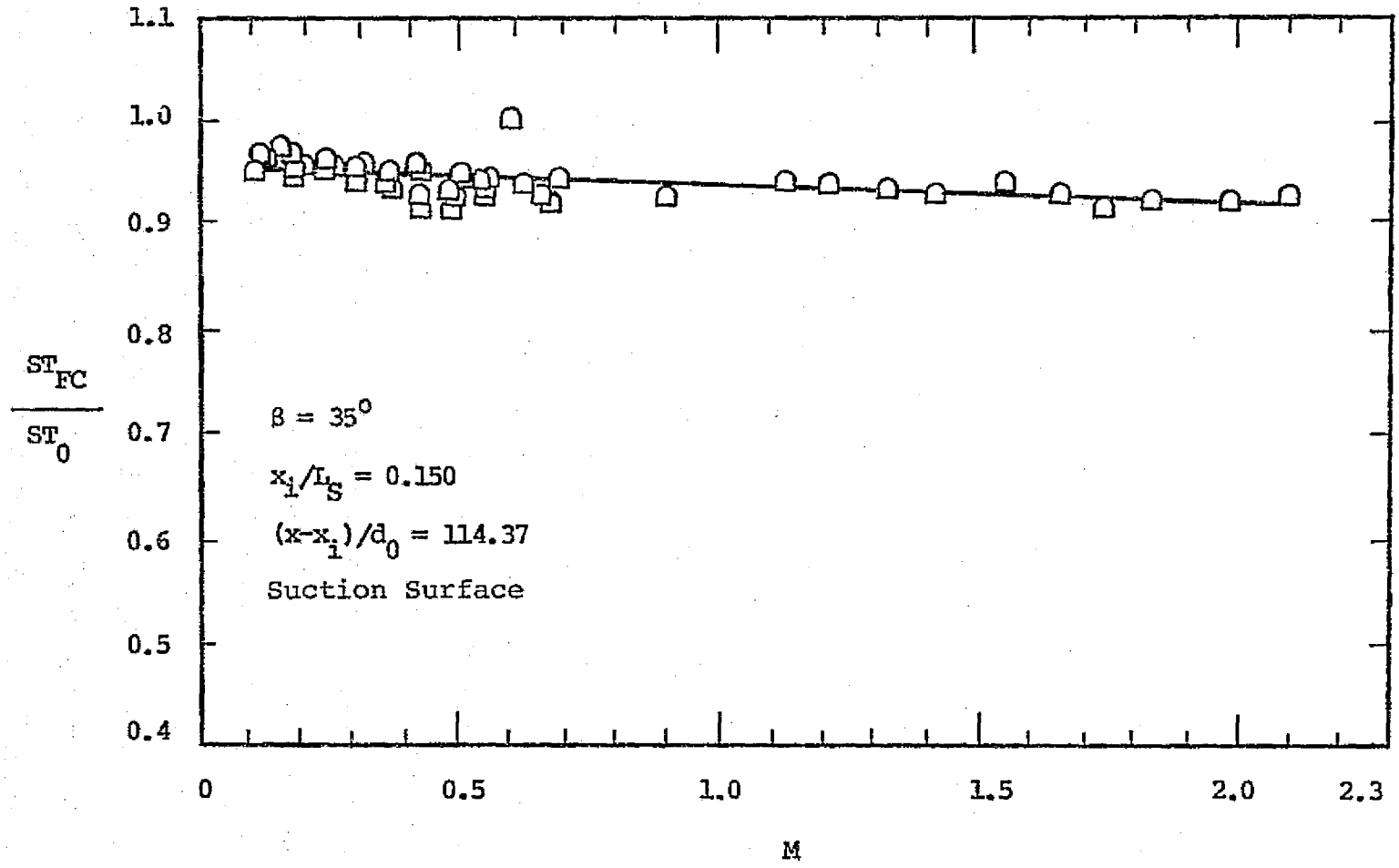

Figure 77. Film Cooling Stanton Number Ratio Variation With M, Case V, $(x-x_i)/d_0 = 114.37$.

CASE V

Figure	$(x-x_i)/d_0$	% Reduction in ST_0	M_{MAX}, M_{OPT}	% Deviation From Least-Squares
72	11.54	32	$0.8(M_{OPT})$	± 5, ± 10
73	29.80	18	2.1	± 5
74	41.76	13	2.1	± 5
75	66.54	15	2.1	± 7
76	90.46	7.5	2.1	± 7
77	114.37	8.0	2.1	± 5

Table 12. Summary of Details From Figures 72 to 77.

Measurements of the local heat flux were taken with and without film cooling for Case VI of the suction surface and Cases VII through XII for the pressure surface. The variation of ST_0 for these cases during the course of investigating a range of coolant conditions was such that the data qualification criterion was not satisfied. Consequently, no film cooling results are presented. The reader is referred to Appendix C for further discussion concerning data qualification.

Table 13 lists all of the least-squares, curve-fit equations used to represent the data of Figures 44 to 77. These equations will be used in a subsequent section for further analysis of the data.

V.3.2. Analysis and Discussion of Film Cooling Results

The previous section presented the results of the study of film cooling of a turbine vane leading edge for three different locations of coolant injection and two injection angles (see Figs. 44 to 77). These results will now be analyzed and discussed to isolate the effects on ST_{FC}/ST_0 due to changes in three primary cooling parameters: (a) the blowing ratio, M, (b) the angle of injection, β, and (c) the location of injection relative to the stagnation point, x_i/L_S. It will be shown that ST_{FC}/ST_0 decreases with increasing M for all the subject configurations (i.e. Cases I - V). However, the value of M at which a minimum value of ST_{FC}/ST_0 occurs (most effective cooling) depends upon the injection angle and the location of injection (indicative of the thickness of the boundary layer at injection). The minimum level of ST_{FC}/ST_0 depends upon the location of injection (which characterizes the local degree of freestream acceleration (K_i)). It is postulated, judging from an

Table 13.

Summary of Least-Squares Equations For Figures 44 to 77.

Least-Squares Curve Fits of Form

$$\frac{ST_{FC}}{ST_0} = AM^2 + BM + C$$

FIGURE	A	B	C
CASE I			
44 $M<M_{OPT}$		-0.298	1.009
44 $M>M_{OPT}$	-0.509	1.960	-1.072
45	0.013	-0.061	0.950
46	0.074	-0.178	0.995
47	0.079	-0.206	0.998
48	0.060	-0.174	1.023
49	0.105	-0.271	1.047
50	0.039	-0.092	0.997
51	0.064	-0.163	1.021
CASE II			
52 $M<M_{OPT}$		-0.426	1.007
52 $M>M_{OPT}$		0.287	0.310
53	0.048	-0.134	0.979
54	0.046	-0.121	0.974
55	0.098	-0.193	0.993
56	0.045	-0.096	0.967
57	0.047	-0.118	0.984
58	0.036	-0.113	0.992
CASE III			
59 $M<M_{OPT}$		-0.355	1.000
59 $M>M_{OPT}$	0.083	-0.054	0.881
60	0.070	-0.123	0.987
61	0.115	-0.118	0.995
62	0.070	-0.131	0.981
63	0.068	-0.144	1.001
CASE IV			
64	0.036	-0.108	0.950
65		-0.0021	0.973
66		-0.029	0.980
67		-0.050	0.993
68		-0.039	1.000
69		-0.027	0.993
70		-0.0075	0.979
71		-0.025	0.990
CASE V			
72 $M<M_{OPT}$		-0.389	0.965
72 $M>M_{OPT}$		0.174	0.535
73		-0.054	0.933
74		-0.043	0.960
75		-0.064	0.953
76		-0.009	0.949
77		-0.017	0.953

Table 13.

analysis of the present data, that large velocity gradients at injection ($K_i \sim 7 \times 10^{-6}$) can cause a significant deterioration in the cooling effectiveness in the form of enhanced turbulent mixing at the outer edges of the boundary layer. Specifying shallower injection angles in regions of severe acceleration can minimize the interaction between the coolant film and the mainstream flow by maintaining the low jet trajectories necessary to avoid penetration into the outer regions of the boundary layer.

V.3.2.1. Effect of Blowing Ratio, M

To evaluate the effect of the blowing ratio on ST_{FC}/ST_0, the results of Figs. 44 to 77 will be presented in a manner which can illustrate the influence of increasing coolant mass addition at all locations downstream from injection. The figures presented in this section were generated from the least-squares curves representing the data in Figs. 44 to 77.

The method for constructing the figures in this discussion is outlined in Fig. 78. For a particular configuration (Cases I - V) a specific value of M was selected, M_1. Figures 78(a), (b) and (c) show a typical least-squares representation of the variation of ST_{FC}/ST_0 with M for three locations from injection (same form as Figs. 44 - 77). For M_1 the values of ST_{FC}/ST_0 at x_1, x_2, and x_3 were noted. Figure 78(d) shows the resulting transformation depicting the ST_{FC}/ST_0 variation with $(x-x_i)/d_0$ at $M = M_1$. Similarly, the procedure is repeated at any value of M, resulting in a family of curves which illustrates the overall effect of M and $(x-x_i)/d_0$ on the film cooling performance.

Since the data will be represented by the least-squares values of ST_{FC}/ST_0 for each M, the smooth curves generated (i.e. Fig. 78(d)) will

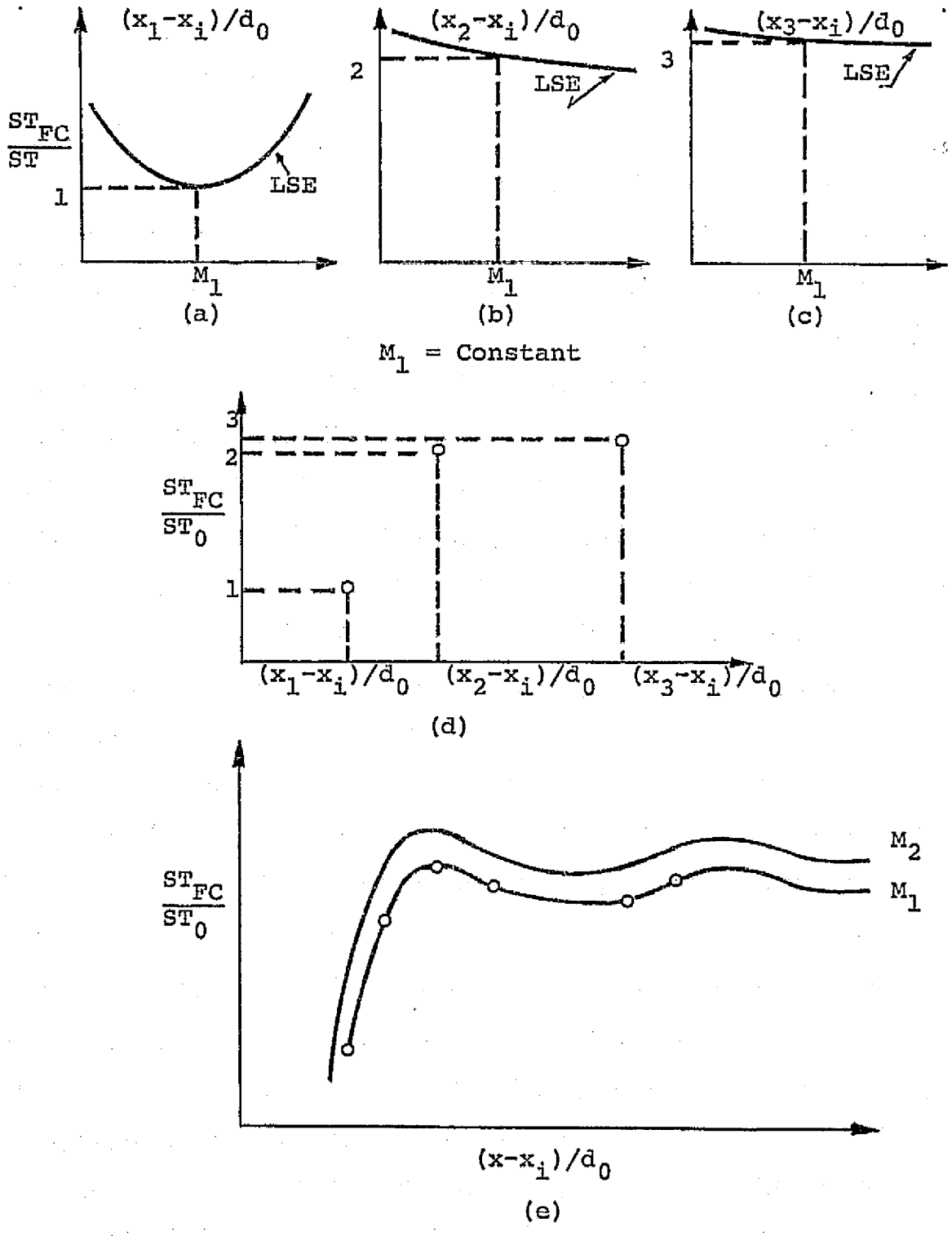

Figure 78. Transformation Technique To Show Blowing Ratio Effect For Figures 44 to 77.

be a function of the least-squares equations. The measured ST_{FC}/ST_0 values were shown in Figs. 44 - 77 to exhibit a definite amount of scatter in varying degrees; therefore, the least-squares curves will reflect this uncertainty to some extent. Because of this transformation procedure, the figures generated will show a certain amount of waviness (as illustrated in Fig. 78(e)). Generally, the waviness occurs in regions far from injection (40 or 50 hole diameters downstream) where the cooling effect has decayed to such an extent that uncertainties in the data are approaching the level of the cooling effect. The waviness should not be given any more significance than the fact that the ST_{FC}/ST_0 level was quite high (i.e. cooling effectiveness fairly low). Rather than curve fit the transformed data (essentially a second curve fit), it was decided to maintain the characteristic transformed waviness and simply draw a smooth faring through the points for selected values of M.

The question may arise as to what effect the nature of any lateral film nonuniformity may have on the data. It would seem plausible that such nonuniformities may tend to produce the waviness previously mentioned. It was not possible to experimentally determine the lateral variation (across the span, i.e. hole-to-hole), of ST_{FC}/ST_0 at any $(x-x_i)/d_0$. However, it is not expected to be sufficient to account for the wavy nature of the transformed data. Recent investigations at the NASA Lewis Research Center (62) indicate that for a similar geometry as the subject investigation, the cooling effectiveness at $(x-x_i)/d_0 = 11$ varied less than 15% across the span. As $(x-x_i)/d_0$ increased, the cooling effectiveness was reduced but became more uniform.

The effect of the blowing ratio on ST_{FC}/ST_0 is illustrated in Figs. 79 through 87. This series of figures is divided into two groups: (1) injection angle of 18°, and (2) injection angle of 35°. Within each group the effects of M on ST_{FC}/ST_0 for the various injection locations will be compared. For each configuration within a group, two figures will generally be presented: the first figure describing the effect of increasing M up to the value corresponding to a minimum ST_{FC}/ST_0 at $(x-x_i)/d_0$ nearest injection ($M_{OPT,NEAR}$) and the second characterizing the dependency of ST_{FC}/ST_0 on M for blowing ratios greater than $M_{OPT,NEAR}$. Presentation of the data in this manner allows for the identification of four main features:

(1) the magnitude of the blowing ratio effect on ST_{FC}/ST_0 in the near injection region, $(x-x_i)/d_0 < 30$,

(2) the degree of persistence of the cool film for various M values by observing the decay of ST_{FC}/ST_0 in the near region,

(3) the shifting of the overall level of ST_{FC}/ST_0 to a lower value as M increases to $M_{OPT,NEAR}$, and

(4) the shifting of the overall level of ST_{FC}/ST_0 when M surpasses $M_{OPT,NEAR}$.

Figures 79 and 80 describe the ST_{FC}/ST_0 variation with $(x-x_i)/d_0$ for $\beta = 18°$ and injection at $x_i/L_S = 0.0833$ (Case I). Figure 79 shows a family of curves for M ranging from 0.2 to $M_{OPT,NEAR} = 1.3$. Figure 80 includes the higher blowing ratio range for M from 1.3 to 2.0.

In Fig. 79, the most significant reduction in ST_{FC}/ST_0 for an increase in M from 0.2 to 1.3 occurs in a region $0 < (x-x_i)/d_0 < 25$. The lowest Stanton number recorded occurred at M = 1.3, amounting to a

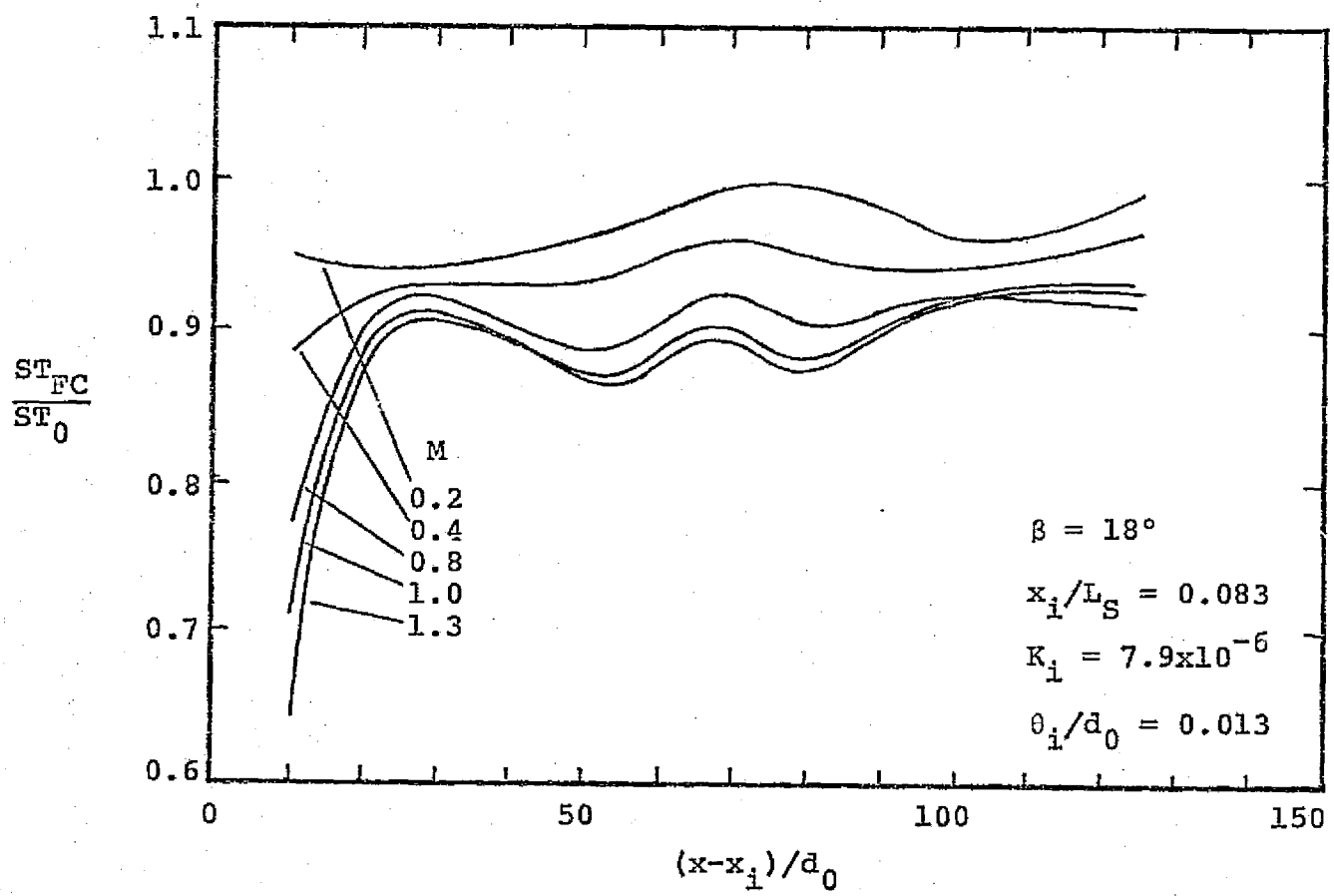

Figure 79. Effect of Blowing Ratio on Film Cooling Stanton Number Ratio For β = 18°, x_i/L_S = 0.083 ($M < M_{OPT,NEAR}$).

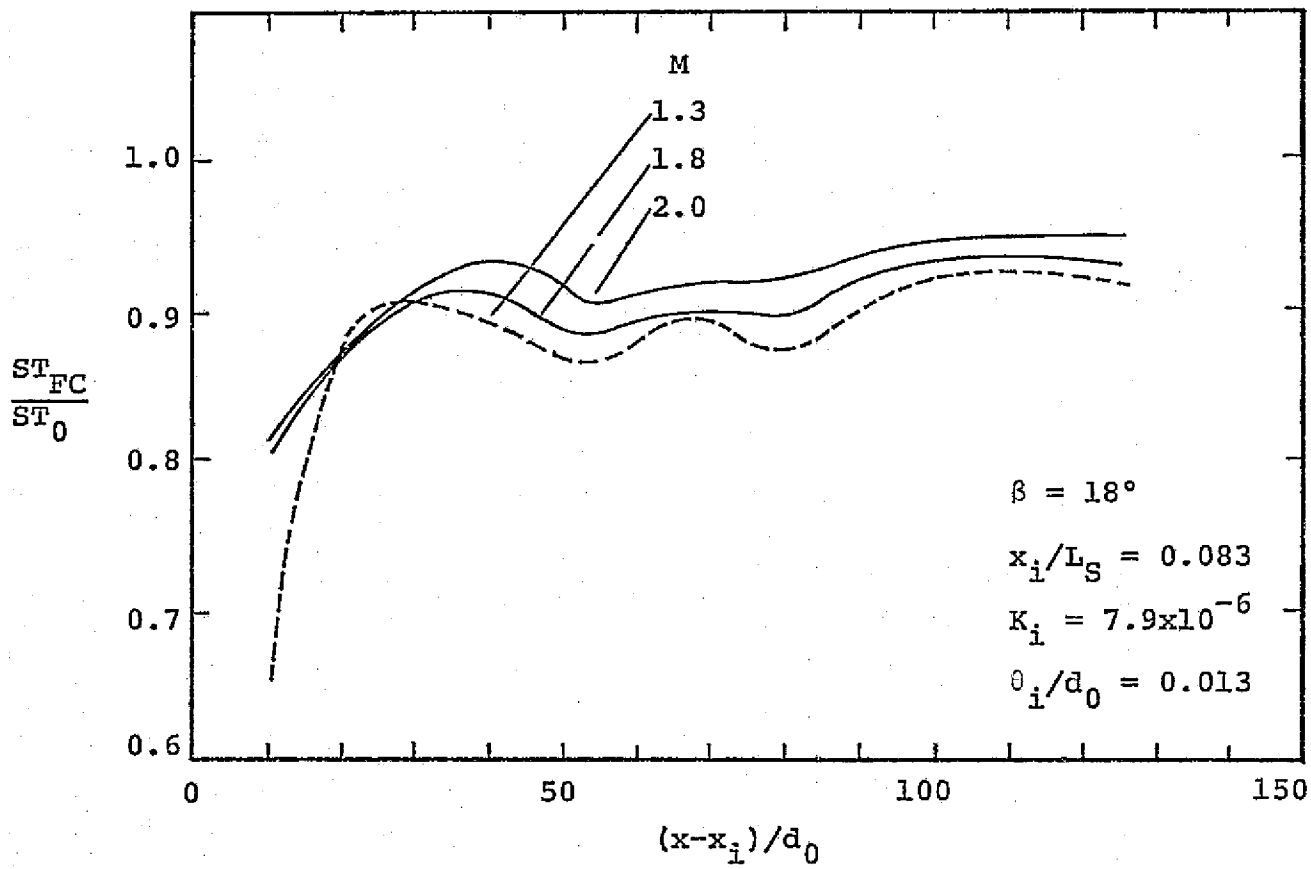

Figure 80. Effect of Blowing Ratio on Film Cooling Stanton Number Ratio, β = 18°, x_i/L_S = 0.083 ($M > M_{OPT,NEAR}$).

35% reduction in ST_0. Near M = 1.3 the deterioration of the cooling effect downstream is severe showing that most of the benefit of increasing M is lost after approximately 25 hole diameters downstream (as shown by the close proximity of the curves for M = 0.8, 1.0 and 1.3). However, farther downstream, for $50 < (x-x_i)/d_0 < 90$, there appears to be an overall, beneficial shifting of ST_{FC}/ST_0 to lower values with increasing M, amounting to approximately an 11% decrease in the Stanton number ratio from M = 0.2 to M = 1.3.

A reversal of the trend shown in Fig. 79 occurs with M > 1.3. Figure 80 illustrates that for $(x-x_i)/d_0 < 20$, ST_{FC}/ST_0 increases as M is increased from 1.3 to 2.0. Between $20 < (x-x_i)/d_0 < 30$, however, the Stanton number ratio remains nearly constant. For $(x-x_i)/d_0 > 30$, ST_{FC}/ST_0 increases with M, but to a lesser degree than near injection for the same change in M. A blowing ratio of M = 1.3 appears to be the value at which ST_{FC}/ST_0 is lowest for all downstream locations.

Figures 81 and 82 illustrate the blowing ratio effect on ST_{FC}/ST_0 for $\beta = 18°$ at $x_i/L_S = 0.150$ (Case II). Since $M_{OPT,NEAR}$ was identified as 1.05 (see Fig. 52) for this case, Fig. 81 presents a family of curves for M = 0.2 to M = 1.05. Figure 82 includes blowing ratios from 1.05 to 1.8.

The region which experiences the greatest benefit from increasing M appears to be concentrated, as shown in Fig. 81, in the range $(x-x_i)/d_0 \leq 30$. At M = 1.05, the lowest value of ST_{FC}/ST_0 amounted to a 38% decrease from ST_0 at $(x-x_i)/d_0 = 11.54$. For $(x-x_i)/d_0 > 30$, ST_{FC}/ST_0 decreases by approximately 5% for an increase of M from 0.2 to 1.05.

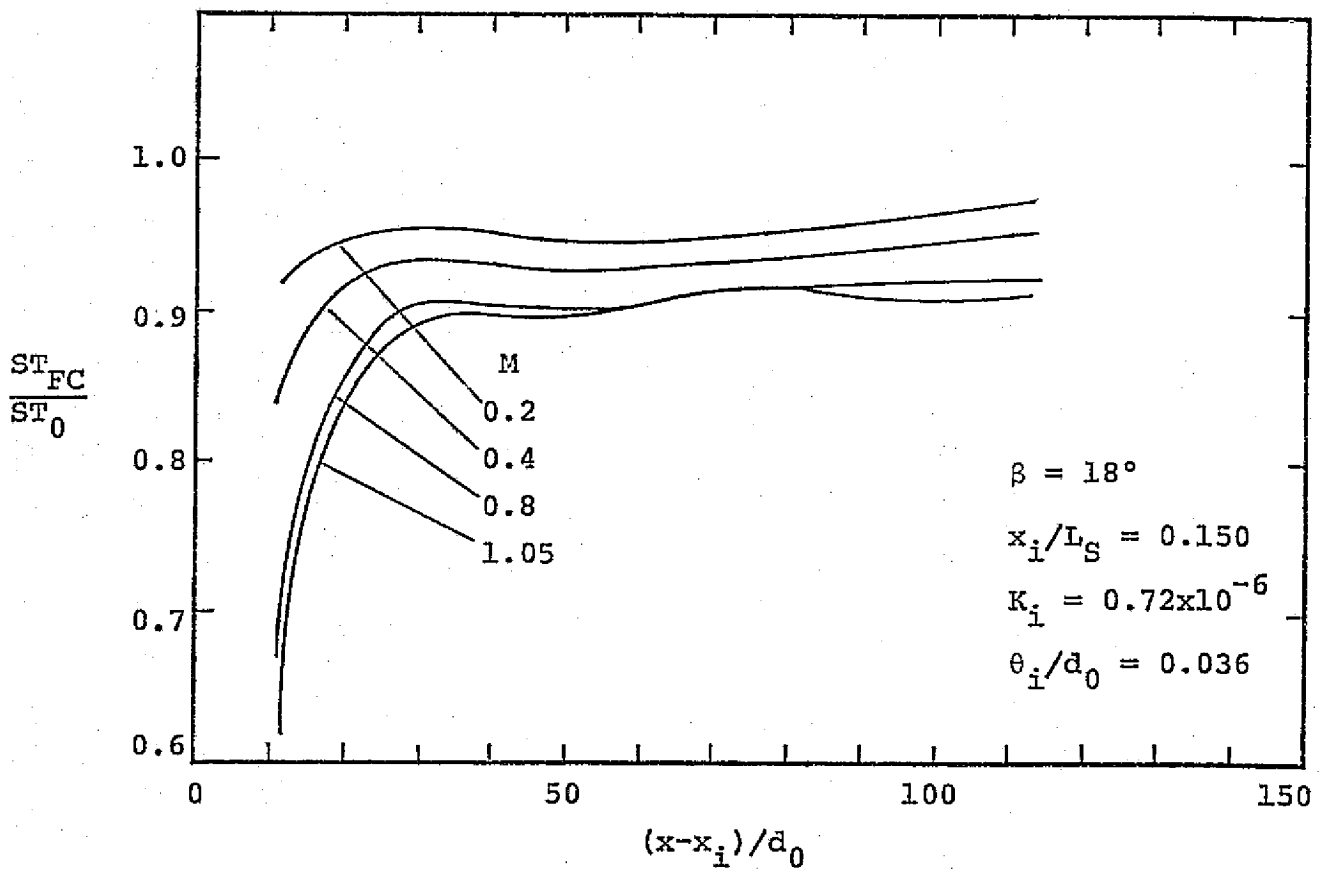

Figure 81. Effect of Blowing Ratio on Film Cooling Stanton Number Ratio, $\beta = 18°$, $x_i/L_S = 0.150$ ($M < M_{OPT,NEAR}$).

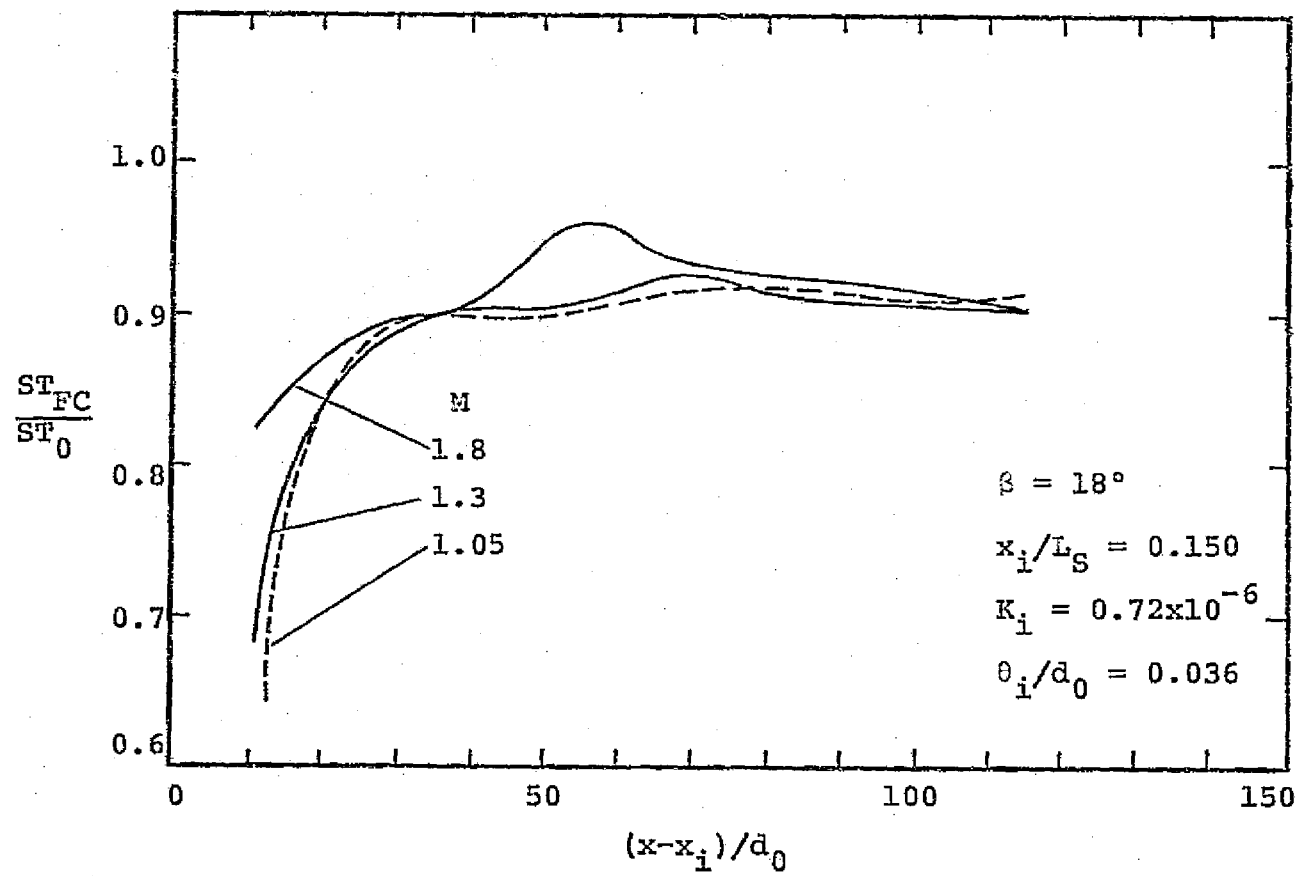

Figure 82. Effect of Blowing Ratio on Film Cooling Stanton Number Ratio, β = 18°, x_i/L_S = 0.150 ($M > M_{OPT,NEAR}$).

Figure 82 shows a reversal of the effects of increasing M past $M_{OPT,NEAR}$ similar to that noted in the previous configuration (Case I). Near $(x-x_i)/d_0 = 11.54$, the value of ST_{FC}/ST_0 increases with increasing M. At M = 1.8, however, the local Stanton number with film cooling was still 17.5% lower than ST_0. For $(x-x_i)/d_0 > 30$, ST_{FC}/ST_0 seems insensitive to increases in M from 1.05 to 1.8. The overall level of ST_{FC}/ST_0 stayed approximately constant for $(x-x_i)/d_0 > 30$. (No significance is assigned to the wave near $(x-x_i)/d_0 = 55$ for M = 1.8.) It appears that the optimum blowing ratio for this configuration is near 1.05.

The results for Case III for $\beta = 18°$ and $x_i/L_S = 0.228$ appear in Figs. 83 and 84 wherein $M_{OPT,NEAR}$ has been identified as approximately 0.5. Figure 83 presents the Stanton number ratio as a function of $(x-x_i)/d_0$ for the range $0.20 < M < 0.50$. Figure 84 includes a range of M from 0.50 to 1.3. An overall decrease in ST_{FC}/ST_0 is noted in Fig. 83 with an increase in M up to a value of 0.5. Near injection at $(x-x_i)/d_0 = 16.29$, a 16% decrease in ST_{FC} from ST_0 was measured at M = 0.5. For $(x-x_i)/d_0 > 40$ and M = 0.5, the reduction in ST_{FC} from ST_0 was approximately 5%.

Figure 84 shows the variation of ST_{FC}/ST_0 for $M > 0.5$. The blowing ratio appears to affect the Stanton number ratio differently for three distinct regions: (1) $(x-x_i)/d_0 < 30$ in which ST_{FC}/ST_0 increases with increasing M, (2) $30 < (x-x_i)/d_0 < 60$ in which a substantial "peaking" and subsequent decrease of ST_{FC}/ST_0 is shown as a function of increasing M, and (3) $60 < (x-x_i)/d_0 < 100$ in which the Stanton number ratio is reduced slightly (~3%) over the value at M = 0.5 but remains essentially constant for M increasing from 0.8 to 1.3. In the initial region, the

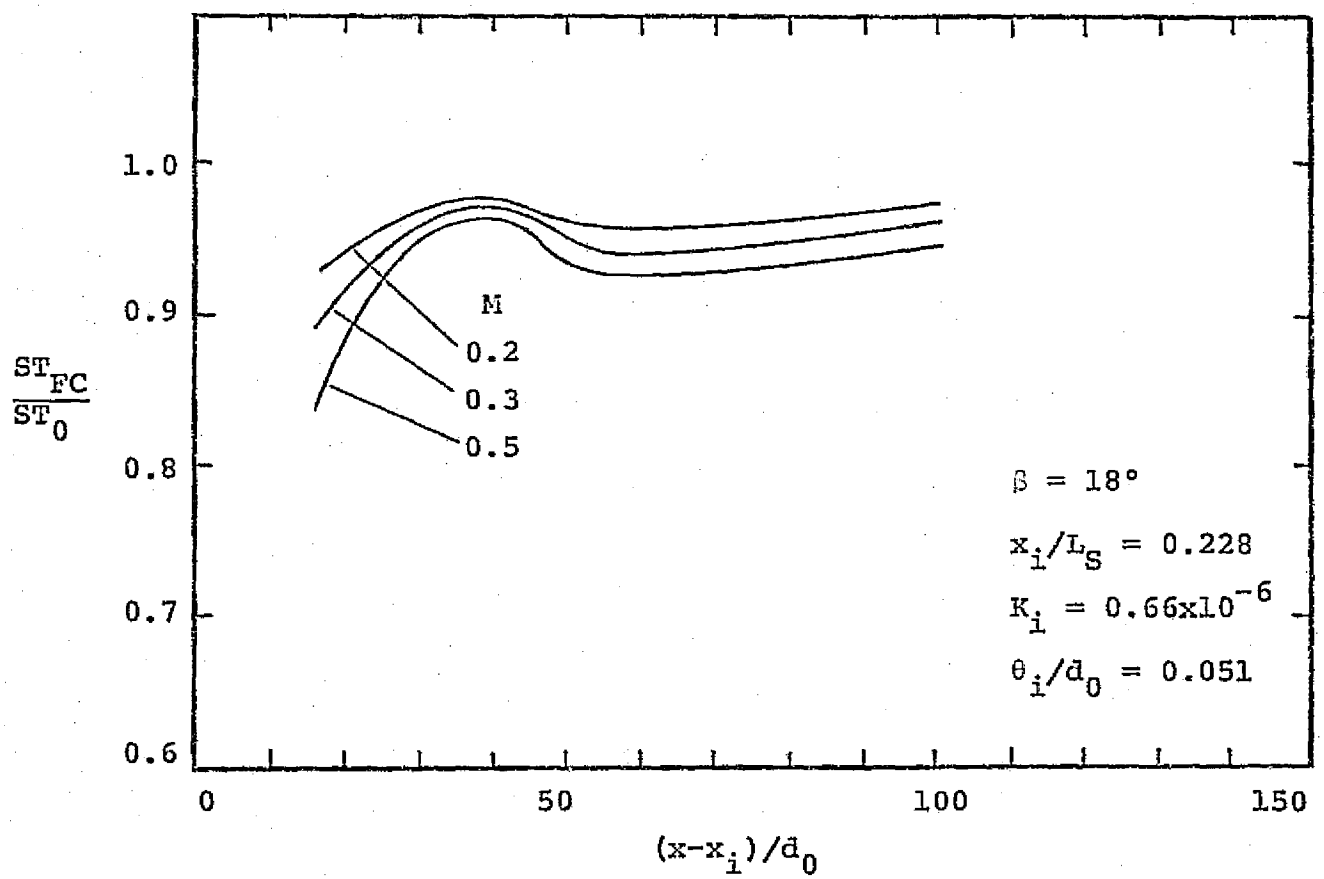

Figure 83. Effect of Blowing Ratio on Film Cooling Stanton Number Ratio, $\beta = 18°$, $x_i/L_S = 0.228$ ($M < M_{OPT,NEAR}$).

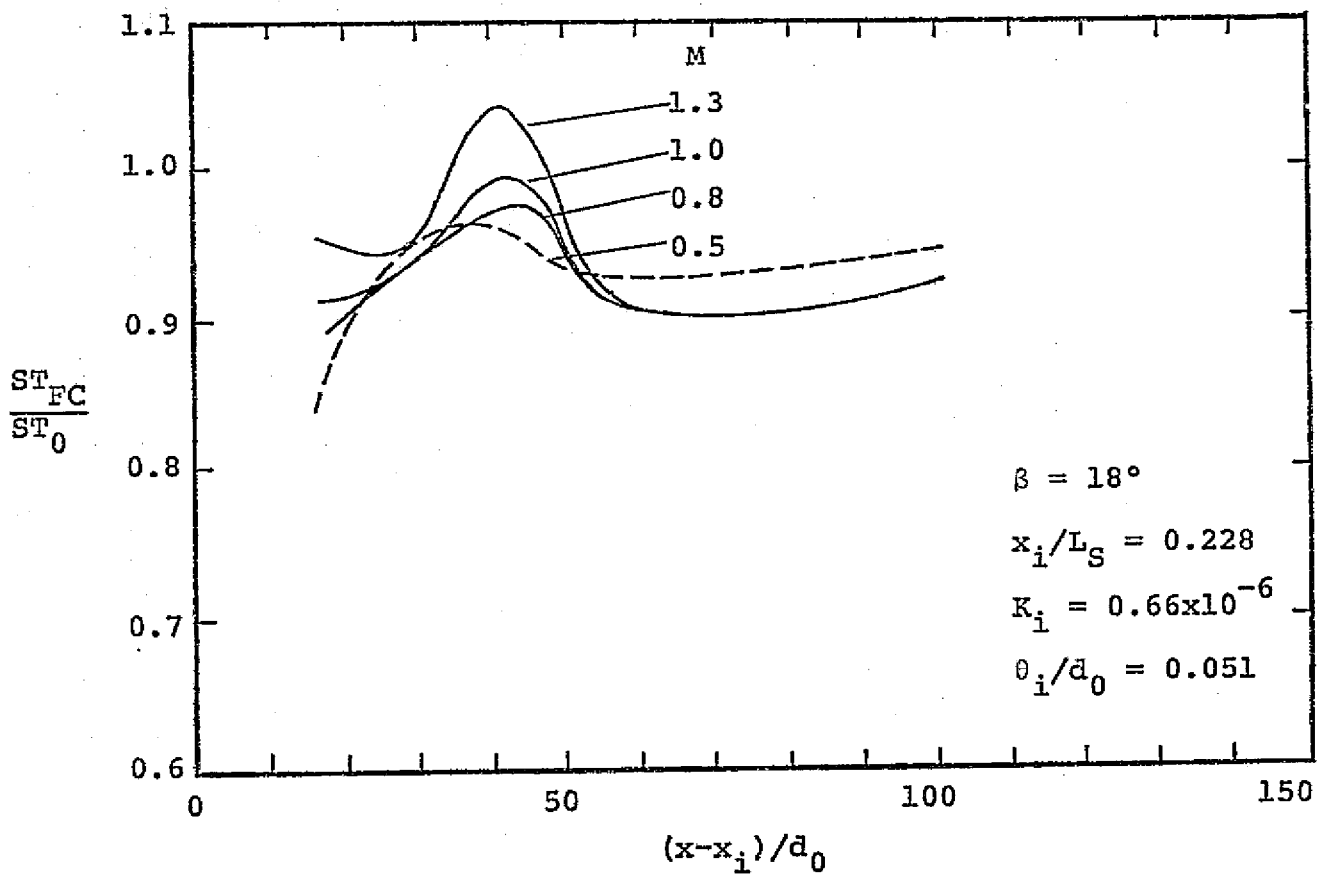

Figure 84. Effect of Blowing Ratio on Film Cooling Stanton Number Ratio, $\beta = 18°$, $x_i/L_S = 0.228$ ($M > M_{OPT,NEAR}$).

local Stanton number at M = 1.3 was still 5% lower than that without film cooling. For the second region, the local Stanton number at M = 1.3 increased to a level 4% greater than ST_0, but then fell to a value nearly 10% lower than ST_0. In the final region, nearly a constant value of ST_{FC}/ST_0 is illustrated, representing a 7 - 10% decrease from ST_0 for M between 0.8 and 1.3.

Figures 85 through 87 illustrate the effective Stanton number reduction with increased blowing for Cases IV and V with injection at $\beta = 35°$. Figure 85 gives results for $x_i/L_S = 0.0833$, and Figs. 86 and 87 describe injection at $x_i/L_S = 0.150$.

Figure 85 describes the Stanton number reduction due to increased blowing which, in contrast to the previous configurations, exhibited no optimum M for blowing up to M = 1.8. Near injection ($(x-x_i)/d_0 \approx 10$) the Stanton number ratio decreases with increased blowing. An increase in M from 0.2 to 1.8 only results in a reduction of ST_{FC} from ST_0 of 7% to 13%, respectively. In the region $35 < (x-x_i)/d_0 < 70$, for the same increase in M, ST_{FC}/ST_0 is reduced, but only in the amount of 2% to 4%.

For Case V, shown in Figs. 86 and 87, injection takes place at $x_i/L_S = 0.150$ for $\beta = 35°$. Figure 86 illustrates the reduction of ST_{FC}/ST_0 due to increased blowing from M = 0.2 to M = 0.85. An optimum blowing ratio of 0.85 near injection ($(x-x_i)/d_0 \approx 11$) is noted. The greatest benefit of increasing the coolant flow is realized in the region $(x-x_i)/d_0 < 30$, with a 32% reduction from ST_0 at $(x-x_i)/d_0 = 11.54$ for M = 0.85. The cooling capacity of the film decays rapidly near injection showing only a 7.5% reduction from ST_0 at $(x-x_i)/d_0 \approx 50$ for M = 0.85. For $90 < (x-x_i)/d_0 < 114$, the value of ST_{FC} converges to

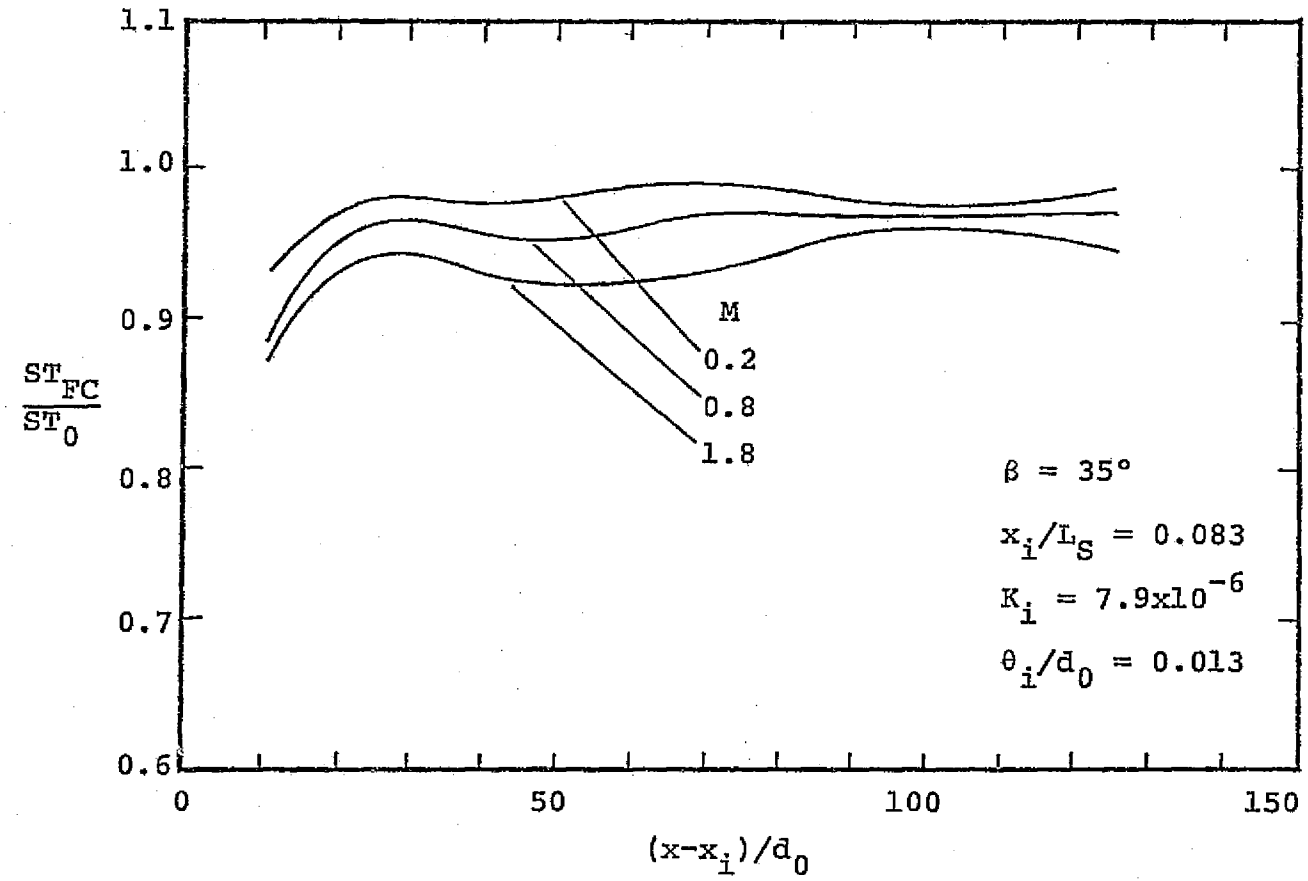

Figure 85. Effect of Blowing Ratio on Film Cooling Stanton Number Ratio, β = 35°, x_i/L_S = 0.083 ($M < M_{MAX}$).

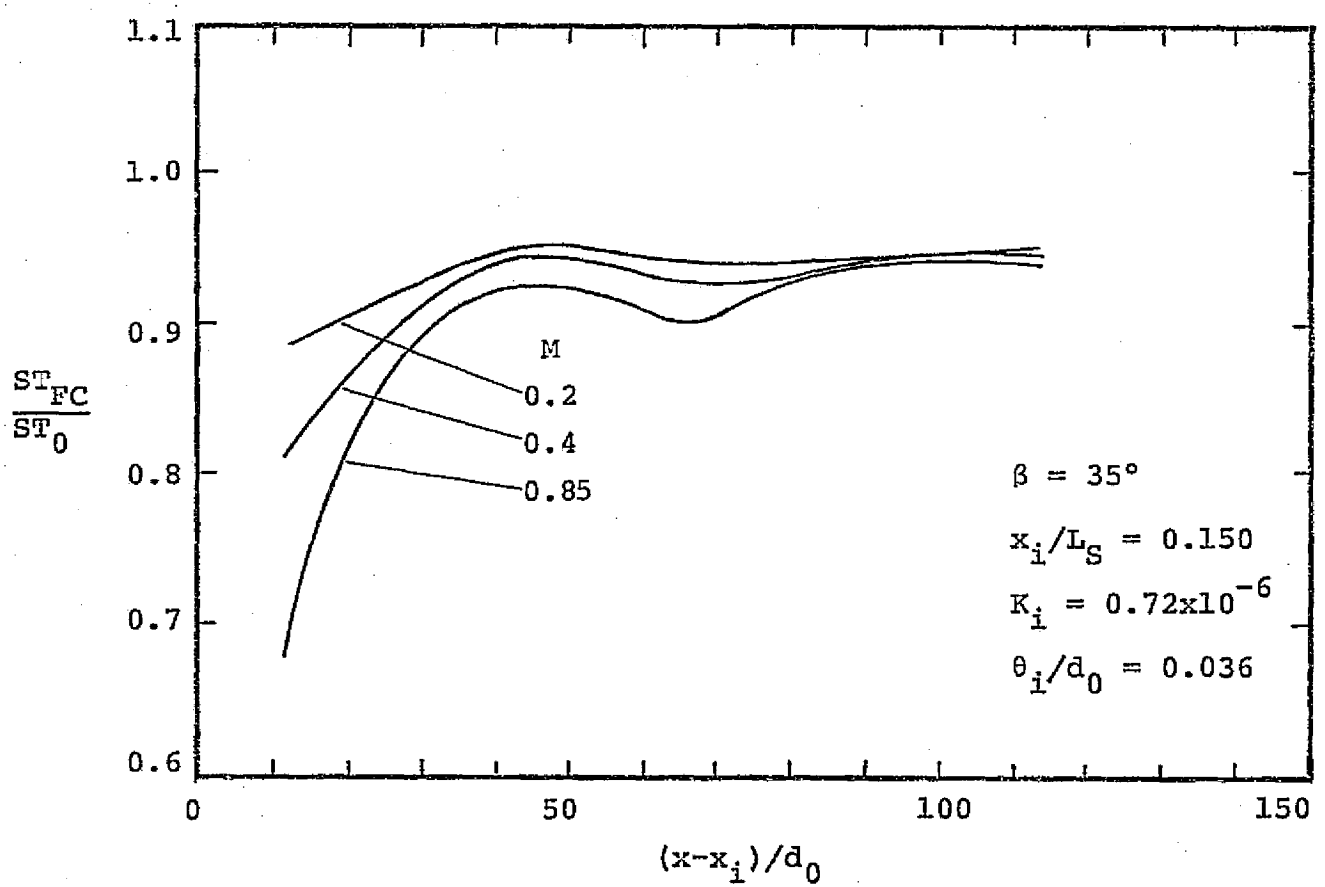

Figure 86. Effect of Blowing Ratio on Film Cooling Stanton Number Ratio, β = 35°, x_i/L_S = 0.150 ($M < M_{OPT,NEAR}$).

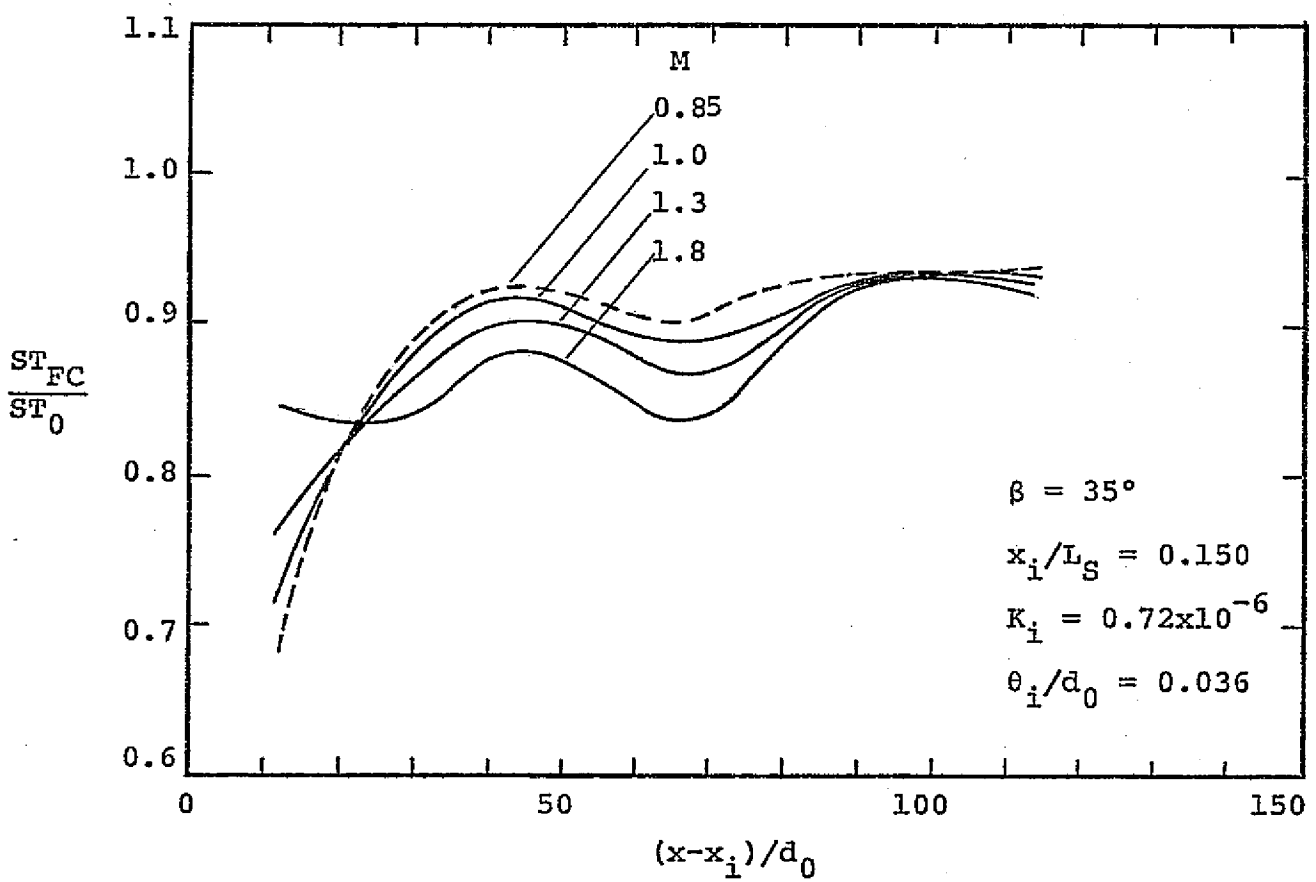

Figure 87. Effect of Blowing Ratio on Film Cooling Stanton Number Ratio, β = 35°, x_i/L_S = 0.150 ($M > M_{OPT,NEAR}$).

approximately a 5.5% reduction from ST_0 for all blowing ratios up to M = 0.85.

Figure 87 includes the higher blowing ratio range for Case V ($0.85 < M < 1.8$). Three regions can be clearly distinguished from this figure: (1) $(x-x_i)/d_0 < 20$ in which ST_{FC} increases for $M > 0.85$, (2) $20 < (x-x_i)/d_0 < 80$ showing a decrease in ST_{FC}/ST_0 (improved cooling) for $M > 0.85$ and (3) $(x-x_i)/d_0 > 80$ in which ST_{FC}/ST_0 appears insensitive to changes in the blowing ratio.

The significant features indicated by the data presented in Figs. 79 to 87 may be summarized as follows:

(1) For the shallow injection angle ($\beta = 18°$), a systematic decrease in the value of ST_{FC}/ST_0 for increasing M up to $M_{OPT,NEAR}$ was noted at all locations downstream from injection, while for $M > M_{OPT,NEAR}$ an increase in ST_{FC}/ST_0 with increasing M was observed. The value of $M_{OPT,NEAR}$ increased as the injection location was moved closer to stagnation.

(2) For the steep injection angle ($\beta = 35°$) the trends varied with the location of injection relative to stagnation. For injection at $x_i/L_S = 0.083$ (Fig. 85), the data exhibited no optimum M value. The value of ST_{FC}/ST_0 decreased continually as M increased for all locations downstream from injection. For injection at $x_i/L_S = 0.150$ a value for $M_{OPT,NEAR}$ was defined. However, only near injection, $(x-x_i)/d_0 \lesssim 20$, did the trend of ST_{FC}/ST_0 vs M follow that outlined in (1) above. Further downstream, the value of ST_{FC}/ST_0 decreased progressively as M was increased.

The data for $\beta = 18°$, for all three injection locations, follow the trends expected for ST_{FC}/ST_0 vs M. As M is increased, the film cooling

performance increases (i.e. lower values of ST_{FC}/ST_0) due to the increased thermal capacity of the coolant flow. However, at some condition, further increases in M enhance the mixing between the coolant and the mainstream such that mixing effects predominate over thermal capacity effects. Thereafter, increasing the value of M results in a decrease in the cooling performance (i.e. ST_{FC}/ST_0 increases). The data for β=35°, x_i/L_S = 0.150, near injection, are also consistent with the aforementioned trenss. However, for the most part, injection at β=35° resulted in some decrease in the value of ST_{FC}/ST_0 as M was continually increased. The change in the level of ST_{FC}/ST_0 was relatively insensitive to M for M values greater than approximately 1.0.

V.3.2.2. Correlation of ST_{FC}/ST_0 With Two-Dimensional Model

In order to make an assessment of the relative effect on ST_{FC}/ST_0 of geometrical configuration changes, such as the injection angle (β) and the injection location (x_i/L_S), the data were correlated with the blowing ratio (M) and the dimensionless distance from injection in a manner suggested by a two-dimensional slot cooling model. By placing each configuration on a common basis in relation to M and the dimensionless distance from injection the effects on ST_{FC}/ST_0 for changes in β from 18° to 35° and x_i/L_S from 0.0833 to 0.150 can be illustrated (Case III, β = 18° and x_i/L_S = 0.228 will not be included in the comparisons due to the uncertainty in $M_{OPT,NEAR}$).

As the spacing between coolant holes for a single row injection configuration approaches zero, two-dimensional slot-type cooling is achieved in the limit. Since models for three-dimensional (hole) injection are few (Eckert) proposes one based on a point heat source moving in a semi-infinite medium which requires knowledge of the eddy diffusivity), it is convenient to correlate the data as if the film coolant was issuing from a slot of total area and span-width equal to that of the row of

holes. Since lateral variations in ST_{FC}/ST_0 are expected to be minimal for the spanwise injection angles of the subject investigation, use of the slot cooling correlating parameters seemed justified.

A two-dimensional model, correlating the effects of the blowing ratio and distance from injection, was developed by Klein and Tribus (63). Assuming a line-source of enthalpy input, the adiabatic cooling effectiveness was expressed

$$\eta_{ADW} = 4.62\ Pr^{2/3}\ Re_C^{0.2}\ \left(\frac{\mu_C}{\mu_\infty}\right)^{0.2}\ \left(\frac{C_{p_C}}{C_{p_\infty}}\right)\ \left(\frac{x-x_i}{MS}\right)^{-0.8} \tag{78}$$

where Re_C = coolant Reynolds number

Defining

$$\lambda \equiv \left(\frac{x-x_i}{MS}\right)\ Re_C^{-0.25} \tag{79}$$

then

$$\eta_{ADW} = 4.62\ Pr^{2/3}\ \left(\frac{\mu_\infty}{\mu_C}\right)^{0.2}\ \left(\frac{C_{p_C}}{C_{p_\infty}}\right)\ \lambda^{-0.8} \tag{80}$$

In the present investigation, the values of Pr, μ_∞/μ_C and C_{p_C}/C_{p_∞} were essentially constant. Therefore, to correlate the effects of $(x-x_i)$ and M variations, the data are presented as a function of the parameter λ.

Figures 88 through 92 present ST_{FC}/ST_0 data for Cases I - V correlated with λ. The data shown in each figure represent ST_{FC}/ST_0 values for $M < M_{OPT,NEAR}$. The effects of boundary layer injection-related turbulent mixing possibly associated with values of $M > M_{OPT,NEAR}$ would not be expected to correlate with the two-dimensional model. Consequently, the data for $M > M_{OPT,NEAR}$ are not included in the correlation at this point, but will be presented in later figures for comparison purposes.

FIGURE	CASE	M RANGE	LEAST-SQUARES EQUATIONS	% DEVIATION FROM LEAST-SQUARES
88	I	0 - 1.3	$\frac{ST_{FC}}{ST_0} = -0.096(\log \lambda)^4 + 0.738(\log \lambda)^3 - 2.058(\log \lambda)^2 + 2.525(\log \lambda) - 0.254$	±8
89	II	0 - 1.05	$\frac{ST_{FC}}{ST_0} = -0.083(\log \lambda)^4 + 0.720(\log \lambda)^3 - 2.318(\log \lambda)^2 + 3.322(\log \lambda) - 0.869$	±8
90	III	0 - 0.5	$\frac{ST_{FC}}{ST_0} = -0.050(\log \lambda)^2 + 0.275(\log \lambda) + 0.609$	±6.5
91	IV	0 - 1.8	$\frac{ST_{FC}}{ST_0} = -0.016(\log \lambda)^2 + 0.100(\log \lambda) + 0.840$	±5
92	V	0 - 0.85	$\frac{ST_{FC}}{ST_0} = -0.032(\log \lambda)^4 + 0.344(\log \lambda)^3 - 1.339(\log \lambda)^2 + 2.285(\log \lambda) - 0.518$	±6

Table 14. Summary of Details From Figures 88 - 92.

Figure 88.

Correlation of Measured ST_{FC}/ST_0 For $\beta = 18°$ and $x_i/L_S = 0.083$ $(M < M_{OPT,NEAR})$.

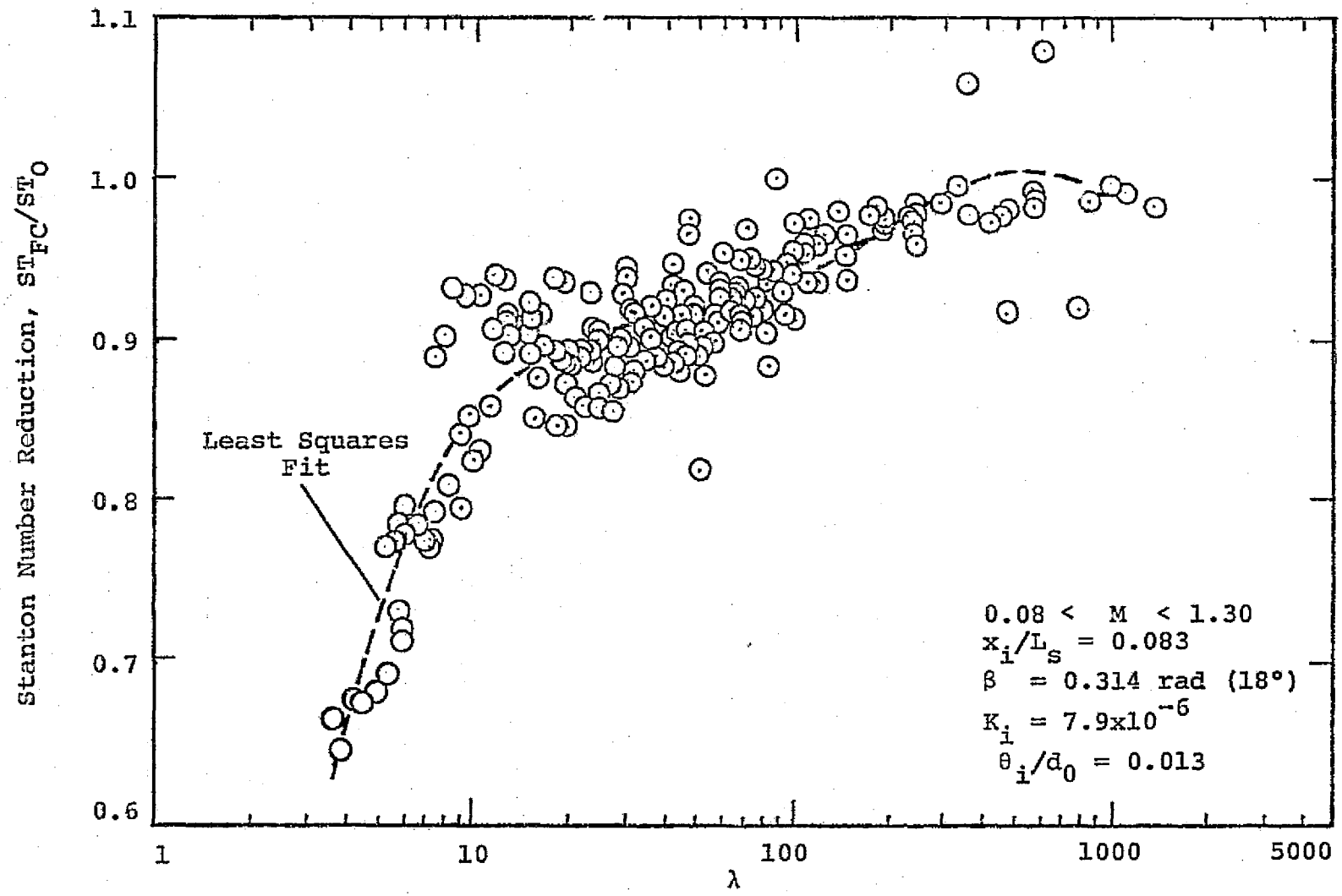

Figure 88.

Figure 89.

Correlation of Measured ST_{FC}/ST_0 For $\beta = 18°$ and $x_i/L_S = 0.150$ ($M < M_{OPT,NEAR}$).

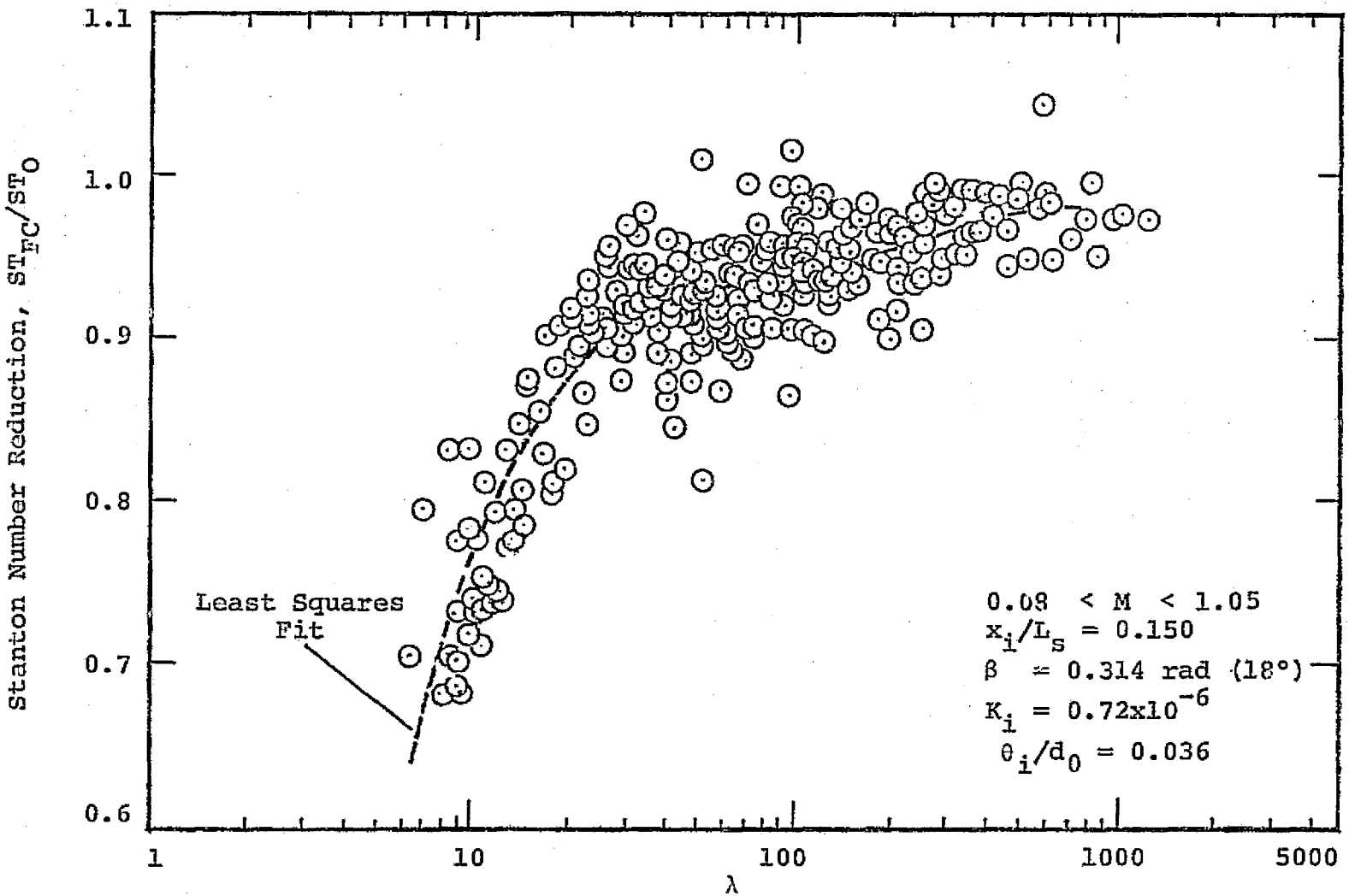
Stanton Number Reduction, ST_{FC}/ST_O
1.1
1.0
0.9
0.8
0.7
0.6
1
10
100
1000
5000
λ
Least Squares Fit
0.08 < M < 1.05
x_i/L_s = 0.150
β = 0.314 rad (18°)
$K_i = 0.72 \times 10^{-6}$
θ_i/d_0 = 0.036

Figure 89.

Figure 90.

Correlation of Measured ST_{FC}/ST_0 For $\beta = 18°$ and $x_i/L_S = 0.228$ ($M < M_{OPT,NEAR}$).

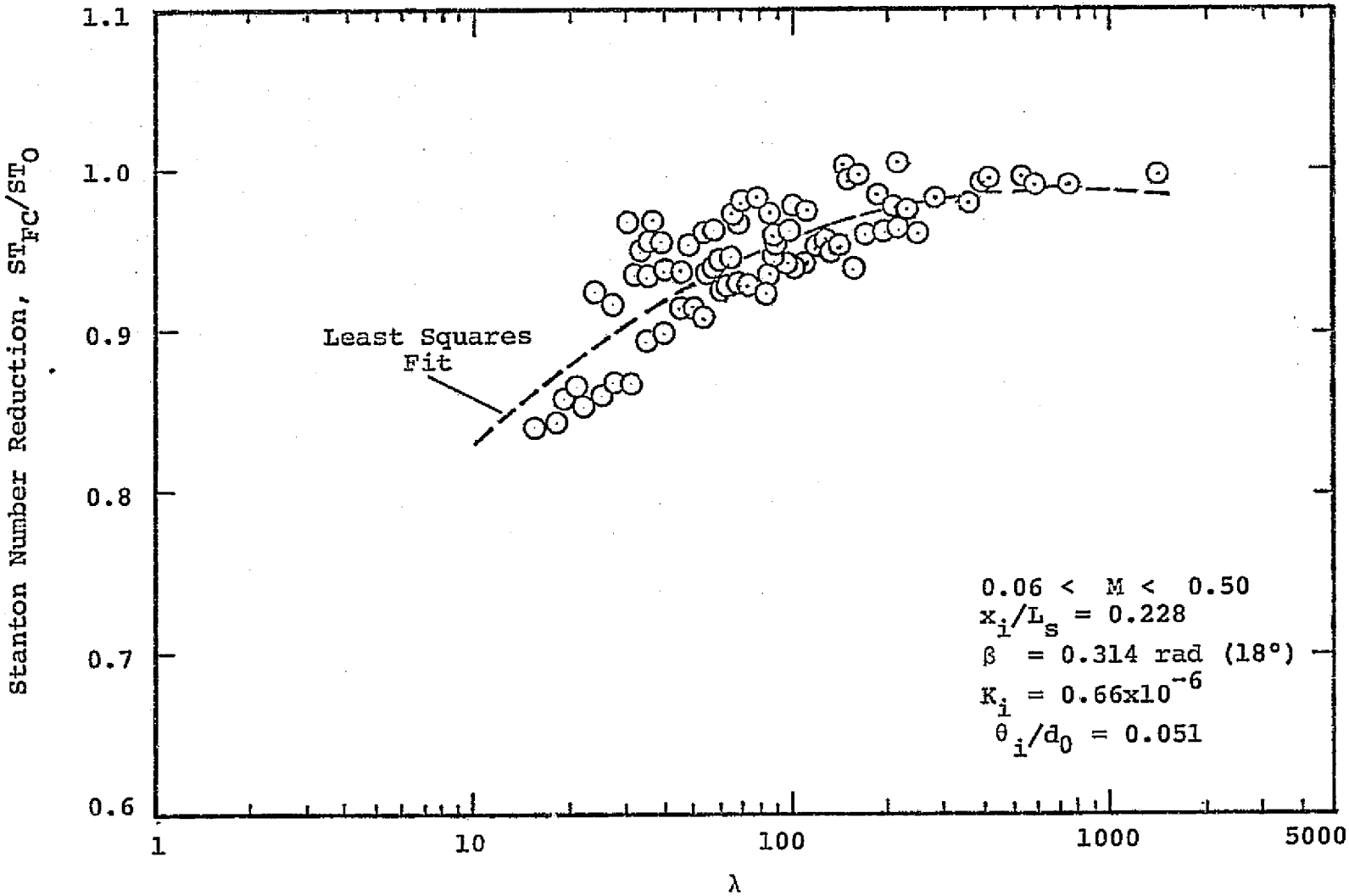

Figure 90.

Figure 91.

Correlation of Measured ST_{FC}/ST_0 For $\beta = 35°$ and $x_i/L_S = 0.083$ $(M < M_{MAX})$.

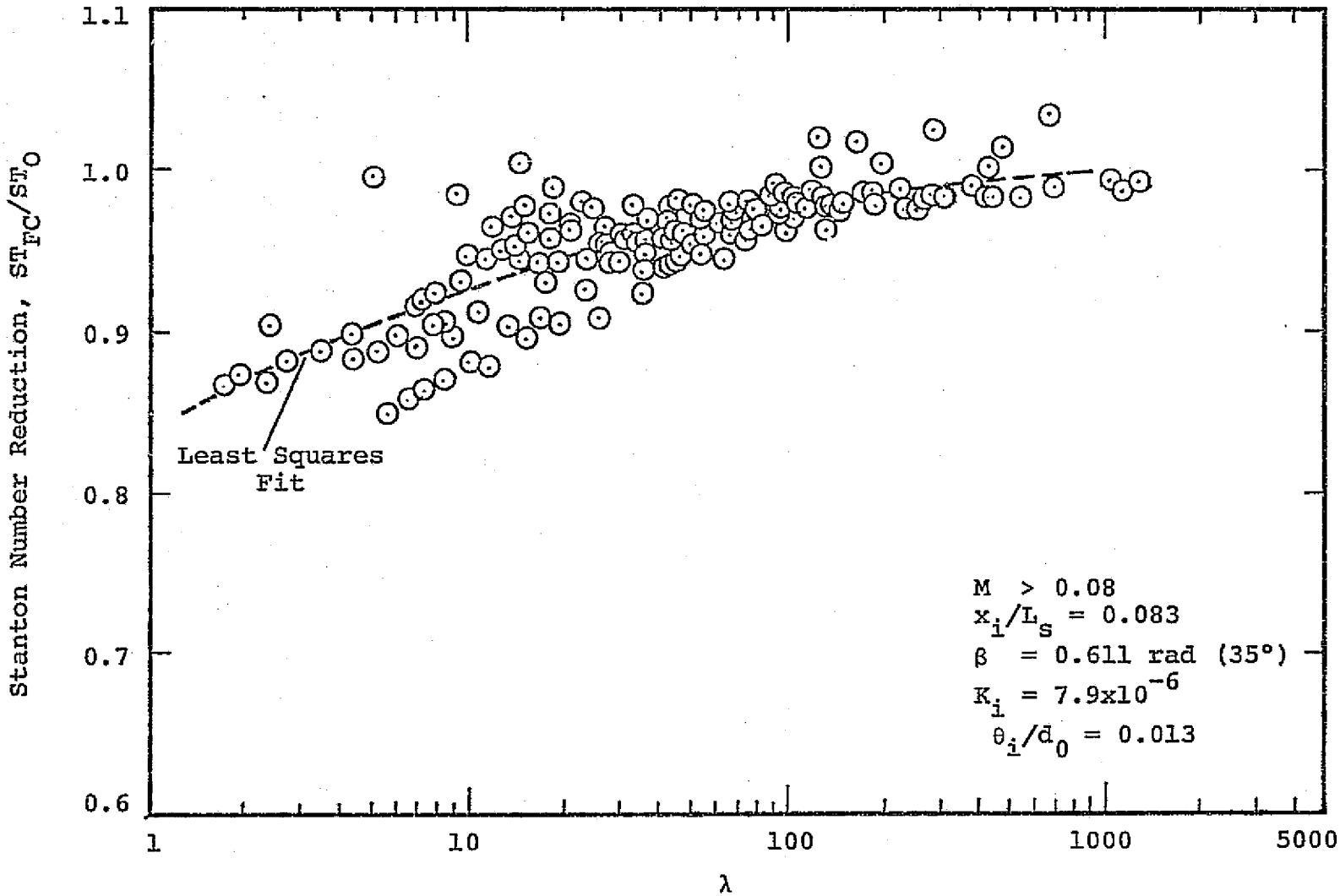
Stanton Number Reduction, ST_{FC}/ST_O
1.1
1.0
0.9
0.8
0.7
0.6
1
10
100
1000
5000
λ
Least Squares Fit
M > 0.08
x_i/L_s = 0.083
β = 0.611 rad (35°)
$K_i = 7.9 \times 10^{-6}$
θ_i/d_0 = 0.013

Figure 91.

Figure 92.

Correlation of Measured ST_{FC}/ST_0 For $\beta = 35°$ and $x_i/L_S = 0.150$ ($M < M_{OPT,NEAR}$).

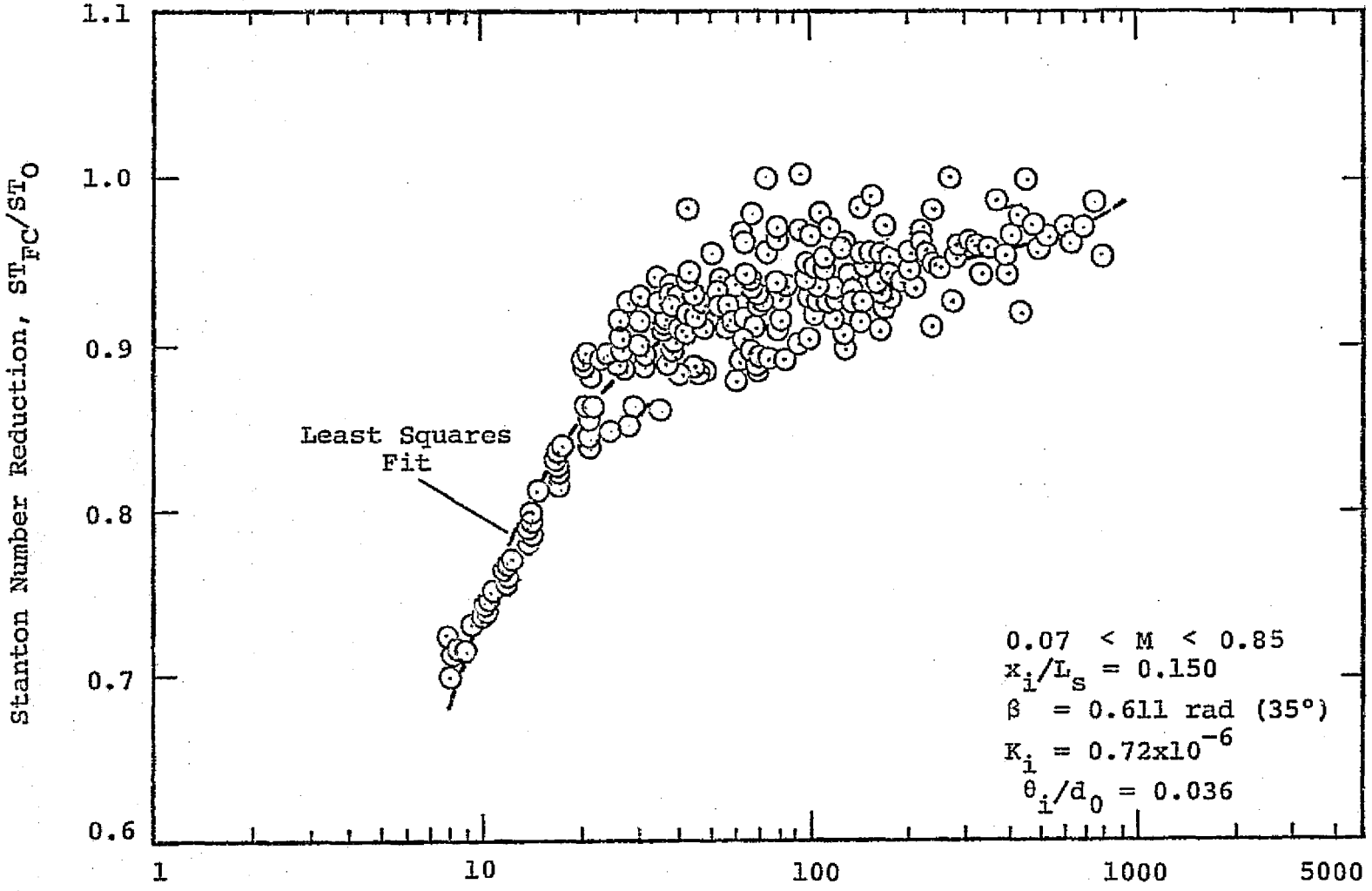
Stanton Number Reduction, ST_{FC}/ST_O
1.1
1.0
0.9
0.8
0.7
0.6
1
10
100
1000
5000
λ
Least Squares Fit
0.07 < M < 0.85
x_i/L_s = 0.150
β = 0.611 rad (35°)
$K_i = 0.72 \times 10^{-6}$
θ_i/d_0 = 0.036

Figure 92.

Table 14 summarizes the pertinent details for the data correlations of Figs. 88 to 92. A least-squares curve fit of the data was developed for each of the figures. A fourth-order polynomial curve fit is shown for the data of Figs. 88 and 89, representing the data within ± 8% in both cases. Cases III and IV are illustrated in Figs. 90 and 91, showing quadratic, least-squares curves that represent the data within ± 6.5% and ± 5%, respectively. The data of Case V are within ± 6% of a fourth-order polynomial, least-squares curve. The data are now in a convenient form in which the effects of changing various injection parameters other than M and $(x-x_i)$ can be illustrated.

V.3.2.3. Effect of Injection Angle, β

By comparing the least-squares representations of ST_{FC}/ST_0 as a function of λ for $M < M_{OPT,NEAR}$, the effect of the injection angle, β, on the Stanton number ratio can be assessed at both $x_i/L_S = 0.0833$ and $x_i/L_S = 0.150$. The reduction of the local Stanton number due to film coolant injection at $x_i/L_S = 0.0833$ is compared in Fig. 93 for injection angles of β = 35° and β = 18°. The broken line is the least-squares curve fit for the data at the 35° injection angle for $0 < M < 1.8$ (this is Case IV in which $M_{OPT,NEAR} = M_{MAX}$ shown in Fig. 91). The solid line (least-squares curve from Fig. 88) represents injection at an angle of 18° for $0 < M < 1.3$. The open, circular symbols designate the Stanton number ratio for values of the blowing ratio greater than $M_{OPT,NEAR}$ for β = 18°; they are not well correlated with λ but are included for comparison and completeness.

The predominate feature which is illustrated in Fig. 93 is that the shallower injection angle (β = 18°) is more effective than the 35°

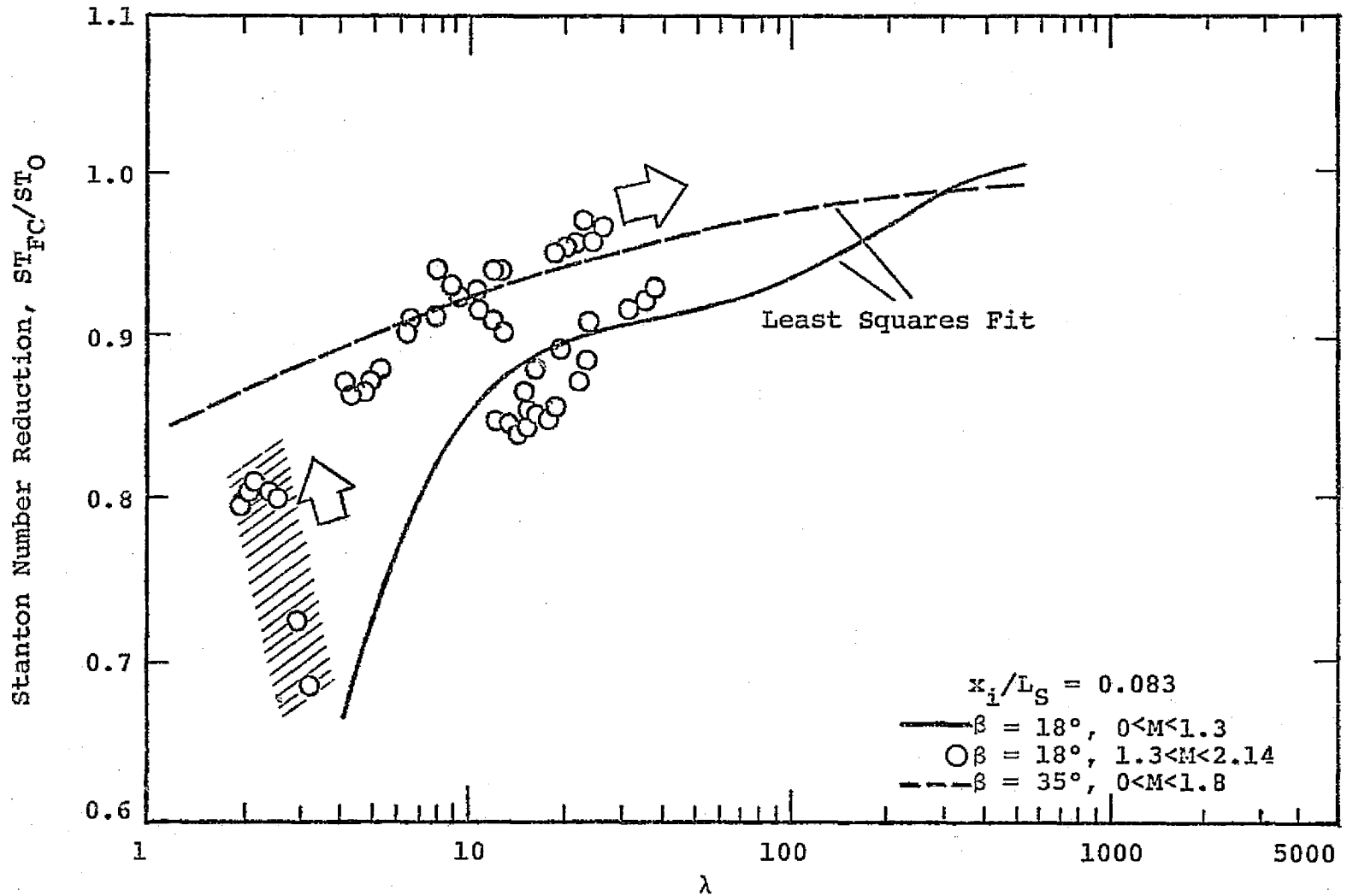

Figure 93. Effect of Coolant Injection Angle For x_i/L_S = 0.083.

injection angle in lowering ST_{FC}/ST_0. Near $\lambda = 4$, the 18° injection angle shows a Stanton number ratio of 0.670 while a value of 0.895 is shown at $\beta = 35°$, a difference of 25%. As the blowing ratio is decreased ($M < 1.3$) and/or the distance from injection increases, λ increases, and in the range $10 < \lambda < 600$ the difference between ST_{FC}/ST_0 for the two angles narrows considerably. At high blowing ratios ($M > 1.3$), as represented by the symbols for $\beta = 18°$, a shaded region is shown indicating the data for $(x-x_i)/d_0 \approx 11$. The effects on ST_{FC}/ST_0 of large scale mixing resulting from M increasing past 1.3 are characterized by the direction of the large vertical arrow. For $M > 1.3$, with increasing $(x-x_i)/d_0$ (shown by direction of large horizontal arrow), ST_{FC}/ST_0 data is quite scattered when correlated with λ.

Figure 94 compares the data for 18° and 35° injection for $x_i/L_S = 0.150$. ST_{FC}/ST_0 is shown as a function of λ for the two least-squares representations of the data. The broken line corresponds to $\beta = 35°$ for $0 < M < 0.85$ (from Fig. 92). The solid line represents $\beta = 18°$ for $0 < M < 1.05$ (from Fig. 89). The circular symbols represent ST_{FC}/ST_0 values for $M > M_{OPT,NEAR}$: open symbols for $\beta = 35°$ and $0.35 < M < 2.10$, and the solid symbols for $\beta = 18°$ and $1.05 < M < 2.37$.

Figure 94 indicates that for $M < M_{OPT,NEAR}$, injection at $x_i/L_S = 0.150$ for $\beta = 18°$ and $\beta = 35°$ produces essentially the same cooling effect (i.e. reduction in ST_{FC}/ST_0). It appears that injection at $\beta = 35°$ is slightly more effective than $\beta = 18°$, however the difference is at most 4% and within the limits of the least-squares representations of the data. As M increases past $M_{OPT,NEAR}$ for both configurations (i.e. $\beta = 18°$ and $\beta = 35°$), the ST_{FC}/ST_0 values are represented by the

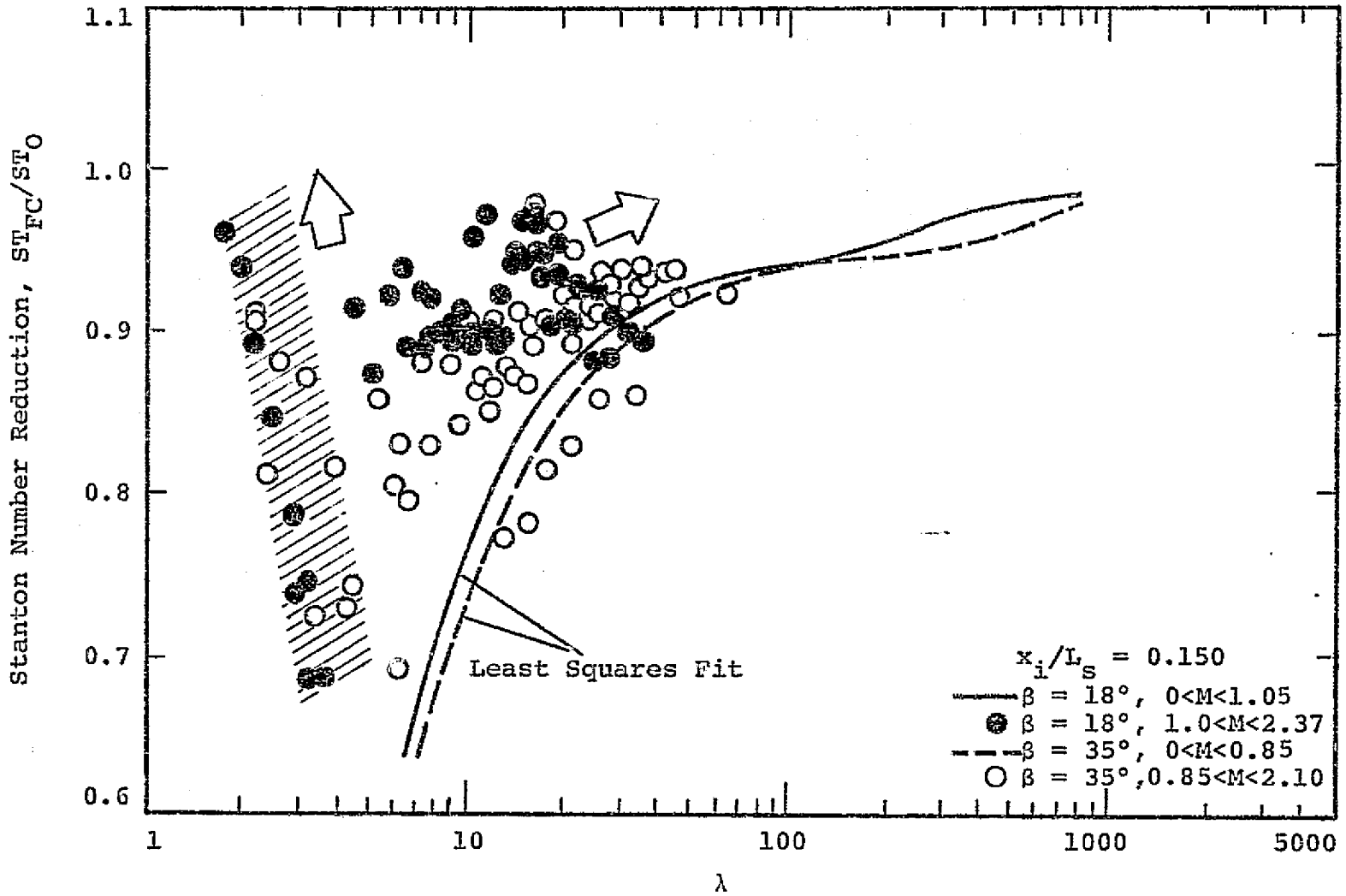

Figure 94. Effect of Coolant Injection Angle For x_i/L_s = 0.150.

circular symbols. Since $M_{OPT,NEAR}$ for $\beta = 18°$ is greater than that for 35° (1.05 compared to 0.85), a small range of M will exist in which the results for 18° are still represented by the least-squares curve while the values of ST_{FC}/ST_0 for 35° are shown as open symbols. For $0.85 < M < 1.05$, the 18° configuration (still shown by the solid line) is more effective than $\beta = 35°$ (now shown as open symbols). For $1.05 < M < 2.37$, the data for both injection schemes are illustrated by symbols. The near injection region ($(x-x_i)/d_0 \approx 11$), characterized by the shaded region, shows a steep rise in ST_{FC}/ST_0 with increasing M (illustrated by the direction of the large vertical arrow). At the high blowing ratios for large distances downstream (large horizontal arrow) the data is quite scattered, generally showing reduced cooling (ST_{FC}/ST_0 increasing).

Figures 93 and 94 indicate that increasing the injection angle from $\beta = 18°$ to $\beta = 35°$ results in the following:

(1) a decrease in the value of $M_{OPT,NEAR}$ with increasing ($M_{OPT,NEAR}$ decreases from 1.05 to 0.85 for β increasing from 18° to 35°, at $x_i/L_S = 0.150$) and

(2) a decrease in the cooling effectiveness (i.e. larger ST_{FC}/ST_0) as injection moves closer to the stagnation point.

Item (1) above can be explained at $x_i/L_S = 0.150$ by analyzing $M_{OPT,NEAR}$ for both the 18° and 35° in relation to the normal component of the coolant momentum flux. It is postulated that the optimum value of M is associated with coolant penetration into the boundary. There is a characteristic penetration distance (y*) corresponding to the value of $M_{OPT,NEAR}$. It is assumed now that y* is proportional to the normal component of coolant momentum flux, expressed as

$$y^* \propto [\rho_c V_c^2 \sin \beta] \tag{81}$$

Referencing Eq. (81) to the constant freestream momentum flux, $\rho_\infty V_\infty^2$, the following is obtained

$$\frac{y^*}{\rho_\infty V_\infty^2} = k^* \frac{\rho_c V_c^2}{\rho_\infty V_\infty^2} \sin \beta = k^* I \sin \beta \tag{82}$$

where k^* = proportionality constant. Equation (82) can be expressed in terms of M as

$$\frac{y^*}{\rho_\infty V_\infty^2} = k^* \left(\frac{\rho_\infty}{\rho_c}\right) M^2 \sin \beta \tag{83}$$

It is assumed that $M_{OPT,NEAR}$ should correspond to a similar penetration distance for each injection angle. In the present experiments, since (ρ_∞/ρ_c) as well as $\rho_\infty V_\infty^2$ remained constant at a particular x_i/L_s, Eq. (83) indicates that $M_{OPT,NEAR}$ and β should be correlated as follows,

$$M^2_{OPT,NEAR_1} \sin \beta_1 \approx M^2_{OPT,NEAR_2} \sin \beta_2 \approx \text{constant} \tag{84}$$

Using the results at $x_i/L_s = 0.150$ and Eq. (84) one obtains,

$$\beta = 18°, \quad M_{OPT,NEAR} = 1.05, \quad M^2 \sin \beta = 0.341$$

$$\beta = 35°, \quad M_{OPT,NEAR} = 0.85, \quad M^2 \sin \beta = 0.414$$

The agreement with Eq. (84) suggests that the normal component of the coolant momentum flux may be useful to correlate the coolant blowing conditions for optimum film cooling performance.

Using Eq. (84) for the results obtained at $x_i/L_S = 0.0833$, $\beta = 18°$, $M_{OPT,NEAR} = 1.3$, gives $M^2 \sin \beta = 0.522$, indicating that the value of the constant varies with x_i/L_S. Although the data for $\beta = 35°$ did not exhibit an optimum M for values up to M = 1.8, there was no significant change in ST_{FC}/ST_0 for M greater than 1.0. This would correspond to $M^2 \sin \beta = 0.574$ which is in reasonable agreement with the data for 18°. It is apparent that the film cooling performance varies with the location of injection, x_i/L_S, or more importantly, the local freestream acceleration at injection. The following section, illustrates the interdependence of the injection angle and the local freestream acceleration as reflected in the film cooling performance for different injection locations.

V.3.2.4. Effect of Local Freestream Acceleration at Injection

For the values of injection angles investigated in this study (18° and 35°), the effect of incorporating shallower injection angles on the film cooling effectiveness (i.e. 35° to 18°) does not appear to be significant in itself. However, under freestream conditions that exist for injection near the stagnation region, the cooling effect of the injected film shows an interrelation between the local value of the freestream acceleration (characterized by K_i) and the angle of injection, β.

Figure 95 shows the variation of ST_{FC}/ST_0 with λ for $\beta = 18°$ at two injection locations, $x_i/L_S = 0.0833$ and $x_i/L_S = 0.150$. The least-squares curves from Figs. 88 and 89 representing the data correlations are shown: the broken curve is indicative of injection at $x_i/L_S = 0.150$, while the solid curve represents injection at $x_i/L_S = 0.0833$. By moving the

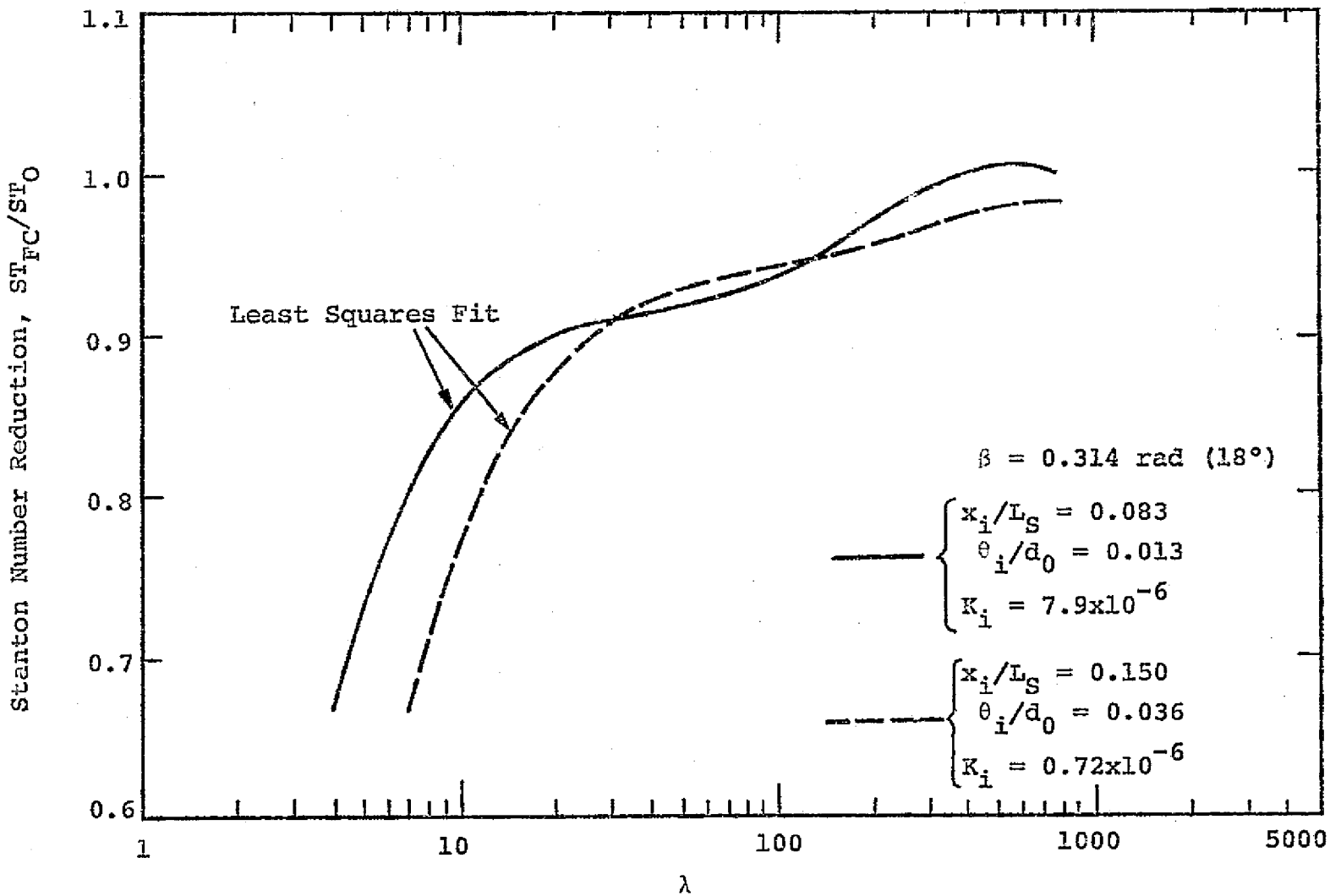

Figure 95. Effect of Injection Location on ST_{FC}/ST_O For β = 0.314 rad (18°).

injection site nearer to the stagnation point, two pertinent freestream parameters are changed: (a) the local freestream acceleration parameter, K_i, increases, and (b) the ratio of the momentum boundary layer thickness to the hole diameter ratio, θ_i/d_0, decreases. At $x_i/L_S = 0.150$, the acceleration prediction scheme) is 0.72×10^{-6} with $\theta_i/d_0 = 0.013$. At $x_i/L_S = 0.083$, the values are $K_i = 7.9 \times 10^{-6}$ and $\theta_i/d_0 = 0.013$.

Figure 95 illustrates that up to $\lambda \approx 30$ film coolant injection nearer stagnation (i.e. $x_i/L_S = 0.0833$) is less effective in reducing ST_{FC}/ST_0 than for injection at $x_i/L_S = 0.150$. As λ is increased from 7 to 30, the difference in ST_{FC}/ST_0 between the two injection locations narrows from 22% at $\lambda = 7$ to zero at $\lambda \approx 30$. The difference in cooling effectiveness may be attributed to the effects of local acceleration. More than an order of magnitude increase in K_i (0.72×10^{-6} to 7.9×10^{-6}) is represented in Fig. 95. Goldstein and Jabbari (64) report a 10% decrease in the cooling effectiveness from a double row of streamwise angled holes (3-diameter spacing) for M between 0.5 and 1.0 for changes in K_i from 0 to 1.0×10^{-6}. Kays, Moffat and Thielbahr (39) measured a 20 to 25% increase in the local transpiration cooled Stanton number (at a strong transpiration blowing ratio of 0.0062) for an increase of K from 0 to 0.77×10^{-6}. The range of K_i exhibited for the subject investigation extends to values nearly an order of magnitude greater than the cited references. Consequently, significant effects of K_i on ST_{FC}/ST_0 near stagnation would appear to be consistent with published data.

In addition to the change in K_i for the data shown in Fig. 95, θ_i/d_0 also changed significantly, from 0.036 to 0.013 for $x_i/L_S = 0.150$

to $x_i/L_S = 0.0833$. The effect of a decreasing boundary layer thickness should result in an improved cooling effect, due to a more shallow trajectory of the coolant jet. In reference to Fig. 95, the influence of a decreasing value of θ_i/d_0 should result in the broken curve both shifting slightly downward and extending to smaller values of λ. However, decreasing θ_i/d_0 accompanied with increasing K_i resulted in just the opposite change in ST_{FC}/ST_0. It appears then, that the effect of increasing K_i may be responsible for the differences in ST_{FC}/ST_0 at the two injection locations. In view of the opposing trends of K_i and θ_i/d_0, the absolute level of the effect of K_i may be even greater than illustrated.

As the injection angle gets steeper, the effects of K_i become more prominent. Figure 96 presents ST_{FC}/ST_0 as a function of λ for $\beta = 35°$ at the same injection locations analyzed in Fig. 95. The solid line is the least squares representation of the data for $x_i/L_S = 0.0833$, while the broken line is the least squares representation of the data for $x_i/L_S = 0.150$.

At $\lambda = 7$, the value of ST_{FC}/ST_0 is 48% higher for $x_i/L_S = 0.0833$ than for the configuration farther from stagnation ($x_i/L_S = 0.150$). Between $\lambda = 7$ and 50 the difference in ST_{FC}/ST_0 between the two configuration narrows. For $\lambda > 50$ a constant difference of approximately 4% is observed. The effect of increasing K_i appears to be more significant for the steeper injection angle ($\beta = 35°$) than previously observed in Fig. 95. The opposing trends of K_i and θ_i/d_0 can be argued similarly as for Fig. 95, indicating that the acceleration influence is even more pronounced than indicated in Fig. 96.

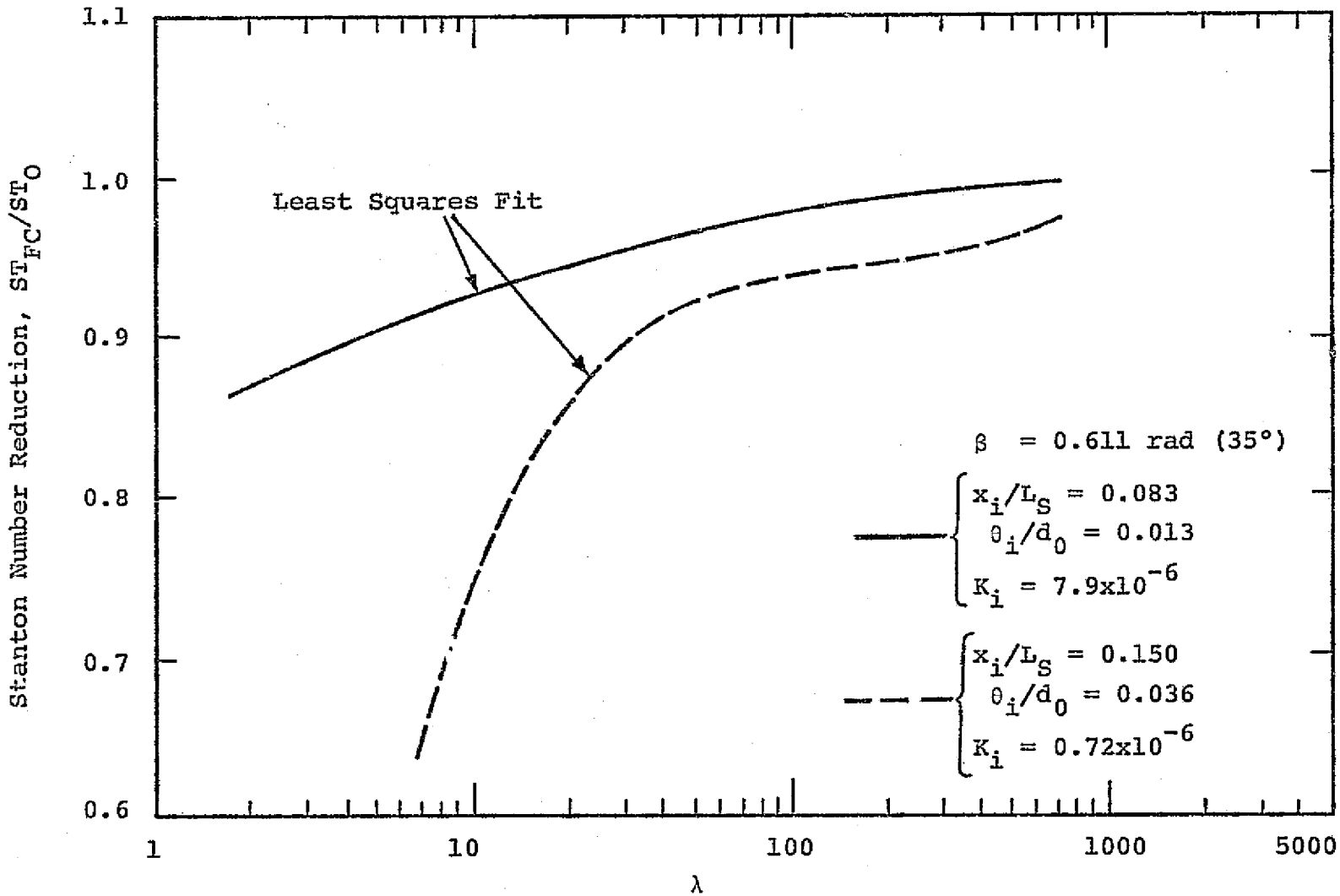

Figure 96. Effect of Injection Location on ST_{FC}/ST_O For β = 0.611 rad (35°).

In comparing Figs. 95 and 96, it appears that the effects of acceleration for injection at $\beta = 35°$, corresponding to a more penetrating jet trajectory, shows a greater dependence of ST_{FC}/ST_0 on the local value of the freestream acceleration at injection than injection at $\beta = 18°$. Specifying shallow injection angles would appear to be most important in regions of high freestream acceleration.

VI. EXTENSION OF RESULTS TO DESIGN APPLICATIONS

The data for Cases I - V of the subject investigation have been presented indicating ST_{FC}/ST_0 results for a film cooling scheme which models a high temperature, high pressure turbine inlet environment. The results of this study were obtained under model operating conditions of T_{T_∞} = 689°K (1240°R), $P_{T_\infty} = 3.1 \times 10^5$ N/m^2 (44.67 psia), T_C = 294°K (530°R) and a specified vane geometry and orientation. The values reported for ST_{FC}/ST_0 are characteristic of a dimensionless coolant temperature, $\theta_C' \approx 1.03$ or coolant-to-gas density ratio of $\rho_C/\rho_\infty \approx 2.15$. Extrapolation of the data to approximate ST_{FC}/ST_0 for other values of θ_C' can be accomplished by utilizing the superposition principle for a linear energy equation which is discussed below.

The superposition principle resulting from the energy equation applies when property variations (more specifically, density) within the thermal boundary layer may be assumed negligible. Two approaches to film cooling predictions, the adiabatic wall temperature method and the heat flux reduction method, rely on the linearity of the energy equation to extend experimental model results to high temperature and high pressure engine conditions.

The following sections will present a discussion concerning the application of film cooling data to high temperature and high pressure conditions. A parallel development of the two models (η_{ADW} and q''_{FC}/q''_0) for predicting the local, reduced heat flux is included. A discussion

is also included illustrating the use of each technique. Finally, the limitations of each method in making film cooling predictions can be noted in light of recent information concerning the effects of large density (ρ_c/ρ_∞) variations.

VI.1. Film Cooling Heat Flux Reduction Predictions

A comparison will now be made of the adiabatic wall temperature model and the heat flux reduction model for predicting the heat flux under film cooling conditions.

VI.1.1. Adiabatic Wall Temperature Method

Using the concept suggested by Eckert (5), the heat flux to a film cooled surface can be calculated if both the hydrodynamic and thermodynamic effects of injection can be determined. The thermodynamic effect is manifest in a reduced boundary layer gas temperature near the wall due to cool mass addition. For an adiabatic surface, this reduced boundary layer temperature is referred to as the adiabatic wall temperature which has frequently been measured in film cooling experiments. The hydrodynamic effect results from enhanced mixing due to injection, resulting in a more effective transport mechanism for mass, momentum and energy. This effect is measured by noting the change in local heat flux due to injection of a coolant at a temperature equal to that of the freestream. The combined thermodynamic and hydrodynamic effects on the local heat flux with film cooling can be expressed as

$$q''_{FC} = h_{\theta_C'=0} \left(T_{ADW} - T_{W,FC}\right)^{*} \tag{85}$$

*$h_{\theta_C'=0} = h'$ as discussed in Chapter II.1.1.1.

where $h_{\theta_C'=0}$ = local heat transfer coefficient reflecting the hydrodynamic effect ($T_C = T_{T_\infty}$)

T_{ADW} = adiabatic wall temperature reflecting the thermodynamic effect ($T_C < T_{T_\infty}$)

The fractional reduction in the local heat flux due to film cooling can be expressed as

$$\frac{q''_{FC}}{q''_0} = \frac{h_{\theta_C'=0}}{h_0} \frac{(T_{ADW} - T_{W,FC})}{(T_{T_\infty} - T_{W,0})} \tag{86}$$

where q''_0 = heat flux without film cooling

h_0 = local heat transfer coefficient without film cooling

Recalling the definition of the adiabatic wall effectiveness,

$$\eta_{ADW} = \frac{T_{T_\infty} - T_{ADW}}{T_{T_\infty} - T_C} \tag{87}$$

one can express T_{ADW} in the following manner

$$T_{ADW} = T_{T_\infty} - \eta_{ADW} (T_{T_\infty} - T_C) \tag{88}$$

such that Eqs. (86) and (88) combine to give

$$\frac{q''_{FC}}{q''_0} = \left(\frac{h_{\theta_C'=0}}{h_0}\right) \frac{(T_{T_\infty} - T_{W,FC})}{(T_{T_\infty} - T_{W,0})} - \eta_{ADW} \frac{(T_{T_\infty} - T_C)}{(T_{T_\infty} - T_{W,0})} \tag{89}$$

If a constant wall temperature is prescribed ($T_{W,FC} \approx T_{W,0}$) to evaluate the fractional reduction of the heat flux due to film cooling, Eq. (29) gives

$$\frac{q''_{FC}}{q''_0} = \left(\frac{h_{\theta_C'=0}}{h_0}\right) \quad 1 - \eta_{ADW}\, \theta'_C \tag{90}$$

Equation (90) states that the fractional heat flux reduction is a linear function of θ_C'. Once a film cooling geometry is fixed and a coolant blowing rate is specified, $(h_{\theta_C'=0}/h_0)$ and η_{ADW} can be determined from experimental data. To achieve a certain fractional heat flux reduction under these conditions, θ_C' is then uniquely determined.

VI.1.2. Direct Heat Flux Measurement Method

Instead of conducting experiments to determine η_{ADW} and $(h_{\theta_C'=0}/h_0)$, the fractional heat flux reduction can be measured directly. This method compares the measured heat flux at a particular location for a specified set of coolant conditions (i.e. θ_C', M, β, S_1/d_0, etc.) to the heat flux measured without film cooling. The ratio is expressed

$$\frac{q''_{FC}}{q''_0} = \frac{h_{FC}}{h_0} \frac{(T_{T_\infty} - T_{W,FC})}{(T_{T_\infty} - T_{W,0})} \tag{91}$$

where q''_{FC}/q''_0 is a function of all the coolant injection parameters. Note, in contrast to Eq. (85), h_{FC} is defined in terms of the gas-to-wall temperature difference, $(T_{T_\infty} - T_{W,FC})$.

To extend the results from experiments wherein q''_{FC}/q''_0 is measured to coolant temperatures other than those investigated, the linearity of the energy equation allows the following development (4). At a fixed position and coolant flow condition (i.e. M) the boundary layer temperature is a function of the boundary condition, θ_C' and can be expressed

$$T(\theta_C') = T(\theta'_{C,1}) + \theta_C' \left[T(\theta'_{C,2}) - T(\theta'_{C,1})\right] \tag{92}$$

where $\theta'_{C,1}$ = dimensionless coolant temperature for $T_C = T_{C,1}$

$\theta'_{C,2}$ = dimensionless coolant temperature for $T_C = T_{C,2}$

$T(\theta'_C)$ = solution for T at arbitrary θ'_C, and specified x, y, and M.

Recalling

$$q'' = -k \left.\frac{\delta T}{\delta y}\right|_{WALL} \tag{93}$$

and using Eq. (93) to operate on Eq. (92), the following results

$$q''_{FC}(\theta'_C) = q''_{FC}(\theta'_{C,1}) + \theta'_C \left[q''_{FC}(\theta'_{C,2}) - q''_{FC}(\theta'_{C,1})\right] \tag{94}$$

Referring Eq. (94) to the condition with no film cooling, q''_0,

$$\frac{q''_{FC}(\theta'_C)}{q''_0} = \frac{q''_{FC}(\theta'_{C,1})}{q''_0} - \theta'_C \left[\frac{q''_{FC}(\theta'_{C,1})}{q''_0} - \frac{q''_{FC}(\theta'_{C,2})}{q''_0}\right] \tag{95}$$

Equation (95) is a linear relation in θ'_C, with $[q''_{FC}(\theta'_{C,1})/q''_0]$ as the intercept of the ordinate, and $[q''_{FC}(\theta'_{C,1})/q''_0 - q''_{FC}(\theta'_{C,2})/q''_0]$ as the slope. If $q''_{FC}(\theta'_{C,1} = 0)/q''_0$ represents the hydrodynamic effects of injection ($\theta'_{C,1} = 0$ with $T_C = T_{T_\infty}$), the slope can be evaluated by letting $\theta'_{C,2}$ correspond to the case in which $T_W = T_{ADW}$ or $q''_{FC}(\theta'_{C,ADW}) = 0$. For the adiabatic case

$$\frac{q''_{FC}(\theta'_{C,ADW})}{q''_0} = 0 = \frac{q''_{FC}(\theta'_C=0)}{q''_0} - \theta'_{C,ADW}\ [\text{slope}] \tag{96}$$

Therefore, Eq. (96) gives

$$\text{slope} = \frac{q''_{FC}(\theta'_C=0)}{q''_0 \cdot \theta'_{C,ADW}} \tag{97}$$

Now Eq. (95) can be written as

$$\frac{q''_{FC}(\theta'_C)}{q''_0} = \frac{q''_{FC}(\theta'_C=0)}{q''_0} - \frac{\theta'_C}{\theta'_{C,ADW}} \frac{q''_{FC}(0)}{q''_0} \tag{98}$$

Since

$$\theta'_{C,ADW} = \frac{T_{T_\infty} - T_C}{T_{T_\infty} - T_{ADW}} = \frac{1}{\eta_{ADW}} \tag{99}$$

therefore, Eq. (98) becomes

$$\frac{q''_{FC}(\theta'_C)}{q''_0} = \frac{q''_{FC}(\theta'_C=0)}{q''_0} [1 - \eta_{ADW}\, \theta'_C] \tag{100}$$

If a constant wall temperature is prescribed ($T_{W,FC} = T_{W,0}$) to evaluate the effect of film cooling in reducing the heat flux, Eq. (91) shows (for $\theta'_C=0$)

$$\frac{q''_{FC}(\theta'_C=0)}{q''_0} = \frac{h_{\theta'_C=0}}{h_0} \tag{101}$$

Therefore, Eq. (100) can be reduced to

$$\frac{q''_{FC}(\theta'_C)}{q''_0} = \frac{h_{\theta'_C=0}}{h_0} [1 - \eta_{ADW}\, \theta'_C] \tag{102}$$

Equation (102) for the heat flux reduction model is now identical to Eq. (90) which was developed using the adiabatic wall temperature model.

Since Eq. (102) is in the linear form

$$\frac{q''_{FC}(\theta'_C)}{q''_0} = A - B\theta'_C \tag{103}$$

measurements of $q''_{FC}(\theta'_C)/q''_0$ at only two values of θ'_C can determine A and B. There will be a unique set of A and B for each blowing ratio and dimensionless distance from injection (geometry held fixed). In general A and B will be different for each change in a parameter associated with film cooling. For similar cooling configurations and injection conditions, A and B are specified from experimental results. Consequently, the fractional heat flux reduction can be determined for any choice of the coolant temperature (θ'_C).

The adiabatic wall temperature and heat flux reduction models were shown to yield identical results in predicting the effects on the local heat transfer due to film coolant injection. It would be helpful, at this point, to illustrate the basic procedure one would follow, using one of these aforementioned methods, to predict q''_{FC}/q''_0 for high temperature and high pressure conditions.

VI.2. Application of Film Cooling Heat Flux Prediction Methods

As an example of applying one of the aforementioned film cooling prediction schemes, consider the problem of cooling a critical area in the leading edge region of an inlet turbine vane. Assume that, prior to incorporating film cooling, the following conditions are specified:

T_{T_∞} = freestream gas total temperature

$T_{W,0}$ = wall temperature without film cooling

Re_∞ = freestream Reynolds number

x/L_S = location of the critical area relative to stagnation

T_i = temperature of the coolant <u>inside</u> the turbine vane used to maintain $T_{W,0}$.

It is desired to introduce film cooling to reduce the vane wall temperature in the critical area. To simplify the example, assume that the following film coolant flow and injection geometry parameters are specified:

M = coolant blowing ratio

x_i/L_S - location of injection holes relative to stagnation

β = injection hole angle

d_0 = injection hole diameter

$(x-x_i)/d_0$ = location of critical area relative to injection holes

S_1/d_0 = hole spacing ratio.

We ask, what value of T_C is required for film cooling to reduce the wall temperature by some fraction, n?

$$T_{W,FC} = n\ T_{W,0} \tag{104}$$

Or, in terms of the dimensionless coolant temperature,

$$\theta'_C = \frac{T_{T_\infty} - T_C}{T_{T_\infty} - T_{W,FC}}$$

what value of θ'_C is required to reduce the wall temperature by some fraction n?

It is assumed that measurements of q''_{FC}/q''_0 were taken at reduced (simulated) conditions for an identical film coolant injection geometry and consequently, a unique relation has been determined from the simulated conditions between q''_{FC}/q''_0 and θ'_C for the specified M, $(x-x_i)/d_0$, etc. for use in the prediction.

Prior to introducing film cooling, the heat flux can be expressed as

$$q''_0 = h_0 \left(T_{T_\infty} - T_{W,0}\right) = \frac{\left(T_{T_\infty} - T_i\right)}{\frac{1}{h_0} + R_W + R_i} \tag{105}$$

where

R_W = thermal resistance of the vane wall

R_i = thermal resistance due to convection on the vane inside surface.

In a similar fashion, the heat flux with film cooling can be written as

$$q''_{FC} = h_{FC} \left(T_{T_\infty} - n\, T_{W,0}\right) = \frac{\left(T_{T_\infty} - T_i\right)}{\frac{1}{h_0}\left(\frac{h_0}{h_{FC}}\right) + R_W + R_i} \tag{106}$$

where R_W and R_i are assumed to be the same as in Eq. (105). The heat flux ratio can be formed from Eqs. (105) and (106) to give

$$\frac{q''_{FC}}{q''_0} = \frac{h_{FC}}{h_0}\, b = \frac{(\Sigma R)_0}{\frac{1}{h_0}\left(\frac{h_0}{h_{FC}}\right) + (\Sigma R)_0 - \frac{1}{h_0}} \tag{107}$$

where

$$b = \frac{1 - n\,\frac{T_{W,0}}{T_{T_\infty}}}{1 - \frac{T_{W,0}}{T_{T_\infty}}} \tag{107a}$$

$$(\Sigma R)_0 = \frac{1}{h_0} + R_W + R_i \tag{107b}$$

Equation (107) can now be solved for h_{FC}/h_0 to give the following

$$\frac{h_{FC}}{h_0} = \frac{\frac{1}{b} - a}{1 - a} \tag{108}$$

where

$$a = \frac{(1/h_0)}{(\Sigma R)_0} \tag{108a}$$

For the subject example, b can be determined from Eq. (107a) for a selected value of n, the desired fractional reduction in wall temperature. The value of "a" can be determined from the information specified at the outset (T_{T_∞}, T_i, $T_{W,0}$, Re_∞, x/L_S) and Eq. (108a). Thus, Eq. (108) can be used to evaluate h_{FC}/h_0 for the specified conditions and the selected value of n. Consequently, Eq. (107) can be employed to determine the value of q''_{FC}/q''_0 for the selected value of n.

Recall that q''_{FC}/q''_0 as a function of θ'_C was assumed known from the model experiments (under simulated conditions) for the specified film coolant injection conditions (M, $(x-x_i)/d_0$, etc.). These results would be in the linear form

$$\frac{q''_{FC}}{q''_0} = A - B\,\theta'_C \tag{109}$$

With the value of q''_{FC}/q''_0 known from Eq. (107), the value of θ'_C required to reduce the wall temperature by some fraction n can be determined from Eq. (109).

The assumption carried along during this example was that data for q''_{FC}/q''_0 as a function of θ'_C, obtained from model experiments are applicable to problems involving large temperature differences between the coolant and mainstream. For example, at a value of $\theta'_C = 1$ the predicted heat flux ratio, q''_{FC}/q''_0, for a prototype condition of $T_{T_\infty} = 1922°K$ (3460°R), $T_{W,FC} = 961°K$ (1730°R) and $T_C = 961°K$ (1730°R) is presumed to be identical to a model condition of $T_{T_\infty} = 330°K$ (594°R), $T_{W,FC} = 290°K$ (526°R)

and T_c = 290°K (526°R) providing identical film coolant conditions (i.e. M, β, S_1/d_0, $(x-x_i)/d_0$, etc.) are employed. For both cases $\theta_c' = 1$; however, the respective values of density ratio (ρ_c/ρ_∞) are 2.0 and 1.14. For a constant value of M, the velocity ratio (V_c/V_∞) will vary inversely with the change in the density ratio. This variation in velocity ratio at constant M and θ_c' can cause difficulties in extending data obtained for a low density ratio (~1) to predictions of q''_{FC}/q''_0 for high temperature applications where a density ratio of the order of 2 is more typical.

Recent evidence presented by Pedersen (24) has shown that the laterally-averaged adiabatic film cooling effectiveness, $\bar{\eta}_{IW}$ (determined using a mass transfer analogy*), depends upon the coolant-to-freestream velocity ratio, V_c/V_∞, for a fixed geometry and blowing ratio. Figures 97(a), (b) and (c) from Pedersen's results show $\bar{\eta}_{IW}$ as a function of x'/d_0 (where $x'=x-x_i$) for blowing ratios of 0.213, 0.515 and 1.05. The coolant-to-gas density ratio was varied between 0.75 and 4.17. The magnitude of the effect of ρ_c/ρ_∞ (as manifested by V_c/V_∞) increases with increasing M. Also, the dependence of $\bar{\eta}_{IW}$ on the density ratio is most pronounced near injection ($x'/d_0 < 30$).

Figure 97(a), at M = 0.213, represents the variation in $\bar{\eta}_{IW}$ with x'/d_0 for the velocity ratio in the range $0.051 \leq V_c/V_\infty \leq 0.282$. As discussed in Chapter V.3.2.1., a value of velocity ratio near $V_c/V_\infty \approx 0.5$ appears to represent an equilibrium condition below which film cooling

*The adiabatic cooling effectiveness, $\bar{\eta}_{ADW}$, and impervious wall effectiveness, $\bar{\eta}_{IW}$, are equivalent when the turbulent Prandtl and Schmidt numbers are identical. Pedersen's results included a verification of this point (24).

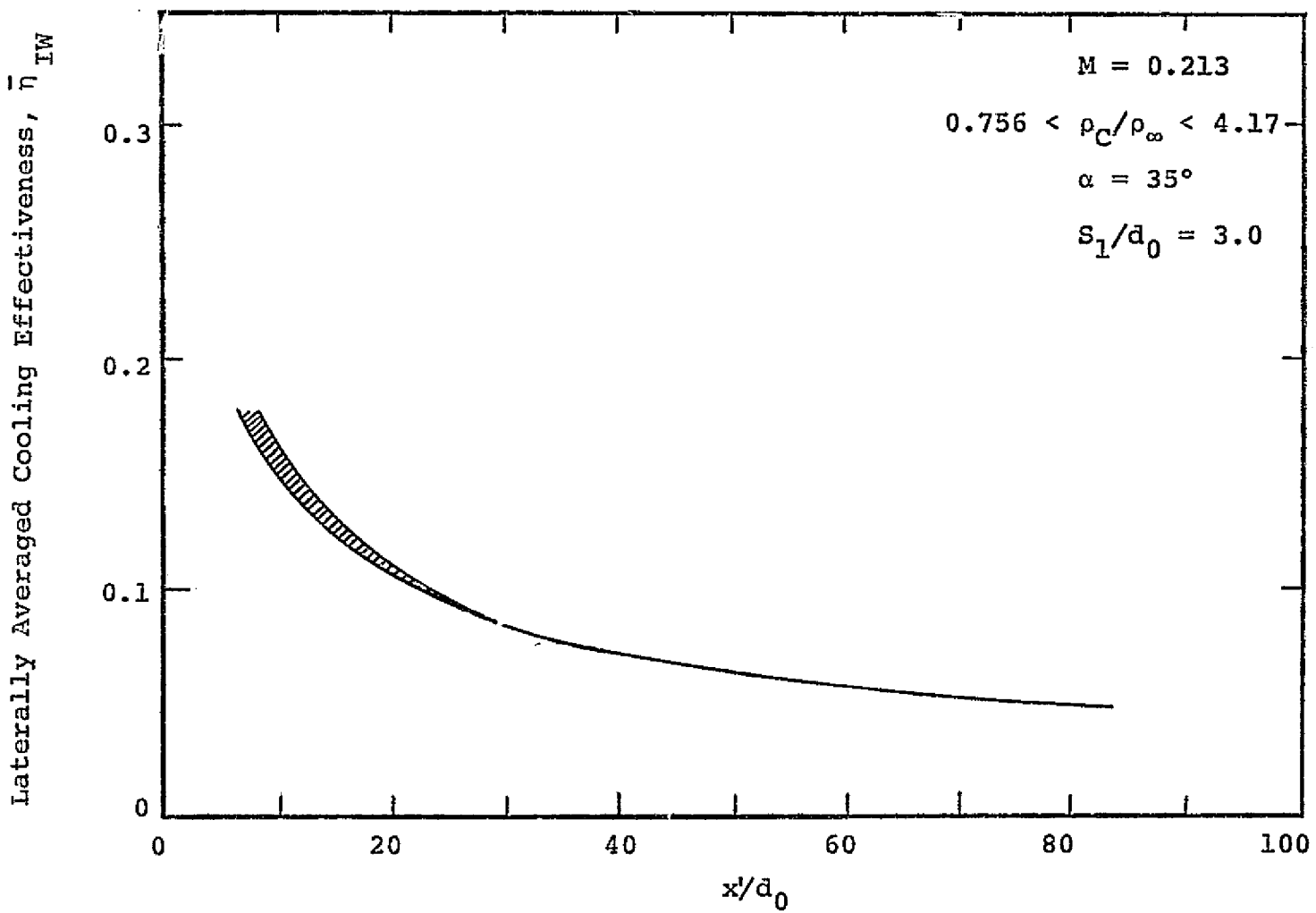

Figure 97(a). Effect of Density Ratio on Laterally Averaged Cooling Effectiveness at M = 0.213 (24).

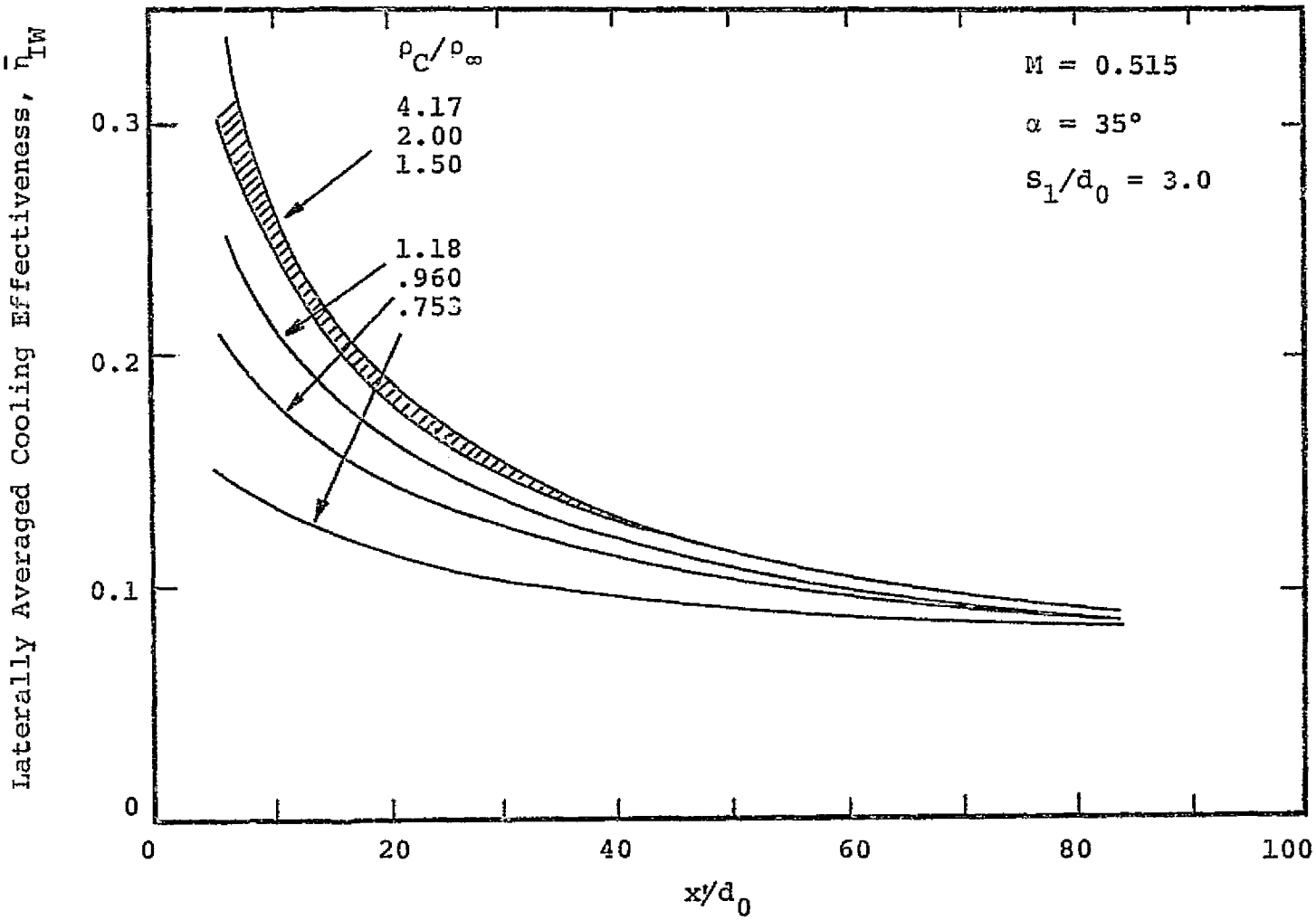

Figure 97(b). Effect of Density Ratio on Laterally Averaged Cooling Effectiveness at M = 0.515 (24).

Figure 97(c). Effect of Density Ratio on Laterally Averaged Cooling Effectiveness at M = 1.05 (24).

performance increases with M (or V_c/V_∞)(due to increased thermal capacity of the coolant) and above which the performance decreases with increasing M (due to enhanced mixing). Consequently, for the range of density ratio associated with Fig. 97(a), V_c/V_∞ never exceeds 0.28 and the mixing effects should be minimal. This is substantiated by the small shaded region which characterizes the variation in $\bar{\eta}_{IW}$ due to the variation of density ratio from 0.76 to 4.17.

For M = 0.515, shown in Fig. 97(b), the velocity ratio ranges from 0.12 to 0.68. The variation in $\bar{\eta}_{IW}$ for ρ_c/ρ_∞ between 1.50 and 4.17 is small since this corresponds to V_c/V_∞ less than 0.34. However, for ρ_c/ρ_∞ between 1.18 and 0.753, V_c/V_∞ varies from 0.44 to 0.68. Since this velocity ratio range includes and surpasses the previously noted value (~0.5) which may be characteristic of significant mixing, this may explain the decrease in $\bar{\eta}_{IW}$ with decreasing ρ_c/ρ_∞ shown by the data.

Figure 97(c), for M = 1.05, shows an even wider separation between the measured effectiveness values for each value of density ratio. The higher values of density ratio (4.17 and 1.97) correspond to velocity ratio values of 0.25 and 0.53, respectively. The lower values of density ratio are characteristic of a coolant-to-gas velocity ratio well above 0.5. Consequently, the data exhibit a strong dependence of $\bar{\eta}_{IW}$ on ρ_c/ρ_∞. However, as ρ_c/ρ_∞ increases above 1.50 ($V_c/V_\infty > 0.7$), the low value of $\bar{\eta}_{IW}$, presumably mixing dominated, is relatively insensitive to further increases in V_c/V_∞. One can also expect that, for higher values of M, all curves begin to collapse into a single correlation since V_c/V_∞ would be greater than 0.5 for all values of density ratio investigated.

Pedersen's findings indicate that the prediction methods illustrated by the previous example may prove inadequate for determining q''_{FC}/q''_0 under conditions wherein there are large differences in density ratio from the model data to the predicted case. The main difficulty, of course, arises from the necessary change in V_C/V_∞ to maintain the same M for increases in ρ_C/ρ_∞. If no velocity-related mixing effects occurred, the extension of the aforementioned prediction methods to other than small density ratio variations would prove valid.

To illustrate the magnitude of the velocity ratio effect, Fig. 98 was prepared using Pedersen's results for effectiveness values as a function of ρ_C/ρ_∞. The predicted fractional reduction of heat flux due to film cooling is shown as a function of θ'_C. The open symbols represent results for M = 0.515 at $x'/d_0 = 20$ (Fig. 97(b). The solid symbols are associated with M = 1.05 at the same distance from injection (Fig. 97(c)). These two values of M and $x'/d_0 = 20$ were chosen since the effectiveness was previously shown to be sensitive to ρ_C/ρ_∞ variations at these conditions. Circular symbols represent values of q''_{FC}/q''_0 predicted using the adiabatic wall effectiveness method assuming that $\overline{\eta}_{ADW}$ was not a function of ρ_C/ρ_∞. Values for $\overline{\eta}_{ADW}$ were obtained from Pedersen's data by interpolating for $\rho_C/\rho_\infty = 1.0$. The square symbols show the heat flux reduction predicted using the results for $\overline{\eta}_{ADW}$ from Pedersen at the correct value of ρ_C/ρ_∞.

A gas temperature of 1922°K (3460°R) and a constant wall temperature of 961°K (1730°R) were assumed for the sample calculations of Fig. 98. The value of T_C was varied between T_{T_∞} and 0.24 T_{T_∞} (θ'_C from 0 to 1.52) and $\overline{\eta}_{ADW}$ was evaluated at the appropriate value of ρ_C/ρ_∞ in one case and

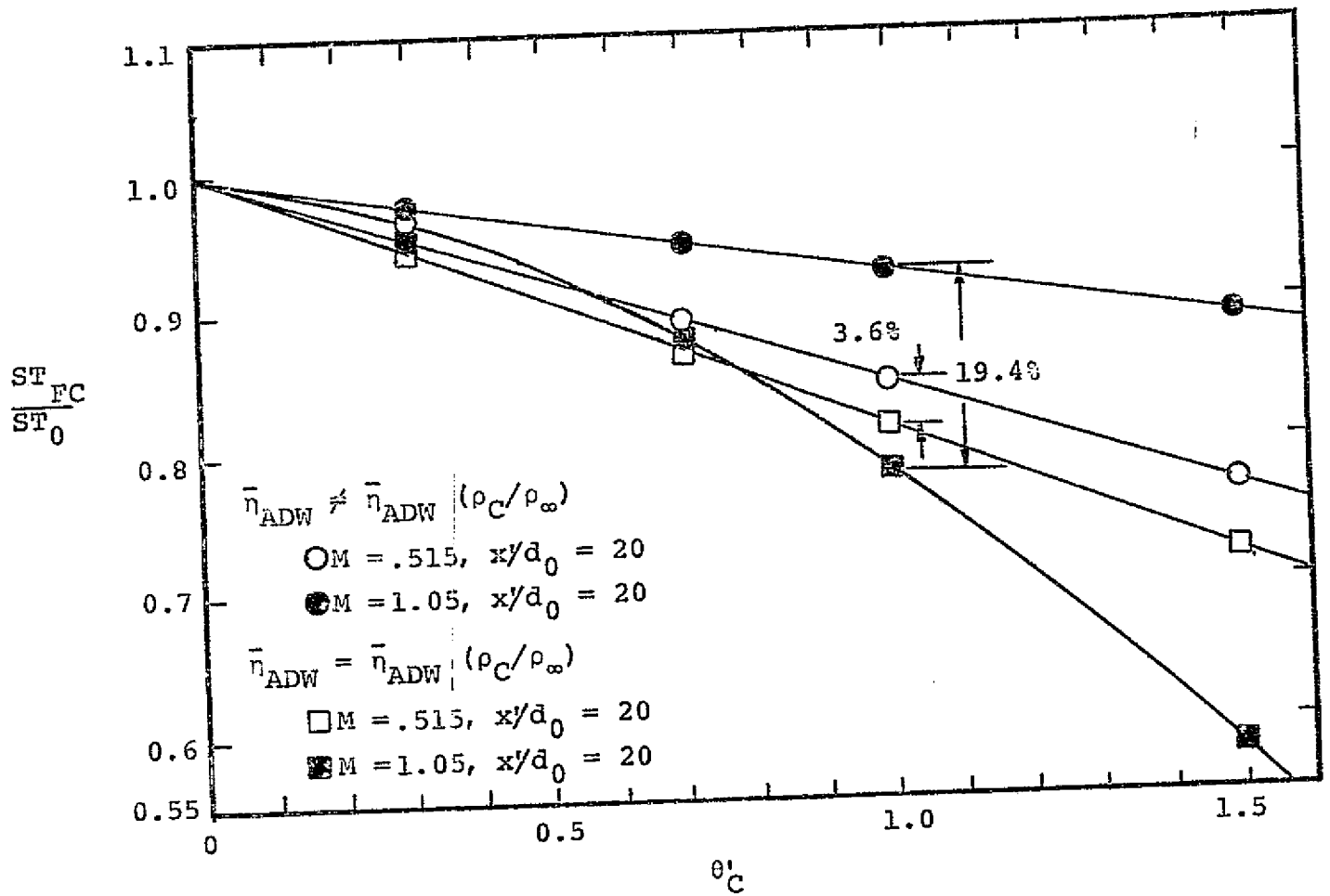

Figure 98. Predicted Film Cooling Stanton Number Ratios Using Both $\bar{\eta}_{ADW}$ at $\rho_C/\rho_\infty \approx 1$ and $\bar{\eta}_{ADW}$ as a Function of ρ_C/ρ_∞.

assumed independent of ρ_c/ρ_∞ in the other. The following relation was used to determine the heat flux reduction due to film cooling,

$$\frac{q''_{FC}}{q''_0} = \left(\frac{h_{\theta'_c=0}}{h_0}\right)\left(1 - \bar{\eta}_{ADW}\,\theta'_c\right) \qquad (110)$$

The hydrodynamic effects of blowing on the heat transfer coefficient were neglected to simplify the comparison (i.e. $h_{\theta'_c=0}/h_0 = 1$).*

The reader is now referenced to the open symbols illustrated on Fig. 98. They correspond to a blowing ratio of 0.515 at $x'/d_0 = 20$. Focusing on $\theta'_c = 1.0$ (a representative condition for turbine cooling applications), a 3.6% difference in q''_{FC}/q''_0 is shown between the prediction which assumes $\bar{\eta}_{ADW}$ is not a function of ρ_c/ρ_∞ (circular symbol) and the prediction which accounts for the $\bar{\eta}_{ADW}$ variation with ρ_c/ρ_∞ (square symbol). As θ'_c increases from unity, the percentage difference between the two prediction methods increases.

Examining similar predictions for M = 1.05 at $x'/d_0 = 20$, represented by solid symbols in Fig. 98, a difference of near 19% is shown between the two prediction techniques due to the effects of ρ_c/ρ_∞. As for the previous case (M = 0.515), the difference in the predicted reduction of heat flux increases significantly as θ'_c increases above 1.0. As θ'_c is increased, ρ_c/ρ_∞ increases (maintaining T_{T_∞} and T_W constant)

---

*It is recognized that at the higher value of M hydrodynamic blowing effects may be significant. However for $\bar{\eta}_{ADW} = \bar{\eta}_{ADW}(\rho_c/\rho_\infty)$, the effect of blowing will diminish as θ'_c increases from zero since V_c/V_∞ must decrease with ρ_c/ρ_∞ increasing (i.e. square symbols on Fig. 98). Therefore the percentage differences between the two prediction methods may, in fact, be even greater than shown.

with a subsequent decrease in V_c/V_∞ required to maintain M constant. Consequently, injection related mixing is diminished resulting in an ever improving cooling capacity relative to the prediction which ignores the dependence of $\bar{\eta}_{ADW}$ on ρ_c/ρ_∞.

The difference between the two predictions of the reduction of heat flux due to film cooling is particularly important to note in relation to calculating q''_{FC}/q''_0 for turbine cooling applications. Typical values of θ'_c for turbine conditions would be somewhat greater than unity; the coolant temperature would approach the wall temperature only after extensive use as an internal convective coolant. Therefore, extending predictions of the reduction of heat flux to lower coolant temperatures ($\theta'_c > 1.0$) would result in progressively more conservative estimates if the effects of V_c/V_∞ (as manifest by ρ_c/ρ_∞) are not considered.

The following section presents a discussion, in light of Pedersen's findings, concerning the extension of the results of the subject investigation to other than the modeled turbine conditions.

VI.3. Use of Present Data

The data for the reduction of heat flux from the subject investigation are a true representation of the film cooling capability of an injection configuration consisting of a single row of spanwise angled holes in the leading edge region of a turbine vane. Specifically, the measured values of q''_{FC}/q''_0 are characteristic of an average gas-to-coolant temperature ratio (T_{T_∞}/T_c) of 2.18 with a gas-to-wall temperature ratio (T_{T_∞}/T_W) near 2.15. Consequently, all of the data from this investigation correspond to $\theta'_c = 1.03$. Typically, turbine cooling

conditions are represented within a rather narrow range of θ_c'. A limiting case in which the coolant air has been utilized to the maximum for internal convection prior to ejection as film coolant occurs at $\theta_c' = 1$ ($T_c = T_w$). However, values of θ_c' up to 1.2 or 1.3 are conceivable. Extrapolation of the results from the subject investigation to θ_c' values in the range of 1.3 would be useful to permit a wider application of the data.

Consider extending the results from Case I herein to predict the reduction of heat flux due to injection of film coolant with a lower T_c, i.e. $\theta_c' > 1.03$. For example, let us examine film cooling of the location $(x-x_i)/d_0 = 10.45$ using a blowing ratio of $M = 1.05$. For the subject experiments, $\theta_c' = 1.03$, and the corresponding value of q''_{FC}/q''_0 is 0.71 (based on the least squares curve from Fig. 44). Figure 99 illustrates the extrapolation of q''_{FC}/q''_0 to higher values of θ_c', indicating the uncertainty in the slope of the extrapolation curve. Depending upon the value of M, both che slope (for a linear approximation) or the degree of the polynomial (for the case in which ρ_c/ρ_∞ effects can be determined) representing the variation of q''_{FC}/q''_0 are unknown. The most significant item to note in Fig. 99 is that the single point shown is a <u>true</u> representation of q''_{FC}/q''_0 for a density ratio, ρ_c/ρ_∞, of 2.18. The major difficulties in extrapolating q''_{FC}/q''_0 are:

(1) the choice of a representative value of q''_{FC}/q''_0 at $\theta_c' = 0$ and

(2) the determination of the proper functional representation of q''_{FC}/q''_0 vs θ_c'.

Fortunately, the value of q''_{FC}/q''_0 at $\theta_c' = 0$, i.e. the hydrodynamic effect, is well documented for a range of blowing ratios and injection

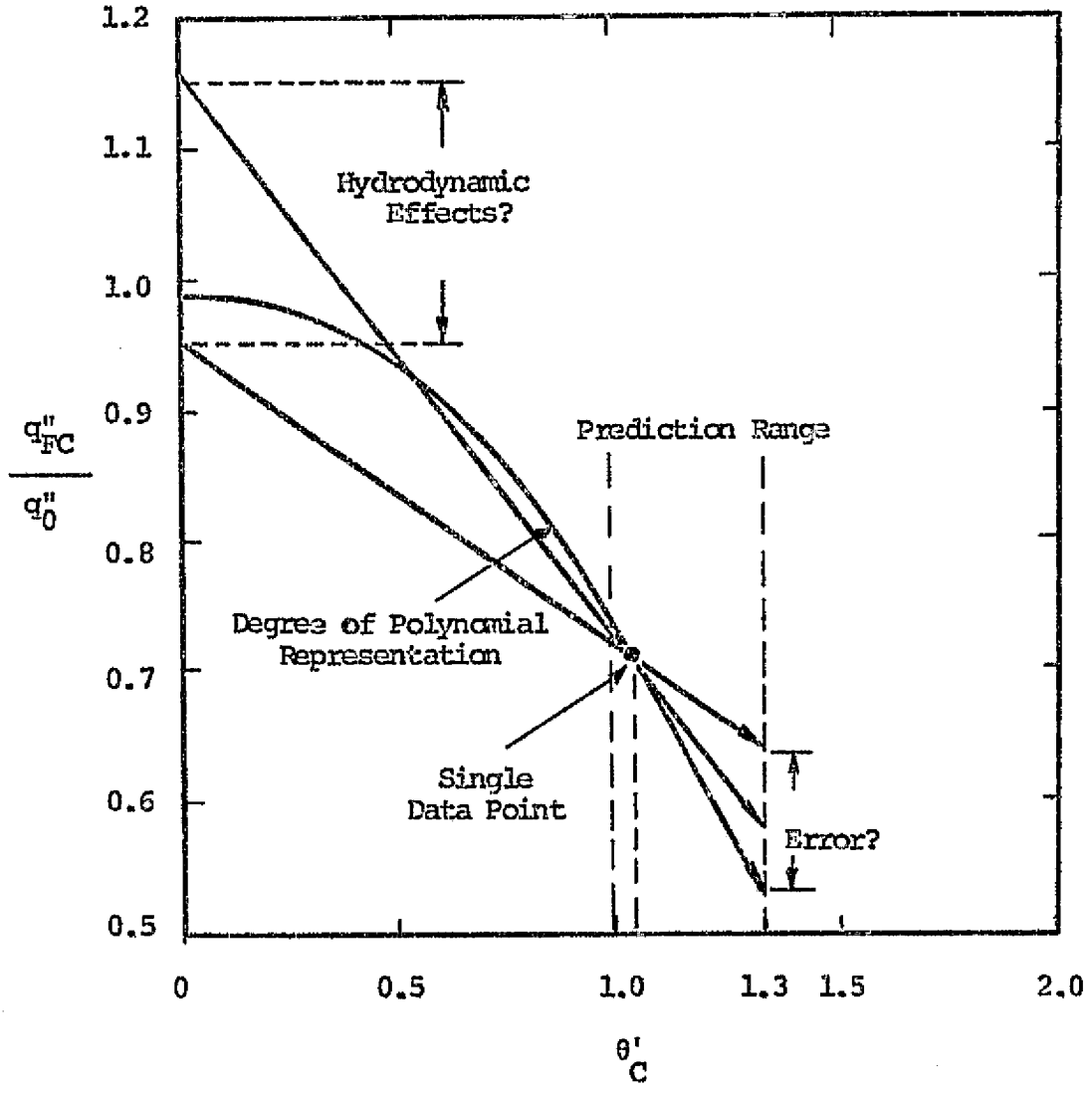

Figure 99. Possibilities in Predicted Film Cooling Heat Flux Using A Single Data Point.

geometries (20). Depending upon M and $(x-x_i)/d_0$, the value of q''_{FC}/q''_0 for $\theta'_C = 0$ (i.e. $T_C = T_{T_\infty}$) may vary from 0.95 to 1.3 for a typical single row configuration of $S_1/d_0 = 3.0$. In the absence of density ratio effects, a linear extrapolation of q''_{FC}/q''_0 from the subject data point to other values of θ'_C can be employed. Figure 99 gives an indication of the extremes of the linear extrapolation depending on the magnitude of the hydrodynamic effect.

The largest error between the linear extrapolation and the true variation of q''_{FC}/q''_0 with θ'_C will occur when the true representation is most nonlinear. Recalling the discussion from Fig. 98, the predictions of q''_{FC}/q''_0 using Pedersen's data showed the greatest nonlinearity with θ'_C at the highest values of blowing ratio (M = 1.05). In addition, the regions rearest injection (i.e. $x'/d_0 \approx 10$) were more sensitive to changes in ρ_C/ρ_∞ or V_C/V_∞ than farther downstream. Pedersen's results have been used to provide a comparison between the proposed linear approximation and the true, nonlinear variation of q''_{FC}/q''_0 vs. θ'_C as presented below.

For Case I of the subject study, with $(x-x_i)/d_0 = 10.45$, $\theta'_C = 1.03$, $T_{T_\infty}/T_W = 2.15$, q''_{FC}/q''_0 has a value of 0.71 for M = 1.05. This corresponds closely to a case for which Pedersen presents data (i.e. $x'/d_0 = 10$, M = 1.05) showing the influence of ρ_C/ρ_∞. Figure 100 shows a linear extrapolation of q''_{FC}/q''_0 vs. θ'_C through the subject data point with the hydrodynamic effect (at $\theta'_C = 0$) evaluated from data presented by Eriksen (20). Also presented in Fig. 100 is a nonlinear representation of q''_{FC}/q''_0 vs. θ'_C derived using the data from Fig. 97. Reference to Eq. (100) shows that q''_{FC}/q''_0 can be expressed as

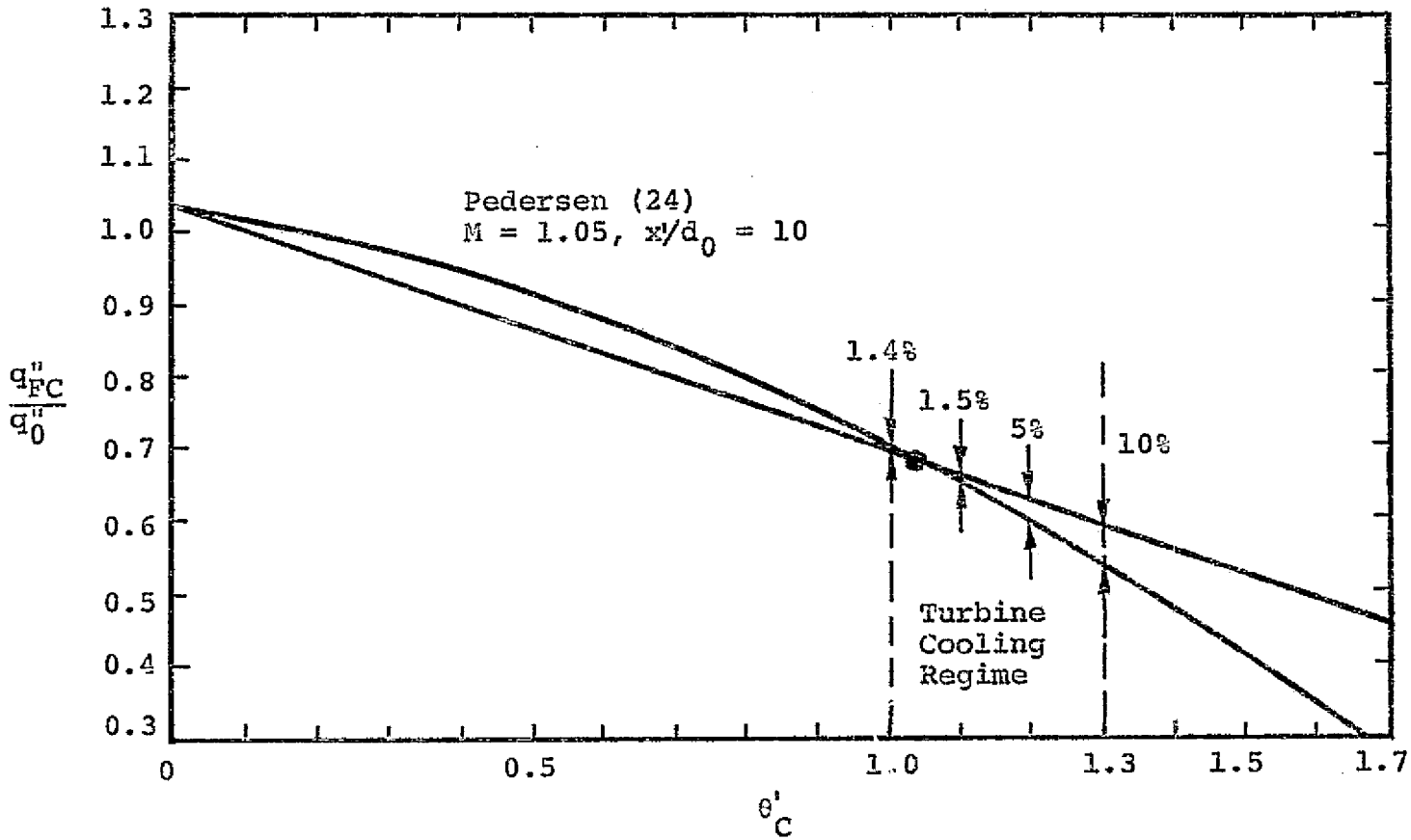

Figure 100. Illustration of Possible Error Incurred By Linear Extrapolation From Single Data Point.

$$\frac{q''_{FC}(\theta'_C)}{q''_0} = \frac{q''_{FC}(\theta'_C = 0)}{q''_0} \left[1 - \bar{\eta}_{ADW}\, \theta'_C\right] \qquad (111)$$

Equation (111) was used to generate the nonlinear variation of q''_{FC}/q''_0 vs. θ'_C as follows. For a selected value of θ'_C (maintaining $T_{T_\infty}/T_W = 2.15$), a value of T_C/T_{T_∞} and ρ_C/ρ_∞ was calculated. For that density ratio, $\bar{\eta}_{ADW}$ (i.e. $\bar{\eta}_{IW}$) was determined from Fig. 97(c) at $x'/d_0 = 10$. Noting that M is to be held constant at 1.05, the value of V_C/V_∞ was computed. This value of the velocity ratio dictates the hydrodynamic effect manifest in $q''_{FC}(\theta'_C = 0)/q''_0$. A value of q''_{FC}/q''_0 for $T_C = T_{T_\infty}$ (i.e. $\theta'_C = 0$) was obtained at the corresponding value of V_C/V_∞ from Eriksen (20) for a cooling configuration identical to Pedersen's. Eq. (111) was used to calculate q''_{FC}/q''_0 for selected values of θ'_C with the nonlinear variation shown in Fig. 100.

In Fig. 100, the region marked "turbine cooling regime" provides an estimate of the error in the predicted value of q''_{FC}/q''_0 due to the linear extrapolation for the subject case. For a known value of q''_{FC}/q''_0 at $\theta'_C = 1.03$, the heat flux ratio at $\theta'_C = 1.0$ and $\theta'_C = 1.3$ predicted from the linear relation would be in error by only 1.4% and 10%, respectively.

Although it is recognized that data for $q''_{FC}(\theta'_C=0)/q''_0$ are not available for <u>exactly</u> the same cooling configuration as used in the present study, values obtainable for similar geometries would probably be representative. For a variation of q''_{FC}/q''_0 with θ'_C that is truly linear, small errors in the assumed value of $q''_{FC}(\theta'_C=0)/q''_0$ will not result in significant errors for extrapolation in the range $\theta'_C = 1.0$ to 1.3. If q''_{FC}/q''_0 at $\theta'_C = 0$ is in error by as much as 10%, the error incurred by

extrapolating linearly from $\theta_C' = 1.03$ to $\theta_C' = 1.3$ is less than 4%. Figure 98 illustrates that the linear relationship improves for low values of M and large values of x'/d_0 and was a good approximation for that case for $M = 0.5$ and x'/d_0 as low as 20.

In summary, it has been shown that the data of the subject investigation can be extended to predict the reduction in heat flux due to film cooling for a narrow range of coolant temperatures. A linear extrapolation of measured values of q''_{FC}/q''_0 at $\theta_C' = 1.03$ should be accurate within 10% for $1.0 \leq \theta_C' \leq 1.3$. The methodology used to extend the current results to a wider range of turbine cooling conditions can be summarized as follows:

(1) For a particular configuration (i.e. Cases I - V), a value of q''_{FC}/q''_0 (i.e. ST_{FC}/ST_0) is known for each M and $(x-x_i)/d_0$.

(2) Choosing values of $(x-x_i)/d_0$ and M of interest, the appropriate q''_{FC}/q''_0 is noted. A coordinate pair $[(q''_{FC}/q''_0)_1, \theta_C' = 1.03]$ can be plotted on a $(q''_{FC}/q''_0) - \theta_C'$ plane.

(3) The value of q''_{FC}/q''_0 at $\theta_C' = 0$ for the M of interest is determined from a published source for a similar geometry, and

(4) A straight line between the two heat flux ratios at $\theta_C' = 0$ and $\theta_C' = 1.03$ is then used to interpolate for q''_{FC}/q''_0 at other values of θ_C'.

VII. COMPARISON OF RESULTS WITH PUBLISHED DATA

As noted in Section II.2. (Literature Review of Important Cooling Parameters), there is a vast amount of information pertaining to previous analytical and experimental studies of film cooling. To provide some perspective it is desired to compare the results of the present study with published data conducted under similar cooling conditions.

The author knows of no available experimental data which would permit a direct comparison. Two features of the subject investigation set the subject results quite apart from published data: (1) film cooling heat transfer measurements were made downstream from a single row of laterally angled holes at a surface spacing-to-diameter ratio of 4.0, and (2) the heat transfer measurements were taken with a coolant-to-gas density ratio of 2.18. The work reported by Pedersen (24) provides similar data for the adiabatic wall effectiveness with density ratio in the same range. Though the injection geometry is different (streamwise angled holes), his investigation is perhaps the best reference for comparison to the present data. By correcting Pedersen's cooling effectiveness data to correspond to the spacing ratio used in the subject investigation (Pedersen had $S_1/d_0 = 3.0$) a comparison can be made between the heat flux reduction due to film cooling from a row of holes (Pedersen) angled at 35° in the streamwise direction and that for injection from a row of holes angled at 35° in the spanwise direction (present study).

Pedersen conducted a mass transfer study. His results, however, are analogous to heat transfer. The data are reported in the form of a laterally-averaged, adiabatic effectiveness, $\bar{\eta}_{ADW}$.

Equation (90), developed for the adiabatic wall temperature method was used to convert Pedersen's results to a heat flux reduction. Recall that Eq. (90) is of the form

$$\frac{q''_{FC}}{q''_0} = \left(\frac{\bar{h}_{\theta'_C=0}}{h_0}\right)\left[1 - \bar{\eta}_{ADW} \cdot \theta'_C\right] \tag{112}$$

Three items are of importance in using Eq. (112) for comparison to the present data:

(1) $\bar{\eta}_{ADW}$ values must be adjusted to correspond to a spacing-to-hole diameter ratio similar to the present study,

(2) values of $\bar{\eta}_{ADW}$ must be consistent with the dimensionless coolant temperature (i.e. effectiveness data must be at same density ratio as subject study) and

(3) the hydrodynamic "blowing" effect, $(h_{\theta'_C=0}/h_0)$, must be determined as a function of M and distance from injection.

Item (1) through (3) will now be discussed in more detail in the following paragraphs.

To contrast the 35° streamwise injection configuration of Pedersen to the 35° spanwise injection of the present study, compensation must be made for the additional geometric parameter not common to both studies; namely, the spacing-to-hole diameter ratio. Pedersen had an $S_1/d_0 = 3.0$ in contrast to $S_1/d_0 = 4.0$ for the subject investigation. Liess and Carnel (16) (as noted in the literature review) examined the spacing ratio effect on the cooling effectiveness for streamwise injection at

$\alpha = 35°$. Spacing ratios of $S_1/d_0 = 2.22$, 3.33 and 4.0 are reported for a single value of the blowing ratio of 0.85. From their results, laterally-averaged adiabatic film effectiveness values can be determined for each spacing ratio out to $x'/d_0 = 25$.

To correct Pedersen's values of $\bar{\eta}_{ADW}$ to a spacing-to-hole diameter ratio of 4.0, the following assumptions were made using the data of Liess and Carnel (16):

(1) the percentage change in $\bar{\eta}_{ADW}$ due to a variation in S_1/d_0 is independent of the value of M, and

(2) a smooth extrapolation of $\bar{\eta}_{ADW}$ from $x'/d_0 = 25$ to $x'/d_0 = 80$ for the three values of spacing ratio investigated by Liess and Carnel.

Interpolating between $S_1/d_0 = 2.22$ and $S_1/d_0 = 4.0$ from reference (16), the corresponding values of effectiveness at $S_1/d_0 = 3.0$ were compared to those at 4.0 at each x'/d_0 from 10 to 80. Generally, $\bar{\eta}_{ADW}$ at $S_1/d_0 = 4.0$ was between 14% and 20% lower than at $S_1/d_0 = 3.0$. This correction factor, transforming the value of $\bar{\eta}_{ADW}$ at $S_1/d_0 = 3.0$ to $S_1/d_0 = 4.0$, can be incorporated into Eq. (112) in the following manner

$$\frac{q''_{FC}}{q''_0} = \left(\frac{\bar{h}_{\theta'_C=0}}{h_0}\right)\left[1 - \bar{\eta}_{ADW}\, S^*\, \theta'_C\right] \qquad (113)$$

where S^* = correction factor to adjust $\bar{\eta}_{ADW}$ from $S_1/d_0 = 3.0$ to 4.0; a function of distance from injection, x'/d_0.

The present investigation was conducted with a coolant-to-gas density ratio of 2.18. With the gas and wall temperatures remaining nearly constant ($T_{T_\infty}/T_W \approx 2.15$), θ'_C was typically 1.03. For $\rho_C/\rho_\infty = 2.18$, $\bar{\eta}_{ADW}$ values from Pedersen were interpolated between $\rho_C/\rho_\infty \approx 2.0$

and 4.17. Equation (113) then takes the form

$$\frac{q''_{FC}}{q''_0} = \left(\frac{h_{\theta'_C=0}}{h_0}\right)\left[1 - 1.03\,(\bar{\eta}_{ADW})_{2.18}\,S^*\right] \qquad (114)$$

where $(\bar{\eta}_{ADW})_{2.18}$ = adiabatic wall effectiveness evaluated at $\rho_C/\rho_\infty = 2.18$.

Eriksen (20) reports values for the hydrodynamic effect ($h_{\theta'_C=0}/h_0$) for x'/d_0 up to 100 and M ranging from 0.2 to 2.0. However, these results were for streamwise injection at 35° with $S_1/d_0 = 3.0$. Since no information was available concerning the hydrodynamic effects for $S_1/d_0 = 4.0$, $h_{\theta'_C=0}/h_0$ was taken as 1.0 in the use of Eq. (114) to transform Pedersen's data.

Figure 101 was prepared using Eq. (114) in conjunction with Pedersen's adiabatic wall effectiveness data. Figures 101(a), (b) and (c) contrast the reduction in heat flux due to film cooling for Case V for the subject investigation (solid curves) to the transformed values using Pedersen's data corrected to $S_1/d_0 = 4.0$ (broken curves). Streamwise injection at 35° to the surface is represented by the broken line, while spanwise injection at 35° is shown as the solid line. Figures 101(a), (b) and (c) are for a blowing ratio of 0.213, 0.515 and 1.05, respectively, for x'/d_0 ranging from 10 to 80.

From the comparison in Fig. 101 it appears that the streamwise injection configuration is more effective in reducing the local heat flux than the spanwise injection scheme. At M = 0.213 (Fig. 101(a)) streamwise injection shows q''_{FC}/q''_0 values approximately 7% lower at $x'/d_0 = 10$. However, at $x'/d_0 = 80$ the difference is less than 2%. At this low value of blowing ratio, the decay of the film cooling effectiveness (i.e. rate

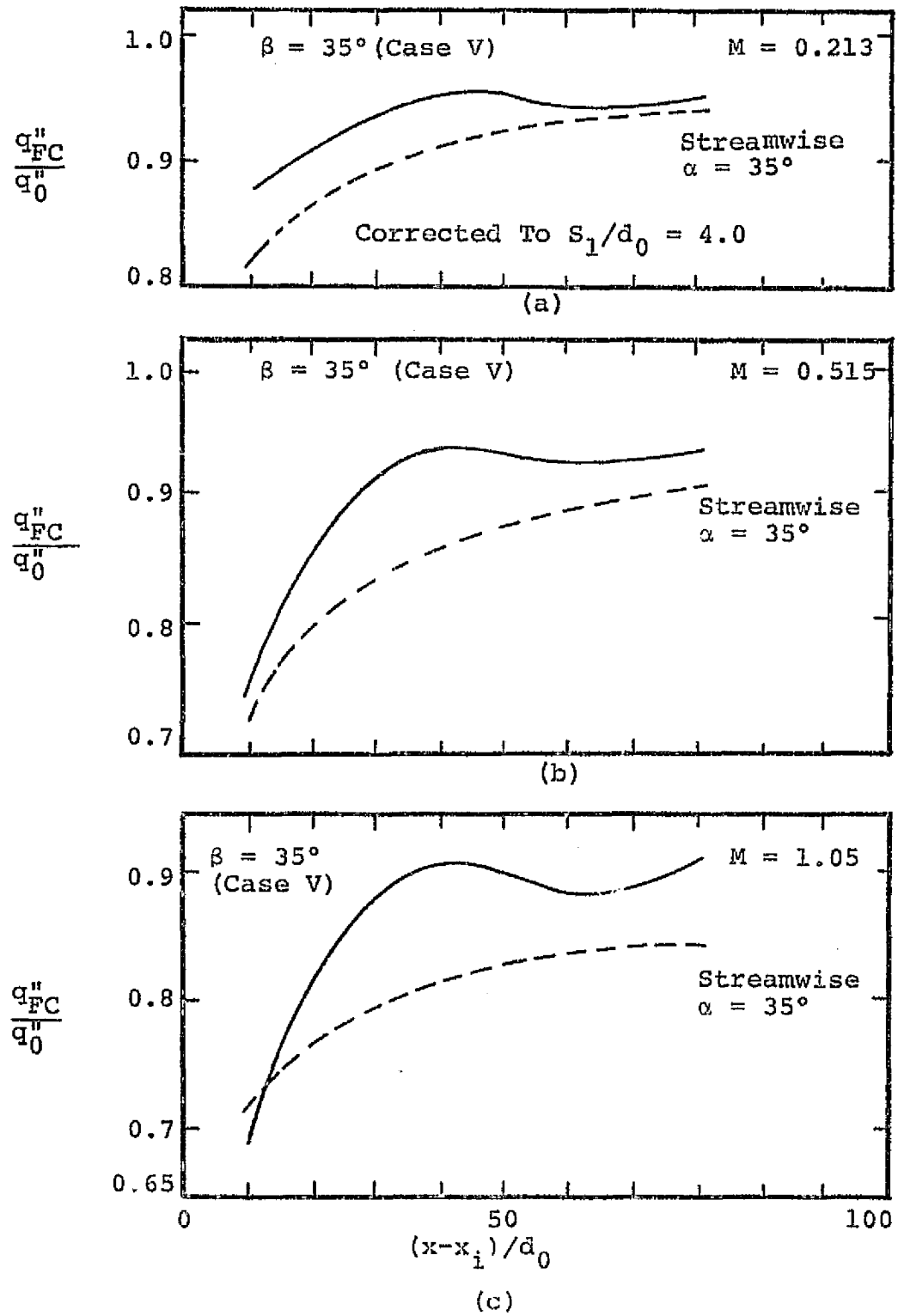

Figure 101. Comparison of Present Data With That of Pedersen, Corrected For Spacing Ratio and Blowing Effects.

of increase of q''_{FC}/q''_0 with x'/d_0) is approximately the same for both configurations.

At M = 0.515, shown in Fig. 101(b), the value of q''_{FC}/q''_0 is nearly the same for $\alpha = 35°$ and $\beta = 35°$ at $x'/d_0 = 10$. However, the rate of increase of q''_{FC}/q''_0 with x'/d_0 is more severe for spanwise injection at this blowing ratio, especially in the range x'/d_0 of 20 to 40. At the farthest location from injection, streamwise injection is still 4% better than the spanwise configuration.

Finally, Fig. 101(c) contrasts the two configurations at M = 1.05. At $x'/d_0 = 10$, the two injection schemes yield essentially the same values for q''_{FC}/q''_0. Again the rate of increase of q''_{FC}/q''_0 with x'/d_0 for $\alpha = 35°$ is more pronounced than for $\beta = 35°$ but roughly the same as was noted for M = 0.515. For spanwise injection, q''_{FC}/q''_0 is nearly 7% higher at $x'/d_0 = 20$ and 11% greater at $x'/d_0 = 40$ compared to injection with $\alpha = 35°$. These differences are somewhat higher than at the lower blowing ratio of 0.515. At $x'/d_0 = 80$ the streamwise configuration is still 7% more effective than spanwise injection.

It should not be surprising that spanwise injection is less effective in reducing q''_{FC}/q''_0 than streamwise injection. With no initial component of the coolant momentum in hhe freestream direction, spanwise injection would probably create a greater flow disturbance near injection. It is noteworthy that spanwise injection appears to be nearly as effective in reducing q''_{FC}/q''_0 near injection (i.e. $x'/d_0 \approx 10$). Overall, the two configurations do not appear to differ more than 11%. For leading edge cooling, where curvature may be a constraint on the minimum

streamwise angle that can be incorporated, the penalty for spanwise injection (as illustrated in Fig. 101) may not be as severe as would be incurred for steeper streamwise injection angles.

VIII. CONCLUSIONS

The results from an experimental investigation of film cooling in the leading edge region of a turbine vane model were presented. A single row of holes, angled spanwise to the main flow at either 18° or 35° to the surface, was used to inject cool air (ρ_c/ρ_∞ = 2.18) into the suction surface boundary layer at x_i/L_s values of 0.0833, 0.150 or 0.228. The effects of cool mass addition on the reduction in the local Stanton number were measured for the six combinations of injection angle and location.

During the entire investigation, all flow conditions external to the test surface were maintained at nearly constant values and corresponded to a simulation of a high temperature and high pressure environment. Gas-to-wall and coolant-to-gas temperature ratios were held nearly uniform with average values of 2.15 and 2.18, respectively. The inlet turbulence intensity remained at 6.6% during the course of the film cooling study.

From the analysis of the results the following conclusions can be drawn concerning the effects of film cooling on the value of ST_{FC}/ST_0 for the investigated configurations:

1. For film cooling injection in the leading edge region of a turbine vane at injection angles of β = 18° and β = 35° (Cases I - V), the local film cooling heat flux was reduced compared to uncooled conditions (i.e. $ST_{FC}/ST_0 < 1$) by increasing the blowing ratio, M.

2. The value of M at which the greatest heat flux reduction occurred ($M_{OPT,NEAR}$) was a function of both the angle of injection, β, and the location of injection, x_i/L_S:

   a. Decreasing the angle of injection reduced the effective normal component of the coolant momentim, I sin β (where $I = (\frac{\rho_\infty}{\rho_C}) M^2$). The use of the shallower injection angle permitted a larger film coolant blowing ratio, M, before the film cooling performance began to decrease due to excessive mixing. The critical value of blowing ratio, $M_{OPT,NEAR}$, was observed to be 0.85 and 1.05 for $\beta = 35°$ and 18°, respectively (for moderate values of freestream acceleration, $K_i \sim 1 \times 10^{-6}$).

   b. Injecting closer to stagnation (i.e. into a thinner boundary layer) caused $M_{OPT,NEAR}$ to increase. It is expected that, for a constant injection angle and blowing ratio, the coolant will remain nearer to the wall for injection into a thinner boundary layer. Steep injection angles allow the coolant to mix more freely with the mainstream, resulting in decreased cooling effectiveness. For injection into a thinner boundary layer, a larger value of M is permitted before the cooling performance begins to deteriorate due to mixing. For $\beta = 18°$, the following trend was noted:

Optimum Blowing Ratio, $M_{OPT,NEAR}$	Momentum Boundary Layer θ_i/d_0
1.3	0.013
1.05	0.036
0.5	0.051

A similar trend was noted for $\beta = 35°$, however, due to the possible influence of local freestream acceleration at this steeper angle, the full impact of changing θ_i/d_0 could not be assessed.

The increase in $M_{OPT,NEAR}$ due to decreasing both β and θ_i/d_0 can be of benefit to a designer who may be concerned with hot gas ingestion into the coolant holes. In the leading edge region, the difference between the local hot gas pressure and the coolant supply pressure may not be large. Consequently, small variations in the total gas pressure or coolant supply pressure could lead to back flow through the coolant holes. The subject investigation has indicated that optimum cooling in the leading edge region is achieved with high values of the blowing ratio which may be helpful to insure a safe margin in pressure between the coolant and hot gas.

3. Values of M corresponding to a minimum in ST_{FC}/ST_0 support the results of Pedersen (24) which indicate that the velocity ratio, V_C/V_∞, may play an important role in determining how effective a given amount of coolant can be in reducing the local heat flux. Values of V_C/V_∞ between 0.4 and 0.5 have been reported (24) to yield the highest cooling effectiveness for all density ratios, ρ_C/ρ_∞, for streamwise injection. For $\beta = 18°$ at $\theta_i/d_0 =$ 0.013 and 0.036, the corresponding (V_C/V_∞) values for the observed $M_{OPT,NEAR}$ were 0.596 and 0.482, respectively.

4. For moderate levels of the freestream acceleration at injection (i.e. $K_i \lesssim 1 \times 10^{-6}$), decreasing the injection angle from $\beta = 35°$ to $\beta = 18°$ appears to have a minimal effect on ST_{FC}/ST_0. Except for extending the value of $M_{OPT,NEAR}$ to a higher level (with a corresponding improvement in ST_{FC}/ST_0), there is little difference between the cooling potential for both angles up to $M_{OPT,NEAR}$ for $\beta = 35°$. This result may have significant economic implications. For regions of the vane with moderate and low freestream acceleration, the designer need not specify extremely shallow angles (i.e. <35°) to achieve reasonable cooling. Shallow angles are costly. Tooling becomes more intricate and tolerances more difficult to hold as smaller angles are specified. A considerable savings in fabrication costs may be realized if the designer is able to identify regions of the vane in which the local reduced heat flux due to cooling will be essentially insensitive to differences in β below a certain threshold level.

5. Large values of the local freestream acceleration parameter, K_i (i.e. $K_i > 1 \times 10^{-6}$) may reduce the cooling effectiveness markedly under certain injection conditions. The effects of acceleration appear to be coupled to the angle of injection. For injection at $x_i/L_S = 0.0833$ and $K_i = 7.9 \times 10^{-6}$ (i.e. Case IV), the Stanton number ratio was as much as 48% higher for $\beta = 35°$ compared to $\beta = 18°$. At $x_i/L_S = 0.150$ and $K_i = 0.72 \times 10^{-6}$, little difference was noted between the Stanton number ratio for both angles. It appears that by specifying as shallow

BIBLIOGRAPHY

1. Esgar, J.B., Colladay, R.S., and Kaufman, A., "An Analysis of the Capabilities and Limitations of Turbine Air Cooling Methods," NASA TN D-5992, September, 1970.

2. Goldstein, R.J., Eckert, E.R.G., Eriksen, V.L., and Ramsey, J.W., "Film Cooling Following Injection Through Inclined Circular Tubes," Israel Journal of Technology, Vol. 8, No. 1-2, 1970, pp. 145-154.

3. Hartnett, J.P., Birkebak, R.C., and Eckert, E.R.G., "Velocity Distribution, Temperature Distribution, Effectiveness and Heat Transfer For Air-Injection Through A Tangential Slot into A Turbulent Boundary Layer," Journal of Heat Transfer, Vol. 83, No. 3, August, 1961, pp. 293-306.

4. Choe, H., Kays, W.M., and Moffat, R.J., "The Superposition Approach to the Film Cooling of a Uniform Temperature Wall," ASME Paper No. 74 WA/HT - 27, 1974.

5. Eckert, E.R.G., "Transpiration and Film Cooling," Heat Transfer; A Symposium, University of Michigan Press, Ann Arbor, Michigan, 1953.

6. Hartnett, J.P., Birkebak, R.C., and Eckert, E.R.G., "Velocity Distributions, Temperature Distributions, Effectiveness, and Heat Transfer in Film Cooling of a Surface With a Pressure Gradient," Proceedings of the 1961 International Heat Transfer Conference, Part IV, Section A, Paper No. 81, 1961.

7. Eriksen, V.L. and Goldstein, R.J., "Heat Transfer and Film Cooling Following Injection Through Inclined Circular Tubes," ASME Journal of Heat Transfer, May, 1974, pp. 239-245.

8. Papell, S.S., "Effect of Gaseous Film Cooling of Coolant Injection Through Angled Slots and Normal Holes," NASA TN D-299, 1960.

9. Metzger, D.E., Carper, H.J., and Swank, L.R., "Heat Transfer With Film Cooling Near Non-Tangential Injection Slots," Journal of Engineering For Power, Vol. 90, No. 2, April, 1968, pp. 157-163.

10. Metzger, D.E. and Fletcher, D.D., "Surface Heat Transfer Immediately Downstream of Flush Non-Tangential Injection Holes and Slots," AIAA Paper No. 69-523, 1969.

11. Metzger, D.E., Biddle, J.R., and Warren, J.M., "Evaluation of Film Cooling Performance on Gas Turbine Surfaces," AGARD Conference, Proceedings No. 73 on High Temperature Turbines, 1970.

12. Goldstein, R.J., Eckert, E.R.G., and Ramsey, J.W., "Film Cooling With Injection Through a Circular Hole," NASA CR-54604 (University of Minnesota Heat Transfer Laboratory Paper No. 82), 1968.

13. Sivasegaram, S. and Whitelaw, J.H., "Film Cooling Slots; The Importance of Lip Thickness and Injection Angle," Journal of Mechanical Engineering Science, Vol. 11, 1969, p. 22.

14. Kacker, S.C. and Whitelaw, J.H., "The Effect of Slot Height and Slot Turbulence Intensity on the Effectiveness of the Uniform Density, 2-D Wall Jet," ASME Journal of Heat Transfer, Vol. 90, No. 4, November, 1968, p. 469.

15. Burns, W.K. and Stollery, J.L., "The Influence of Foreign Gas Injection and Slot Geometry on Film Cooling Effectiveness," Journal of Heat and Mass Transfer, Vol. 12, 1969, pp. 935-951.

16. Liess, C. and Carnel, J., "Application of Film Cooling To Gas-Turbine Blades," AGARD Conference, Proceedings No. 73 on High Temperature Turbines, 1970.

17. Eckert, E.R.G., "Film Cooling With Injection Through Holes," AGARD Conference, Conference Proceedings No. 73 on High Temperature Turbines, 1970.

18. Eckert, E.R.G., Goldstein, R.J., and Ramsey, J.W., "Film Cooling With Injection Through Holes: Adiabatic Wall Temperature Downstream of a Circular Hole," Journal of Engineering For Power, Vol. 90, No. 4, October, 1968, pp. 384-395.

19. Goldstein, R.J., Eckert, E.R.G., Eriksen, V.L., and Ramsey, J.W., "Film Cooling Following Injection Through Inclined Circular Tubes," University of Minnesota Heat Transfer Laboratory Paper No. 91, 1969.

20. Eriksen, V.L., "Film Cooling Effectiveness and Heat Transfer With Injection Through Holes," University of Minnesota Heat Transfer Laboratory Paper No. 102, 1971.

21. Eriksen, V.L. and Goldstein, R.J., "Heat Transfer and Film Cooling Following Normal Injection Through a Round Hole," ASME Paper No. 74-GT-6, 1974.

22. Amana, O.M., Demuren, H.O., and Louis, J.F., "Studies on Transonic Turbine With Film Cooled Blades: A First Annual Report," MIT Report No. 74-1, 1974.

23. Louis, J.F., Goulios, G.N., Demirjian, A.M., Topping, R.F., and Wiedhope, J.M., "Short Duration Studies of Turbine Heat Transfer and Film Cooling Effectiveness," ASME Paper No. 74-GT-131, 1974.

24. Pedersen, D.R., "Effect of Density Ratio on Film Cooling Effectiveness For Injection Through a Row of Holes and For a Porous Slot," Ph.D. Thesis, University of Minnesota, March 1972.

25. Hiroki, T. and Katsumata, I., "Design and Experimental Studies of Turbine Cooling," ASME Paper No. 74-GT-30, 1974.

26. Metzger, D.E., Takeuchi, D.I., and Kuenstler, P.A., "Effectiveness and Heat Transfer With Full-Coverage Film Cooling," Journal of Engineering For Power, July, 1973, pp. 180-184.

27. Liess, C., "Experimental Investigation of Film Cooling With Ejection From a Row of Holes For the Application To Gas Turbine Blades," ASME Paper No. 74-GT-5, 1974.

28. Sutera, S.P., Maeder, P.F., and Kestin, J., "On the Sensitivity of Heat Transfer in the Stagnation Point Boundary Layer To Freestream Vorticity," Journal of Fluid Mechanics, Vol. 16, 1963, pp. 497-520.

29. Sadeh, W.Z., Sutera, S.P., and Maeder, P.F., "An Investigation of Vorticity Amplification in Stagnation Flow," Journal of Applied Mathematics and Physics, Vol. 21, 1970, pp. 717-742.

30. Sadeh, W.Z., Sutera, S.P., and Maeder, P.F., "Analysis of Vorticity Amplification in the Flow Approaching a Two-Dimensional Stagnation Point," Journal of Applied Mathematics and Physics, Vol. 21, 1970, pp. 699-716.

31. Traci, R.M. and Wilcox, D.C., "Analytical Study of Freestream Turbulence Effects on Stagnation Point Flow and Heat Transfer," AIAA Paper No. 74-515, 1974.

32. Ramsey, J.W. and Goldstein, R.J., "Interaction of a Heated Jet With A Deflecting Stream," University of Minnesota Heat Transfer Laboratory Paper No. 92, 1970.

33. Junkhan, G.H. and Serovy, G.K., "Effects of Freestream Turbulence and Pressure Gradient on Flat-Plate Boundary Layer Velocity Profiles and on Heat Transfer," ASME Journal of Heat Transfer, Vol. 89, No. 2, May, 1967, p. 169.

34. Kearney, D.W., Kays, W.M., and Moffat, R.J., "The Effect of Freestream Turbulence on Heat Transfer to a Strongly Accelerated Turbulent Boundary Layer," Thermosciences Division, Report HMT-9, Stanford University, February, 1970.

35. Julien, H.L., Kays, W.M., and Moffat, R.J., "Experimental Hydrodynamics of the Accelerated Turbulent Boundary Layer With and Without Mass Injection," ASME Journal of Heat Transfer, November, 1971, pp. 373-379.

36. Thielbahr, W.H., Kays, W.M., and Moffat, R.J., "The Turbulent Boundary Layer on a Porous Plate: Experimental Heat Transfer With Uniform Blowing and Suction, With Moderately Strong Acceleration," ASME Journal of Heat Transfer, February, 1972, pp. 111-118.

37. Moretti, P.M. and Kays, W.M., "Heat Transfer to a Turbulent Boundary Layer With Varying Freestream Velocity and Varying Surface Temperature; An Experimental Study," International Journal of Heat and Mass Transfer, Vol. 8, 1965, pp. 1187-1202.

38. Kays, W.M., "Heat Transfer to the Transpired Turbulent Boundary Layer," ASME Paper No. 71-HT-44, 1971.

39. Kays, W.M., Moffat, R.J., and Thielbahr, W.H., "Heat Transfer to Highly Accelerated Turbulent Boundary Layers With and Without Mass Addition," ASME Journal of Heat Transfer, Vol. 92, No. 3, August, 1970, p. 499.

40. Carlson, L.W. and Talmor, E., "Gaseous Film Cooling at Various Degrees of Hot Gas Acceleration and Turbulence Levels," International Journal of Heat and Mass Transfer, Vol. 11, 1968, pp. 1695-1713.

41. Nicolas, J. and Le Meur, A., "Curvature Effects on a Turbine Blade Cooling Film," ASME Paper No. 74-GT-156, 1974.

42. Schlichting, H., Boundary Layer Theory, Sixth Edition, McGraw-Hill, New York, 1968, pp. 258-266.

43. Abramovich, G.N., The Theory of Turbulent Jets, MIT Press, Cambridge, 1963, p. 549.

44. Goldstein, R.J., "Film Cooling," Advances in Heat Transfer, Academic Press, New York, Vol. 7, 1971, pp. 321-379.

45. Hinze, J.O., Turbulence, McGraw-Hill, New York, 1959, pp. 204-219.

46. Batchelor, G.K. and Townsend, A.A., "Decay of Isotropic Turbulence in the Initial Period," Proceedings of Royal Society, London, Vol. 193A, 1948, p. 539.

47. Gardon, R., "A Transducer For the Measurement of Heat-Flow Rate," ASME Journal of Heat Transfer, Vol. 82, No. 4, 1960, pp. 396-398.

48. Coffin, G.R., "A Study of Miniature Heat Flux Meters," M.S. Thesis, Brigham Young University, 1964.

49. Brookley, C.E., "The Circular Foil Heat Flux Gage," Thermogage, Inc. Report.

50. Colladay, R.S. and Stepka, F.S., "Similarity Constraints in Testing of Cooled Engine Parts," NASA TN D-7707, June 1974.

51. Von Karman, T. and Howarth, L., "On the Statistical Theory of Isotropic Turbulence," Proceedings of Royal Society, London, Vol. 164A, 1938, p. 192.

52. Baines, W.D. and Peterson, E.G., "An Investigation of Flow Through Screens," Transactions of the ASME, Vol. 73, 1951, p. 467.

53. Newman, L.B., Sparrow, E.M., and Eckert, E.R.G., "Free-Stream Turbulence Effects on Local Heat Transfer From a Sphere," ASME Journal of Heat Transfer, February, 1972, pp. 7-16.

54. Tsuji, H., "Experimental Studies on the Spectrum of Isotropic Turbulence Behind Two Grids," Journal of the Physical Society of Japan, Vol. 11, No. 10, October, 1956, pp. 1096-1104.

55. Kestin, J. and Wood, R.T., "The Influence of Turbulence on Mass Transfer From Cylinders," ASME Journal of Heat Transfer, November, 1971, pp. 321-327.

56. Van Der Hegge Zijnen, B.G., "Measurements of the Intensity, Integral Scale and Microscale of Turbulence Downstream of Three Grids in a Stream of Air," Applied Science Research, Vol. 7A, 1957, pp. 149-174.

57. Crawford, M.E. and Kays, W.M., "STAN-5--A Program For Numerical Computation of Two-Dimensional Internal-External Boundary Layer Flow," Stanford University, Department of Mechanical Engineering, Report, HMT No. 23, 1975.

58. Patankar, S.V. and Spalding, D.B., "A Finite Difference Procedure For Solving the Boundary Layer Equations For Two-Dimensional Flows," International Journal of Heat and Mass Transfer, Vol. 10, 1967, p. 1389.

59. Horton, H.P., "A Semi-Empirical Theory For the Growth and Bursting of Laminar Separation Bubbles," ARC C.P. 1073, June, 1967.

60. Dunham, J., "Predictions of Boundary Layer Transition on Turbomachinery Blades," AGARD Report No. 164, ONERA, Chatillon-sous-Bagneaux, France, April, 1972, pp. 57-71.

61. Erlich, E., "Methods of Visualizing the Leading Edge Separation Bubble and Analysis of the Results," La Recherche Aerospatiale, No. 1973-4, pp. 41-53.

62. Communications With Dr. R. S. Colladay, Turbine Cooling Branch, NASA Lewis Research Center, Cleveland, Ohio, 1975.

63. Klein, J. and Tribus, M., "Forced Convection From Non-Isothermal Surfaces," Heat Transfer; A Symposium, University of Michigan Press, Ann Arbor, Michigan, 1953.

64. Jabbari, M.Y. and Goldstein, R.J., "Film Cooling Downstream of Two Staggered Rows of Holes Including Effects of Free Stream Acceleration," Reported by R. J. Goldstein, Workshop on Film Cooling, University of Minnesota, May 8, 1975.

65. Librizzi, J. and Cresci, R.J., "Transpiration Cooling of a Turbulent Boundary Layer in an Axisymmetric Nozzle," AIAA Journal, Vol. 2, No. 4, April, 1964, p. 617.

66. Kutateladze, S.S. and Leont'ev, A.I., "The Heat Curtain in the Turbulent Boundary Layer of a Gas," Thermal Physics at High Temperature, Vol. 1, No. 2, 1963, p. 281.

67. Stollery, J.L. and El-Ehwany, A.A.M., "On the Use of a Boundary Layer Model For Correlating Film Cooling Data," International Journal of Heat and Mass Transfer, Vol. 10, 1967, pp. 101-105.

68. Goldstein, R.J. and Haji-Sheikh, A., "Prediction of Film Cooling Effectiveness," Japan Society of Mechanical Engineers, 1967, Semi-International Symposium, Tokyo.

69. Seban, R.A., Chan, H.W., and Scesa, S., "Heat Transfer to a Turbulent Boundary Layer Downstream of an Injection Slot," ASME Paper No. 57-A-36, 1957.

70. Hatch, J.E. and Papell, S.S., "Use of a Theoretical Flow Model to Correlate Data For Film Cooling or Heating by Tangential Injection of Gases of Different Fluid Properties," NASA TN D-130, 1959.

71. Seban, R.A. and Back, L.H., "Velocity and Temperature Profiles in Turbulent Boundary Layer With Tangential Injection," ASME Journal of Heat Transfer, Vol. 84, No. 1, February, 1962, p. 45.

72. Spalding, D.B., "Prediction of Adiabatic Wall Temperatures in Film Cooling Systems," AIAA Journal, Vol. 3, No. 5, May, 1965, pp. 965-967.

73. Nishiwaki, N., Hirata, M., and Tsuchida, A., "Heat Transfer on a Surface Covered by Cold Air Film," International Developments in Heat Transfer, 1961, pp. 675-681.

74. Eriksen, V.L., Eckert, E.R.G., and Goldstein, R.J., "A Model For Analysis of the Temperature Field Downstream of a Heated Jet Injected Into an Isothermal Crossflow at an Angle of 90°", University of Minnesota Heat Transfer Laboratory Paper No. 101, 1971.

75. Wieghardt, K., "Hot-Air Discharge For De-Icing," AAF Translation, Report No. F-TS-919-RE, 1946.

76. Scesa, S., "Effect of Local Normal Injection on Flat Plate Heat Transfer," Ph.D. Thesis, University of California, 1954.

77. Metzger, D.E., "A Summary and Design Recommendations-Film Cooling," Airesearch TR-5025, May, 1968.

78. Samuel, A.E. and Joubert, P.N., "Film Cooling of an Adiabatic Flat Plate in Zero Pressure Gradient in the Presence of a Hot Mainstream and Cold Tangential Secondary Injection," ASME Journal of Heat Transfer, Vol. 87, No. 3, August, 1965, pp. 409-418.

79. Chemical Engineering Progress Symposium, Series No. 41, Vol. 59, 1963, pp. 47-51.

APPENDIX A. MODELS AND CORRELATIONS FOR FILM EFFECTIVENESS

A.1. Analytical Models

A very thorough discussion concerning the differences in film effectiveness predictions for 2-D slot-type models is contained in a review of film cooling by Goldstein (44). Familiarity with those cooling parameters which result from these modeling analyses is essential to the understanding of the vast library of film cooling data and its extension to practical applications. The following discussion on 2-D slot models is summarized from Goldstein (44).

The effectiveness of an injected coolant has been evaluated analytically by a number of investigators using simplified models to solve the integral energy equation. Heat sink models that have been developed differ considerably due to the assumptions concerning the interaction of the coolant and the mainstream boundary layer at injection. The models of Librizzi and Cresci (65) and Kutateladze and Leont'ev (66) both assume a uniform boundary layer temperature, $\bar{T}$, and account for mass addition into the boundary layer at injection. Tribus and Klein (63) use a representative temperature profile but do not account for mass entrainment at injection. Stollery and El-Ehwany (67) neglect mass addition into the boundary layer at injection and assume an average boundary layer temperature, $\bar{T}$. Goldstein and Haji-Sheikh (63) incorporate both phenomena of a reduced temperature profile in the boundary layer as well as mass addition and predict effectiveness values between (65) and (63).

The heat sink model analysis predicts that the adiabatic cooling effectiveness, η_{ADW} can be expressed

$$\eta_{ADW} = \frac{1}{1 + \left(\frac{\dot{m}_\infty}{\dot{m}_C}\right)\left(\frac{C_{p_\infty}}{C_{p_C}}\right)} \qquad \text{(A-1)}$$

where $\dot{m}_\infty$ = entrained freestream mass flow

$\dot{m}_C$ = coolant mass flow

C_{p_∞} = specific heat at constant pressure of the freestream

C_{p_C} = specific heat at constant pressure of the coolant

The essential differences between all the models stems from how $\dot{m}_\infty/\dot{m}_C$ is handled.

Librizzi and Cresci assume the point of injection and the initial location of the boundary layer development are coincident. Using a 1/7 power velocity profile they found

$$\dot{m}_\infty/\dot{m}_C = 0.329\ (x'/MS)^{0.8}\ [Re_C(\mu_C/\mu_\infty)]^{-0.2} \qquad \text{(A-2)}$$

defining

$$\varsigma = (x'/MS)[(\mu_C/\mu_\infty)Re_C]^{-0.25} \qquad \text{(A-3)}$$

$$\eta^*_{LC} = \frac{1}{1 + 0.329(C_{p_\infty}/C_{p_C})\varsigma^{0.8}} \qquad \text{(A-4)}$$

Kutateladze and Leont'ev assume that the boundary layer starts upstream of injection and that its mass flow at injection equals that

---

*Note subscripts on η refer to initials of investigators responsible for development of the particular expression.

of the coolant. Such an analysis yields

$$\eta_{KL} = \frac{1}{1 + (C_{p_\infty}/C_{p_C})(0.329(4.01 + \zeta)^{0.8} - 1)} \qquad \text{(A-5)}$$

Stollery and El-Ehwany assume that the total mass flow within the boundary layer at the point of injection is zero. This analysis yields

$$\eta_{SE} = \frac{1}{1 + (0.329\ \zeta^{-0.8} - 1)(C_{p_\infty}/C_{p_C})} \qquad \text{(A-6)}$$

Tribus and Klein, neglecting any effects of injection on the mainstream flow, modeled a cooling slot using a line heat source. They found

$$\eta_{TK} = 5.76\ Pr^{2/3}\ (C_{p_C}/C_{p_\infty})\ \zeta^{-0.8} \qquad \text{(A-7)}$$

Goldstein and Haji-Sheikh accounted for the temperature variation through the boundary layer and for the effects of injection on thickening the boundary layer to predict an effectiveness for tangential injection of

$$\eta_{GH} = \frac{1.9\ Pr^{2/3}}{1 + 0.329\ (C_{p_\infty}/C_{p_C})\zeta^{0.8}} \qquad \text{(A-8)}$$

Figure A1 shows the variation in the predicted cooling effectiveness as a function of the dimensionless distance from the cooling slot for all the models previously described. The curves represent M = 0.5 and Re_C = 1000. Lribrizzi and Cresci along with Kutateladze and Leont'ev both assume an average boundary layer temperature while accounting for freestream mass entrainment. They predict the lowest effectiveness.

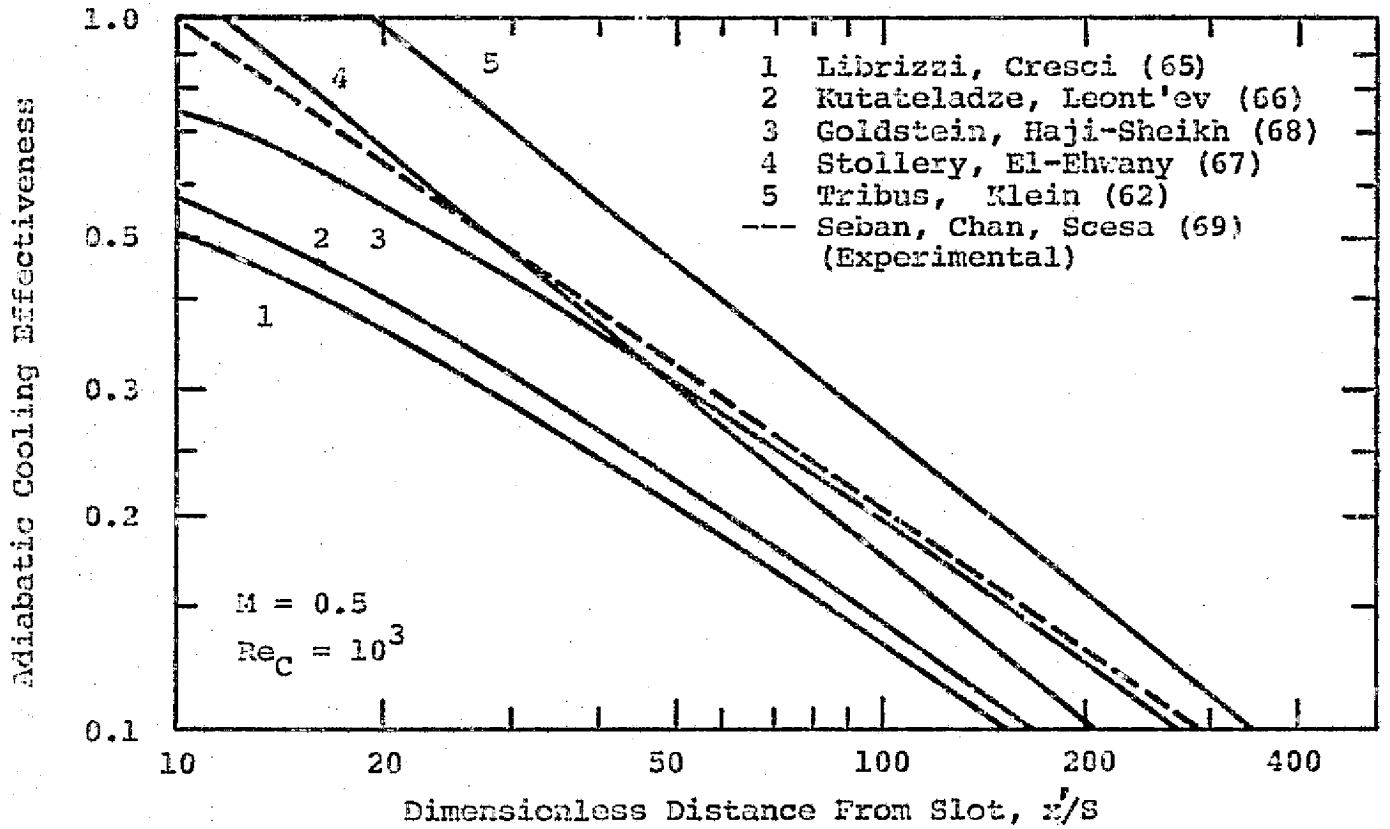

Figure A1. Comparison of Film Cooling Models (2-D).

Tribus and Klein use a representative temperature profile but do not account for entrainment. Their prediction is the highest. Goldstein and Haji-Sheikh incorporate both phenomena and predict effectiveness values between the other two groups. Obviously, neglecting mass addition at injection is too liberal an assumption, while assigning an average temperature to the boundary layer is too stringent. Actually the two effects are counterbalancing as shown by the agreement of the predicted η between Stollery and El-Ehwany (neglecting entrainment and assuming $\bar{T}$ in the boundary layer) and Goldstein and Haji-Sheikh. An empirical correlation from the data of Seban, Chan and Scesa (69) is superimposed on the analytical model comparison of Fig. A1. Their results are in good agreement with Goldstein and Haji-Sheikh as well as Stollery and El-Ehwany.

A.2. Semi-Empirical Relations

Hatch and Papell (70) describe a model in which the coolant is assumed to remain as an unmixed protective film along an adiabatic wall. The effectiveness is described, using an empirical correlation for the effect of V_c/V_∞, as

$$\ell n\, \eta_{ADW} = - \frac{hLx'}{(\dot{w}C_p)_c} - 0.04 \left(\frac{SV_\infty}{\alpha_c}\right)^{0.125} f\left(\frac{V_\infty}{V_c}\right) \qquad (A\text{-}9)$$

for

$$\frac{hLx'}{(\dot{w}C_p)_c} > 0.04$$

and $$\eta_{ADI} = 1 \quad \text{for} \quad \frac{hLx'}{(\dot{w}C_p)_C} < 0.04 \tag{A-10}$$

where $$f\left(\frac{V_\infty}{V_C}\right) = 1 + 0.4 \tan^{-1}\left(\frac{V_\infty}{V_C} - 1\right) \tag{A-11}$$

$$\text{at} \quad \frac{V_\infty}{V_C} \geq 1.0$$

and $$f\left(\frac{V_\infty}{V_C}\right) = \left(\frac{V_C}{V_\infty}\right)^{1.5(V_C/V_\infty - 1)} \tag{A-12}$$

$$\text{at} \quad \frac{V_\infty}{V_C} < 1.0$$

where h = convective external heat transfer coefficient

L = length of coolant slot

$\dot{w}_C$ = flow rate of coolant

C_{p_C} = specific heat at constant pressure of coolant

α_C = thermal diffusivity of coolant

Seban and Back (71) describe the slot injection phenomenon as being similar to a free jet boundary which becomes altered by the proximity of the wall. For thin initial boundary layers at injection, an initial mixing region exists near the slot having velocity profiles similar to those found in a jet boundary flow. The extent of the mixing within this region is strongly dependent on the ratio of coolant to mainstream velocity. Far from injection ($x'/S > 40$), the boundary layer resembles the typical turbulent power law profile. Assuming uniform eddy diffusivity consistent with experimental results and similarity of the temperature profiles, an effectiveness relation was derived of the form

$$\eta^2_{ADW} = 1 + \pi(25.3 \times 10^{-4})M^2 Re_S^{-0.3} \left(\frac{\bar{\beta}}{S}\right)^{1.7} - \left(\frac{\bar{\beta}_1}{S}\right)^{1.7} \qquad \text{(A-13)}$$

where Re_S = Reynolds number of coolant based on slot height, S

$\bar{\beta}$ = $(x + x_0)$, distance downstream from effective origin of boundary layer

$\bar{\beta}_1$ = $(x + x_1)$, where x_1 is distance from slot to where effectiveness was unity

Spalding (72), independently using the same model as Librizzi and Cresci but accounting for entrainment into the boundary layer, developed an effectiveness parameter, ε

where $\varepsilon = \eta_{ADW} = 1$ for $X < 7$ (A-14)

$\varepsilon = \eta_{ADW} = 7/X$ for $X \geq 7$ (A-15)

where $X = 0.91 \left(\frac{x'}{MS}\right)^{0.8} (Re_C)^{-0.2} + 1.41 \left\{\left|1 - \frac{V_\infty}{V_C}\right| \frac{x'}{S}\right\}^{0.5}$ (A-16)

This expression is valid for all velocity ratios, V_C/V_∞. X has been adjusted as shown with properly chosen constants to fit a vast group of experimental data ranging from $V_C/V_\infty = 0$ to 14.

Assuming that the boundary layer starts from the point of injection and that the thermal and hydrodynamic boundary layer thicknesses are equal, Nishiwaki, Hirata and Tsuchida (73) derived an expression for cooling effectiveness of injection through a porous strip along an adiabatic plate.

$$\eta_{ADW} = 0.0877\ B\ (16 - 11\ m\delta)\ m\delta \qquad \text{(A-17)}$$

for $0 < m\delta < 1$

where $(m\delta)$ is the root of the following

$$(m\delta)^3 - 1.5\,(m\delta)^2 + 0.0417 + \frac{1.14}{B} = 0 \qquad \text{(A-18)}$$

and $$B \equiv \left(\frac{\mu_\infty}{q}\right) Re_{x'}^{0.8} \qquad \text{(A-19)}$$

q = weight flow of coolant per width of plate

Eriksen, Eckert and Goldstein (74) present a three-dimensional film effectiveness model in which cooling from a discrete hole is simulated by a moving point source in a semi-infinite medium. An expression for the effectiveness downstream of the source can be shown to be

$$\varepsilon_p = \frac{MV_\infty d_0}{8\eta_{ADW}(x',z')\,\frac{x}{d_0}} \exp\left[\frac{-V_\infty d_0}{4\varepsilon_p\,\frac{x}{d_0}}\left(\frac{y_0}{d_0}\right)^2 + \left(\frac{z}{d_0}\right)^2\right] \qquad \text{(A-20)}$$

where ε_p = point source thermal diffusivity

d_0 = hole diameter

z' = lateral distance from centerline of hole directed along X axis

y_0 = horizontal virtual origin of source above X-Z plane

This analytical model relies on empirical input for both the thermal diffusivity and y_0. At low blowing ratios (M ≈ 0.1) the model agrees well with their effectiveness data (74) for a single hole. At blowing ratios greater than 0.1 and less than 0.5, the model can be useful provided reasonable values of y_0 are inserted to account for separation of the coolant jet from the surface. Provided negligible jet interaction is assumed, the superposition principle can be used with the

model to predict the additive effect of a row of holes or other relatively complex injection configurations.

A.3. Experimental Correlations

Consistent with the predicted governing film cooling parameters derived from a heat sink analysis, a large portion of film cooling data can be represented in the following form where A, b, and c are constants.

$$\eta = A \left(\frac{x'}{MS}\right)^{b} Re_C^{c} \qquad (A\text{-}21)$$

The next few paragraphs will deal with a few studies that were able to describe their data in such a way. All the correlations apply to slot type cooling with essentially negligible differences between the coolant and mainstream temperatures.

Weighardt (75), in his pioneer work on aircraft wing de-icing, found that the film heating data correlated well with the following effectiveness expression for a slot at 30° to the surface.

$$\eta_{ADW} = 5.44 \left(\frac{x'}{MS}\right)^{-0.8} Re_C^{0.2} \qquad (A\text{-}22)$$

Hartnett, Birkebak and Eckert (3), show a similar effectiveness dependency on the blowing ratio for a 30° slot and have correlated their results for $x'/MS \geq 60$ by using

$$\eta_{ADW} = 16.9 \left(\frac{x'}{MS}\right)^{-0.8} \qquad (A\text{-}23)$$

Scesa (76) conducted a study of normal injection that supported the use of the adiabatic wall temperature approach in calculating heat fluxes. Performing both heat transfer and adiabatic wall temperature

tests, development of the expression

$$\eta_{ADW} = 2.20 \left(\frac{x'}{MS}\right)^{-0.5} \qquad \text{for } M > 0.3 \tag{A-24}$$

proved useful in heat transfer calculations by use of the adiabatic wall temperatures for downstream locations not near the injection site.[1]

Seban, Chan, and Scesa (69) provide a tangential slot correlation that shows a somewhat different dependency of η_{ADW} on (x'/MS) and Re_C compared to the previous correlations.[2] They found

$$\eta_{ADW} = 0.83 \, (Re_C)^{1/3} (x'/MS)^{-0.7} \qquad x'/MS > 40 \tag{A-25}$$

and

$$\eta_{ADW} = 0.16 \, (Re_C)^{1/3} (x'/MS)^{-0.25} \qquad x'/MS < 40 \tag{A-26}$$

Samuel and Joubert (78) present the following relation, valid for M less than unity and tangential slot injection

$$\eta_{ADW} = 1 \tag{A-27}$$

for $\left(\frac{x'}{S}\right) M^{-1.75} < 40$

$$\eta_{ADW} = 10.8 \left[\left(\frac{x'}{S}\right) M^{-1.75}\right]^{-0.65} \tag{A-28}$$

for $40 < \left(\frac{x'}{S}\right) M^{-1.75} < 400$

Metzger and Fletcher (10), using a transient heat transfer measuring technique, calculated local heat transfer rates at a wall with and without coolant injection. The ratio of the average heat flux to the wall

---

[1,2]Summarized from review by Metzger (77).

with injection to the heat flux without injection, Φ', was found to be a function of the mass velocity ratio, temperature difference ratio θ_C', x'/S, and the geometry. The value of θ_C' at $\Phi' = 0$ corresponds to the inverse of the standard cooling effectiveness parameter.

$$\theta'_{C,\Phi'=0} = \frac{T_C - T_{T_\infty}}{T_{ADW} - T_{T_\infty}} = \frac{1}{\eta_{ADW}} \tag{A-29}$$

They found for angled slots:

$$\frac{1}{\eta_{ADW}} = 1.0 + 0.00619M^{-1.35}(x'/S) \tag{A-30}$$

for $0.25 \leq M \leq 0.75$, $0 \leq x'/S \leq 70$, $\alpha = 20°$

and

$$\frac{1}{\eta_{ADW}} = 1.0 + 0.01155M^{-0.75}(x'/S) \tag{A-31}$$

for $0.25 \leq M \leq 0.75$, $0 \leq x'/S \leq 70$, $\alpha = 60°$

where α = injection angle.

The list of existing empirical correlations could go on and on with the band of predicted effectiveness values continually widening. Figure A2 makes a simple comparison of the previously presented correlations at a nominal blowing ratio of M = 0.5 and a coolant slot Reynolds number of 10^4. The effectiveness is presented as a function of nondimensional distance from injection. The normal injection of Scesa is understandably low compared to the others. For 30° slot injection (Hartnett, Birkebak and Eckert) the effectiveness improves from the normal configuration. At 20° injection (Metzger and Fletcher) the effectiveness shows even more improvement. There is much inconsistency, however, even in the few correlations that are shown. Wieghardt's 30° slot data seems more

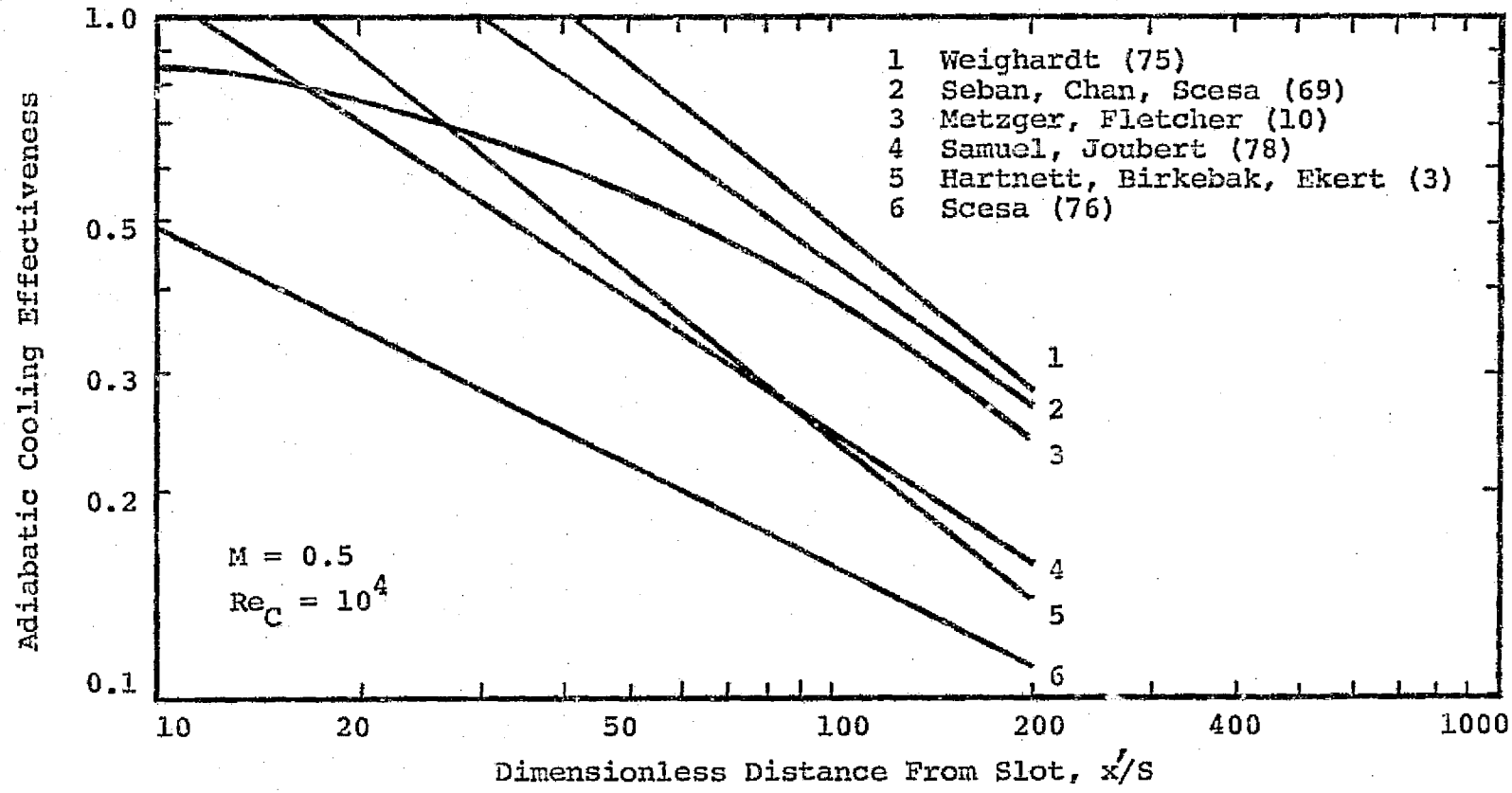

Figure A2. Comparison of Experimental Film Cooling Correlations (2-D).

effective than the tangential cooling results from Seban, Chan and Scesa. Samuel and Joubert's tangential data is shown as less effective than Metzger and Fletcher's 20° correlation.

There is much discrepancy among the various empirical correlations in predicting the film cooling effectiveness for a given injection geometry. As shown in Fig. A1, the analytical model predictions also show the same inability to universally characterize the cooling effect of injection from a specified geometric configuration. This brief review of some of the more important cooling correlations was introduced solely as a means to familiarize one with the parameters that characterize film cooling in general and to emphasize the need to exercise caution in applying film cooling data to real problem situations. No one correlation is recommended as the most suitable for a given application. At present, with such previous information, one can, at best, make only approximate calculations to determine the benefit of a proposed cooling scheme.

APPENDIX B. EXPERIMENTAL APPARATUS DETAILS

B.1. Turbulence Generation Assembly

To estimate the inlet Tu variation by locating grids of different size at varying upstream locations, the theory of isotropic turbulence decay downstream of screens was incorporated (45,46). This theory reveals a linear dependency of the inverse square of the intensity with the distance downstream from the generating grid, x.

$$\frac{1}{Tu_\infty^2} = \frac{c}{C_D}\left[\frac{x}{M_S} - \left(\frac{x}{M_S}\right)_0\right] \qquad \text{(B-1)}$$

where $Tu_\infty = \overline{u'^2}/\overline{V}_\infty$

u' = fluctuating component of freestream velocity

$\overline{V}_\infty$ = time average of freestream velocity

c = constant

C_D = drag coefficient of screen

$\left(\frac{x}{M_S}\right)_0$ = value of $\left(\frac{x}{M_S}\right)$ at $Tu_\infty = 0$

M_S = center-to-center spacing of grid wires

The following constraints were imposed on Eq. (B-1) in designing the turbulence generation system:

(1) $x/M_S \geq 15$ for measurements to insure isotropy;

(2) $M_S/d_W = 2$, set as a lower limit for establishing isotropy at the shortest distance downstream of the grid;

(3) turbulence generation assembly must be as compact as possible;

(4) the point of intensity measurement downstream from the grid assembly must be 1.5 to 2 characteristic model dimensions upstream of the test surface to insure that the presence of the model will not affect the value of the intensity at the measuring location.

An overall working length for the assembly was set at 0.533m (21 in), corresponding to a practical length for a relatively low, estimated turbulence level. This overall length was then subdivided into 3 sections of 0.46m (1.31 in), 0.065m (2.54 in) and 0.381m (13.84 in). Figure B1 shows an exploded view of the three sections in one arrangement relative to the point at which a hot wire probe can be inserted. The 0.046m section serves as a screen holder and allows either of two grids to be positioned at eight different locations upstream of the measuring site.

The three stainless steel rectangular ducts of the turbulence section measure 0.114m (4.5 in) in the lateral direction and 0.244m (9.6 in) in height. The main flow channel prior to the turbulence production assembly consists of a 6.096m (20 ft) straight circular 0.254m (10 in) OD pipe with a slight contraction in the lateral direction when mating to the rectangular turbulence section.

B.2. Instrumentation

B.2.1. Mass Flow Measurement

Orifices, constructed to ASME standards, were the prime means of mass flow measurement for the basic flow system. The main by-pass air was metered through a 0.0737m (2.9004 in) diameter orifice having a

β' = 0.3481 (β' = ratio of orifice diameter to pipe diameter). The combustor was mixed with supply air from a 0.0598m (2.3533 in) venturi with a β' = 0.5796 and natural gas through either of two orifices. For low flow fuel, a 0.0209m (0.824 in) diameter orifice with β' = 0.4238 was used, while higher temperature conditions required using a 0.0266m (1.049 in) diameter orifice with a β' = 0.2852.

Downstream of the test section, the flowrate through each leg of the cascade was monitored with orifice plates. The upper and lower bypass legs had orifice diameters of 0.076995m (3.0318 in) and 0.076990 (3.0311 in) and β' of 0.49980 and 0.49977, respectively. The main test channel flow passed through a 0.1268m (4.9933 in) diameter orifice with a β' = 0.62564.

Film coolant flowrate measurements were handled in three ranges: low, intermediate, and high. For cooling at low blowing ratios, 0.00102m (0.040 in) diameter venturis with β' = 0.1333 measured the mass flow to both the suction and pressure surface coolant plenums. An intermediate set of venturis with β' = 0.2667 and diameters of 0.00204m (0.080 in) covered the widest range of coolant flows. For blowing ratios (M) from 1.25 to 2.0, small 0.0127m (0.5 in) diameter turbine flowmeters handled from 0.708 to 3.305 liter/sec (1.5 to 7 cubic feet per minute).

B.2.2. Test Surface Temperature Measurements

Wall temperature measurements were made using 0.00102m (0.04 in) and 0.00127m (0.05 in) diameter, swedge-type copper constantan thermocouples. A small portion of the magnesium oxide insulation was removed from the stainless sheathing, exposing the copper and constantan

Figure B1.

Locations For Screen Placement in
Turbulence Generation Assembly.

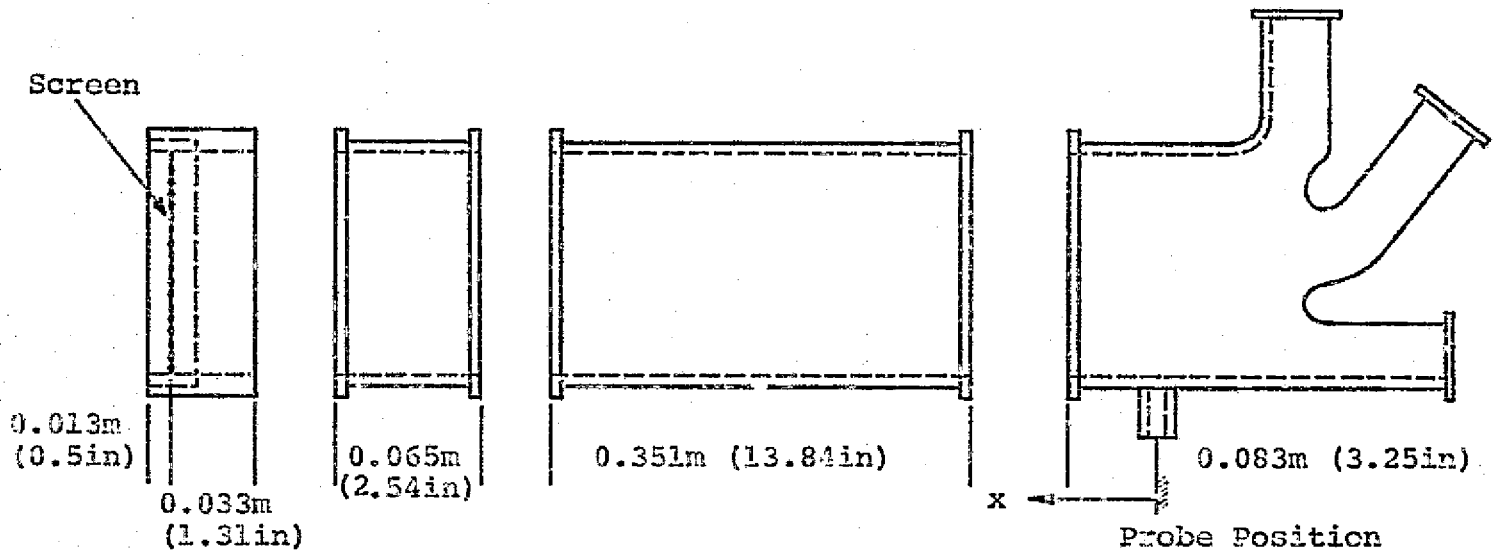

	Screen #1		Screen #2	
x	x/M_S	x/d_W	x/M_S	x/d_W
0.095m (3.75in)	15.00	30.00	12.00	60.00
0.115m (4.56in)	18.24	36.50	14.59	72.95
0.160m (6.29in)	25.16	50.30	20.13	100.7
0.180m (7.10in)	28.40	56.80	22.72	113.6
0.447m (17.59in)	70.36	140.7	56.29	281.5
0.467m (18.40in)	73.60	147.2	58.88	294.4
0.511m (20.13in)	80.50	161.0	64.42	322.1
0.532m (20.94in)	83.76	167.5	67.01	335.1
	M_S = 0.0064m d_W = 0.0032m		M_S = 0.0079m d_W = 0.0016m	

Figure B1.

conductors. A stainless tube with an outside diameter slightly smaller than the sheath inside diameter was placed around the conductors within the outer sheath. This arrangement was heli-arched, the insert tubing providing a filler material for the evacuated space and serving as a conductive medium for the thermocouple junction formed during the arcing process. The wall thermocouples were furnaced brazed at 1089°K - 1144°K (1960°R - 2060°R) into designated hole locations on the test surface and were finished flush with the wall. Exposed-ball or bead-type thermocouples were used in the film plenum cavities. The exposed couples were positioned with the junctions at the center of the plenum, indicating the characteristic mixed film temperature.

B.2.3. Test Surface Pressure Measurements

Static pressure measurements were made with flush mounted 5.08×10^{-4}m (0.02 in) copper tubes brazed into the copper test surfaces. Plenum pressure ports consisted of 5.08×10^{-4}m (0.02 in) holes drilled through to the plenum and sealed on the backside with 0.00102m (0.04 in) OD stainless extension tubing.

B.2.4. Inlet Conditions Measurements

To measure the inlet parameters, three, wedge-shaped, pitot-static, total temperature probes were used: two to traverse the inlet conditions and the remaining probe to monitor the flow conditions at midstream between data points.

Each probe had a head diameter of 0.0043m (0.189 in) and a total length of 0.61m (24 in), 0.559m (22 in) of which incorporated a 0.00635m (0.25 in) diameter reinforcement tube. A chromelalumel thermocouple,

operational to 811°K (1460°R), as well as the pitot tube were located at the apex of the wedge with a static tap on each side of the probe head. Due to the unusual length of traverse, 0.244m (9.6 in) vertically and 0.114m (4.5 in) laterally, the probes were permanently part of a 0.9127m (0.5 in) diameter support sleeve. L. C. Smith actuator systems were used to drive the three probes.

Figure B2 demonstrates the probe measurement system. A differential pressure between both static pressure taps gave an indication of the probe alignment. These two pressures were also fed to a United Sensor Corporation pressure dividing choke that averaged the nearly balanced pressures. The average static condition was referenced to the measured total pressure for a dynamic pressure reading, while the total pressure was read directly against the atmosphere (gage pressure). Factory supplied calibration data showed the total temperature and pressure and static pressure were accurate to within 1/2% up to a Mach number of 0.40.

Prior to the initiation of the actual test program, measurements of the cascade inlet turbulence levels were made over a range of inlet Reynolds numbers and turbulence-generating grid-locations.

Figure B3 illustrates the electrical network used in measurement of the cascade inlet turbulence intensity. A Thermo-Systems Incorporated (TSI) 1220-20 hot film probe was used in conjunction with a TSI 1054 A linearized anemometer for measuring the raw turbulent signal. The anemometer output was fed to both a Fairchild digital voltmeter and an oscilloscope for simultaneous monitoring of the average and instantaneous probe output. In addition, the anemometer output was fed to both a Hewlitt-Packard 3400 A RMS voltmeter and a DISA RMS voltmeter for

Figure B2.

Pressure Measurement Set-Up for Pitot-Static Probe.

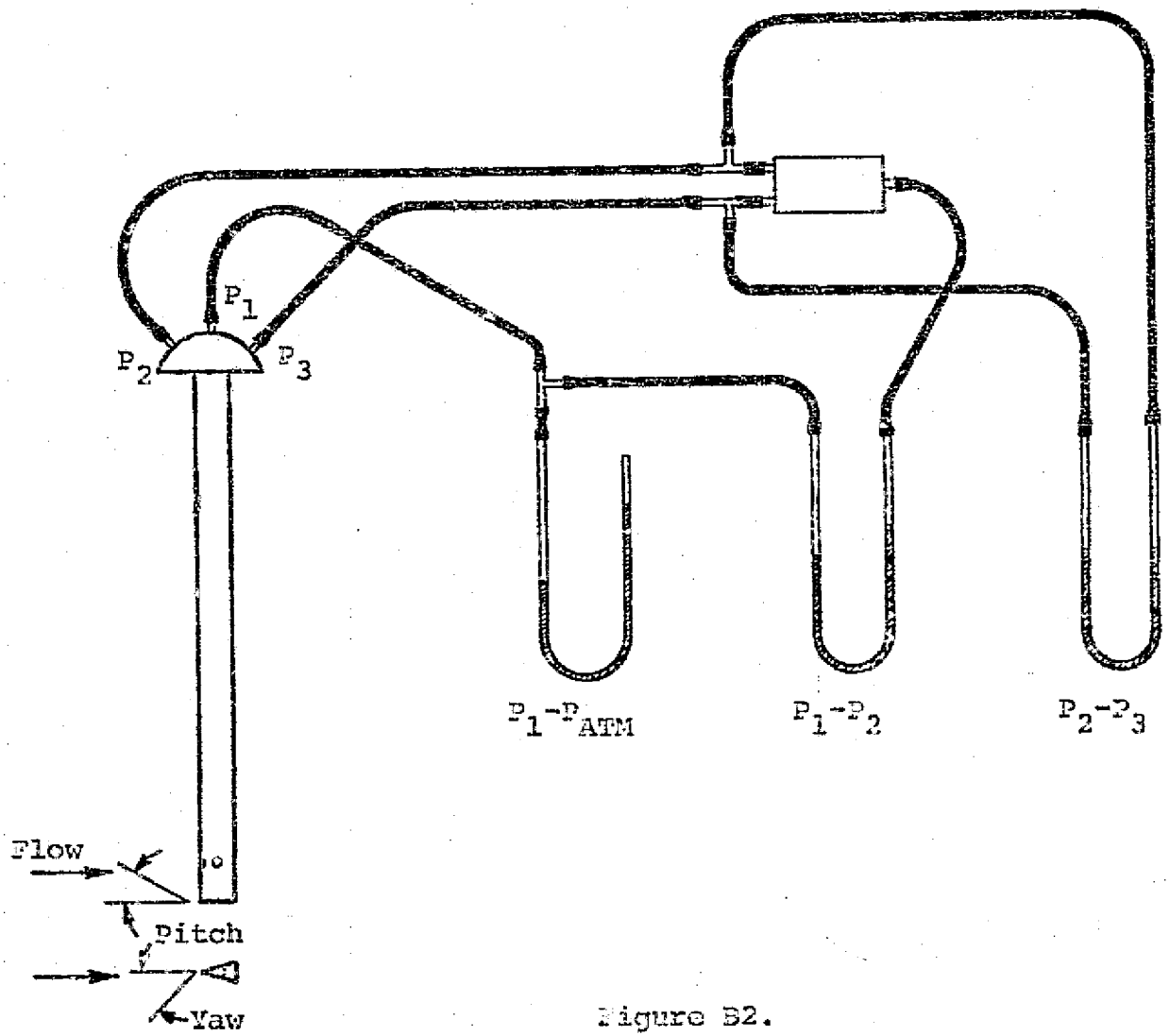

Figure B2.

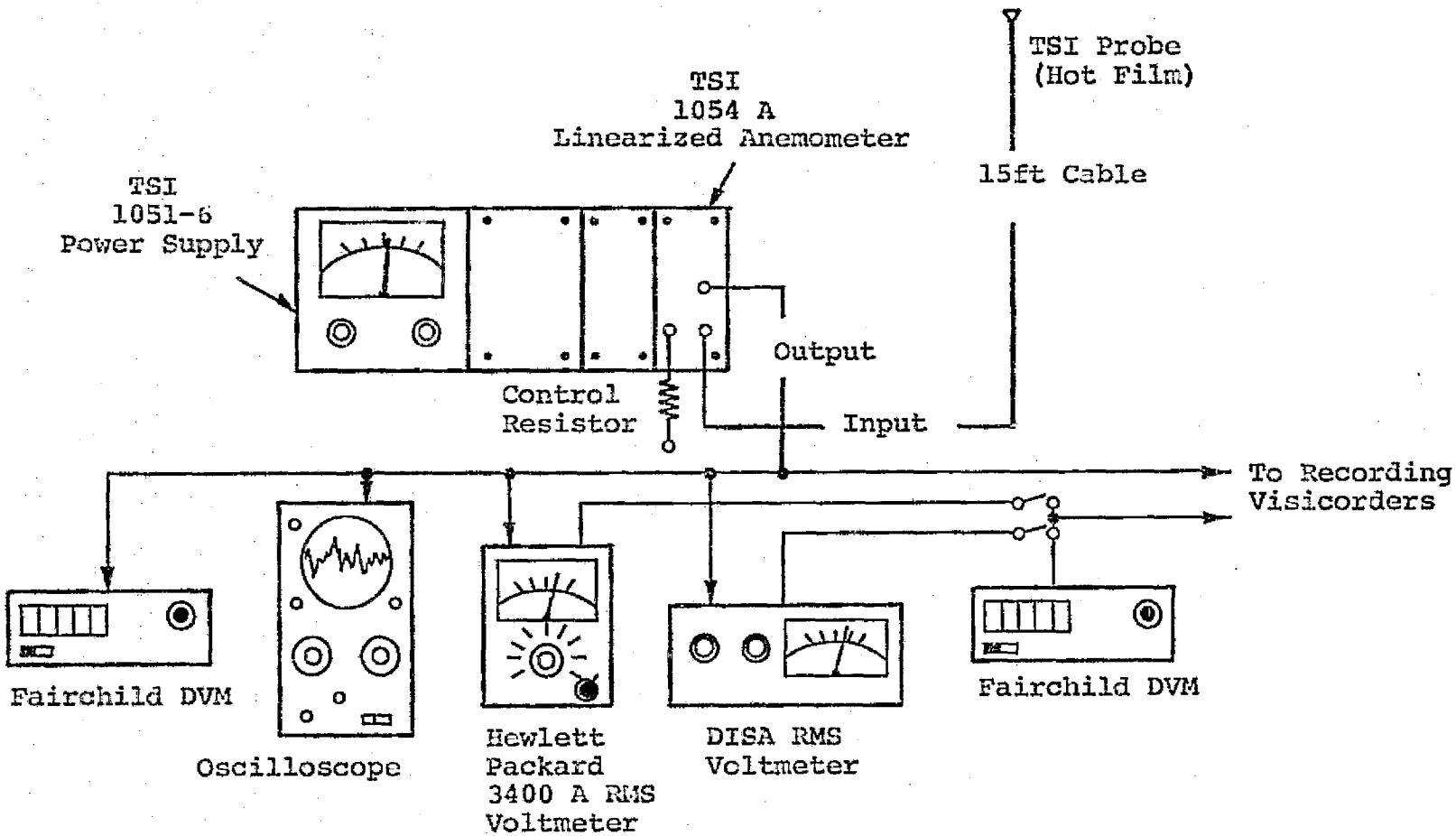

Figure B3. Electronics Set-Up For Turbulence Measurements.

comparison purposes. Direct monitoring of the RMS signal was also obtained using another digital voltmeter. Permanent records of the average and RMS turbulent signals were made on a Visicoder, Model 1108, high response oscillograph.

B.3. Measurement Systems

B.3.1. Raw Data Conversion

All pressure measurements were made using two methods: strain-gage type transducers or a digital automatic multiple pressure recording (DAMPR) system. With DAMPR, the pressures to be measured were all brought into a pressurized chamber, each separated from the main chamber by a pressure sensitive switch. Once the chamber was opened to atmospheric conditions, the chamber pressure decreased and the time to reach equilibrium was recorded with a digital counter. As the chamber pressure fell and reached the input levels of the multiple unknown pressures, the pressure switches opened and recorded a digital opening time with respect to the initial chamber depressurization. A comparison of the time at which each switch opened with a calibration of "time-to-equilibrium" for the depressurized chamber gave an accurate reading of each unknown inlet pressure.

The raw millivolt signal from each thermocouple was referenced to a 338°K (610°R) oven.

The output from the heat flux sensors was brought up to the millivolt range using operational amplifiers with gains near 1000. As mentioned previously, each gage-amplifier set was individually calibrated with the gain adjusted to give 8.64×10^{-3}mv output for each joule/sec-m^2

of incident heat flux. Preston, Model 8300, wide band, floating, differential amplifiers were used as a buffer system to provide both additional gain capability as well as remote zero-setting for the heat flux operational amplifiers.

B.3.2. Data Monitoring

Excluding pressure measurements under the DAMPR system, there were 110 basic measurable quantities in this experiment, generating characteristic output voltages of 0 to 1000 millivolts. The test facility was equipped with a VIDAR, Model 5218, integrating digital voltmeter and a VIDAR, Model 610, low level scanner to continuously monitor these 110 channels. The scanner-voltmeter combination simultaneously scanned the 110 channels every 5 seconds.

Following a complete scan, the VIDAR unit transmitted the information from the 110 channels to a Digital Equipment Corporation, Model PDP-11, minicomputer. A tape-loaded, data reduction program converted the millivolt VIDAR signals to engineering units and proceeded in calculating basic flow parameters. The output routine from the PDP-11 was linked to both a Setchell-Carlson, Model 10M915, and a Tektronix, Model 4010-1, visual display system.

After each scan by the VIDAR unit, the PDP-11 sent updated information to the Setchell-Carlson display unit. The following items appeared after each scan and were used by the test operator to set the desired flow condition at the test section:

Weight Flows:

...by-pass leg
...combustor leg
...fuel flow

...test section, all three channels
...film coolant flow, suction and pressure vane

Temperature:

...total inlet
...film coolant plenum

Pressure:

...total inlet

Inlet Mach Number

Inlet Reynolds Number

Exit Mach Number of Suction Vane

The output routine was interrupted after a specified number of scans and was transferred to the Tektronix Visual display. More detailed information concerning the conditions within the test section was displayed on this unit. A permanent record of the Tektronix display was made using a Model 4610 hard copy unit. A sample copy is shown in Fig. B4. The Tektronix unit was a convenient means for recording test section conditions prior to each data point.

B.3.3. Data Acquisition, Storage and Processing

Once a data call has been placed, the VIDAR scanned channels and the DAMPR signals were simultaneously sent to a central processing center where the digital data was recorded on tape and sent to the computer for temporary storage in a program data set.

As with the PDP-11, a data reduction program was permanently filed in the library of the center's IBM Model 360 Computer. Because the IBM 360 unit was a time sharing system (TSS), the data was processed from any of the numerous remote IBM 2741 terminals. The test facility had both a remote terminal and a Versatech, Model 200A, matrix

ECRL-2 PROGRAM 15 RESULTS AT 01:58:19

WCA :	0.000	WHG :	0.000	WG :	0.000	WBY1:	0.000
WBY2:	0.000	WMT :	0.000	WFC1:	0.0000	WFC2:	0.0000
WIN :	0.000	WTO2:	0.000	WTO1:	0.000	TTOT:	72.184
PTOT:	14.330	VIN :	0.000	MIN :	0.000	PSND:	14.313
PSTA:	14.313	RER :	0.00				

	PRESSURE VANE	SUCTION VANE
COOLANT MASS FLUX	MFCP: 0.0	MFCS: 0.0
HOT GAS MASS FLUX	MFPI: 0.0	MFSI: 0.0
MASS VELOCITY RATIO	MVRP: 0.000	MVRS: 0.000
MOMENTUM FLUX RATIO	MORP: 0.000	MORS: 0.000
COOLANT TEMPERATURE	TFCP: 79.4	TFCS: 79.9
REYNOLDS # AT INJECTION	REYP: 0.0	REYS: 0.0
GAS TO WALL TEMP RATIO	TRP : 0.986	TRS : 0.987
COOLANT TEMP RATIO	CTRP: 0.987	CTRS: 0.986

PRESSURE VANE				SUCTION VANE			
HEAT FLUX	WALL TEMPERATURES			HEAT FLUX	WALL TEMPERATURES		
201.620	79.53	79.49		684.068	79.49	79.40	
-331.233	79.75			374.437	79.49		
36.004	79.40	79.66		64.806	79.66	79.88	
36.004	79.57	79.49	79.66	50.405	79.49	79.35	79.31
72.007	79.71			43.204	79.40		
28.803	79.66			50.405	79.31		
43.204	79.88			-648.065	79.44		
				50.405	79.27		

PLENUM TEMPERATURES

79.18 79.44 79.18 79.53 79.88 79.35

SUCTION VANE EXIT MACH NUMBER

0.00

PROBE CALCULATIONS

Z1: 4.721 Y : 9.839 Z3: -0.226

Figure B4. Sample of Permanent Record of Test Conditions From Textronix Visual Display Unit.

printer/plotter. Any data that was taken could be immediately reduced using the TSS system.

The printed output could be displayed on the 2741 terminal or on the Versatec.

B.4. General Test Procedure

The recording of a typical data point began by setting the overall flow conditions within the test section. With a pitot-static, total temperature probe positioned at midchannel, just upstream of the test surfaces, the total temperature, total pressure, exit Mach number at the suction vane, and test section flow-splits were adjusted for proper reduced-condition simultation of a high pressure, high temperature environment.

The film coolant flow rate was set and a permanent record of the test conditions was taken with the hard copy unit. The set-point probe was then fully retracted from the stream, leaving a clear channel.

The heat flux levels at the test vanes were then recorded, on a Visicoder, Model 1108, high response oscillograph, in the absence of any upstream probes. This served simply as back-up data in the event that some malfunction occurred in the VIDAR system.

The next step in the data taking procedure was the actual test call. However, a brief description should be made of the sequence of events that constitute a data call. The call itself initiated a sixteen-cycle process wherein the vertical and horizontal pitot-static, total temperature probes mapped the inlet conditions. Cycle one began with the vertical probe fully extended to the top of the test channel, at which

point the VIDAR unit scanned the first 68 input channels, sending the signals to the central processing center. The vertical probe then stepped down the channel, stopping automatically every 0.0152m (0.6 in) for a 68 channel scan. At the ninth cycle, the horizontal probe actuated 0.0127m (0.5 in) into the stream. The two probes traversed together the last 8 cycles until, after the 16th cycle, the vertical probe was entirely retracted and the horizontal probe reached the opposite wall. The 16th cycle was a special scan in that all 110 channels were sampled. The computer program then averaged the sixteen, cycle signals from the first 68 channels and used this information with the 16th cycle signals from channels 69-110 to perform the required data reduction. Figure B5 is a diagram of the 16-cycle, probe-actuation process. The same procedure can be accomplished without the probes in the stream by manually signaling VIDAR that the probes were in the proper location to execute a scan. This, of course, requires simulating the probe actuation with 16 manual calls.

Continuing, then, to describe the data taking procedure, sixteen manual cycles were recorded, followed immediately by 16 automatic cycles using the probes as previously described. The reason for the dual nature of the cyclic data was due to the influence of the inlet probes on the measured heat transfer to the test surfaces. The manual cycles were recorded with no probe influence. The heat flux data obtained from this manual procedure was temporarily stored. Immediately following, the automatic cyclic data was sent for reduction with the temporarily stored heat flux signals from the previous manual process substituted one-to-one into the automatically actuated cyclic data. In essence,

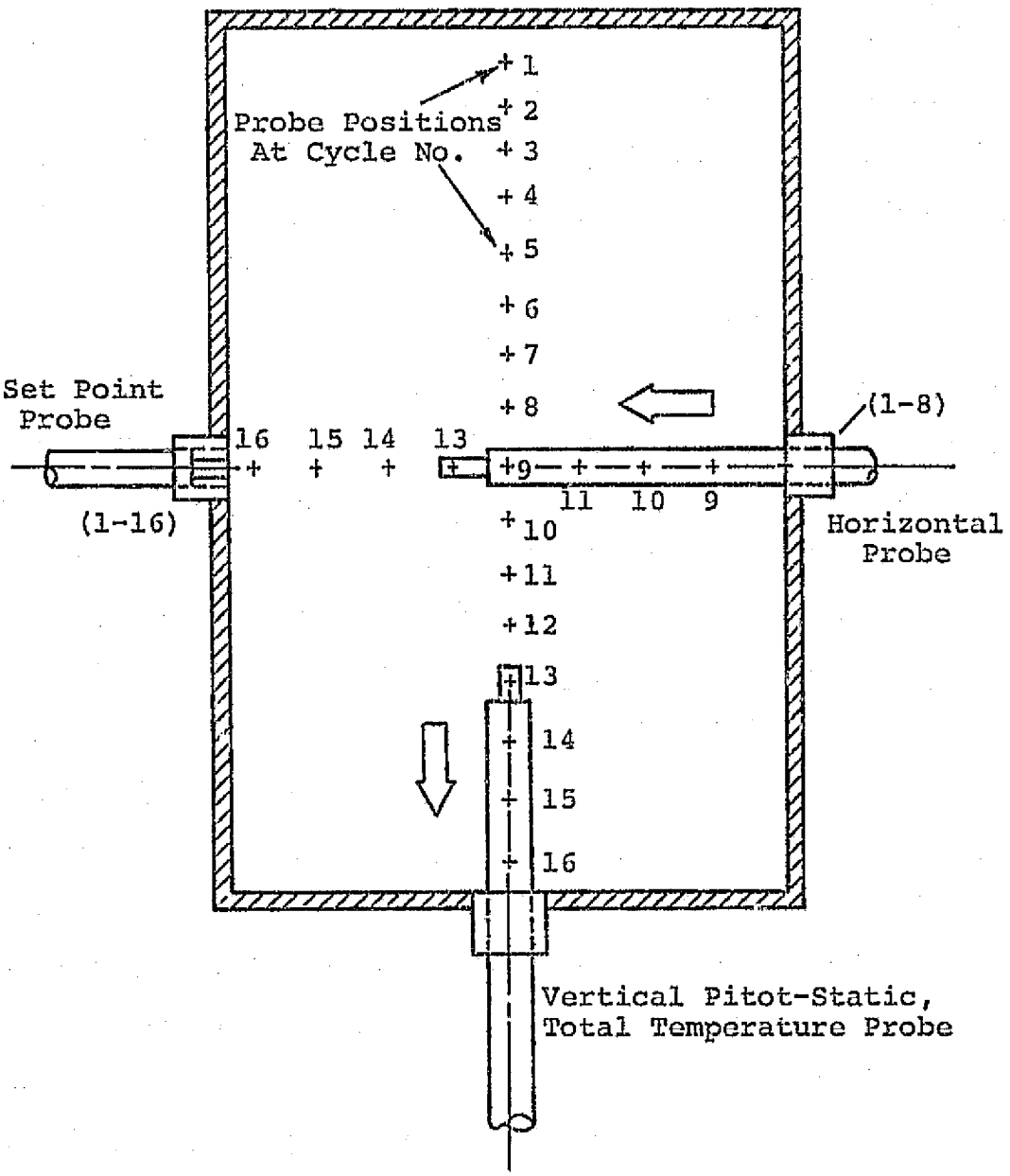

Figure B5. Illustration of Horizontal and Vertical Probe Actuation During a Data Call.

two data points were required for processing a true test condition. The printed output data indicated from which reading the measured heat flux was chosen.

The horizontal set-point probe was returned to midstream following the probe cycling. Any changes in the flow conditions could be made and the procedure was ready to be repeated.

APPENDIX C. HEAT FLUX SENSOR PERFORMANCE

Generally, the miniature, Gardon heat flux transducers used in the subject investigation functioned satisfactorily; providing film cooling effectiveness information while operating within a severe thermal environment. The nature of the Gardon gage operation (as previously described in IV.1.4.5.) allowed heat transfer measurements to be made under conditions of large temperature differences through the boundary layer (i.e. gage at cool, wall temperature with hot mainstream). This is one important requirement for modeling high temperature and pressure gas turbine vane heat transfer. The dimensions of the subject heat flux transducers were small in comparison to the test surface characteristic length, providing, essentially, point measurements while offering little disturbance to the external flow and boundary layer development.

During the course of the subject investigation some difficulty was encountered with the operation of a few gages, especially on the pressure surface of the vane channel. It became exceedingly more difficult, as time passed, for these gages to reproduce the heat flux reference conditions necessary to qualify the film cooling data.

Recall for a moment the data qualification criterion. Heat flux measurements under film cooling conditions were referenced to the uncooled conditions (i.e. q''_{FC}/q''_0) to define a cooling effectiveness. If q''_0 changed more than 3% during the time the cooling data were taken, no cooling effectiveness values could be calculated and the data was discarded.

During a period following the dry-wall heat transfer measurements, q''_0 at each gage location on the pressure surface was very difficult to reproduce.

Figure C1 illustrates the variation in the reference heat flux level (as characterized by $ST_{0,X}$) for the pressure surface as a function of time during a run and as a function of day to day operation. The vertical bands represent the variation in $ST_{0,X}$ (i.e. q''_0 reference) during a given day. Four different days during which film cooling heat transfer was measured are illustrated by the bands labeled a, b, c, and d. Generally, the majority of the reference q''_0 levels (bands at each of the various Re_X represent output from a single gage; 6 gages are represented in Fig. C1) varied much more than 3% during the time interval in which film cooling data were recorded. Consequently, few q''_{FC}/q''_0 values satisfied the data qualification criterion.

In contrast to the pressure surface, a similar display of the variation in the reference conditions is shown in Fig. C2 for the suction surface for the same time interval as Fig. C1. Most of the bands of $ST_{0,X}$ variation for the suction surface are within 3% of a mean value, thus satisfying the qualification condition.

By examining both Figs. C1 and C2, a trend of an increasing average reference condition can be detected (i.e. mean value of bands increases as one proceeds from "a" to "d"). This phenomenon is more pronounced for the pressure surface than the suction surface. The reason for this occurrence was found to be a sensitivity change in the basic sensor. A recalibration of the sensors on the pressure surface verified that some gage sensitivities had changed by a factor of 2 over an extended

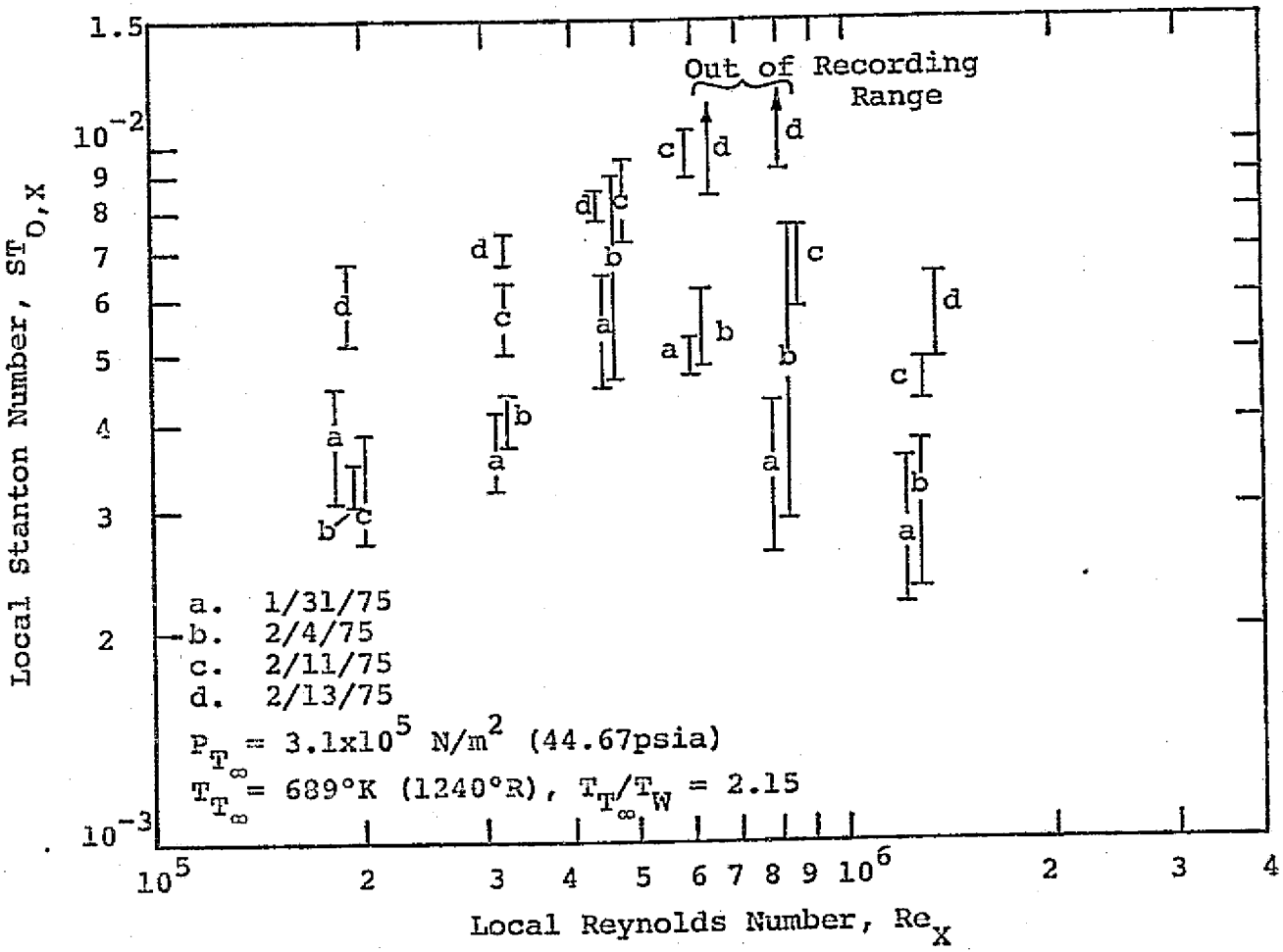

Figure C1. Variations in Pressure Surface Reference Conditions.

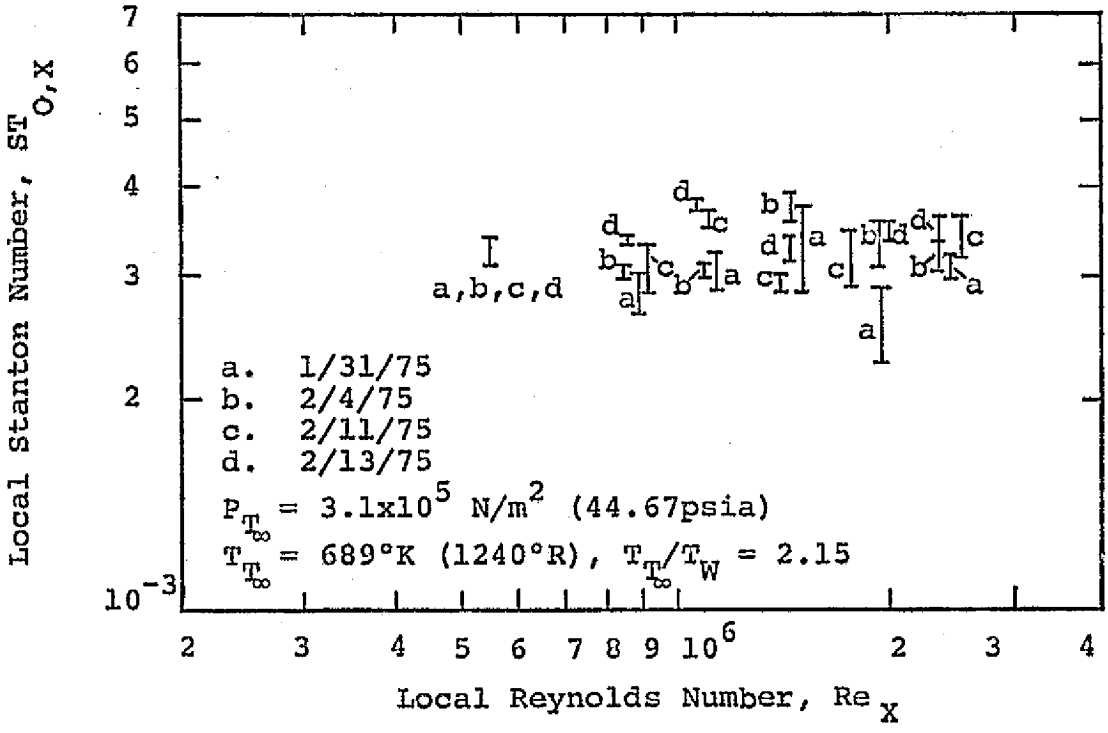

Figure C2. Variations in Suction Surface Reference Conditions.

exposure period to the hot combustor gages. A spectrographic analysis of a residue which formed on the test surface during a run time of extended duration (cleaning of this residue from the test surface using a non-corrosive solution was a regular practice following each test) offered a plausible explanation for this sensitivity change.

Large amounts of copper as well as traces of clorides and nitrates were detected in the residual specimen. The presence of nitrates suggests that nitric acids may have been forming in the combustion products, creating a corrosive environment at the test vane surfaces. Since the heat flux gage sensitivity is inversely proportional to the foil thickness (48), the gradual decay of the thin foil (2.54×10^{-6}m, 0.001 inch) resulted in a much larger ΔT across the foil for a constant incident heat flux.

Fortunately, film cooling effectiveness data was the primary information to be obtained and was of a relative nature. Therefore, if the sensing device was linear and remained linear with time, even though the sensitivity changed (as was verified by the recalibration of the pressure surface gages), the cooling effectiveness would be unaffected. This is true, however, only if the time interval between measurements of q''_{FC} and q''_0 for a particular set of coolant conditions is much smaller than the time for the gage sensitivity to change significantly. Consequently, all data that were taken in which a film cooling data point was immediately followed by a reference reading were determined to be accurate due to the short time interval between data points relative to the time for a sensitivity change. For the cases in which many film cooling conditions were set between reference checks, only that data was acceptable in which

the reference points, from beginning to end, did not deviate much from the initial reference. Small variations were acceptable (less than ~ 3% change), and an average reference was defined using the initial and final reference values.

APPENDIX D. CALIBRATION OF FILM COOLING PLENUM

Although the film coolant temperature was monitored prior to the vane plenum chambers, uncertainty in the exit temperature of the coolant increases as the wall temperature increases and the blowing ratios approach zero. An attempt was made to model those conditions which were expected to influence the degree of heat addition experienced by the coolant as it passed through the injection holes.

A simple experiment to approximate fluid heat addition by flow through tubes with hot walls consisted of passing heated coolant air into a water-cooled vane film plenum. The water maintained a relatively constant, cool, wall temperature for various flowrates of heated plenum air. A stainless steel, plenum supply-line was electrically heated using a heater tape capable of reaching 478°K (400°F) at a maximum voltage level of 110 volts AC. A Variac was used to control the voltage to the heater tape such that coolant temperature, measured just at the entrance to the plenum, could be varied from ambient conditions to 367°K (200°F). A fine, open-bead, copper-constantan thermocouple was attached to the outside of the vane wall with the couple positioned at the exit of a coolant hole. This exit temperature thermocouple was small in comparison to the coolant hole diameter and was positioned at the centerline of the hole. The vane wall temperature averaged 302°K (83.9°F) and varied only 0.2% from this mean over all coolant flowrates and temperatures.

A prediction of the heat addition through the coolant holes was made using a simple heat balance on the flow through a tube of constant diameter and wall temperature. Entrance effects were considered concerning the local heat transfer coefficient using a relation suggested in (79)

$$h_x = (0.036)\frac{k}{d_0}(Re_{d_0})^{0.8}(Pr)^{0.4}\left(\frac{T_B}{T_W}\right)^{0.18}\left(\frac{d_0}{x}\right)^{0.2} \qquad (D\text{-}1)$$

where k = thermal conductivity of coolant

T_B = bulk coolant temperature

The differential equation for the bulk fluid temperature passing through a tube with a wall temperature, T_W, and heat transfer coefficient as in Eq. (D-1) is

$$\dot{m}_C\, C_{p_C}\frac{dT_B}{dx} = h_x(T_W - T_B)\pi d_0 \qquad (D\text{-}2)$$

where $\dot{m}_C$ = coolant mass flow rate

C_{p_C} = specific heat at constant pressure for the coolant

Assuming that $\left(\frac{T_B}{T_W}\right)^{0.18}$ in Eq. (D-1) does not differ significantly from unity over the temperature ranges of interest, Eq. (D-2) can be solved with the following result

$$\frac{T_W - T_B}{T_W - T_{C,i}} = e^{-C_1 x^{*-0.8}} \qquad (D\text{-}3)$$

where $T_{C,i}$ = coolant bulk temperature at inlet ($x = 0$)

x^* = dimensionless distance (x/d_0)

and

and $$C_1 = \frac{0.2059 k_c}{\dot{m}_c^{0.2} \mu_c^{0.8}} \qquad \text{(D-4)}$$

where k_c = thermal conductivity of coolant

μ_c = dynamic viscosity of coolant

Equation (D-4) assumes that both the Prandtl number and specific heat do not change significantly over the temperature range of interest.

Figure D1 shows the variation in the coolant temperature rise ratio with the parameter $C_1 x^{*0.8}$ for $x^* = 4.4$ (value for $x = L'$ for this test). The data is shown for five coolant flowrates ranging from 5.45×10^{-4} to 4.32×10^{-3} kg/sec (0.0012 to 0.0095 lbm/sec). The prediction using Eq. (D-1) for h_x can be adjusted to fit the data provided the 0.036 constant in Eq. (D-1) is increased by a factor of 8. Such an adjustment is not unreasonable considering the short length-to-diameter ratio of the hole ($L'/d_0 = 4.4$). Figure D1 is the calibration curve used to correct the inlet film coolant temperature for the present study. Over the range of coolant flowrates investigated, the change in the exit coolant temperature represented, at most, a 7% change in θ_c' from a mean value of 1.03.

Figure D1.

Calibration of Film Coolant Plenum
For Heat-Pick Through Coolant Holes.

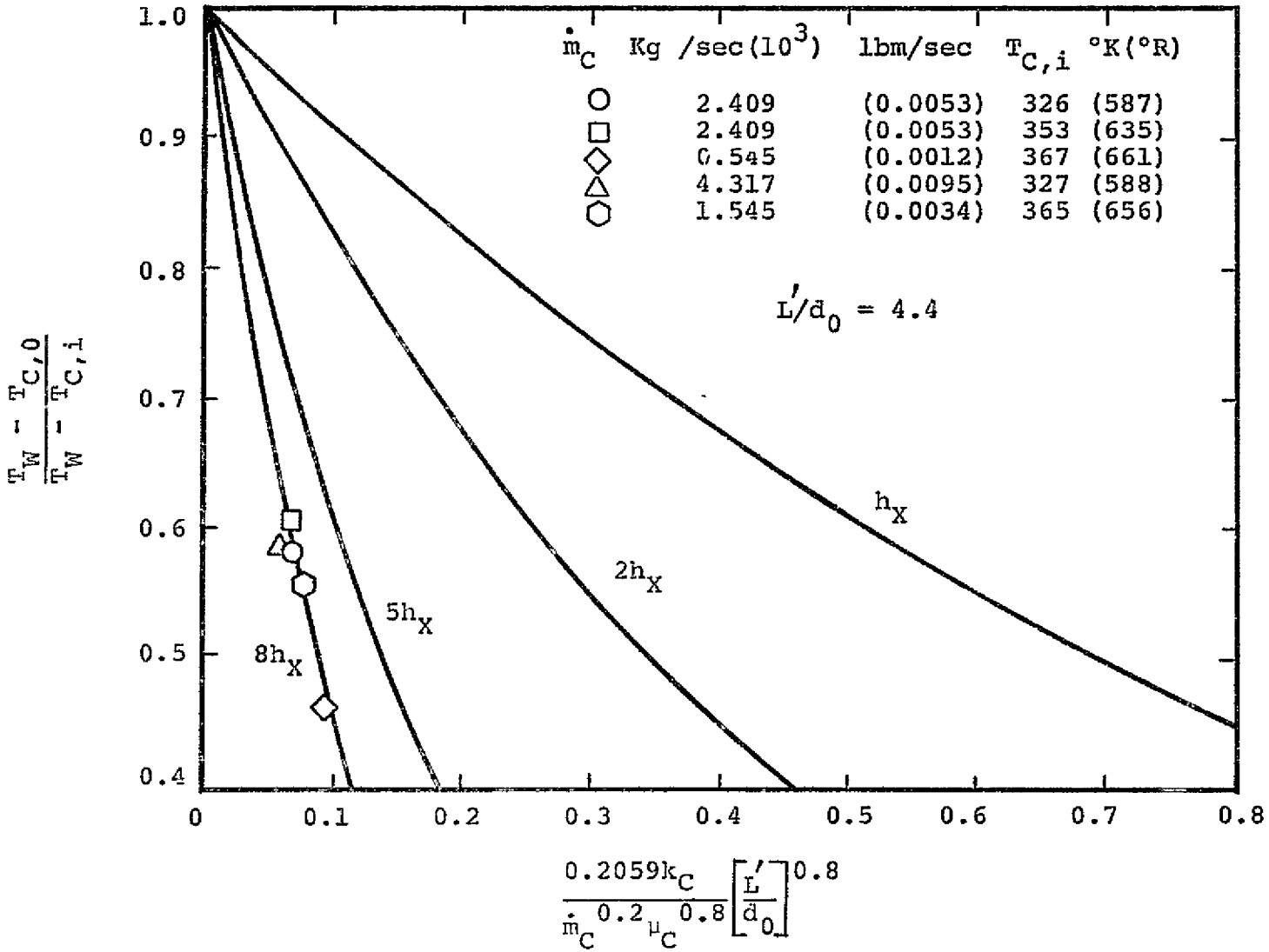
$\dot{m}_C$ Kg /sec(10^3) lbm/sec $T_{C,i}$ °K(°R)
2.409 (0.0053) 326 (587)
2.409 (0.0053) 353 (635)
0.545 (0.0012) 367 (661)
4.317 (0.0095) 327 (588)
1.545 (0.0034) 365 (656)
$L'/d_0 = 4.4$
h_X
$2h_X$
$5h_X$
$8h_X$
$\frac{T_W - T_{C,0}}{T_W - T_{C,i}}$
$\frac{0.2059 k_C}{\dot{m}_C^{0.2} \mu_C^{0.8}} \left[\frac{L'}{d_0}\right]^{0.8}$
1.0
0.9
0.8
0.7
0.6
0.5
0.4
0
0.1
0.2
0.3
0.4
0.5
0.6
0.7
0.8

Figure D1.